RF-MEMS switches for reconfigurable antennas

A thesis submitted for the degree of

Doctor of Philosophy

by

Michail N. Spasos

School of Engineering & Design

Brunel University

July 2011

ABSTRACT: Reconfigurable antennas are attractive for many military and commercial applications where it is required to have a single antenna that can be dynamically reconfigured to transmit or receive on multiple frequency bands and patterns. RF-MEMS is a promising technology that has the potential to revolutionize RF and microwave system implementation for next generation telecommunication applications.

Despite the efforts of top industrial and academic labs, commercialization of RF-MEMS switches has lagged expectations. These problems are connected with switch design (high actuation voltage, low restoring force, low power handling), packaging (contamination layers) and actuation control (high impact force, wear, fatique). This Thesis focuses on the design and control of a novel ohmic RF-MEMS switch specified for reconfigurable antennas applications.

This new switch design focuses on the failure mechanisms restriction, the simplicity in fabrication, the power handling and consumption, as well as controllability. Finally, significant attention has been paid in the switch's electromagnetic characteristics.

Efficient switch control implies increased reliability. Towards this target three novel control modes are presented. 1) Optimization of a tailored pulse under Taguchi's statistical method, which produces promising results but is also sensitive to fabrication tolerances. 2) Quantification of resistive damping control mode, which produces better results only during the pull-down phase of the switch while it is possible to be implemented successfully in very stiff devices. 3) The "Hybrid" control mode, which includes both aforementioned techniques, offering outstanding switching control, as well as immunity to fabrication tolerances, allowing an ensemble of switches rendering an antenna reconfigurable, to be used.

Another issue that has been addressed throughout this work is the design and optimization of a reconfigurable, in pattern and frequency, three element Yagi-Uda antenna. The optimization of the antenna's dimensions has been accomplished through the implementation of a novel technique based on Taguchi's method, capable of systematically searching wider areas, named as "Grid-Taguchi" method.

This work is dedicated to my wife Karin for her comprehension, patience and unconditional support all these three years.

Contents

Acknowledgements

I gratefully acknowledge Dr Rajagopal Nilavalan for giving me the opportunity to pursue my Ph.D. under his guidance. I sincerely appreciate his time and support for my research on RF-MEMS switches and reconfigurable antennas, as well as his help in improving this dissertation.

I would like also to thank the Council of Alexander Technological Educational Institute of Thessaloniki for their support.

List of Tables

List of Figures

List of Symbols

A	m^2	electrode surface area
C	F	capacitance
C_{el}	F	capacitance created between electrode and cantilever
C_c	F	capacitance created between contact and cantilever
C_{sw}	F	total capacitance of the switch
Q	C	electronic charge
V_{pi}	V	pull-in voltage
V_{pd}	V	pull-down voltage
V_s	V	applied voltage
V_b	V	buckling voltage
V_{pk}	V	peak voltage
f_0	Hz	resonance frequency
ω_0	rad	circular resonance frequency
I	A	current
m	kg	mass
t_s	s	switching time
$t_{p(on)}$	s	tailored pulse time for pull-down phase
$t_{p(off)}$	s	tailored pulse time for release phase
t_r	s	rise time of the tailored pulse
t_f	s	fall time of the tailored pulse
v	m/s	velocity
ε_0	F/m	permittivity of the free air (8.86×10^{-12})
e_r		relative permeability
$e_{r(eff)}$		effective relative permeability
g_0	m	cantilever's initial height from electrode
g	m	cantilever's remaining height from electrode
d	m	idealized parallel deflection of the cantilever
w	m	the width of the cantilever
l	m	the length of the cantilever
t	m	the thickness of the cantilever

k	N/m	spring constant
E	GPa	Tensile (Young's) modulus (E_{Au}=57)
I_Z	m^4	the area (second) moment of inertia about the z-axis
ρ	Kg/m^3	density (ρ_{Au}=19280)
α	m	distance from the anchor to the middle of the electrode,
F_a	N	applied force
F_m	N	mechanical force
F_e	N	electrostatic force
F_r	N	restoring force
F_c	N	contact force
d_C	m	contact material vertical deformation
μ_0	H/m	magnetic permeability of the air ($1.25x10^{-6}$)
ρ	Kg/m^3	density (ρ_{Au}=19280 Kg/m^3)
σ	S/m	conductivity (σ_{Au} =$4.09x10^7$)
δ	m	skin depth
μ	kg/ms	viscosity of ideal gases at STP (1.845×10^{-5})
c_{res}	Nm/s	resonance damping coefficient
c_{crit}	Nm/s	critical damping coefficient
ζ	nd	damping ratio
a	s^{-1}	Rayleigh damping parameter
b	s	Rayleigh damping parameter
λ_0	m	wavelength of the open air
λ_g	m	quided wavelength
U	J	energy
U*	J	co-energy
S11	nd	reflection coefficient
S21	nd	gain coefficient
P	W	power
Z_0	Ohm	characteristic impedance
L_s	H	self inductance of the cantilever
R_s	Ohm	DC resistance of the cantilever
Rc	Ohm	contact resistance
R_{sw}	Ohm	total DC resistance of the cantilever

List of publications

1. **Spasos M. and Nilavalan R.,** *On the investigation of a reliable actuation control method for ohmic RF MEMS switches,* Microelectronics journal, Elsevier, 2011, (In press)

2. **Spasos M., Tsiakmakis K., Charalampidis N., Nilavalan R., Cheung S. W.,** *Optimization of a 12GHz microstrip antenna array using Taguchi's method,* International Journal of Antennas and Propagation, 2011, (In press)

3. **Spasos M., Tsiakmakis K., Charalampidis N., Nilavalan R.,** *RF-MEMS Switch actuation pulse optimization using Taguchi's method,* Springer, Microsystems Technologies, 2011, DOI 10.1007/s00542-011-1312-0

4. **Spasos M., Charalampidis N., Tsiakmakis K., Nilavalan R.,** *Improving controllability in RF-MEMS switches using resistive damping,* EUMA, MEMSWAVE 2011, Athens, Greece, June 2011

5. **Spasos, M., Charalampidis N., Tsiakmakis K., Nilavalan R.,** *An easy to control all-metal in-line-series ohmic RF-MEMS switch,* Springer, *Journal of* Analog integrated circuits and signal processing, 2010, DOI 10.1007/s10470-010-9573-6.

6. **Spasos, M., Charalampidis N., Tsiakmakis K., Nilavalan R.,** *Analysis and design of an all metal in line series ohmic RF-MEMS switch for microwave applications,* In Proceedings DTIP, Seville, Spain, May 2010, pp. 27-32.

7. **Spasos M., Charalampidis N., Tsiakmakis K., Nilavalan R.,** *Design considerations of an all metal in line series RF-MEMS switch,* In Proceedings, 3rd STIMESI Workshop on MEMS and Microsystems Research and Training, Prague, Chech Republic, November 2009.

8. **Spasos, M., Charalampidis N., Kampitaki D, Mallios, N., Tsiakmakis K., Nilavalan R.,** *On the design of an Ohmic RF-MEMS Switch for reconfigurable microstrip antenna applications,* WSEAS, TRANSACTIONS on COMMUNICATIONS, 2009, Vol. 8, pp. 153-161.

9. **Spasos M., Charalampidis N., Kampitaki D., Mallios N., Tsiakmakis K., Nilavalan R.,** *An ohmic RF-MEMS Switch for reconfigurable microstrip array antennas built on PCB,* WSEAS, CSECS'08, Tenerife December 2008, pp. 98-103.

10. **Spasos, M., Charalampidis N., Kampitaki D., Mallios N., Tsiakmakis K., Nilavalan R.,** *A novel design for an RF-MEMS resistive switch on PCB substrate,* In Proceedings, 2nd Stimesi Workshop on MEMS research and education: II, Berlin, Germany, November 2008.

Under Review

1. **Spasos M. and Nilavalan R.,** *On the comparison between two all-metal in-line-series ohmic RF-MEMS switches,* Microelectronics journal, Elsevier, 2011, (Under review)

Under Preparation

1. **Spasos M. and Nilavalan R.,** Grid Taguchi antenna

2. **Spasos M. and Nilavalan R.,** Reconfigurable Yagi-uda Antenna

1. Introduction

1.1. Switches

The principal parts in an electric circuit are a source of electrical energy, a load and a complete path for the flow of current. If any one of the above requirements is not fulfilled, current cannot flow in the circuit and the energy from the source cannot be delivered to the output device. "*A switch is an electrical component for opening and closing the connection of a circuit or for changing the connection of a circuit device.*" [1]. Switches are vital components of all automated systems as they provide an interface between systems and devices with the capability for automatic redirection of signals, enhancing their flexibility and expandability. An ideal switch exhibits zero resistance to current flow in the ON state and infinite resistance to current flow in the OFF state; in real world a practical switch design exhibits a certain amount of resistance in the ON state and a finite resistance in the OFF state. The exponential growth of electronic applications resulted to the development of several types of switches with different characteristics. Thus, the choice of the proper switch is essential in order to achieve as less interference as possible to the circuit operation.

1.2. RF switches

RF switches are playing a key role in the development of the modern communications systems. When an RF system is considered, the simple wire or bus connectors used in standard electric circuits are replaced by coaxial and microstrip lines and the switches are become more complicated devises as they introduce resistance, capacitance and inductance in signal-to-signal and signal-to-ground paths. The wide frequency spectrum used for RF applications requires different switch technologies for various frequency-bands of application. The appropriate selection of the most suitable RF switch can make the difference in not only meeting the intended design goals but also reaching marginal performance. Taking great care of the specifications, an RF switch can be optimized to achieve the desired performance for specific applications [2].

1.2.1. Specifications of RF Switches

The RF characterization of switches is defined by the scattering (S) parameters. These parameters describe the switch's behavior when RF signals are passing through them. Additionally there are some more parameters which do not have the same significance for all types of switches, but they describe efficiently the operation of the switches and their capability to work adequately in different RF applications.

1.2.1.1. Insertion loss

The insertion loss of an RF device describes its efficiency in signal transmission. In the case of a switch, the insertion loss is specified only when the switch is in the ON state or in any way a signal is getting transmitted through. This is specified in terms of the transmission coefficient S_{21} (dB), between the input and output terminals of the switched circuit. The understanding of the concept of insertion loss can be done considering a switch as a low-pass filter. Every switch has some parasitic capacitance, inductance and resistance. The combination of these parasitic components attenuates and degrades the signal the switch is routing. The power loss and voltage attenuation caused by these components, varies with the frequency of the input signal and can be quantified by the insertion loss specification of the switch.

1.2.1.2. Isolation

Isolation is defined as the magnitude of a signal that gets coupled across an open circuit. The isolation of a switching system is specified when there is no signal transmission through the switch. This is also defined as transmission coefficient S_{21} (dB), between the input and output terminals of the switched circuit when the switch is in the OFF state. Isolation is also a frequency depended feature, either in the case of semiconductor-based solid–state switches, where it is represented mainly by parasitic capacitances, or, in the case of electromechanical switches, where it is relied on the value of the capacitance created between the contacts.

1.2.1.3. Impedance matching

Impedance matching is a critical element in high-frequency design. The switching device should be matched at both input and output sides, for both ON and OFF state of the switch, to minimize its influence on the performance of the rest of the system.

This is specified in terms of the input reflection coefficient S_{11} (dB), between the input of the system and the input of the switch as well as of the output reflection coefficient S_{22} (dB), between the output terminals of the switch and the output of the switched system. Improper matching results in unwanted reflections within the circuit, which can cause major damage to the rest of the system. Although ideal matching is seldom achieved, care should be taken to minimize the reflections within acceptable limits.

1.2.1.4. Transition time

The transition time is a measure of speed at which the position of a switch can be toggled. For a mechanical switch, this is defined as the time required for the moving contact to leave one stationary position and strike the opposite stationary contact. For a solid state switch, the transition time is the time required for the output RF signal to rise from 10% to 90% of its maximum value for OFF-ON transition and 90% to 10% for ON-OFF transition. In other words, it is the time taken for the output voltage to change to within 1 dB of the final state [3].

1.2.1.5. Switching speed

The switching speed also represents the time for toggling from one state of the switch to the other. However, in this case, the time is measured from 50% on the *control voltage* to 90% of the RF envelop when the switch is turned on [4]. Similarly, when the switch is turned OFF, the time is measured till the RF signal voltage reaches 10% of the original signal. Hence, the switching rate is the time required for the switch to respond at the output due to the change in control voltage. Various delays such as driver delay and driver rise time are added to the mechanical switching time or the transition time. Therefore, a semiconductor controlled switch is much faster than a mechanical one. The switching speed is always larger than the transition time of a switch.

1.2.1.6. Power handling

Power handling is a measure of how efficiently the RF signal is passing through a switch. This is commonly specified in terms of a 1 dB compression point, which is adopted from the amplifier characterization industry. It is commonly assumed that the

output power level follows the input power with a linear ratio. Nevertheless in many devices there is a maximum power handling above which this linearity does not hold. The 1 dB compression point is defined as the maximum input power level at which the output power differs by 1 dB with respect to linearity.

1.2.1.7. Bandwidth

Switching systems, with the exception of capacitive RF-MEMS switches and PIN diodes, do not have a limit on their lowest frequency of operation, but all of them have an upper limit. For semiconductor solid-state devices this is due to the finite time in carrier mobility. In the case of electromechanical switches, the losses that created from resistance and parasitic reactances, due to their shapes and values, are the main cause limiting the performance at higher frequencies.

1.2.1.8. Actuation voltage

All automated switching systems require a control signal for actuation. Depending on the scheme and its efficiency, these control voltages vary significantly. For semiconductor-based solid–state switching systems, this is not an important problem, although if electromechanical switching systems are concerned, bringing down these voltages to levels compatible with the rest of the circuit may become a serious design issue.

1.2.1.9. Lifetime

This is also not a significant issue considering semiconductor-based solid-state switches, but in electromechanical switches that involve moving parts, lifetime may have to be considered. The breakdown of such moving components is due to arcs created during switching especially under hot mode operation [2]. Additionally fatigue and environmental effects limit the lifespan of these systems.

1.2.1.10. Resonant frequency

This is another parameter that concerns only electromechanical type of switches [5]. Their moving parts have resonant frequencies that can be modeled in terms of effective spring constants and resonating mass. At this frequency, the potential energy and the kinetic energy tend to resonate. This frequency limits the maximum rate at

which the switch can be toggled, although it virtually has no bearing on the frequency of the actual RF signals the switch carries, as this is many orders higher.

1.2.2.Types of RF switches

The RF switches, according to their principle of operation, can be divided in two main categories, the electromechanical and the solid state RF switches.

1.2.2.1. The electromechanical RF switches

The mechanical switching is done through a make or break in the transmission line by a control signal. According to their size and activation mode can be divided also to the following categories:

1.2.2.1.1. **Traditional electromechanical switches**

The traditional waveguide and coaxial electromechanical switches and relays use electromagnetic force in order to cause a metallic contact physically to open or close. These mechanical switches can be designed to turn on and off in different ways. For example in a latching system, the switches can be built in normally open mode with all output ports disconnected from the input until the actuating voltage is applied, or normally close mode with all output ports connected to the input until the applied actuating voltage removes them from their closed position [6].

These switches are fabricated and packaged in a variety of combinations and support a wide range of signal characteristics, from low voltage/current to high voltage/current and from DC to GHz frequencies. The drive circuitry in electromechanical relays is galvanically isolated from the relay contacts, and the contacts themselves are also isolated from each other [3]. Generally the waveguide and coaxial electromechanical switches offer outstanding isolation and insertion loss, generate very low intermodulation products, and can handle a lot of RF power; therefore they are the preferred switches for high-performance power applications.

From the other hand they are bulky devices and their electromagnetic operation requires high power consumption. Additionally, due to their mechanical operation, these types of switches generally have a very slow switching speed (2 to 50ms),

forbidden figure for many RF applications while they are unreliable for long-life applications.

1.2.2.1.2. RF Micro Electromechanical Systems (RF- MEMS) switches

Thanks to the progress of technology and batch fabrication, the exceptional RF characteristics of mechanical switches can be transferred into the micro-world.

There are two distinct parts to an RF MEMS switch: the actuation (mechanical) section and the electrical section. The force required for the mechanical movement is obtained using electrostatic, magnetostatic, piezoelectric, or thermal designs. The switches can also move vertically or laterally, depending on their layout. As concerns the electrical part, a MEMS switch can be placed either in series or shunt configurations and can be a resistive or a capacitive contact switch.

Electrostatic actuation is the most prevalent technique in use today due to its virtually zero power consumption, small electrode size, thin layers used, relatively short switching time and they have overcome some of the major manufacturing shortcomings of their conventional macroscopic mechanical counterparts [5].

The RF-MEMS switches presents almost ideal RF characteristics from DC to 100GHz depending on the type (resistive or capacitive), almost zero power consumption, small size, linearity and integration compatibility with electronics.

This ideal picture is disturbed by reliability and lifetime issues that have to be solved, since up to now very few efforts managed to get commercialised [7]. Additionally they require an actuation voltage of 30–80 V, which necessitates the use of CMOS step-up converters to raise the input 3–5 V control voltage (mobile applications) to the required actuation voltage.

1.2.2.2. Solid state electronic RF switches

When high switching speed, ruggedness, low cost and commercial availability is concerned, solid-state electronic RF technologies (PiN diodes and GaAs-FET switches) are preferred instead of electromechanical switches. In spite of this design flexibility, two major areas of concern with solid-state switches exist: linearity issues and upper limits for frequency bandwidth. When operating at high RF power, nonlinear switch behavior leads to spectral regrowth and causes adjacent channel power violations (jamming) as well as signal noise problems. The other serious

drawback of solid state switches is their fundamental degradation of insertion loss and isolation at signal frequencies above 1-2 GHz.

1.2.2.2.1. **PiN diode RF switch**

A PiN diode is created with a wide, lightly doped near intrinsic semiconductor region between a p-type and n-type semiconductor regions, which are used for ohmic contacts. At dc and low frequencies, the PiN diode is similar to a PN diode; the diode resistance is described by the dynamic resistance of the I-V characteristics at any quiescent bias point [8].

At RF and microwave frequencies, when the diode is forward biased, holes and electrons are injected into the intrinsic-region and the diode behaves like an almost perfect (very linear, even for large signals) resistor (R_S). This high-frequency resistance R_S may vary over a wide range (from 0.1 ohm to 10 kΩ) and is determined only by the forward biased dc current. When the PiN diode is reverse biased, there is no stored charge in the intrinsic-region and the device behaves like a Capacitance (C_T) shunted by a parallel resistance (R_P), essentially independent of reverse voltage. The lowest frequency at which this effect begins to predominate is related mainly to the dielectric relaxation frequency of the intrinsic region [9].

In switching applications, the PiN diode should ideally control the RF signal level without introducing distortion which could potentially change the shape of the RF signal. An important additional feature of the PiN diode is its ability to control large RF signals while using much smaller levels of dc excitation. The main drawbacks of PiN diodes are the relatively high power consumption (5-100mW), and the degradation of RF characteristics (insertion loss and isolation) above 1-2GHz [5].

1.2.2.2.2. **GaAs-FET RF-switch**

Gallium arsenide Field-effect-transistors (GaAs FETs) are used as two-state switch elements in RF control device applications. The RF signal flows from source to drain, while the RF isolated gate is the voltage control. The high impedance OFF state is attained by applying a DC voltage on the gate more negative than the pinch-off voltage (V_P). In this condition the source-drain channel is closed and the behavior of the switch is capacitive. The peak (gate-source or gate-drain) voltages in this state may not exceed the gate-source or gate-drain breakdown voltage, to prevent

avalanching. The capacitance is typically 0.25 pF per mm of gate periphery. The ON state occurs when 0 V bias is applied to the gate. The channel from source to drain is open and represents a 2.5–3.5 Ω resistance per mm of gate periphery [10].

The GaAs FET's are very fast switches easily adapted to monolithic design as they interface with other FET circuits, without additional processing steps to be necessary. They dissipate essentially no power, as the only DC current that flows is the leakage of the gate-source and gate-drain reverse biased junctions and since no further external bias circuitry is required, the switch is inherently broadband.

The power handling of the switches is primarily limited by their current handling capability, which is related to the IDSS of the FET. The IDSS is a function of the gate periphery which then determines the source-drain capacitance [11].

However, for signal frequencies above 1 GHz, these solid-state switches have a large insertion loss (typically 1–2 dB) in the pass-through state and a poor isolation (typically on the order of -20 dB) in the blocking state [12].

1.3. Applications of RF Switches

RF switches and switching networks are used in virtually every communication system. Their application areas are focused mainly in reconfigurable apertures for defense and telecommunication systems, switching networks for satellite communications, instrumentation and wireless applications (portable units and base stations) [13]. More specifically they create switching sub systems such as: Transmit/Receive (T/R) switches, Programmable attenuators, Phase shifters (digital), Switched filter banks, Switched diversity antennas, Reconfigurable matching networks, Reconfigurable antennas, etc.

1.3.1. Transmit/Receive (T/R) RF switches

Transmit/Receive (T/R) RF switches are main building blocks in radar and communication systems RF front-ends. Their ability to get fully integrated with other circuits and operate over very wide bandwidths is essential to enable wideband systems on chip. A T/R RF switch is a two-pole single-throw arrangement that multiplexes the use of the antenna between the Power Amplifier (PA) of the transmit

section and the Low Noise Amplifier (LNA) of the receive section. T/R RF switches must be highly linear to ensure that high power signals at the output of the PA will be transmitted to the antenna with minimum distortion. This linearity requirement comprises a serious challenge in integrating T/R RF switches into on-chip designs especially as the supply voltage in standard CMOS drops continuously [14] [15].

1.3.2. Programmable RF attenuators

The RF attenuator is another universal building block within the RF design arena. The main job of RF attenuators is to reduce the level of the signal in order to protect a stage from receiving a signal level that is too high to handle. An attenuator may also be used to provide an accurate impedance matching as most attenuators offer well defined impedance. Switched Programmable RF attenuators are widely used in test systems where signal levels may need to be changed. They are often seen as small boxes with a number of switches, typically for 1, 2, 4, 8, etc dB change for each one, respectively [16].

1.3.3. Phase shifters

Microwave and millimeter-wave phase shifters are essential components in phased-array antennas for telecommunications and radar applications. The fundamental function of a phase shifter circuit is to produce a replica of the signal applied to its input, but with a modified phase. Its performance is characterized by its insertion loss, bandwidth, power dissipation, power handling capability, and insertion phase [17].
In the switching (digital) phase shifter, the incoming input signal is routed / switched through one of many alternate paths to the output, so as to introduce specific phase shifts with minimum loss. There are four essential types of digital phase shifters as described below:

1.3.3.1. Switched line phase shifters

The switched line phase shifters consist of different length transmission lines interconnected via RF switches. The phase shift can be easily computed via the difference in the electrical lengths of the reference arm and the delay arm [18]. The

phase of any transmission line is equal to its length multiplied by its propagation constant β and the differential phase shift is given by:

$$\Delta\varphi = \beta(l_{long} - l_{short})$$

1.3.3.2. Switched low-pass/high-pass filter phase shifters

The switched low-pass/high-pass filter phase shifters consist of two parallel arms one of low pass filter and one of high pass filter created by dual lumped LC networks exploiting the phase shift displayed by them. The high-pass/low-pass phase shifter can provide almost constant phase shift over an octave or more. Moreover it offers a very compact and smaller layout because lumped elements are used instead of delay lines [19].

1.3.3.3. Reflection type phase shifters

The principle of operation of the reflection type phase shifters is based on switchable terminations, which create switchable reflection coefficients. They practically use switched line lengths to alter the electrical length. With the added length the signal incurs twice the extra electrical length as the signal is reflected back. This implementation also tends to save space, compared to the switched-line topology [20].

1.3.3.4. Loaded line phase shifters

The loaded line phase shifters, is consists of switchable stubs which are separated by a spacing of line, and disposed along a main transmission line. Each stub is terminated in switches that enable a connection to ground depending on whether they are in the ON or OFF state. These phase shifters work by adding a shunt reactance to the transmission line resulting to a phase shift to the incident signal [21].

1.3.4. Switched RF filters

The switched RF filters are essential units in broadband communications systems and can be distinguished in two categories, the switched filter banks and the tunable/switched filters.

1.3.4.1. Switched filter banks

The complex signal processing requirements of broadband communications systems have long employed switched banks of filters before the receiver's front end, to remove out-of-band spectral components from the signals captured by the antenna. The simplicity of their name contradicts with the complex nature of these subsystems, which combines multiple types of filters and topologies as well as high-performance RF switches and other components to achieve the desirable result in each channel [22].

1.3.4.2. Tunable/switched RF filters

The tunable/switched RF filters are used for multiband communication systems, radars, and wideband tracking receivers. In this case RF switches are used to add or subtract capacitance (usually lumped elements) in the tunable capacitor banks to vary the resonant frequency of the filter. Choosing the correct type of RF switch in this category of tunable filters has to be done carefully, in order to avoid incompatibility and linearity problems that degrade the efficiency of the filter [23].

1.3.5. Switched diversity antennas

Switched antenna diversity is a transmission method in which more than one antennas are used to receive or transmit signals along different propagation paths to compensate for multipath interferences. Due to multipath propagation interference effects between network nodes, the received signal-strength may strongly vary, even for small changes in the propagation conditions, affecting the link quality. These fading effects may result in an increased error floor or loss of the connection between devices. Applying antenna diversity transmission techniques in such scenarios improves the reliability of an RF connection between network nodes. Switching is the easiest and the least power consuming of the antenna diversity processing techniques although periods of fading and desynchronization may occur while the quality of one antenna degrades and another antenna link is established [24] [25].

1.3.6. Reconfigurable matching networks

Reconfigurable impedance matching networks are key components in any multi-band RF transceiver circuit. They are used to increase the overall system performance in terms of power efficiency and linearity by compensating for the input/output impedance variations between the various building blocks within an RF front-end. Impedance variations in PAs, antennas and LNAs, are caused by switching the frequency band of operation or by adjusting the output power level [26]. Various tuning techniques such as the Distributed Transmission Line (DTL) and the transmission lines with periodic Defected Ground Structures (DGSs) have been developed to construct tunable impedance matching networks employing RF switches [27].

1.3.7. Reconfigurable antennas

A Reconfigurable antenna should be able to vary its operating frequency, impedance bandwidth, polarization and radiation pattern independently, to meet any potential changes in the operating requirements. However, the development of antennas with the above characteristics introduces significant challenges to both antenna and system designers. These challenges lie not only in obtaining the desired levels of antenna functionality but also in integrating this functionality into complete systems. As in many cases of technology development, most of the system complexity and incompatibility will come from the surrounding technologies that enable reconfigurability rather than the actual antenna itself [28].

The characterization of an antenna requires two types of information: the input impedance characteristic over frequency (frequency response) and the radiation characteristic (radiation pattern). Usually, frequency response is considered first because without a reasonable input matching, a T/R system may suffer from severe reflections, which deteriorates its efficiency. Once the antenna's frequency response is known, the radiation patterns are examined. The characteristics of the antennas can be manipulated through reconfiguration of physical parameters using RF switches. Several approaches have been proposed for implementing reconfigurable antennas and array antennas as described below.

1.3.7.1. Planar dipole antennas

The control of the resonant frequency of a planar dipole antenna, can be accomplished simply by changing its physical length, adding or subtracting t-lines via RF switches [29].

1.3.7.2. Slot antennas

Slot antennas can also become reconfigurable as concerns resonant frequency by using RF switches and small indentations in the slot gap. The antenna tuning is realised by changing its effective electrical length, which is controlled by RF switches along the slot antenna [30].

1.3.7.3. Microstrip Antennas

Microstrip antennas can be easily reconfigured by placing MEMS series switches at the radiating edge. RF switches connect extra sections of t-lines to the microstrip antenna, thereby lowering its resonant frequency [31].

1.3.7.4. Aperture Antennas

A reconfigurable aperture antenna is a planar array of electrically small, metallic patches that are interconnected by RF switches. The antenna can be reconfigured to meet different performance goals such as bandwidth and pattern, simply by changing the state of the switches [32].

1.3.7.5. Microstrip-Patch array antennas

In this configuration, groups of patches are electrically connected via RF switches. The various groups operate at multiple frequencies, according to their size. By electrically connecting or disconnecting the microstrip patches, the resulting overall patch geometry acquires a side effective length and shape that is concomitant with the desired frequency of operation [33].

1.3.7.6. Reflect Arrays.

Reflect antenna arrays are designed to behave like a parabolic reflector [34]. This is achieved either by inserting a fixed phase shift at each antenna element or by slightly changing the length, thus the reflected phase, of each antenna element. Reflect

antenna arrays can also rotate the polarization of an incoming wave if a dual-polarized element is used. An advantage of reflect arrays is the possibility of electronic scanning, which is easily done by using a variable phase shifter at each element or by slightly controlling the length of each element. It is therefore evident that RF switches and controllable phase shifters can be used in combination with reflect arrays to build multiple frequency systems and polarization rotation systems [35].

1.3.7.7. Multiple layers array antennas.

In this configuration, each layer may be either an array of antennas optimized to radiate in a particular frequency range or an image plane intended to reflect within a particular frequency range. The RF switches are then used to appoint which layer is operative [36]

1.4. Motivation for this Thesis

RF-MEMS switches comprise an excellent choice for reconfigurable antennas implementations due to their exceptional electromagnetic characteristics. Nevertheless they are not considered as mature devices since some reliability issues have not been addressed adequately yet. Nowadays some design efforts managed to be commercialized (Radant, Memtronics, etc) but there is plenty of room for improvements. Great effort is put in developing designs capable of facing specific issues such as controllability, robustness, as well as handling of relatively high RF power.

Efficient control of RF MEMS is a very important issue as it is correlated to main failure mechanisms/modes such as the impact force and bouncing phenomena. Considerable work towards this field is presented, indicating that different techniques have to be applied depending on the type of switch which in principle is a mechanical device. Another important point is the role of the actuation control system due to its capability to confront efficiently manufacturing uncertainties as, in the particular field of reconfigurable antennas, an ensemble of switches has to be used.

1.5. Scope of the Thesis

The contents of this thesis describe a two-fold application: a design of an ohmic RF-MEMS switch and the development of a generic multi-target statistical optimization method based on Taguchi's technique. The novel ohmic RF-MEMS switch design is specified for use in microwave reconfigurable antennas applications. A novel approach of Taquchi's optimization technique is used to control the actuation pulse of RF-MEMS switch in order to minimize its failure modes. Additionally this novel method is used for more complex electromagnetic applications for optimization of frequency response and radiation pattern of a reconfigurable antenna.

In general, the objectives of this thesis are:

- Design and development of an in-line-series ohmic RF-MEMS switch for microwave antennas applications. The special characteristics that appoint this switch suitable for this type of applications are: simplicity, controllability, relatively high power handling, linearity, longevity and reliability.
- Development of a novel, multi-target, multi-parameter global statistical optimization method based on Taguchi's technique, in order to control the actuation pulse of the ohmic RF-MEMS switch. The objective of this is to eliminate unwanted switching effects such as the high impact force and bouncing phenomena during the switch's ON and OFF transitions, which is the main failure mechanism. Ameliorating the operation features will significantly increases the longevity and the reliability of the switch.
- A thorough comparison between the simple "Uniform" switch design the developed "Hammerhead" switch as well as the well known "NEU" switch.
- A new extended version of Taguchi's technique named "Grid Taguchi" has been developed in order to solve the only drawback of this technique (the narrow search area), compared to other stochastic optimization methods such as PSO.
- Finally, all the above are combined together in order to create a novel reconfigurable (frequency and pattern) Yagi-Uda antenna configuration.

1.6. The original contribution of this work

This thesis contributes to design of a novel ohmic RF-MEMS switch for reconfigurable antennas aims at simplicity in order to confront manufacturing yield and to controllability in order to make it operational efficient. Author's main contributions in this thesis include:

- A novel ohmic *RF MEMS switch design* –The proposed design it is focused on simplicity controllability and power handling and is intended to be used in reconfigurable antennas structures. [37], [38], [39], [40], [41], [42].

- Development of Taquchi's optimization method for multi parameter, multi-target RF applications. [162]

- Optimization of the tailored actuation pulse control method for RF-MEMS switches using Taguchi's technique. [161]

- Quantifying of Resistive Damping to control very fast RF-MEMS switches [163].

- Development of the "Hybrid mode", a novel control method for RF-MEMS switches consisted by a compination of Optimized tailored Pulse and resistive damping techniques that offers good switching results and fabrication uncertainties immunity [164], [165].

- A new version of Taguchi's statistical optimization method "Grid-Taguchi" capable for efficient and systematical searching of a wider area.

- A switchable 3 elements Yagi-Uda antenna prototype with frequency and radiation pattern reconfiguration.

1.7. Thesis structure

The thesis is divided into 6 chapters. Following the introductory chapter, which comprises a review of RF-switches their types and applications, **Chapter 2** presents the various types of RF-MEMS switches and their critical review while concentrates mainly on the ohmic type and its reliability issues. **Chapter 3** focuses on the design and modeling of a novel ohmic RF-MEMS switch and its comparison with existing designs. The control methods for ohmic RF-MEMS which include step pulse control, tailored pulse control, optimized tailored control pulse via Taguchi's statistical technique, resistive damping and optimized hybrid mode control via Taguchi's technique are presented in **Chapter 4**. In **Chapter 5** a pattern and frequency reconfigurable printed 3-elements Yagi-Uda antenna, which is using 32 RF-MEMS switches, is designed and optimized through an evolution of Taguchi's method, the Grid-Taguchi's optimization technique. Finally, conclusions and future work are discussed in **Chapter 6**.

2. RF-MEMS switches

2.1. Introduction

In the field of microwave communication technologies, ultra miniaturized system architectures are of significant interest especially those featuring additional functionalities in combination with minimized energy requirements. RF-MEMS switches, comprising valuable part of this emerging technology, brought the revolution in RF and microwave applications. These switches are basic building blocks exhibiting outstanding RF performance, very low insertion loss and high isolation. In addition, they operate at ultra-low power levels with excellent linearity and extremely low signal distortion.

2.2. RF MEMS switches

Components built with MEMS and micromachining have demonstrated significant improvements over conventional ones, in several areas and the Holy Grail of MEMS devices is the micromechanical RF switch. [43]. The first RF MEMS switch specifically designed for microwave applications was introduced in 1991 by Dr Larry Larson at Hughes Research Lab [44]. The switch's ability to perform well up to few tens of GHz was a significant advantage over solid-state and mechanical switches (Table 1). While the first RF MEMS switch was far from perfect, its attractive performance brought many research institutes, companies and universities on its track. The release of the first RF-MEMS switch was followed by a number of other designs and there were great expectations in the idea of developing a new generation of devices capable of outperforming the current mechanical and semiconductor switching technology. RF circuits based on RF-MEMS switches such as phase shifters, reconfigurable antennas, and impedance tuning circuits, can be used to replace the solid state switching technology in low and medium power applications while they have the potential to be used for creating highly flexible RF systems.

Table 1 Performance comparison of switches based on RF-MEMS, PiN Diodes, GaAs FETs and electromechanical relay (EMR) technology [45].

PARAMETER	RF-MEMS	PIN-DIODE	GaAs FET	EMR
Voltage (V)	20 – 80	± 3 – 5	3 – 5	3-24
Current (mA)	0	0 – 20	0	15-150
Power Consump. (mW)	0.05 – 0.1	5 – 100	0.05 – 0.1	<400
Switching time	1 – 300 μs	10 – 100 ns	1 – 100 ns	>1ms
C_{up} (series) (fF)	1 – 6	40 – 80	70 – 140	-
R_s (series) (Ω)	0.5 – 2	2 – 4	4 – 6	<0.1
Cutoff Freq. (THz)	20 – 80	1 – 4	0.5 – 2	0.005
Isolation (1–10 GHz) (dB)	>40	>35	15-25	>40
Isolation (<10 GHz) (dB)	25-40	20-35	<20	-
Loss (1–10 GHz) (dB)	0.05 – 0.2	0.3 – 1.2	0.4 – 2.5	<0.3
Loss (>10 GHz) (dB)	0.1-0.2	0.7-2	>2	-
Power Handling (W)	<1	<10	<5	10
3^{rd} order Int. (dBm)	+66 – 80	+27 – 45	+27 - 45	>60
Life cycles	$>10^8$	10^9	10^9	$0.5\text{-}5x10^6$
Size	small	small	very small	large

RF–MEMS switches are well known for their remarkable electrical characteristics. These are listed below:

- Very low insertion loss, consequently better noise Fig. and sensitivity of RF systems.
- Very high isolation, allowing high frequency the switching operation with very high frequencies.
- Extremely high linearity, which keeps harmonics or intermodulation products low. Thus they are excellent candidates for broadband communications systems, especially for those requiring high dynamic range.
- Very low power consumption, due to electrostatic operation, which makes them suitable for battery-hand-held devices, as well as satellite and space systems.

On the other hand they are also characterized by:

- Low switching speed, which is the Achilles Heel of all RF-MEMS switches, a characteristic which is related to their mechanical resonant frequency. Electrostatically operated devices have typical switching-time in the order of microseconds up to 10s of microseconds. Despite the fact that MEMS switches operate slower than their electronic counterparts, they are still useful in many applications.
- Low power handling, nowadays most of the RF-MEMS switches cannot handle more than few watts of RF power.
- High-Voltage Drive, the electrostatically actuated RF-MEMS switches require 20-100V for reliable operation and this necessitates a voltage step-up-converter when used in mobile telecommunication systems.
- Reliability issues, mature RF-MEMS switches can operate properly up to 1 trillion cycles under cold cycling mode. However, under hot mode of operation this number is reduced significantly. Long-term reliability (years) has not yet been addressed.
- Packaging, RF-MEMS switches need to be packaged in inert atmospheres (nitrogen, argon, etc.) and in very low humidity, implying in hermetic seals, which itself may adversely affect the reliability of the RF-MEMS switch.
- Cost, although RF-MEMS switches have the potential of very low manufacturing cost, similar to VLSI design, the cost is increased dramatically due to the devise-level hermetic packaging

Technology maturity is defined relative to the performance requirements. Current switch designs perform within the specifications set by some commercial communications applications, and the first commercial RF-MEMS switches became available recently [7]. Although many advances have been made in the last two decades, the overall maturity level in RF-MEMS switch technology remains low and there is plenty of room for more improvements to meet customers' expectations for quality and reliability.

2.3. RF-MEMS switch types

RF-MEMS switches can be distinguished in two main categories the capacitive switches and the ohmic switches. Their actuation forces can be generated by several

methods such as electrostatic, magnetostatic, piezoelectric and thermal. Among them the most prevalent, is the electrostatic actuation, as it requires almost zero current consumption. In the electrostatic method the potential difference between two charged plates produces mechanical movement. The switches can also move in the vertical or lateral axis, depending on their layout while, as regards their electrical part, this can be placed in either series or shunt configurations, as shown in Fig. 1.

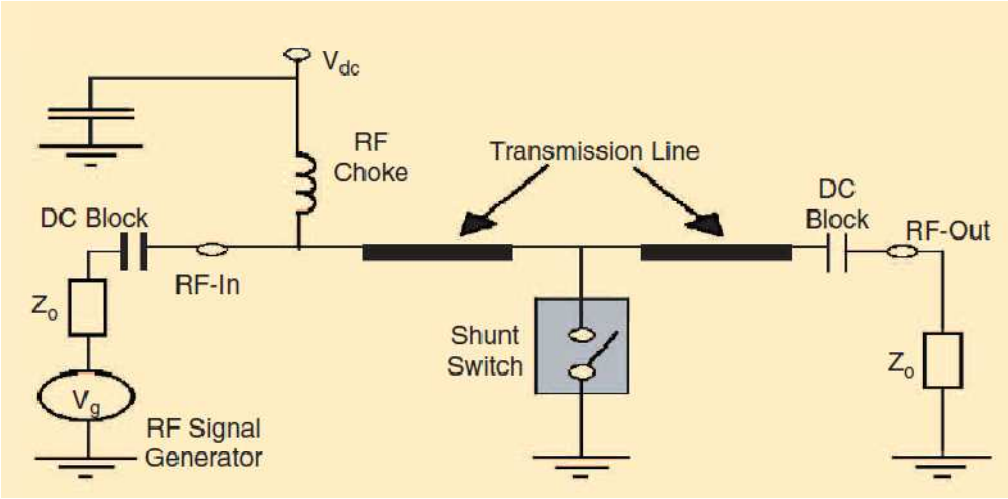

(a)

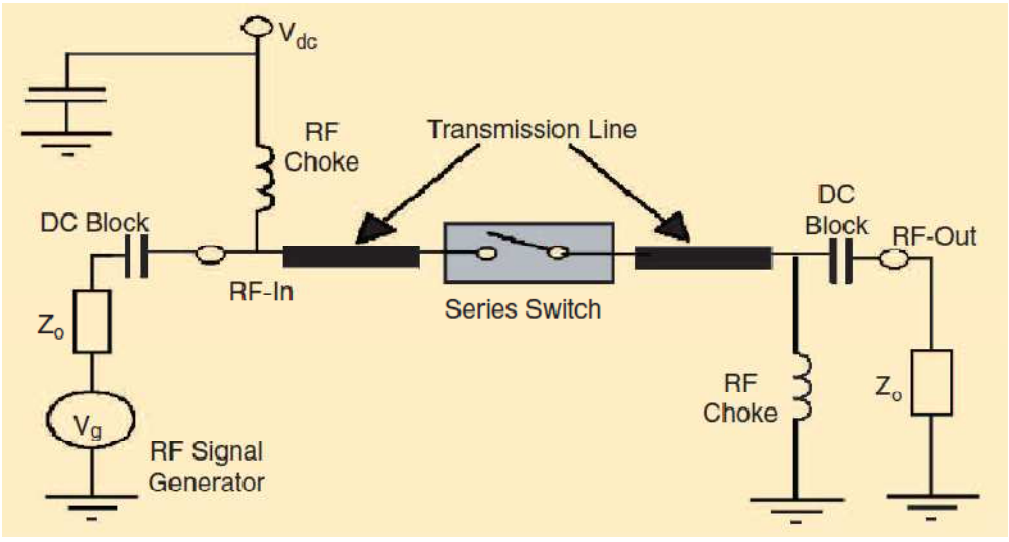

(b)

Fig. 1. (a) Parallel RF-MEMS switch configuration, (b) Series RF-MEMS switch configuration

Most of the switches are fabricated using surface micromachining and are compatible with post-CMOS, SiGe, and GaAs integration [46].

2.3.1. Capacitive RF-MEMS switches

Capacitive RF-MEMS switches use a thin layer of dielectric material to separate two conducting electrodes when actuated. The dielectric layer prevents direct metal-to-metal contact. These switches generally operate in a shunt switch configuration where the RF signal is shorted to ground by a variable capacitor, as shown in Fig. 2 & 3.

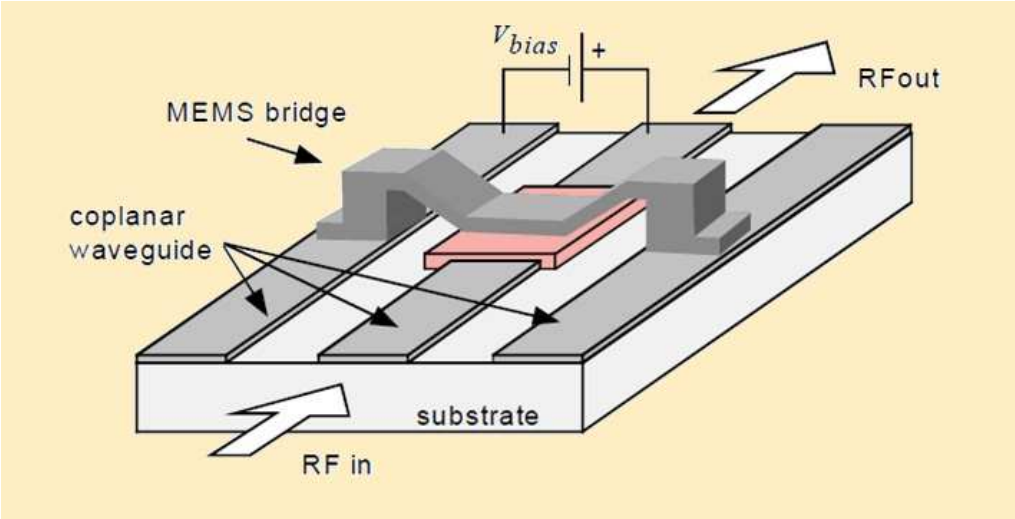

Fig. 2. Parallel capacitive RF-MEMS switch [47]

In this case, a grounded fixed-fixed beam is suspended over a dielectric pad on the transmission line. When the beam is in the up position, the capacitance that created is on the order of fF, which is translated to a high impedance path to ground and the switch in the OFF state. When an appropriate dc voltage is applied between the transmission line and the electrode, the induced electrostatic force pulls the beam down acting as a coplanar waveguide with the dielectric pad, while the capacitance increases to pF levels, reducing the impedance of the path through the beam for high frequency RF signal and driving the switch in the ON state.

In a series configuration the fixed-fixed beam is replaced by a cantilever and the switch is placed along the RF line.

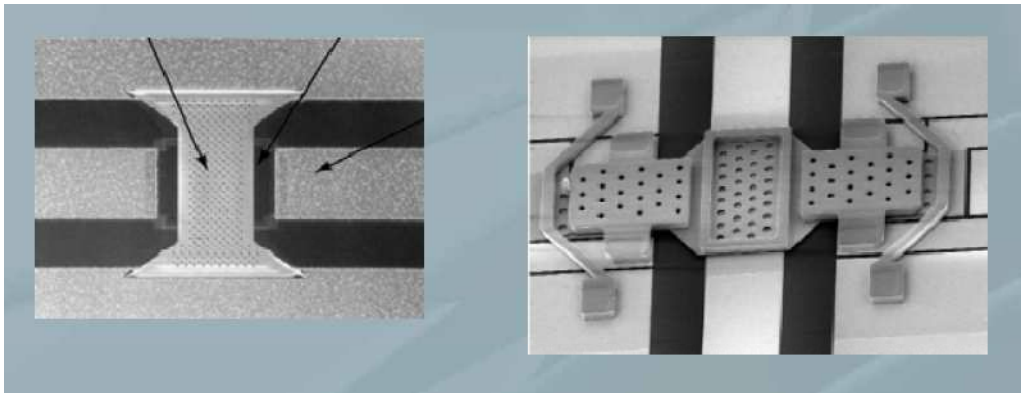

Fig. 3. Different types of fabricated capacitive RF-MEMS switches [48]

However, the thin layer of dielectric material will only conduct signals with reasonable insertion loss when the coupling between conductor electrodes, is above a certain frequency. Moreover, their bandwidth is limited by the capacitance ratio between the ON and OFF states and generally the RF signal range for capacitive RF-MEMS switches is 4GHz-120 GHz [46].

2.3.2. Ohmic RF MEMS switches

The basic structure of an ohmic RF-MEMS switch consists of a conductive beam suspended over a break in the transmission line. Ohmic or resistive or metal to metal contacting switches are generally used as series switches, as shown in Fig. 4 & 5

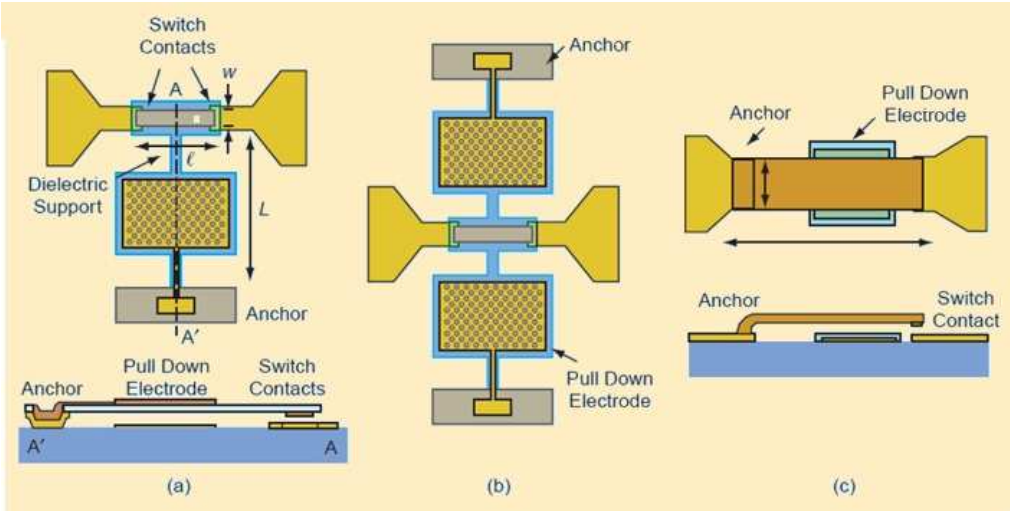

Fig. 4. Series RF-MEMS switch configurations (a) Broadside series cantilever type, (b) Broadside series fixed-fixed type, (c) in-line-series [49]

This type of switch is engineered in two types: broadside series and inline series. In the broadside series configuration the switch actuates perpendicularly to the transmission line, as shown in Fig. 4(a) & 4(b).

In the ON-state, the metal contacting part of the switch provides the signal path shorting together the open ends of the transmission line. The non-contact part of the beam is used for switch actuation and can be configured as a single fixed end cantilever or a fixed-fixed cantilever.

In inline series configuration the actuation is in the same plane as the transmission line, as illustrated in Fig.4(c). The signal enters at the anchor or the fixed end, travels across the length of the cantilever beam and exits to the transmission line through the contacts at the end of the cantilever beam. The signal range for ohmic switches is DC to 40 GHz, with the upper limit to be set by the parasitic capacitance which is formed between the metallic contacts.

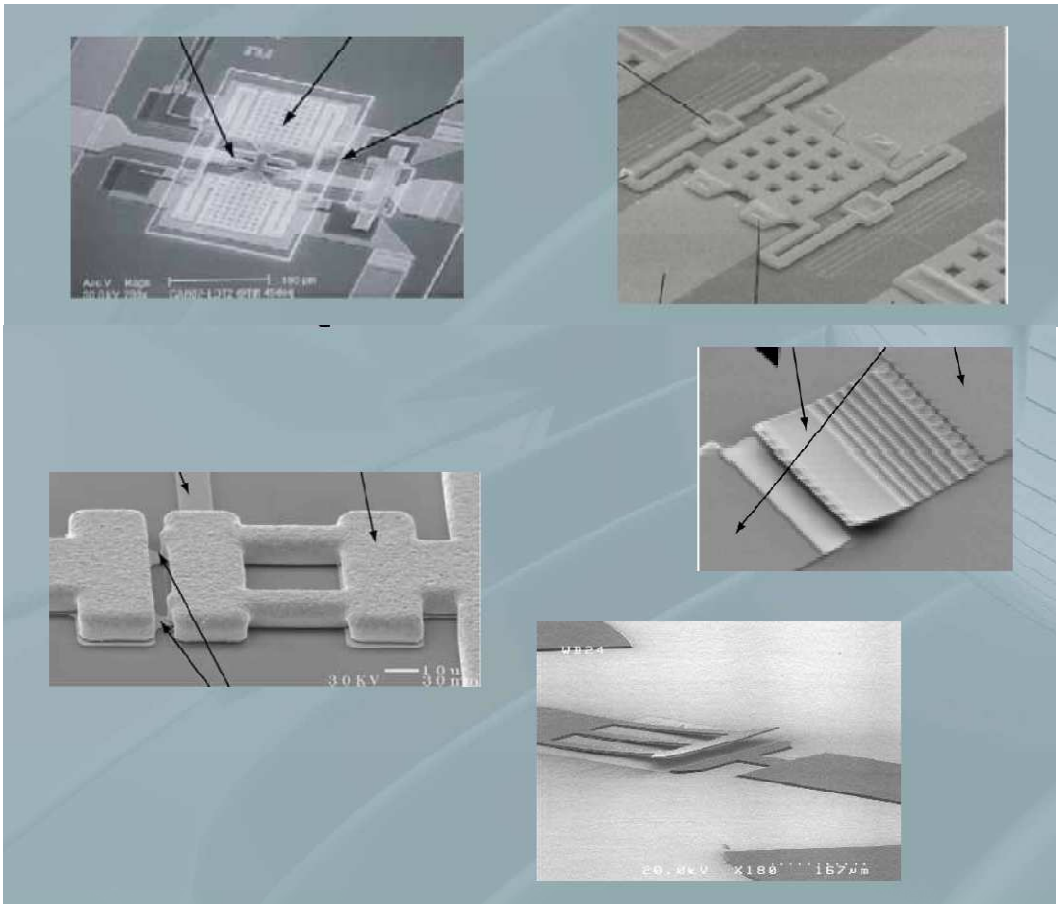

Fig. 5. Different types of fabricated ohmic RF-MEMS switches [48]

2.4. Ohmic RF-MEMS switches reliability issues

Reliability is defined as the ability of a system or component to perform according to its specifications under stated conditions for a specified period of time [50]. The reliability of RF-MEMS switches is of major concern for long term applications and is currently the subject of an intense research effort. The mechanical failure (metal fatigue in the anchored area) of well-designed micromachined cantilever or fixed-fixed beams is not a significant problem since their displacement is less than 5% in the worst case. Actually, many MEMS switches have been tested up for 100 billion cycles with no observed mechanical failure around the anchors [51].The presence of mechanical contact introduces a whole new class of reliability issues, related to both mechanical and electrical phenomena. The vast majority of field failures for ohmic RF MEMS switches today, are due to:

1. **"Contamination".** Contact degradation is one of the primary failure reasons for MEMS switches with ohmic contacts. The contact resistance increases due to organic deposits, absorbed hydrocarbon layers and contamination around the contact area. The dielectric layer composition will vary depending on the switch contact material. At low current and low contact loads, this unstable insulating layer between the contacts is responsible for an unusually high contact resistance, sometimes several orders of magnitude greater than the predicted values. The above phenomenon is the reason for one of the most prevalent failure modes among ohmic RF-MEMS switches, which is a sudden large increase in contact resistance. In certain cases, it was also found that thin dielectric layers were formed between the contact metals, and the switch was failing on its role as a series capacitor. These contamination layers can be mechanically removed either with a contact force of hundreds of μNs [52] or by hot-switching operation which can be thought as an internal electrical heating method [53]. Unfortunately, the above techniques create additional problems as wear and metal transfer. Correct choice of the contact material and improvements in cleaning process and package integrity (in-line chip scale hermetic packages that are sealed in a clean room) [7], along with the elimination of contamination from other materials [54] will dramatically improve product lifetime.

2. "Stiction". The requirement for low contact resistance necessitates the use of relatively soft contact metals and/or high contact force, which sometimes make the contacts stick together and causing failure [55]. Stiction phenomena arise when the surface interaction energy at a contact point is greater than the restoring force which tend to bring the switch into the equilibrium/open position. In such a case the RF MEMS switch will stick in the closed position and it will be unable to open. The adhesive force can come either from the capillary forces of condensed water at the contact surface or from the molecular Van der Waals force between very clean surfaces [56]. Capillary forces and humidity problems can be confronted within hermetically package devices as well as filling the package with an inert gas like nitrogen [57]. Van der Waals forces arise from the interaction between two very clean planar surfaces. In the real world the existence of asperities and the absorbed layer of hydrocarbons that exists even in noble metals like gold, don't allow the development of this kind of forces. At high current conditions, stiction will generally be generated by hot-welding.

As a rule of thumb, in order to overcome stiction problems and to establish reliable operation conditions, stiff switch elements capable of providing enough return force and hermetic packaging are required [58].

On the other hand high return force requires rather a high operating voltage to generate enough closing force to overcome this stiffness and achieve an efficient contact. To fulfill this requirement additional circuitry is needed (especially for low-voltage wireless applications) which, in conjunction with the hermeting packaging increases significantly the total cost.

3. "Wear". The wear rate or contact degradation of an ohmic switch is mainly due to the impact velocity of the contacts and is highly dependent on the switching mode, cold or hot and the switch's power handling capability. In RF-MEMS switches this failure mode has been identified that increases resistance with cycling, leading to degraded performance. The switch may bounce a few times before making permanent contact, due to the elastic energy stored in the deformed contact materials and the actuator. The existence of this bouncing behavior increases the effective closing time of the switch [46]. Meanwhile, the contact may be damaged by a large impact force which can be much greater than the high static contact force needed for low contact

resistance. This repeated instantaneous high impaction, induces local hardening or pitting of materials at the contact area and dislocations in the metal crystal structure.
Thus the lifetime of an RF MEMS switch could be increased by eliminating the high-speed impact of the switch onto the transmission line in the case of low power handling [7], [59].

4. "Cycling mode". Depending on the application, another factor that has to be taken into consideration regarding reliability is the cycling life of the switch under cold or hot switching mode of operation. In the case of cold switching, where the RF signal is applied right after the switch is closed and removed before the switch opens, mechanical wear dominates. Contact damage, pitting, and hardening of the metal occur since the same point is repeatedly hit during cycling. In the long term the contact area is reduced, increasing the contact resistance.
During hot switching, the RF signal is continuously ON, even during the opening and closing of the switch. Hot switching presents a completely different set of contact and thermal conditions than cold switching. During the contacting period, which can take up to several ms and include several switch bounces, the contact area is very small; due to the asperities consequently contact resistance is rather large. Under these conditions a voltage transient produces metal arcing at the contact site with temperatures high enough to melt the asperities. Softening or melting the asperities leads to additional failures such as switch shorting from nanowire formation and welding. Significant material transfer and micro-welding can occur under these circumstances, especially under 'high' RF power conditions (100-1000 mW) and the switch remains permanently closed (stiction effect) [54]. A solution that improves dramatically the Joule heat effect under the same power and force conditions, is to increase the actual contact area either by reducing the height of the asperities, or the increase of the nominal contact area [60], [61].
Nevertheless, the RF power handling capability for most MEMS switches typically provide reliable behavior in the 1mW to 100mW range. High power (P>100mW) applications available nowadays are limited to cold switching conditions [62].
On the other hand, continuous wave RF power operation (hot switching) is clearly of interest for a variety of high power microwave devices such as front-end components and tunable oscillators. It appears that power handling capability in the power range

over 100mW, would be a major breakthrough for the integration of MEMS components in ‘high’ power reliable systems.

A comprehensive understanding of all the ohmic RF-MEMS switch failure mechanisms has not been achieved due to the absence of a systematic study of micro-contact degradation modes, the quantitative failure characterization and the complexity of the related phenomena. Instead of this and due to the fact that researchers have been driven by the urge of developing high-reliability switches, coincidental approach has been followed in many cases. For example, failure analysis at high power level under hot switching operation is particularly difficult to be explained because the degradation process can be complicated due to the several possible factors such as arcing, transient current heating, static current heating and mechanical wear which can be also affected by the actuation voltage, conduct geometry and material properties.

2.5. Design considerations on an ohmic in-line-series RF-MEMS switch

The exponential growth of wireless communications requires more sophisticated system design to achieve higher integration, power saving and robustness. System design concentrates in developing high frequency, low scale configurations to follow the trends of the market for smaller, technologically more advanced applications. In the same manner, technological advances in radio-frequency (RF) front-ends, such as reconfigurable antennas, tunable filters, phase sifters, switching networks etc require state of the art switches to allow operation in cognitive wireless networks [7] [28].

Ohmic switches utilize physical contact of metal with low contact resistance to achieve low insertion loss when actuated. Their isolation is defined by the coupling capacitance of the electrodes when the switch is open. Thus, the ohmic MEMS switches are used where low loss devices are necessary, capable of reliably handling a few watts of RF power and operating in the frequency range from DC to 40GHz. Ohmic switches are generally divided into two categories according to the way they get actuated, the broadside series and the inline series. The broadside series (ohmic relay), is a four-terminal device that separates the control signal from the load signal within the body of the component package or even at the individual MEMS device

itself and actuates perpendicular to the transmission line. The inline series (ohmic switch), is a simpler three-terminal device architecture, straightforwardly comparable to the traditional transistor switch and its operation while its actuation is in the same plane as the transmission line. The ohmic switches can, also, be split into two subcategories depending on the existence or not (all-metal) of a dielectric layer over the electrode [63].

Criteria on the choice of the in-line-series type of ohmic RF MEMS switch for reconfigurable antennas applications are the direct correspondence with the electronic switch (which is intended to replace) and the simplicity in order to achieve robustness and long term reliability since the switch has to be able to perform millions/billions of switching cycles [59].

2.5.1.Mechanical modelling

The actuation of a cantilever type RF-MEMS can be reproduced by a beam which has one of its ends anchored while the other is free, as illustrated in Fig. 6 [64].

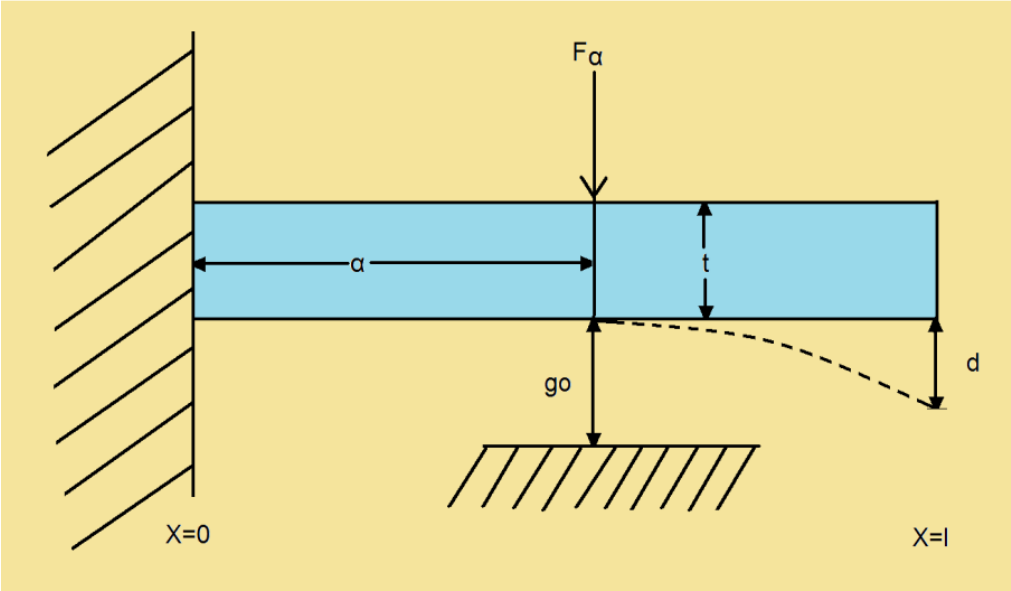

Fig. 6 Cantilever beam model with a fixed end at (x=0), a free end at (x=l), and an intermediately placed external load, F_a

The maximum beam tip deflection under the force F_a of an external intermediately placed load is given by [65]:

$$d = g_0 = \frac{F_a \alpha^2}{6EI_Z}(3l - \alpha) \quad (1)$$

g_0=the initial distance of the cantilever from electrode area
d=the deflection of the cantilever under electrostatic force
E=the Young modulus of cantilever's material
l=the length of the cantilever
α=the distance from the anchor to the middle of electrode

The area moment of inertia about the z-axis of a rectangular beam is expressed as:

$$I_Z = \frac{t^3 w}{12} \quad (2)$$

where w=is the width of the cantilever

In eq. (1), all the inputs are determined by the beam properties except the external load (F_a) and the maximum beam tip deflection (d). If the deflection is relatively small, the relation of the force and the deflection obeys Hookes' law and the maximum external force (d=g_0) equals with:

$$F_a = kg_0 \quad (3)$$

k=the spring constant of the cantilever

The spring constant k for the beam shown in Fig. 6 with the electrostatic force to distribute in a part of the cantilever, can be found by solving eq. (1) for the applied force and substituting to equation 2 for area moment of inertia. It can be expressed as [46]:

$$k = 2Ew\left(\frac{t}{l}\right)^3 \frac{1-\frac{x}{l}}{4-3\left(\frac{x}{l}\right)^3+\left(\frac{x}{l}\right)^4} \quad (4)$$

t=the thickness of the cantilever

x=the distance of the anchor to the end of the electrode when the length of the electrode is smaller than the length of the cantilever

2.5.2.Electrostatic modelling

The governing equations for electrostatic ohmic RF-MEMS cantilever type switches are based on the parallel plate capacitor model [66]. The actuation force is generated by charging up the metal electrode pads on both the switch's upper cantilever and bottom part. The electrostatic force applied to the beam is found by considering the power delivered to a time dependent capacitance and can be expressed by [46]:

$$F_e = \frac{e_0 A V^2}{2g^2} \quad (5)$$

e_0=the permittivity of the free air
A=the area of the electrode
V=the applied voltage
g=the remaining gap between cantilever and electrode (g_0-d)

The upper electrode snaps against the lower one if the electrostatic force is larger than the spring force. That is the case when the distance between the electrodes reduces below a critical distance and can be explained by the positive feedback mechanism in the electrostatic actuation. When the voltage source is increased, the force is increased too, due to an increase in the charge. Simultaneously the increased force decreases the beam height which in turn, increases the capacitance and thus the charge and the electric field. At $(2/3)g_0$, the increase in the electrostatic force is greater than the increase in the restoring force, resulting in an unstable position of the beam.
The critical distance is $d = \frac{g_0}{3}$ and is independent of the design geometry. For an electrostatic MEMS switch, the electrostatic force F_e equals the cantilever restoring force F_s when the cantilever is in equilibrium. Therefore, the pull-in voltage (V_{pi}) is given by:

$$V_{pi} = V\left(\frac{2}{3}g_0\right) = \sqrt{\frac{8kg_0^3}{27e_0A}} \quad (6)$$

Equating the applied electrostatic force with the mechanical restoring force F_r due to the stiffness of the beam, the restoring spring force results in:

$$F_r = -k(g_0 - g) = -kd \quad (7)$$

2.5.3.Contact area modelling

For electrostatic ohmic RF-MEMS switches, the contact force is relatively low with values to range from tens of μN's up to a few mN's. This contact force is determined by the mechanical switch design the applied electrostatic force. When a pull-in voltage Vpi is applied, the cantilever is brought into contact with the lower contact area. However, in this case, the resulted contact force is low; the material deformation usually is too small (elastic region) and the generated ohmic resistance is high [67]. The solution is to increase the actuation voltage well above the pull-in voltage. Thus the upper cantilever begins to bend after pull-in so that additional force is supplied to the contact area. Friction between the contacts caused by cantilever bending may also help to mechanically wipe contaminant films from the contact area [68].

After pull-in, the cantilever can be modeled as a beam with an anchored end at x=0, a supported end at x=l, an intermediately-placed external load F_a (this is the electrostatic force F_e) at x=a, and a supporting force R_2 at x=l (this is the contact force F_c), as illustrated in Fig. 7 [69].

$$F_c = \left[\frac{e_0AV^2}{4l^3(g_0-g)^2}a^2(3l-a)\right] - \left[\frac{3EI_Z}{l^3}(g-d)\right] \quad (8)$$

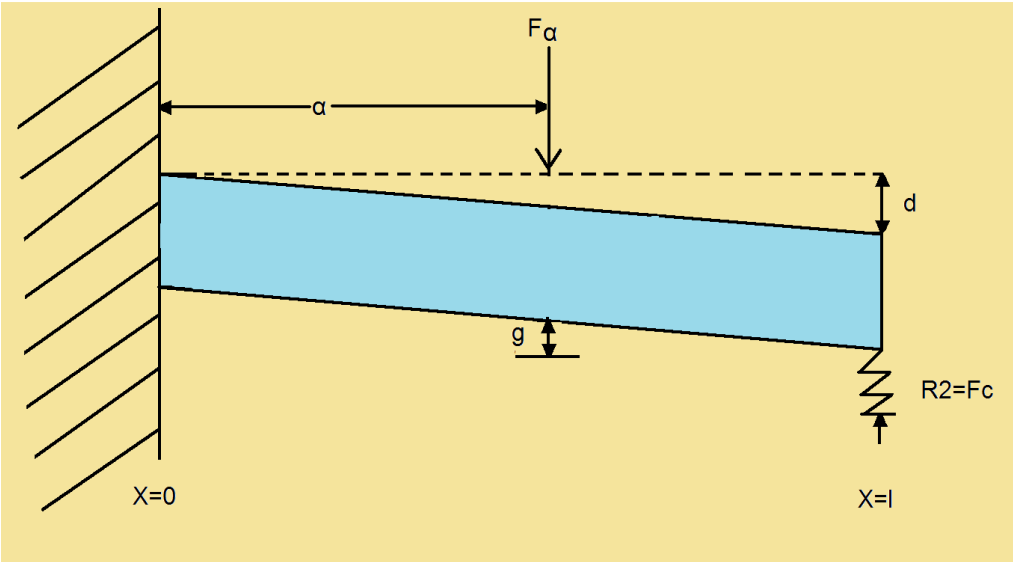

Fig. 7. The additional cantilever deflection after pull-down

The contact force can also be given by (9) as a combination of the electrostatic and restoring forces of the cantilever.

$$F_c = (F_e - F_r) \cdot W_f\% \tag{9}$$

Where, the weighting factor W_f% denotes that the contact force is dependable of the contact conditions and can vary between 40-60% of the total electrostatic force with the remaining part contributing to beam flexure, to gas damping or lost to the contact area [45].

2.5.4. Effect of the Fringing Capacitance

In the most popular model of electrostatic parallel-plate actuators, only the main electrical field (perpendicular to both electrodes) is considered. This formulation leads to a simple model of parallel-plate devices, but it is not accurate when the gap size separating the electrodes is comparable to the geometrical extent of the plates [70], [71]. Thus, the capacitance of the structure including the effect of fringing field has to be considered. To study the effect of the fringing capacitance on the switch mechanics, the following equation describing the switch capacitance applies [46]:

$$C_{el} = \frac{e_0 A}{g}\left(1.25 - 0.2\frac{d}{g_0}\right) \tag{10}$$

which, gives a 25% fringing capacitance at $d = g_0$ and a 5% fringing capacitance at $g = 0\mu m$. The electrostatic forcing function is similarly modified and is given by

$$F_e = \frac{C_{el}V^2}{2g}\left(1.25 - 0.2\frac{d}{g_0}\right) \quad (11)$$

The fringing capacitance reduces the pull-down time due to the additional force on the beam in the upper two-thirds of the switching cycle. Depending on the relation between g_0 and d, the fringing fields can affect and the other aspects of the switching mechanics.

For the case that $d = \frac{2}{3}g_0$, the electrostatic force is increased by about 11%, the pull-down time is reduced and the velocity is increased and consequently the initial impact force, the final contact force and the conductance are increased.

Nevertheless, for the case that $d = g_0$ contact force and consequently the conductance of the switch are not altered because the fringing capacitance is greatly reduced in the last one-third of the switching cycle. For the same reason the initial impact force remains about at the same level.

2.5.5. Perforation

The RF-MEMS switches, especially those with wide cantilever designs, use small diameter holes (2‑10 μm) in the beam to speed up the release etch while allowing easier sacrificial layer removal [4]. These holes also reduce the stiffness of the cantilever as well as the squeeze film damping increasing the switching speed of the MEMS switch. When holes are used throughout in the entire surface of the beam, the perforation pattern is characterized by the ligament efficiency, μ=l/pitch, defined as the ratio of the distance between the holes, to the distance between the centers of the holes (pattern pitch) [72]. The holes also result in a lower beam mass resulting to a higher mechanical resonant frequency.

The effect of holes on the up-state capacitance is negligible if the diameter of the holes is less than $3‑4g_0$.That is due to the fringing fields that fill the area of the holes. Therefore, the electrostatic force is not affected by the holes density or placement as long as the above condition is satisfied [46].

2.5.6.Skin depth

If a conductor with nonzero resistance is present in a propagating electromagnetic field, the field will penetrate the conductor. The penetration depth depends on the resistivity of the conductor and the frequency of the electromagnetic wave.

It is well known that at higher frequencies almost the entire electric current tends to flow to a very thin layer in the surface of a conductor, called the "skin effect". In an ideal conductor it is assumed that its thickness of the conductor is very much greater that the depth of penetration, so that there is no reflection from the back surface of the conductor. Thus, the surface resistance of a flat ideal conductor at any frequency is equal to the dc resistance of a thickness δ of the same conductor. However, when the thickness of the metallic conductor is comparable to the depth of penetration, wave reflection occurs at the back surface of the conductor resulting to a potential very high insertion loss in the transmission line [73].

In the case of an inline-series RF-MEMS switch, since the cantilever creates a part of the t-line, its insertion loss comprises from resistive loss, skin depth loss and contact loss. Assuming that the environmental conditions are stable and the resistive losses and contact losses are stable, the only loss that is frequency dependant is that created by skin depth effect. Skin depth is defined as the distance at which the field is decayed to e^{-1}=36.8% of its value at air-conductor interface and is given by:

$$\delta = \frac{1}{\sqrt{f\pi\mu_0\sigma}} \qquad (12)$$

μ_0=the magnetic permeability of the air

σ=conductivity of cantilever's material

It has been shown that it needs to be at least 2 times the skin depth **δ** of the material used in the lowest frequency, to be independent to frequency variations. Additionally, thick cantilever structures allows more power handling avoiding skin effects that cause Joule heating to be localized near the surface of the cantilever [74]

2.5.7. Gas damping

The two forces that limit the switching speed of an RF-MEMS switch are the inertial force (material damping), which dominates at low pressures (vacuum) and the gas damping force which exceeds the inertial force at higher pressures (ambient) [54]. To obtain sufficiently fast RF-MEMS switches it is essential to understand the effects of gas damping. The damping force is dissipative and changes as a function of cantilever position and speed. It reaches a maximum just before the switch's top contact meets the lower electrodes. At this point the switch is traveling at maximum speed while the gap distance is minimized [75].

Additionally, the dimensions and the shape of the cantilever, the existence of perforation as well as the modal movement (which also determines and the effective surface of the cantilever), have great influence on the damping coefficient. Increasing damping increases the switching time but also decreases the number and the amplitude of bounces.

A very convenient way of accounting for damping in numerical models, although the physical meaning of this approach is not clear, is Rayleigh damping [76]. Coventor Finite Element Method (FEM) code uses Rayleigh damping parameters into dynamic simulations, in order to determine the modal behavior of a RF-MEMS switch under various gas damping conditions.

However, systems with multiple degrees of freedom such as cantilever type RF-MEMS, it is very difficult to predict accurately the Rayleigh damping parameters from a set of gas damping coefficients [77] and a lot of assumptions have to be made showing the limits of this approach [78].

The dynamic vibration equation can be described as:

$$[M][\ddot{x}] + [C][\dot{x}] + [K][x] = [F] \qquad (13)$$

where [M], [C], [K]and [F] are symmetric mattrices referred respectively as the mass, damping, stiffness and force matrices. The matrices are nxn square matrices where n is the number of degrees of freedom of the system.

On orthogonal transformation using eigenvectors instead of individual translations and rotations, this dynamic vibration equation can be reduced to the form:

$$[m_j][\ddot{z}_j] + [c_j][\dot{z}_j] + [k_j][z_j] = [F_j] \quad (14)$$

m=the effective mass,
c=the damping coefficient,
k=the spring constant,
F=the applied force

In this form, the equation represents a collection of uncoupled eigenvector equations for a multi degree of freedom system with: $k_j = \omega_j^2 m_j$, $c_j = \zeta_j c_{crit.j}$, $c_{crit.j} = 2m_j\omega_j$ and the Eq. (14) becomes:

$$[\ddot{z_j}] + 2\zeta_j\omega_j[\dot{z_j}] + \omega_j^2[z_j] = [f_j] \quad (15)$$

ω is the circular frequency
c_{res}=resonance damping coefficient
c_{crit}=critical damping coefficient
ζ=damping ratio

Rayleich Damping uses a convenient mass and spring dependent relationship to describe the overall damping,

$$[C] = \alpha[M] + \beta[K] \quad (16)$$

which in orthogonal transformation reduces to the damping relationship,

$$2\zeta_j\omega_j = \alpha + \beta\omega_j^2 \quad (17)$$

From Eq. (17) it can be concluded that in a multi degree of freedom system, there could be n number of such equations and only two unknowns, α and β. In order to derive a set of Rayleigh damping parameters two assumptions have to be made.
The first assumption is that only the first modes of most engineering systems matter for such a damping analysis [77], and second that in the application of interest (RF-

MEMS switch), is operating below the first resonance frequency in the driven direction [46]. The reason for this is that according to mechanical theory as long as the frequency of actuation is below the first resonance frequency, the system response is purely in the shape of the first resonance (mode) shape if the actuation is in that shape [78].

Thus, according to the above assumptions there is no need to satisfy Rayleigh damping relationship equation beyond the first resonance frequency. Nevertheless, since it is an equation with two unknown parameters, α and β, the second resonance frequency is needed to solve for it.

$$2\zeta_1\omega_1 = \alpha + \beta\omega_1^2 \tag{18}$$

$$2\zeta_2\omega_2 = \alpha + \beta\omega_2^2 \tag{19}$$

The solution to this system given by:

$$\alpha = 2\omega_1\omega_2\frac{(\zeta_1\omega_2 - \zeta_2\omega_1)}{(\omega_2^2 - \omega_1^2)} \tag{20}$$

$$\beta = 2\frac{(\zeta_2\omega_2 - \zeta_1\omega_1)}{(\omega_2^2 - \omega_1^2)} \tag{21}$$

The damping ratio for the two resonance frequencies can be computed by:

$$\zeta_1 = \frac{c_{res.1}}{c_{crit.1}} \tag{22}$$

where $c_{crit.1} = 2m_1\omega_1$

$$\zeta_2 = \frac{c_{res.2}}{c_{crit.2}} \tag{23}$$

where $c_{crit.2} = 2m_2\omega_2$

Using the Analyzer module of Coventorware, the terms, ω_1, ω_2, m_1 and m_2 can be determined from MemMech-Modal Analysis. The terms $c_{res.1}$ and $c_{res.2}$ can then be determined from DampingMM-Mode Shape Analysis.

2.5.8.Quality factor

The main losses that contribute to the total Q-factor of a cantilever are gas damping, material damping and losses through anchors. The total quality factor is given by:

$$\frac{1}{Q} = \frac{1}{Q_{gas}} + \frac{1}{Q_{material}} + \frac{1}{Q_{Anchor}} \quad (24)$$

Because most RF-MEMS devices are operated at atmospheric pressure, the total quality factor is dominated by squeeze-film damping which arises from the interaction of the device with the ambient gas in the package. An approximate formula that describes the Gas quality factor (Q_{Gas}) of a cantilever beam at resonance is given by [46]:

$$Q_{GAS} = \frac{\sqrt{E_{Au}\rho_{Au}}}{\mu A_{cant(eff)}^2} t^2 g_0^3 \quad (25)$$

Au=gold

ρ=density of the material

μ=coefficient of viscosity

Squeeze gas damping is modeled in FEM code using Rayleigh damping parameters, taking into account various gas-damping effects in dynamic simulations. For weak to moderate Rayleigh damping $\zeta \leq 0.5$, there is a simple relation between the Gas quality factor (Q_{Gas}) and the nondimensionalised damping ratio ζ:

$$Q = \frac{1}{2\zeta} = \frac{2m_{eff}\omega_0}{2c_{res}} \quad (26)$$

m_{eff}=the effective mass of the cantilever

ω_0=is the resonance circular frequency

Material or structural damping is primarily caused by crystallographic defects like dislocations, twins, and grain boundaries that affect the propagation of stress waves through the material. Material damping depends on both the material and the

manufacturing technique. Experimental methods shows that the material damping of thin gold beams is about $Q_{Material}$=250 [79].

Anchor loss is the less significant parameter of the total quality factor and occurs when elastic energy is transferred from the device to the substrate through the anchors.

An important point to consider is the effective mass of the resonant mode, since only the end portion of the cantilever is moving. Modal analysis simulations indicate that the effective mass is around 0.25 to 0.5 of the actual mass of the cantilever [80].

Another point that has to be mentioned is that for high-Q structures Q_{Total}>3 the switching speed of the device is not affected. However, it has a large effect on the settling time during the release phase of the switch [81].

2.5.9. Switching speed

Finally, the switching time of the cantilever type switch is depended on all the above (mechanical structure, electrostatic energy, perforation, modal movement, environmental conditions, modal damping, resistive damping). For cantilever beams with a small squeeze-film damping coefficient b and Q>2, the mechanical switching time (t_s) can approximately be estimated by [46]:

$$t_s \approx 3.67 \frac{V_{pi}}{V_s \omega_0} \quad (27)$$

V_S=the applied voltage

In (27) various delays such as driver delay and driver rise time have to be added in order the final switching time or the transition time to be investigated [4].

2.5.10. Self actuation

Self actuation is another failure phenomenon which degrades the RF MEMS switch operation under hot mode cycling. When an RF signal is applied to the RF MEMS switch, with frequency much higher than its resonant frequency, an equivalent DC

voltage will unavoidably be applied to the switch. For high-power RF signals this DC voltage may generate large actuation force which can excite the switch and finally close it. This type of failure is more significant in capacitive RF MEMS but it can, also, be observed in ohmic RF MEMS with relatively large contact areas and low actuation voltage V_{pi} [46]. When no biasing voltage is applied between the cantilever and the actuation electrode, the cantilever stands in the up state position and the capacitance loading of the line is minimum. For an incident wave of power P, the RF voltage on the t-line is given by:

$$V_{AC} = 2V^{+} = 2V_{Pk}sin\omega t \quad (28)$$

where $V^{-} \approx V^{+}$=V_{PK} the peak values of a sinusoidal voltage

The small up state capacitance provides negligible reflection (S_{11}≈1) and the resulting DC equivalent voltage V_{DC-eq} is computed as:

$$V_{DC-eq} = \sqrt{2}V_{Pk} = 2\sqrt{PZ_0} \quad (29)$$

Self actuation failure can occur when the equivalent V_{DC} of the RF signal exceeds the actuation voltage Vpi of the cantilever.

This phenomenon in cantilever type switches can occur during the transition of the signal from the OFF to the ON state reducing the closure time and raising the impact force. During the ON to the OFF state transitions the equivalent DC voltage of RF signal may generate electrostatic force, large enough to hold the switch down even when the bias voltage has already been turned off.

2.5.11. Electromagnetic characteristics

The inline series ohmic RF MEMS switch can be represented with its equivalent circuit in the OFF and the ON state (without the t-line connections), as shown in Fig 8a and 8b respectively.

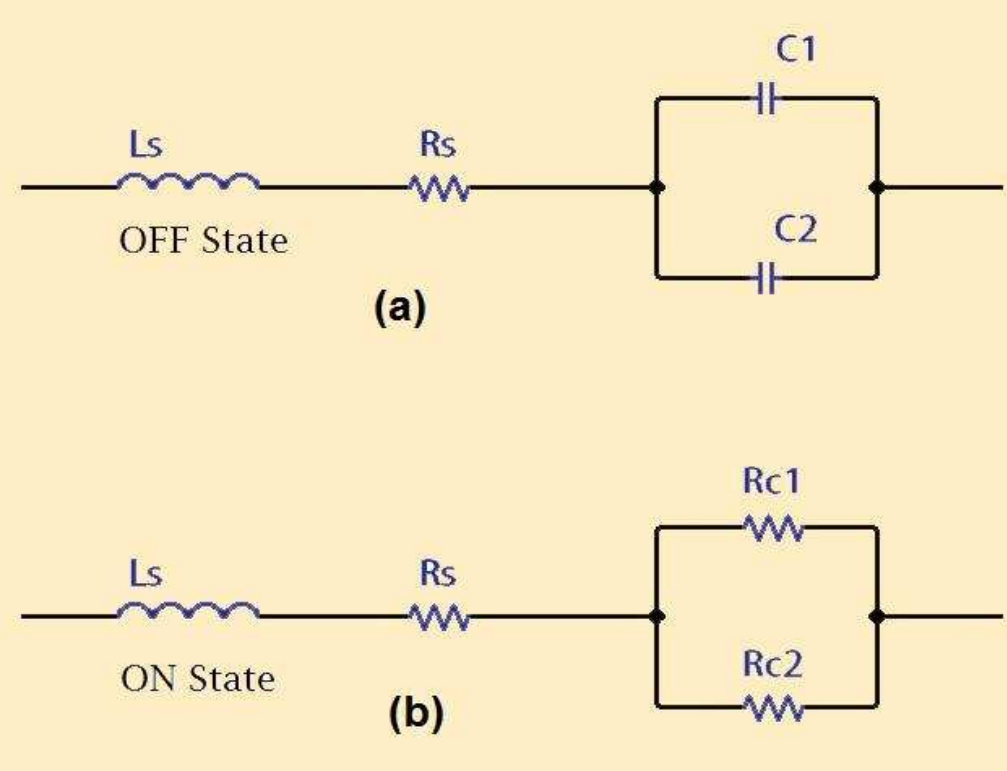

Fig. 8. The electrical equivalent circuits of the switch

The cantilever can be modeled as a piece of t-line composed by an ohmic resistance Rs in series with an inductance L_s. The value of DC resistance R_s depends on the dimensions and the material of the cantilever and is given by:

$$R_S = \frac{l \cdot \rho}{w \cdot t} \tag{30}$$

l=length
ρ=resistivity
w=width
t=thickness

The self-inductance L_s of the cantilever is shape dependant and if the shape is a straight rectangular bar with length l, width w and thickness t, the self inductance can be calculated as [82], [83]:

$$L_S = 2 \cdot 10^7 \cdot l \cdot \left[ln \frac{2l}{w+t} + \frac{1}{2} + \frac{w+t}{3l} \right] \text{ Henry} \tag{31}$$

In the OFF-state two parallel capacitors are created between the contact areas and the cantilever. Due to the fringing fields the perforation of the cantilever does not affects the total contact capacitance. The parasitic capacitances which are created between the two contact areas are negligible compared to the relatively big Cc and therefore can be omitted from the calculations. The capacitance which formed in each contact area is given by:

$$C_c = \frac{e_0 A_c}{d} \tag{32}$$

A_c=contact area
d=distance between the plates of the capacitor

And the final capacitance of the switch, since two capacitors are formed in parallel out of the contact areas, becomes:

$$C_{sw} = 2C_c \tag{33}$$

The total impedance of the switch and its modulus in the OFF-state is given by:

$$Z_{s-OFF} = R_s + j\omega L_s + \frac{1}{j\omega C_{sw}} \tag{34}$$

$$|Z_{s-OFF}| = \sqrt{R_s^2 + \left(\omega L_s - \frac{1}{\omega C_C}\right)^2} \tag{35}$$

In the ON state the impedance of the switch can be modelled as an ohmic resistance in series with an inductance. The series resistance is composed by the cantilever's resistance R_s together with the two contact resistances R_c in parallel. For ohmic contact switches, the contact resistance R_c depends on the size of the contact area, the mechanical force applied and the quality of the metal-to-metal contact.

$$R_{sw} = \frac{R_c}{2} + R_s \tag{36}$$

The impedance of the switch and its modulus in the ON-state is given by:

$$Z_{s-ON} = R_{sw} + j\omega L_s \quad (37)$$

$$|Z_{s-ON}| = \sqrt{R_{sw}^2 + \omega {L_s}^2} \quad (38)$$

The loss can be derived from the scattering parameters obtained from the measured values or the simulated values using a full wave circuit simulator:

$$Loss = 1 - |S_{11}|^2 - |S_{21}|^2 \quad (39)$$

The correlation between scattering parameters and the RLC components of the switch under certain conditions is very helpful in order to estimate either the S-parameters or the dimensions of the switch. As an example, when the switch is in the OFF-state S_{21}≤-10dB, the C_{sw} created between the cantilever and the contact areas, for the frequency of interest, is calculated as:

$$C_c = \frac{|S_{21}|^2}{4\omega^2 Z_0^2} \quad (40)$$

The switch's ohmic resistance R_{sw}, is formed from cantilever's and the contact's resistance. The inductance of the cantilever can be determined from the Return loss (S_{11}) parameter when the switch is in the ON-state.

$$|S_{11}| = \frac{\sqrt{R_{sw}^2 + (\omega L_s)^2}}{2Z_0} \quad (41)$$

Making use of the above equation it's easy to calculate the R_{sw} and the L_s if there are two boundary measurements of the S_{11}. In low limit frequency where R_{sw}>>ωL_s the equation becomes:

$$|S_{11}| = \frac{R_{sw}}{2Z_0} \quad (42)$$

In high frequency limit the ωL_s>>R_{sw} the equation becomes:

$$|S_{11}| = \frac{\omega L_S}{2Z_0} \quad (43)$$

Therefore, it is straightforward to determine R_{sw} and L_s from the reflection coefficient. Care must be taken when the above results are evaluated as they do not include the t-line effects; consequently they are only useful for comparison with simulated data under restricted conditions.

2.6. Modeling of RF-MEMS (Numerical-CAD Methods)

The development process of RF-MEMS switches is complex, involving product design, manufacturing, packaging and systemic integration as described within the research community [84], [85], [86], [87]. Like an IC circuit and its common mechanical structures, RF-MEMS devices can use computer aided design (CAD) to facilitate their performance and reliability to reduce the development cycle and cost. For electronic products design, the technology of electronic design automation (EDA) serves as a platform to enable circuit designers to design and analyze, making use of computer help and model libraries provided by foundries and related design kits, in order to complete the design, development, and testing of devices in the most economic and efficient method. SABER, OrCad and Simulink are software packages commonly used. For mechanical products design, MDA (Mechanical Design Automation) there are numerous and large-scale common software to aid design, manufacturing, and analysis, such as IDEAS, UGII, and ProPEngineer.

A linking device between EDA and MDA is required for MEMS-CAD to determine multiple physical coupling effects, such as the mechanical-electrical coupling effect and the nonlinearity of the structure and electrostatic force. Additionally, effects such as the non-ideal boundary conditions, fringing fields, pre-deformation due to the initial stresses, and non-homogeneous structures further complicate the modeling and increase the development difficulties of MEMS-CAD. Numerical simulation of MEMS devices mainly uses numerical methods, such as the Finite Element Method (FEM) or and the Boundary Element Method (BEM), capable of simulating the actions of various

structural components with high accuracy [88]. Their drawbacks are high computation complexity and low analysis efficiency.

Many researchers concentrate their efforts in reducing the large amount of computations. Among them Stewart [89] who developed a set of simulation methods, which can be used for microstructures in small vibration situation; and Swart et al [90] who invented a CAD software, named AutoMM, capable of automatically producing dynamic models for microstructures.

Some others have been worked on the above numerical methods through commercial simulation software like CoventorWare and improving significantly their efficiency. Pamidighantam et al [91] simulated the system as a discrete system of an equivalent spring and a parallel plate capacitor in CoventorWare, in order to obtain a relation of the pull-down voltage of the micro-bridge-shaped beams; however, the deviation was as high as 18%. O'Mahony et al [92] also analyzed the microbridge-shaped beams exposed to electrostatic loads using CoventorWare, and inferred the numerical solution of the microbridge-shaped beams by taking fringing capacitance effect, the efficiency of the plate-like phenomenon, and different boundaries into consideration. Lishchynska et al [93] derived the numerical solution of the pull-in voltage of cantilever beams, using the CoventorWare simulation software, and achieved an error within 4%.

In the movement process, beams are affected by the interaction between electrostatic force, elasticity-restoring force, and damping force. As a result, the equation of motion in coupling is often a simultaneous partial differential equation of an electrostatic force equation, an Euler beam equation, and an air-damping equation, which explain the dynamic actions of the devices in all three spatial dimensions. It would be very difficult to solve this equation using only a numerical method. Therefore, mathematical operations, such as state-variable analysis and basic function expansion methods, are usually employed to translate a partial differential equation of infinite dimensions into a system of ordinary differential equations of finite dimensions. This is well known as the reduced order method. Hung et al [94] examined the methods to define grids, capable of generating more effective reduced model. Clark et al [95] determined an effective method for analyzing the dynamic actions of MEMS devices, according to which, the complicated system is divided into several basic structural units, and then the equivalent circuit model, consisting of those basic structures, is built using the simulation protocols between similar systems.

A reduced-order model for the analysis of the behavior of microbeams actuated by electrostatic force is also presented by Younis et al [96]. The model was obtained by discretizing the distributed-parameter system using Galerkin procedure into a finite-degree-of-freedom system, which considered the effects of moderately large deflections, dynamic loads, linear and nonlinear elastic restoring forces, the nonlinear electrostatic force generated by the capacitors, and the coupling between the mechanical and electrostatic force. Wen et al [97] employed a model analysis method based on linear disposal near the bias point in order to analyze the AC small signal in frequency domain of beams. Zhang and Li [98] set an electrostatic-driven cantilever beam equivalent to a single-degree-of-freedom model to conduct its analytical form, and used a feedback mechanism to realize the coupling. Time and frequency domain analyses were conducted, too. In the time domain analysis, stronger driving voltage leads to more obvious beams overshoot. In the frequency domain analysis, the natural frequency of the cantilever beams would gradually get reduced, with an increase of voltage. Hu et al [99] established an analysis model for dynamic characteristics and stability of electrostatic-driven devices, and found that the stiffness of a microstructure will be softened periodically depending on the frequency of applied voltage.

The field of RF-MEMS switches modeling is much more complicated as microwave characteristics also needs to be extracted under electrostatically actuated non-linear mechanical motion and deformation. In order to avoid remeshing during up and down states Wang et al [100] proposes a hybrid method, which uses the method of moments (MOM) in conjunction with FEM-BEM for better results. For ohmic RF-MES devices, contact physics [68], [69] and non contaminated hermetic environments [101], [102] also need to be considered.

2.7. Commercial software packages for RF-MEMS modelling

Commercial FEM/BEM tools usually used for RF-MEMS design, divided in generic multi-physics software packages such as Comsol [103] and ANSYS [104], which perform a wide range of mechanical applications and more specialized on MEMS applications such as Intellisense [105] and CoventorWare [80].

Comsol and ANSYS perform static analysis of the actuation mechanism of MEMS devices. They also simulate dynamic behaviors, effects of routing parameters (voltage and temperature) on electrostatic force, inherent nonlinear stiffness softening effect device reliability, related failure modes and mechanisms, material selection, and reasonable design. Additionally, they offer 3D Finite Element Models (FEM) for mechanical, electrical, electrostatic, damping, transient and thermal analysis. The accuracy of these packages depends on the knowledge of the mechanical characteristics of the materials used for the RF-MEMS beams and is highly dependent on the deposition process and the operating temperature. Additionally, they can be used in combination with Full Wave electromagnetic simulators such as HFSS [106], FEKO [107] in order to calculate the S-parameters of the RF-MEMS switches when they placed in a t-line structure.

Intellisense and CoventorWare software packages apart from the multi-physics FEM analysis they offer reduced-order analytical (lumped-element) models for small-signal dynamic analysis. This allows investigation of the effective mass, resonant frequency and mechanical Q of the MEMS beams. They also include a full-wave electromagnetic solver in order to analyze the RF characteristics of MEMS devices.

2.7.1. COMSOL Multi-physics®

The COMSOL Multi-physics simulation software environment facilitates all steps in the modeling process − defining geometry, meshing, specifying physics, solving, and then finally visualizing results.

Model set-up is quick, thanks to a number of predefined physics interfaces for applications ranging from fluid flow and heat transfer to structural mechanics and electromagnetic analyses. Material properties, source terms and boundary conditions can all be arbitrary functions of the dependent variables.

Predefined multi-physics-application templates solve many common problem types. There is also the option of choosing different physics and defining the interdependencies, or specifying partial differential equations (PDEs) and link them with other equations and physics.

2.7.2. ANSYS Microsystems (MEMS) Industry

Multi-physics simulation from ANSYS provides high-fidelity engineering analysis tools that enable the accurate simulation of complex coupled-physics behavior. ANSYS multi-physics solutions combine industry-leading solver technology for all physics disciplines - structural mechanics, heat transfer, fluid flow and electromagnetics - with an open and adaptive ANSYS Workbench environment, flexible coupled-physics simulation methods, and parallel scalability. Together these cutting-edge technologies form the foundation for comprehensive multi-physics simulation capable of facing the industry's most complex engineering challenges.

2.7.3. Intellisense Software®

IntelliSuite contains a wide range of closely integrated tools to seamlessly go from schematic capture and optimization to design verification and tape out. A flexible design flow allows MEMS designers to start their design at schematic, layout or 3D level. This feature allows the use of MEMS at a schematic level, much like SPICE for electrical circuits. The design can then be quickly iterated and optimized at different granularities. Sophisticated synthesis algorithms can automatically convert the schematic into mask layout, 3D or better yet a meshed structure for full multi-physics analysis. Advanced Fast-field Multi-physics tools feature include fully coupled electrostatic, mechanical, fluidic, and electromagnetic engines. Additionally, includes advanced model order reduction based extraction techniques, electromechanical, fluidic and damping behavior into compact models.

2.7.4. CoventorWare®

CoventorWare supplies the MEMS industry with MEMS Design automation software. Whether it's for research on new devices, process technology development, preparing for prototype runs or full production, CoventorWare is a comprehensive suite of software tools for MEMS design and product development allows simulation off the physical coupled fields of MEMS devices. With CoventorWare, MEMS developers can quickly and easily design new devices, adapt designs to different requirements and study the impact on yield.

MEMS process technology is 3D in nature and is used in areas outside of MEMS as well such as 3D-ICs. The SEMulator3D product enables MEMS designers and process engineers to visualize the effects of design and process modifications in 3D before fabricating the actual device. It provides a rapid return on investment by running virtual prototype wafer runs and saving wafer starts.

In this Thesis CoventorWare software package is chosen for the analysis, design and evaluation of MEMS switches as it is considered one of the most integrated and reliable software packages for RF-MEMS modeling. A lot of work including publications and product evolution in this field have been extracted or have been tested using this commercial software package [91], [92], [93]. Besides, the author also had the opportunity to be educated in a training course about “Sensonor” and “Tronics” MEMS processes organized by the “Europractice” and “Stimesi” organizations using this software.

2.8. Summary

RF MEMS switches have been studied in this chapter, starting with a brief historical review and some comparison between RF-MEMS switches and other types of RF switches. The two main categories of RF-MEMS switch designs, the capacitive and the ohmic with their subcategories have been discussed, too. Moreover, the reliability issues of ohmic RF-MEMS switches have been analyzed as they will be extensively examined and referred to throughout this thesis. Besides, the design considerations and the governing equations for the static and dynamic modeling of a cantilever type ohmic in line series RF-MEMS switch have also been presented. Finally, the numerical (CAD) modeling evolutions in the last ten years, as well as, the existing commercial modeling tools for RF-MEMS analysis, have been reviewed.

3. Investigation of ohmic in-line series RF MEMS switches: designs and simulations

3.1. Introduction

The motivation of this Thesis is the design of a simple and reliable switch for use mainly in reconfigurable antennas. An all-metal in-line-series ohmic switch was chosen as it comprises the simplest configuration and it can directly replace the existing RF-switches such as GaAs-FETs and PIN diodes. Another reason for choosing this type of RF-MEMS switch among several other types is that in comparison with the rest of the configurations it is the one which managed to overcome all the reliability issues and to be commercialised [108].

The design approach followed in this work was mainly towards simplicity, reliability, controllability and power handling of the RF-MEMS switch, while great effort has been paid in analyzing all possible failure mechanisms. To validate all these features a thorough comparison between other switch configurations of the same type such as the simple “Uniform switch” and the well known North Eastern University’s “NEU” switch [108], are performed. The investigation of all the designs has been carried out using Coventorware 2010 software package. Apentix A.1 includes the steps involved in the modeling process using Coventorware.

3.2. Analysis and design of an Ohmic RF-MEMS switch with “Hammerhead” cantilever shape

The main disadvantage of the in-line-series switch compared to the ohmic relay is the controllability [63], [109]. In order to overcome this drawback a novel switch design with “Hammerhead” shaped cantilever and distributed electrode area as shown in Fig. 9 & 10, was developed [42].

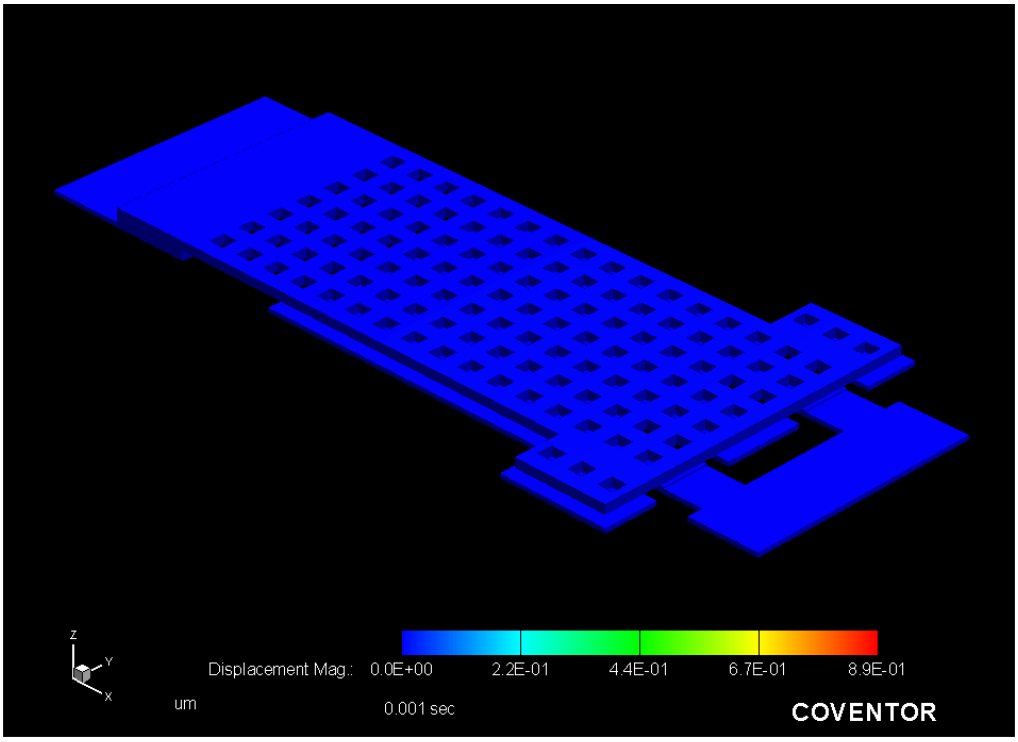

Fig. 9. The “Hammerhead” ohmic RF MEMS switch

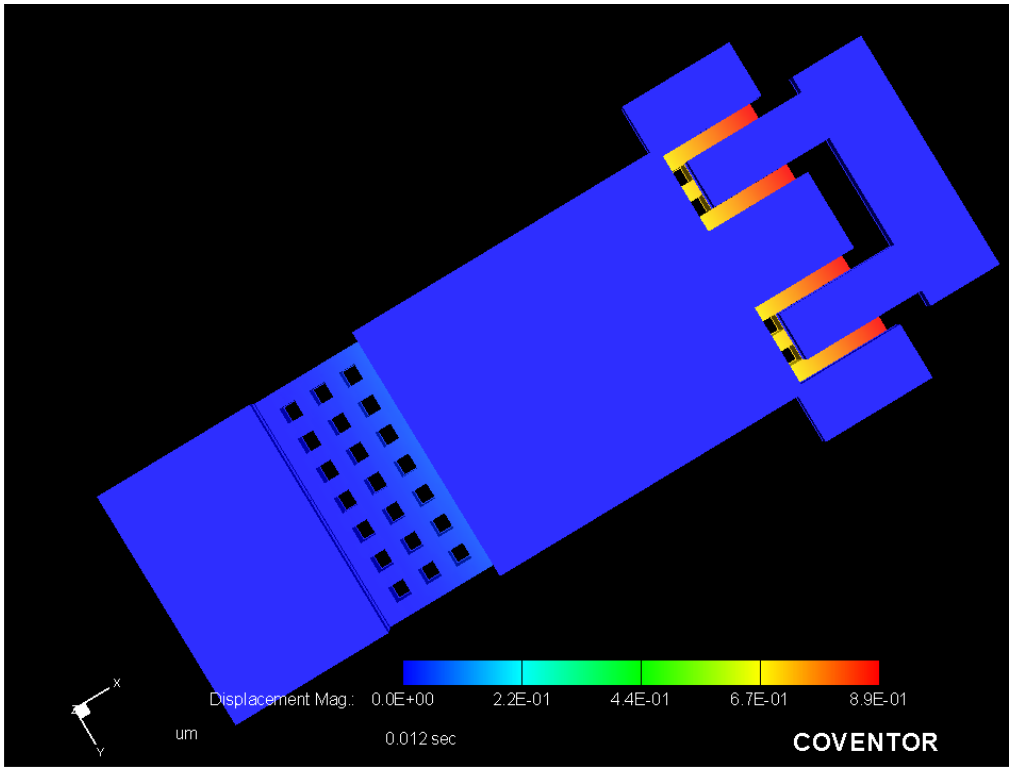

Fig. 10. The electrode area of the switch

The design process took into consideration several constraints listed below:

- Material choice;
- Contact area considerations;
- Power handling capability and linearity issues;
- Actuation voltage in a reasonable range ($V_{pd} \leq 30V$, $V_s \leq 60V$);
- Restoring force of the cantilever high enough to avoid stiction
- Switching at a reasonable speed $t_s \leq 20\mu s$;

Finally, the proposed switch has to present good performance as concerns electromagnetic characteristics in the frequency range DC to 10GHz which can be quantificated as follows:

- Very low insertion loss in the "ON" condition ($S_{21} \leq 0.02dB$)
- Very high isolation in the "OFF" condition ($S_{21} \leq -20dB$)

3.2.1. Material choice

To fulfil the criterion of simplicity and robustness, the proposed switch is an all-metal in-line-series type. The lack of dielectric charging makes all-metal RF-MEMS switches ideal candidates for space-based applications, where the impact of radiation on the switch would normally a concern related to reliability [110].

The design is using only one material, gold (Au), for the whole structure. Gold has been chosen due to its exceptional electrical, mechanical and chemical characteristics as well as for low ultra-loss consideration and ease/low-cost of fabrication compared to the highly precise control of dopants [111]. More precisely gold is the most appropriate material for the following reasons:

i. Low resistance. The high conductivity of Au implies very low contact resistance and less skin depth, an important parameter for lossless RF signal transmission via the cantilever.

ii. Easy deformation. The Au Young modulus is around 57GPa [80]. Consequently, the stiffness of a cantilever made of Au will be low enough, fulfilling the requirement for low actuation voltage.

iii. Low propensity to form alien surface films. Even in the case of hermetic packaging it is inevitable to face contamination issues in the long term. Au is a

noble metal and chemically one of the most stable materials since it does not form oxides or sulfides, offering greater longevity. In addition to that, it has been shown that switches with Au-Au ohmic contact can reach up to 10^8 cycles of lifetime [112].

iv. Monolithic microwave integrated circuit (MMIC) compatibility. Au is widely used in micro-fabrication as it is easily deposited by sputtering, evaporation, or electroplating fabrication processes, it has high melting point while it is corrosion resistant [113].

As Au is the only material of the structure, no problems could be created due to technology mismatches in between dissimilar materials (residual stress, thermocouple phenomena, adhesion problems etc) [114]. The main problem with MEMS switches with Au electric contacts is their propensity for high adhesion due to gold's relatively low hardness (1–2 GPa), which may lead to failure if restoring forces are not large enough to break the contact [115].

3.2.2.Contact area considerations

The size of the contact area, the conductivity of the Au, the gap between the contacts, the contact force as well as, fabrication process issues such as the deposition method, the roughness and surface contamination, are parameters that must be taken into consideration in order to maintain high isolation, and low insertion loss in the operating frequency range [116]. Additionally, operation conditions such as, current, environmental conditions (type of gas, temperature, pressure) and switching history have to considered, too [54].

To achieve all these targets a relatively large contact area has been chosen, which consists of two contact areas of $1500\mu m^2$ each. These two parallel conductors are separated by a gap of 2μm and create a capacitance of 13.29fF in the OFF-state of the switch, which, results to an isolation of -28dB in 5GHz.

Large nominal contact areas do not directly lower the contact resistance if the contact force is not increased. Thus, an increased actuation voltage (about twice the pull-down voltage) is applied in order to achieve S-shape deformation of the cantilever and contact forces in the order of 100μN. Under these conditions two very small resistances in parallel are created with a total value of 0.15Ω which, results in an insertion loss of about 0.015dB in 5GHz.

3.2.3.Power handling capability and linearity issues

Another factor that has to be considered in order to investigate the ability of the switch for low resistance, power handling and good linearity is the actual contact area. This area in an ohmic RF-MEMS switch under electrostatic actuation (maximum a few hundreds of μN), due to the existence of asperities, can reach (even under high power conditions) only the 5-7% of the nominal contact area [117]. Thus, a choice of a bigger contact area provide a better heat distribution from the effective contact spots, which heated by the dissipated power of the signal current flowing over the contact interface [118]. Avoiding local overheating is one of the main factors to increase reliability for switching larger currents [54] [111].

The overheating of the contact areas, also results in non-linear intermodulation products. Intermodulation distortion occurs as a result of the variation of the resistance of switch contacts with temperature. The temperature and resistance are modulated at the difference frequency under two-tone intermodulation conditions. The switch resistance then modulates the signals at the difference frequency, leading to upper and lower sideband signals [119].

Additionally, the softening of the asperities which has been observed under high power implementation on big contact surfaces, minimize adhesion and doesn't allow stiction phenomena [67].

In general, better heat dissipation of larger effective contact areas is the critical design criterion to maintain low contact resistance, high power handling capability, better linearity and a minimum of surface adhesion wear.

3.2.4. Restoring force, Actuation voltage and reliability issues

The requirement for low contact resistance necessitates the use of relatively soft contact metals (Au) and/or high contact force, which makes the contacts stick together and fail. On the other hand, reliable operation requires stiff switch elements capable in providing enough return force to overcome stiction. High return force in turn requires a high operating voltage in order to generate enough closing force so as to overcome this stiffness and finally achieve an efficient contact. The correlation between material

properties, design parameters and key failure mechanisms requires sophisticated switch design in order to meet the specifications.

Although low stiffness is essential in obtaining low-voltage switches, preventing from down-state stiction is equally important. A low-voltage switch experiences a relatively weak restoring force in the down state, which may not be sufficiently high to pull the switch up, particularly in humid or contaminated environments.

Switching operation requires not only stable contact but also reliable opening of the closed contacts. When the cantilever touches the signal line, the metal-to-metal contact surfaces may stick in the form of strong adhesion. This undesirable interfacial adhesion is referred to as stiction. Consequently, the switch is electrically shorted, and it may take a considerable amount of force to separate the cantilever from the signal line. Due to the difficultly in controlling all reasons responsible for stiction, the switch is designed by increasing the restoring force. The switch shorting problem can be solved if the restoring force is sufficient to overcome stiction. This solution should be effective no matter what the actual cause of stiction is [120].

The stiffness of the cantilever is determined by the width, the thickness, the Young Modulus of the Au, the existence of perforation, the gap between cantilever and electrode and affects significantly the magnitude of the pull-in voltage, the restoring force and the resonance frequency of the cantilever, which in turns, affects the speed of the switch.

Another factor that affects dramatically the final stiffness of the cantilever is its deformation, arc or S [69]. When a cantilever, after the first touch in the contact area (arc-shape deformation) is forced to bend more, in order to be deformed in S-shape, it acts like a fixed-fixed beam and presents a spring constant about 16 times higher than before [46].

Thus, a much higher actuation voltage $V_s >> V_{pi}$ has to be applied for this purpose.

Taking into account all the above, the shapes of the cantilever and electrode area are not uniform in order to apply distributed actuation force all around the “head” of the switch, resulting in better switching control and “low” initial pull-in voltage (V_{pi}). As the cantilever bends in S-shape deformation at its wider part, the stiffness of the switch is getting increased significantly and the final actuation voltage (V_s) becomes twice the V_{pi}. Thus, much greater electrostatic force F_e is applied, as it is proportional to the square of the final actuation voltage (V_s^2). Therefore enough restoring force is produced capable of eliminating any stiction problems.

In the proposed design, holes have been applied to the structure of the cantilever, which contribute in the removal of the sacrificial layer and the release of the cantilever. Nevertheless, it also reduces the initial stiffness of the cantilever as well as the gas damping coefficient.

The reliability of the presented switch is enhanced by the specific shape of cantilever, the big distributed electrode area which is about 5 μm wider than the cantilever in order to take advantage of the fringing fields, as shown in Fig.11 and its S-shape deformation. All these result in better controllability, relatively low final actuation voltage (V_s=60V), large restoring force [121], and, finally, a satisfactory switching speed of around 15μS.

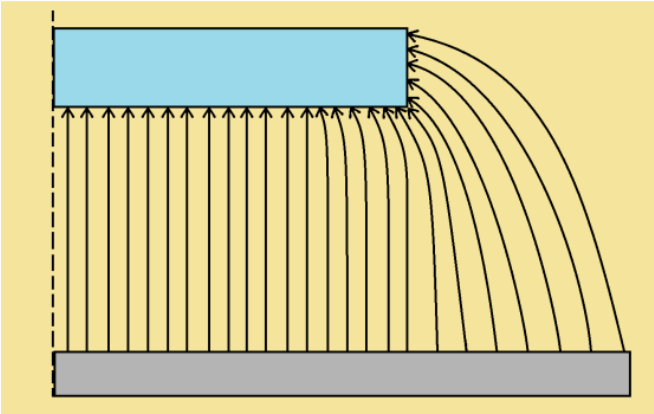

Fig. 11. Fringing fields action of the wider electrode area

The bending process can be divided into 4 different stages including the failure stage, shown in Fig.12. The reaction force F_1 (V_{arc} is applied) at the end of stage 1 is considered to be the spring force of the beam for the first ohmic contact and for the Arc–shape deformation of the cantilever (Fig. 12a).

The reaction force F_2 ($V_{s(min)}$ is applied) obtained at the end of stage 2 is the force needed to bend the beam for a full ohmic contact and for the S–shape deformation of the cantilever (Fig. 12b).

The reaction force F_3 ($V_{s(max)}$ is applied) at the end of the third stage indicates the point of full contact up to the maximum actuation voltage. The larger the $\Delta F = F_3-F_2$ is, the larger the contact force with a full ohmic contact is and the larger the immunity to switch parameters uncertainty will be (Fig. 12c). Friction between the contacts caused by cantilever bending may also help to mechanically wipe contaminant films in the contact area [69]. As a result the switch presents both low resistance and high restoring force.

The fourth stage is the buckling stage ($V_b > V_{s(max)}$). This is the failure stage where full contact no longer exists, the reaction force increases sharply and becomes non-linear (Fig.12d).

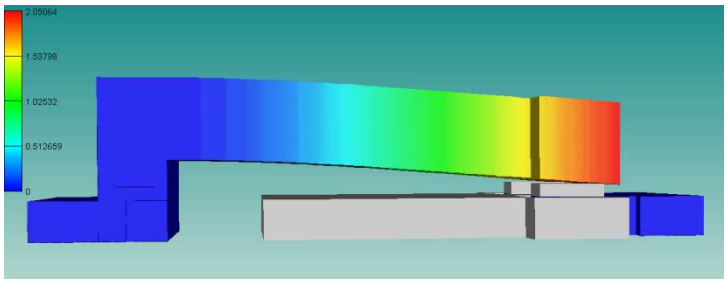

(a)

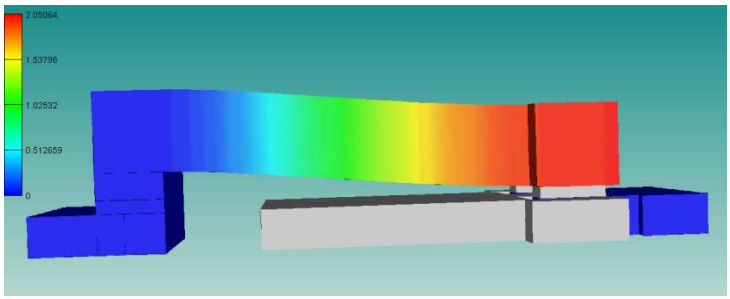

(b)

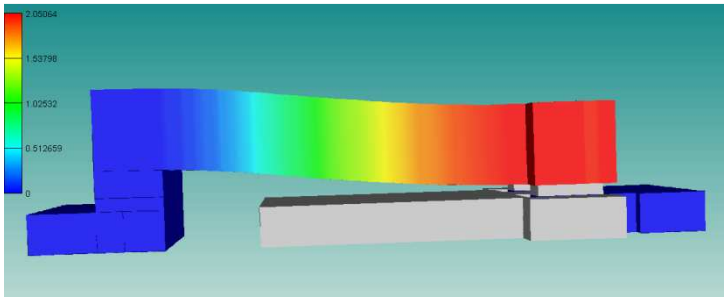

(c)

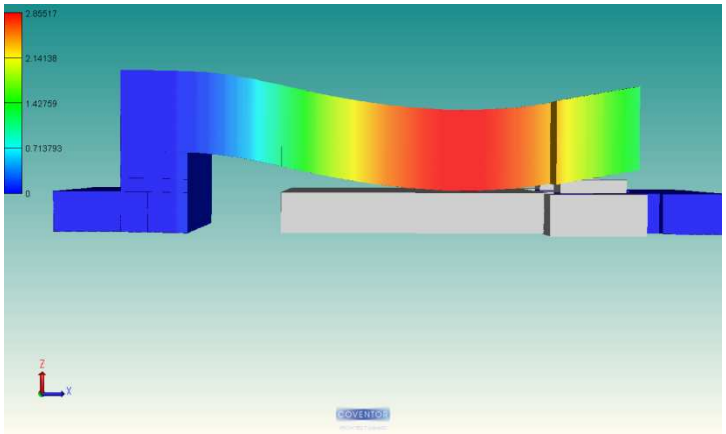

(d)

Fig. 12. The different stages of the bending process

3.2.5. Actuating the switch

A DC sweep can be used to investigate the pull-down voltage when contact is achieved. Initially, the contact force is very low and rises as the pull-down voltage increases; additionally, the conductance which is low at the beginning, takes its higher value in the full contact state. Nevertheless, under nominal switching conditions, when contact is achieved, the contact force is very high due to the high impact velocity of the collapsed cantilever. Instantly, the conductance becomes very high but unstable, due to the bouncing of the cantilever which follows after the first contact. Consequently, additional time is necessary for a stable contact force and thereof a stable conductance to be achieved. This bouncing behavior due to the elastic energy stored in the deformed contact materials and in the actuator increases the effective closing time of the switch [122].

Meanwhile, the contact may get damaged by the large impact force which can be much greater than the high static contact force needed for low contact resistance. This instantaneous high impact force may induce local hardening or pitting of materials at the contact. Besides, bounces facilitate material transfer or contact welding, which are not desirable for a high-reliability switch. All the above increase the adhesive force which resists contact separation and is a function of the maximum contact force. Thus the impact force increases the force required to separate the contact by a large factor. This is usually observed in gold-contact switches that stick immediately or after a few cycles of operation with square wave actuation, but operate for extended periods when actuated with slower waveforms [123] [119]

3.3. Simulations results

The simulation results have been extracted under the following environmental conditions: Temperature: 293^{o}K (20^{o}C), Pressure: 730mTorr (1Atm) and Gas type: Nitrogen.

In order to improve contact convergence, a softening parameter as regards to asperities named **“contact softening”** with a value of 50nm is added. **“Contact softening”** acts as an exponential delay function that smoothens the pressure force applied at the moment of contact. The improvement in contact convergence comes at the cost of an artificially deep penetration of the two contact surfaces.

Contact stiction can be added to the Architect contact models by setting the parameter **“adhesion force per area”** to a value of 100Pa. The adhesion force is applied as a pressure load whenever the gap between the two contact planes is less than the **“adhesion distance”** which has a value of 50nm. In order to avoid discontinuities during the contact simulation, the change of the adhesion pressure load is softened by a sinusoidal transition function. The sinusoidal function ensures a gradual rise or fall of the adhesion pressure whenever the contact gap gets smaller or bigger than the **“adhesion distance”**. The period of the sinusoidal transition function is defined as “**adhesion softening”** with a value of 10nm.

A detailed drawing of the “Hammerhead” switch in a) top view and b) side view is illustrated in Figure 13.

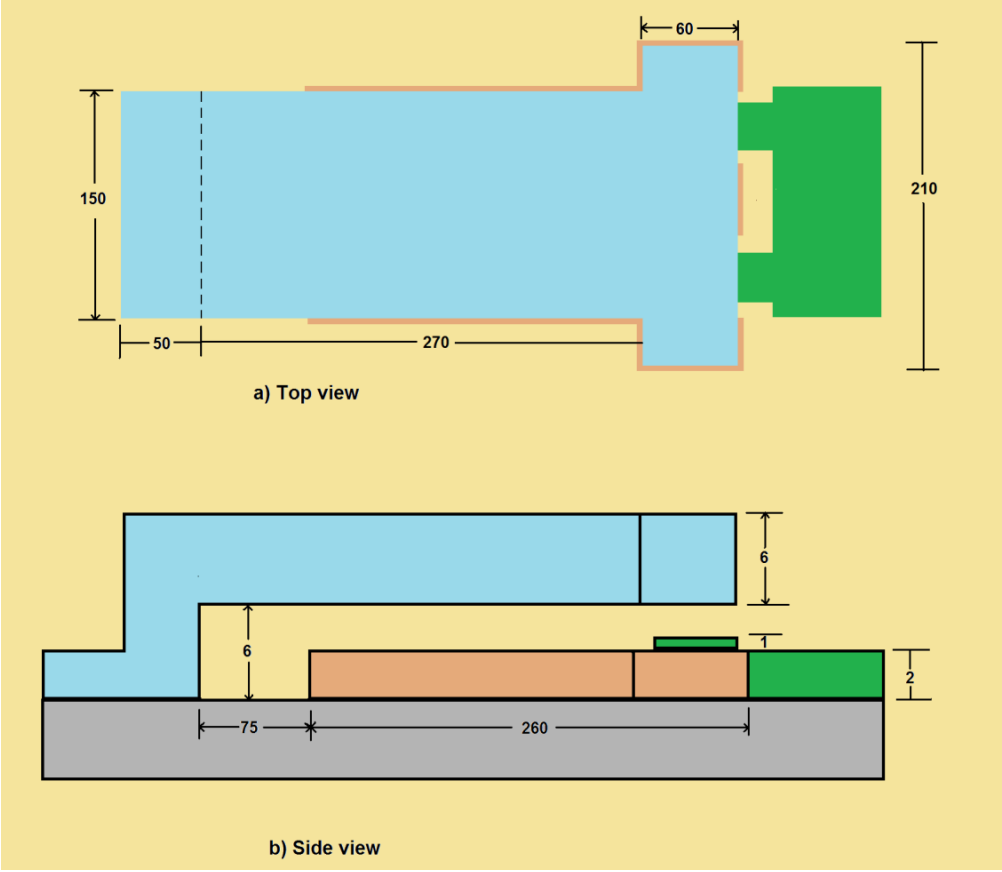

Fig. 13 Dimensions of the “Hammerhead” RF-MEMS switch

A meshed 3D view of the new design, produced in the Designer module, with the switch in the OFF state is shown in Fig.14. For illustration purposes the z-axes has been magnified ten times.

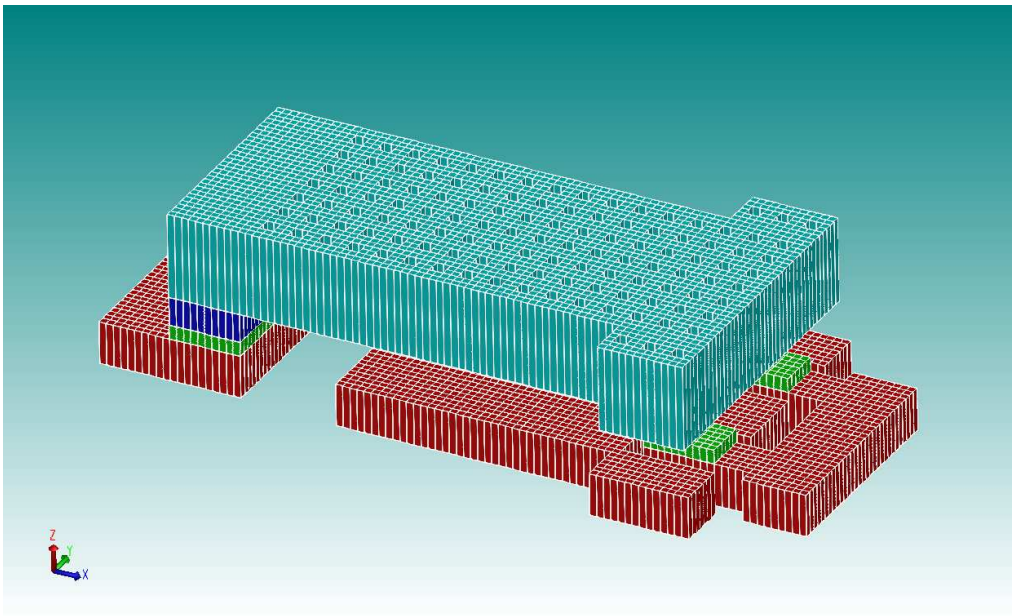

Fig. 14. The meshed 3D ohmic RF MEMS switch

3.3.1.DC transfer analysis

A DC transfer analysis via Architect module has been carried out by applying a ramp voltage to investigate: actuation voltage, contact force, conductance, contact area and capacitance.

The pull-in voltage V_{pi}, the arc contact Voltage V_{arc}, the full contact voltage V_s and the maximum allowable voltage $V_{s(max)}$, as well as the evolution of the contact force in both edges of the contact area are shown in Fig. 15. The results indicate pull-in voltage V_{pi}=25.2V (when the cantilever has drive the 1/3 of the distance to electrode), a first contact at V_{arc}= V_{pd} = 27V, full contact at V_s = 58V, full contact just before the buckling stage (the cantilever collapses to the electrode) at $V_{s(max)}$=69V. Therefore, the active area of the switch ΔV_s =$V_{s(max)}$-V_s = 11V is large enough providing immunity to high RF signals affect. Another significant factor that has to be considered is the ratio V_s/V_{arc}, which varies between 2.15 and 2.55 and denotes high enough electrostatic forces capable to offer good contact conditions and enough restoring force. An ideal figure for the applied actuation Voltage would be 63.5V where the contact force is uniformly distributed in all contact area and is about 99μN (this is shown in Fig. 15 when both edges of the cantilever's contact area tz1, tz2, have the same contact force 49.534N)

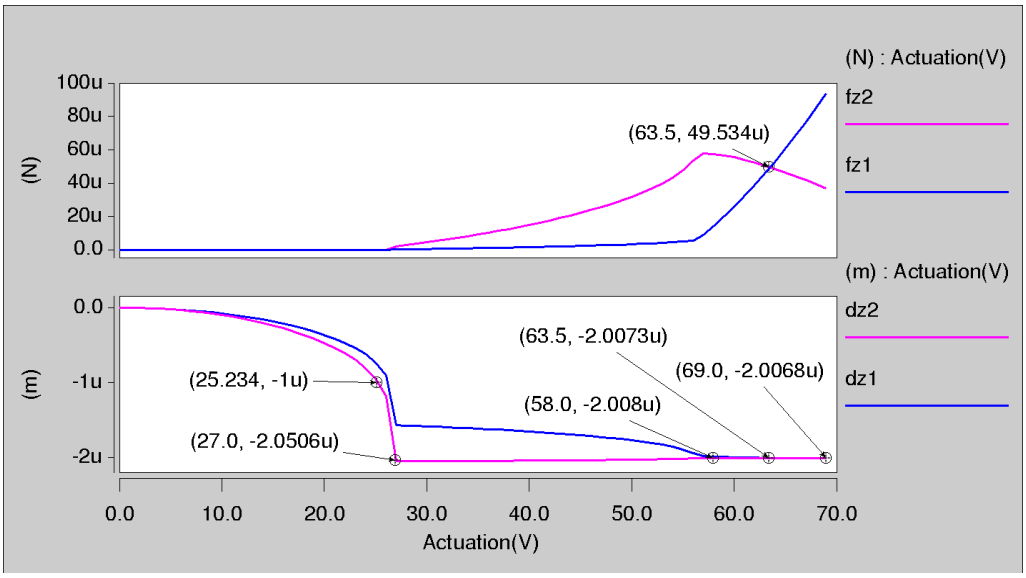

Fig. 15. Evolution of pull-down voltage and contact force of Hammerhead switch

Fig. 16 illustrates the main characteristics of the switch obtained via simulation under DC transfer analysis, which are:

The OFF state capacitance, created between the contact area and the cantilever, is around 6.15fF for each contact. Thus, the capacitance of the whole switch which is responsible for the Isolation feature, is around C_c = 12.3fF since both capacitors are in parallel.

Full contact is recognised considering the dimensions of the touch 50μm x 30μm = 1.5nm^2, at 58V. The conductance for one contact area at the full contact point is 3.1712 S and the equivalent resistance is 0.315Ω, which means that the contact resistance of the complete switch is about half, R_C = 0.155Ω, since the two resistances are in parallel.

At the first touch, when the cantilever is still arc-shaped the contact force is $F_{c(arc)}$ = 2.42μN (V_{arc} = 27V).The contact force (F_c),applied under full contact conditions ($V_{s(min)}$ = 58V) when the cantilever is S-shaped is around $F_{c(smin)}$ = 71uN. When the contact force is equal at all the contact area (V_s = 63.5V) the contact force is around F_c = 99uN. Finally the maximum contact force before buckling is $F_{c(smax)}$ = 130.87uN ($V_{s(max)}$ = 69V).

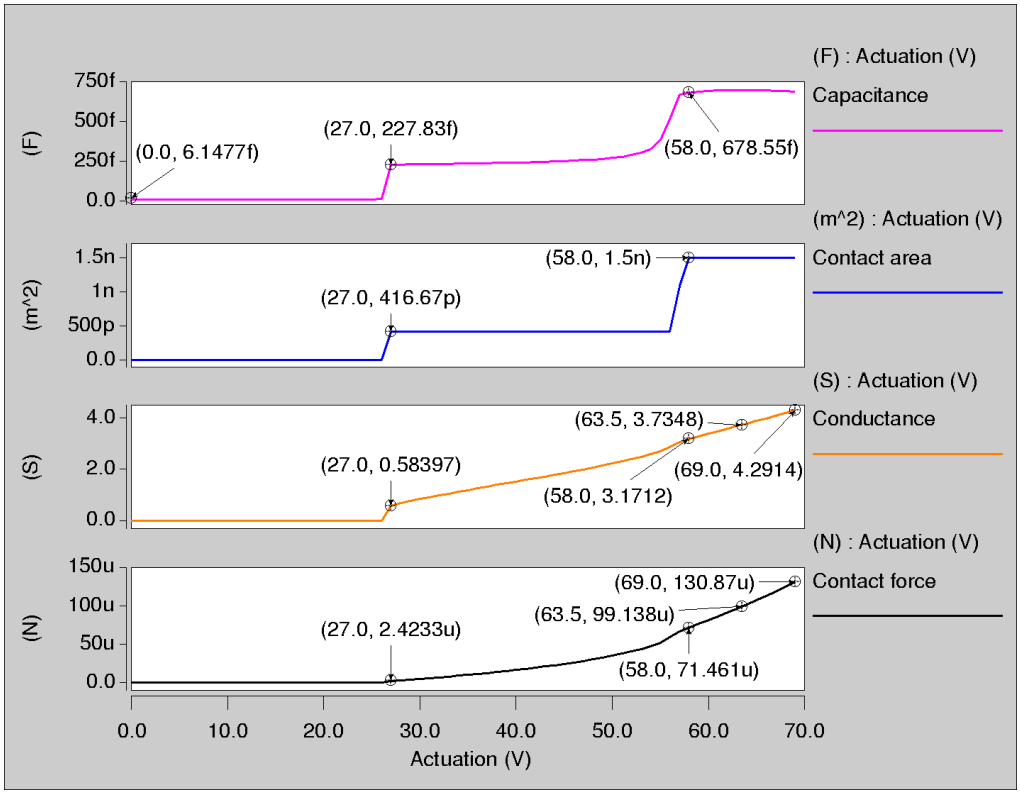

Fig. 16. DC analysis results of the Hammerhead switch

Some of the results can also be estimated through calculations.

The electrostatic force $F_{e(arc)}$, applied for arc-shape deformation of the cantilever, is calculated as:

$$F_{e(arc)} = \frac{e_0 \cdot A \cdot V_{arc}^2}{2g_{arc}^2} = 32.34\mu N$$

where: g_{arc} = 2μm the remaining gap between cantilever and the middle of the electrode,

V_{arc} = 27V, the actuation voltage for the first touch (arc-shape).

The minimum electrostatic force $F_{s(min)}$, applied for full contact under S-shape deformation of the cantilever.

$$F_{e(smin)} = \frac{e_0 \cdot A \cdot V_{smin}^2}{2g_s^2} = 332\mu N$$

g_s = 1.34μm the remaining gap between cantilever and the middle of the electrode,
V_s = 58V, the minimum actuation voltage for full contact (S-shape).

The maximum allowable electrostatic force $F_{s(max)}$, which can be applied for full contact under S-shape deformation of the cantilever, is calculated as.

$$F_{e(smax)} = \frac{e_0 \cdot A \cdot V_{smax}^2}{2g_{smin}^2} = 585\mu N$$

g_{smin} = 1.2μm the remaining gap between cantilever and the middle of electrode,
V_{smax} = 69V, the maximum allowable actuation voltage.

The mechanical spring constant k of the cantilever is calculated as:

$$k = 2Ew_1\left(\frac{t}{l}\right)^3 \cdot \frac{1-\frac{x}{l}}{4-3\left(\frac{x}{l}\right)^3+\left(\frac{x}{l}\right)^4} = 27.34\,N/m$$

where: E=57GPa, the Young modulus of Au that is used by the Coventor,
w_1 = 150μm, the width of the first part of the cantilever,
t = 6μm, the thickness of the cantilever
l = 330μm, the length of the cantilever
x = 70μm, the distance from the anchor to electrode

The restoring force of the cantilever under arc-shape deformation $F_{r(arc)}$ is calculated as:

$$F_{r(arc)} = k(g_0 - g_{arc}) = 27.34\mu N$$

A rough estimation of the contact force under arc deformation condition is given by (9) and is in good agreement with simulations results

$$\mathrm{F_{c(arc)}} = \left(\mathrm{F_{e(arc)}} - \mathrm{F_{r(arc)}}\right) \cdot \mathrm{W_f\%} = (32.34\mu N - 27.34\mu N) \cdot \mathrm{W_f\%} = 5\mu N \cdot \mathrm{W_f\%}$$
$$\Rightarrow 2\mu N - 3\mu N$$

The pull-down voltage (when the cantilever has covered the $g_0/3$) of the cantilever is calculated as:

$$V_p = \sqrt{\frac{8kg_0^3}{27e_0A}} = 24.84V$$

where: A = $4x10^{-8}$ m^2, the area of the electrode,

$\varepsilon_0 = 8.86 \times 10^{-12}$ F/m, the permittivity of free space,

g_0 = 3μm, the gap between cantilever and electrode,

k = 27.34N/m the calculated spring constant of the cantilever

3.3.2.Squeeze Gas damping

To fulfill the criterion for reliable simulations in time domain, the squeeze gas damping effect under the settled environmental operating conditions has to been taken into account. For this purpose Rayleigh damping parameters have been extracted to be used in Architect transient analysis.

Using the Analyzer module of Coventorware, and running the MemMech-Modal Analysis the resonance frequency and the generalized mass for each mode is extracted as shown in Table 2.

Table 2. 1st & 2nd mode of resonance frequencies and generalized masses

Modes	Frequency	Generalized mass
1	1.21731E04	1.372445E-09
2	4.774515E04	5.477391E-10

The critical damping coefficient C_{crit} can be determined from the above;

$\omega_1 = 2\pi f_1 = 76447\ rad,$ $\quad c_{crit.1} = 2m_1\omega_1 = 209.838 \times 10^{-6}\ Ns/m$

$\omega_2 = 2\pi f_2 = 299839.5\ rad,$ $\quad c_{crit.2} = 2m_2\omega_2 = 328.467 \times 10^{-6}\ Ns/m$

The terms $c_{res.1}$ and $c_{res.2}$ for the two first resonance modes can then be determined by running the DampingMM-Mode Shape Analysis. Fig 17 shows the evolution of the damping force coefficient in time domain, where $c_{res.1}$ = 27.14812 x 10^{-6} Ns/m for f_1 = 12.173KHz and c_{res2} = 27.14755 x 10^{-6} Ns/m for f_2 = 47.745KHz.

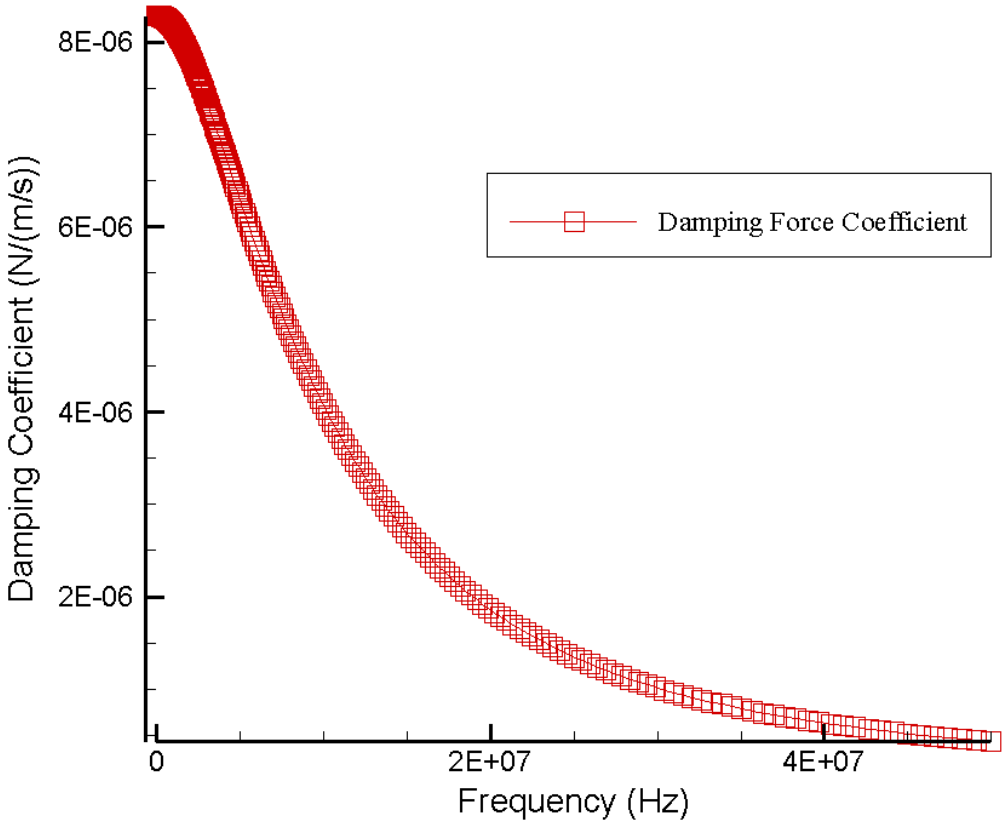

Fig. 17. Damping Force Coefficient

The damping factor ratio for f_1 and f_2 are:

$$\zeta_1 = \frac{c_{res.1}}{c_{crit.1}} = \frac{27.14812\text{x}10 - 6\ \text{Ns/m}}{209.838 \cdot 10^{-6} Nm/s} = 0.1293$$

$$\zeta_2 = \frac{c_{res.2}}{c_{crit.2}} = \frac{27.14755\text{x}10 - 6\ \text{Ns/m}}{328.467 \cdot 10^{-6} Nm/s} = 0.082$$

From the above results the Rayleigh damping parameters are calculated as:

$$\alpha = 2\omega_1\omega_2\frac{(\zeta_1\omega_2 - \zeta_2\omega_1)}{(\omega_2^2 - \omega_1^2)} = 16547/s$$

$$\beta = 2\frac{(\zeta_2\omega_2 - \zeta_1\omega_1)}{(\omega_2^2 - \omega_1^2)} = 351 \cdot 10^{-9}s$$

From the damping coefficient ζ of the first resonance mode, the Gas Quality factor (Q_{GAS}) which is the dominant factor over the total value of Q, can be computed as:

$$Q = \frac{1}{2\zeta_1} = \frac{1}{2 \cdot 0.1293} = 3.865$$

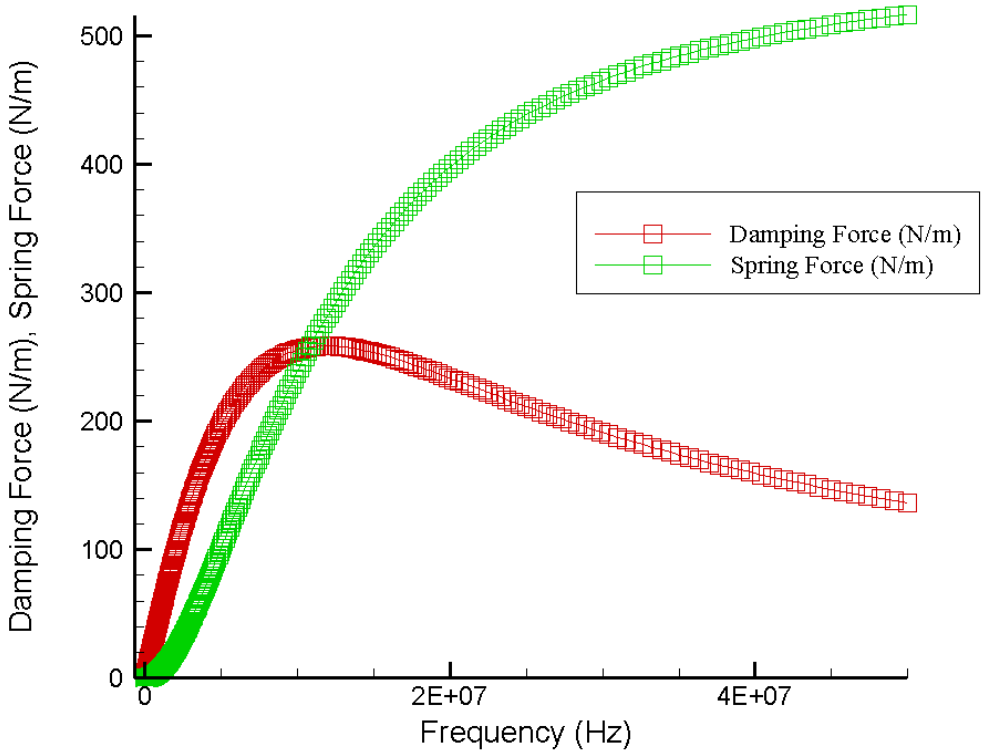

Fig. 18. Damping Force & Spring Force evolution in frequency domain

A general behavior of the switch under squeezed gas damping in frequency domain is shown in Fig. 18. As expected it is shown that at lower frequencies the viscous damping force is dominant. At higher oscillations the trapped layer of fluid acts increasingly like a pure spring. The cut-off frequency, f_c=10.8MHz, is defined as the frequency at which the spring force equals the damping force S_F=D_F=254N/m and

represents the frequency above which the air underneath the moving beam can no longer respond fast enough to the movement of the beam and starts behaving like a spring [124].

A summary of the design parameters of the "Hammerhead" switch is presented in Table 3.

Table 3: Design parameters of the "Hammerhead" switch

Parameter	Value	Parameter	Value
Length (movable)	330μm	Contact force	2.42μN (V_{arc}) 71.46μN ($V_{s(min)}$) 130.87μN ($V_{s(max)}$)
Width	150μm 210μm	Conductance	0.58S (V_{arc}) 3.17S ($V_{s(min)}$) 4.29S ($V_{s(max)}$)
Height from electrode	3μm	Pull-in(V_{pi}) First contact (V_{arc}) Full contact ($V_{s(min)}$) Full contact ($V_{s(max)}$)	25.234 27V 58V 69V
Height from contacts	2μm	Capacitance (OFF)	12.3fF 6.15fF/per contact area
Cantilever Type	Gold	Rayleigh gas damping parameters	α=16547/s β=0.351μs
Cantilever thickness	6μm	Q_{GAS}	3.865
Holes to cantilever	Yes	Contact Area	2x1.5nm^2

3.3.3.Transient analysis

A transient analysis is performed first under step pulse implementation with 60V amplitude, width p_w = 148μs, rise time t_r = 2μs and fall time t_f = 2μs.

The amplitude of 60V is chosen so as to ensure full contact (60V > 58V). This amplitude ensures immunity to switch parameters uncertainty due to the tolerances in the fabrication process, while simultaneously is lower than the maximum allowable voltage (60V < 69V) ensuring enough room for RF signal. Besides the rise and fall

times have a reasonable value that can be relatively easy to be generated by fast step-up converters (slew rate = 30V/μs).

The switching time obtained was around 15μs for the OFF-ON transition and roughly 12μs for the ON-OFF transition, as shown in Fig. 19. This figure shows the fastest ON-OFF switching time that can be achieved. Besides, the same figure illustrates the bouncing problems during the pull-down and release phases. Concentrating on the release phase, the step pulse actuation creates high bouncing phenomena with the maximum displacement value to reach the 3.59μm creating exceptionable results.

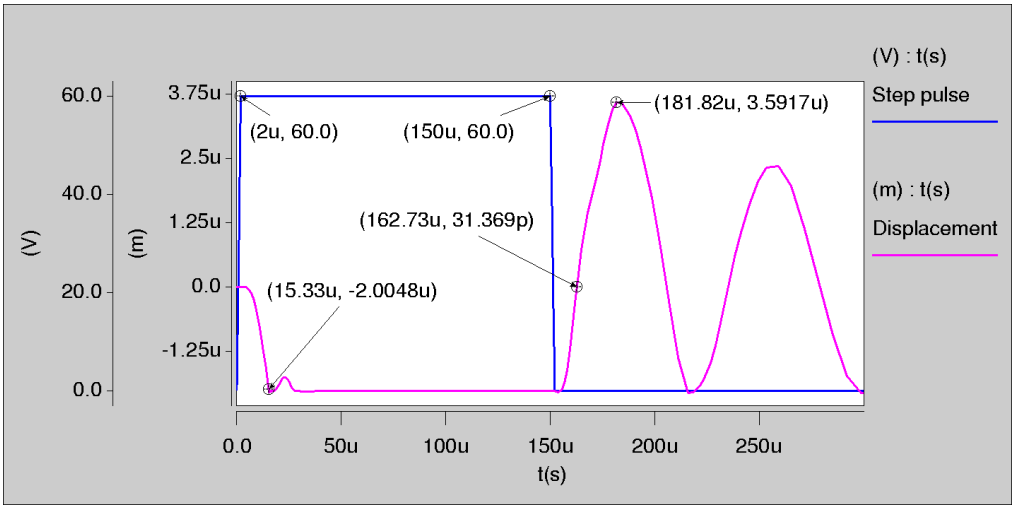

Fig. 19. Displacement under step pulse implementation

The switching time during the OFF-ON transition can also be calculated as:

$$t_s = 3.67\frac{V_p}{V_s\omega_0} = 20\mu s$$

Fig. 20 illustrates the rest of the switch's characteristics under step pulse implementation; that is the contact area ($1.5nm^2$), conductance (3.38S which corresponds to a resistance of 0.29Ω) and contact force (81μN). Some control difficulties are also illustrated as concerns the initially high contact force (around 350μN) due to the high impact velocity (around 31cm/sec) which introduces high settling time, too, during the pull-downstage (around 55μsec).

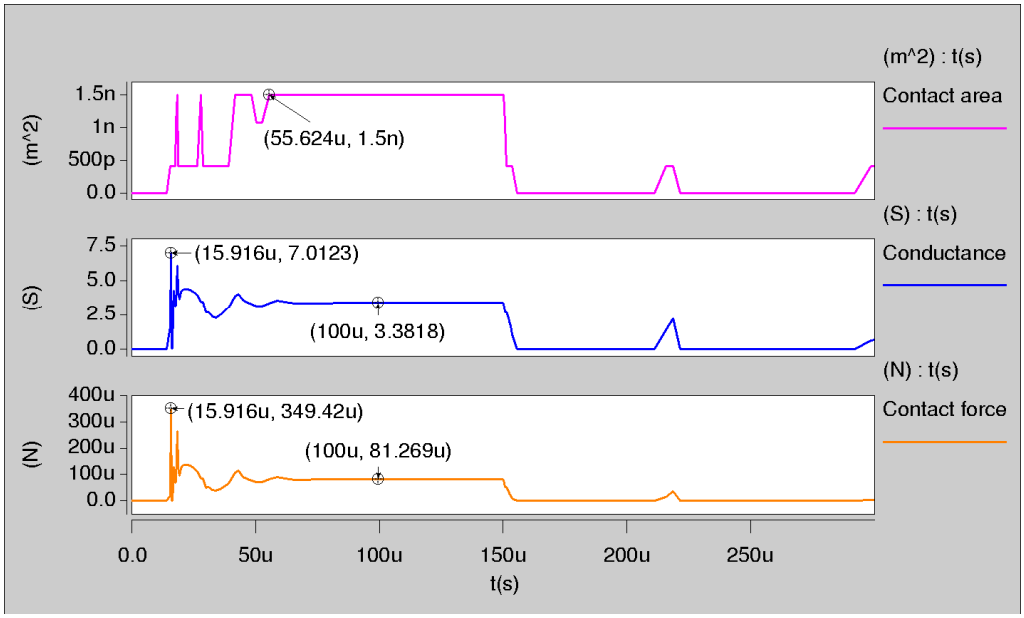

Fig. 20. Characteristics of the switch under step pulse implementation

3.3.4.Current and power consumption

In RF MEMS it is often supposed that there is no current/power consumption as there isn't any ohmic contact between the cantilever and the electrode. Nevertheless, this quick movement of the cantilever during the pull-downphase and release phase changes rapidly the capacitance and creates a transient phenomenon. Thus for this small time periods there is an instantaneous current request which can rise up to 6μA, as illustrated in Fig.21. The affect of damping resistance R_b = 17MΩ on the actuation step pulse source (Voltage, current and power) is also shown in Fig. 21.

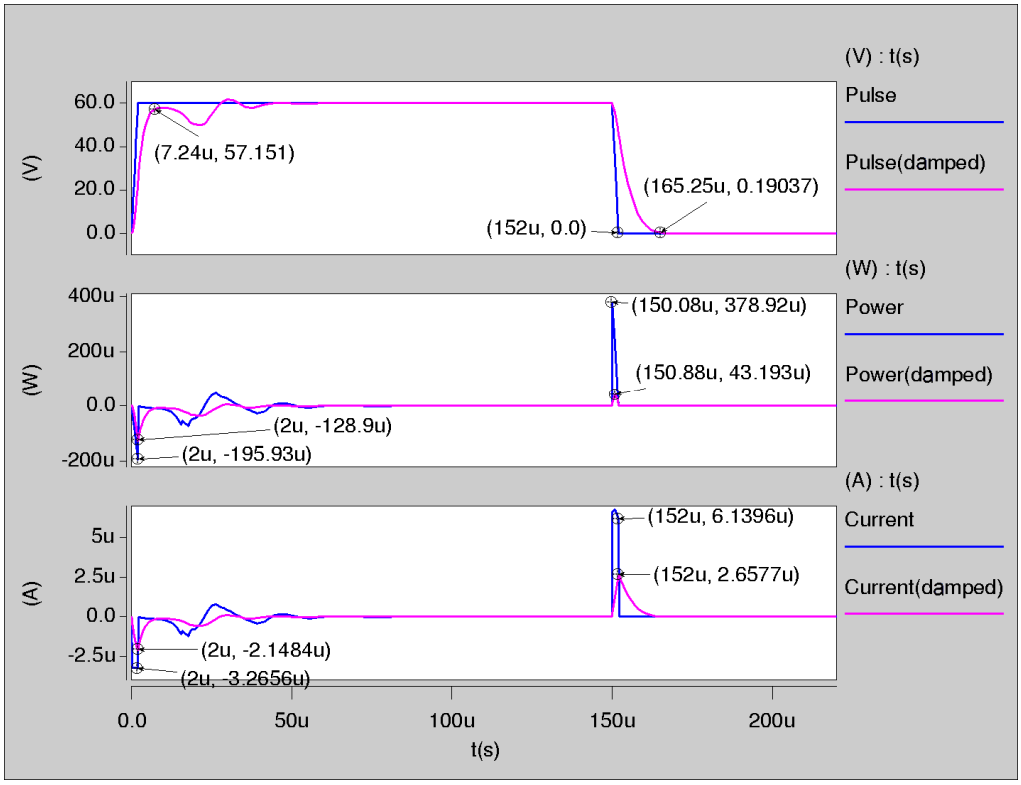

Fig. 21. Current and power consumption

3.3.5.Control under tailored pulse

High impact force and bouncing phenomena shown in Fig. 22, can be elliminated by applying a tailored actuation pulse [131]. Under these conditions the switching time is now increased to around 18.5μSec for the ON-OFF transition, 3μs slower compared to the step-pulse implementation. The switching time for the OFF-ON transition has also been increased by 2.2μs reaching 14.9μs but the maximum variation of the cantilever over the null position during the settling time is reduced from 3.5μm to 0.37μm.

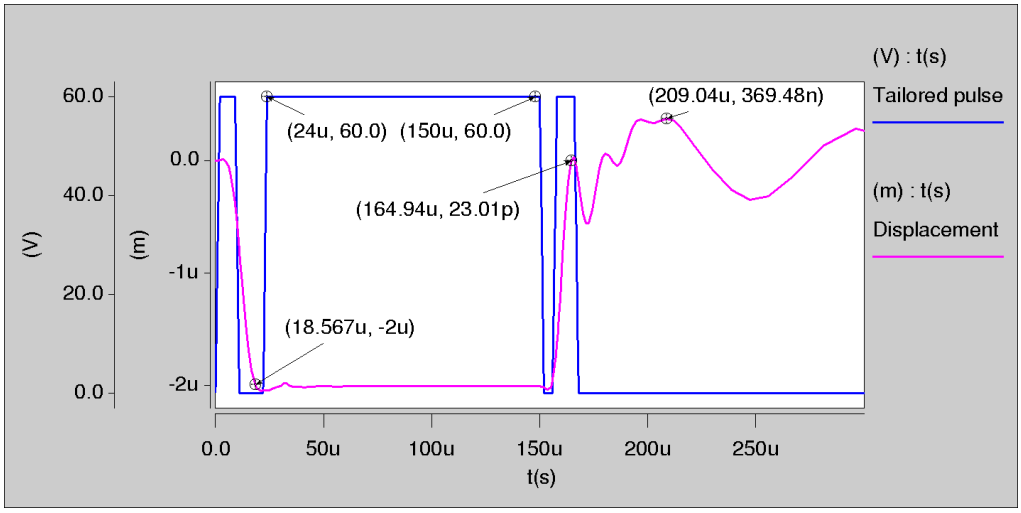

Fig. 22. Switch's behavior under tailored actuation pulse

Fig. 23 illustrates the rest of the characteristics of the switch under tailored pulse implementation where an obvious optimization is observed. The impact velocity is reduced from 31 to 5.1cm/sec resulting degradation in the initial impact force from 349 to 174μN, the maximum conductance is reduced to 4.9S instead of 7S and the full contact (1.5nm^2) is obtained at about 45μs instead of 55μs under step pulse.

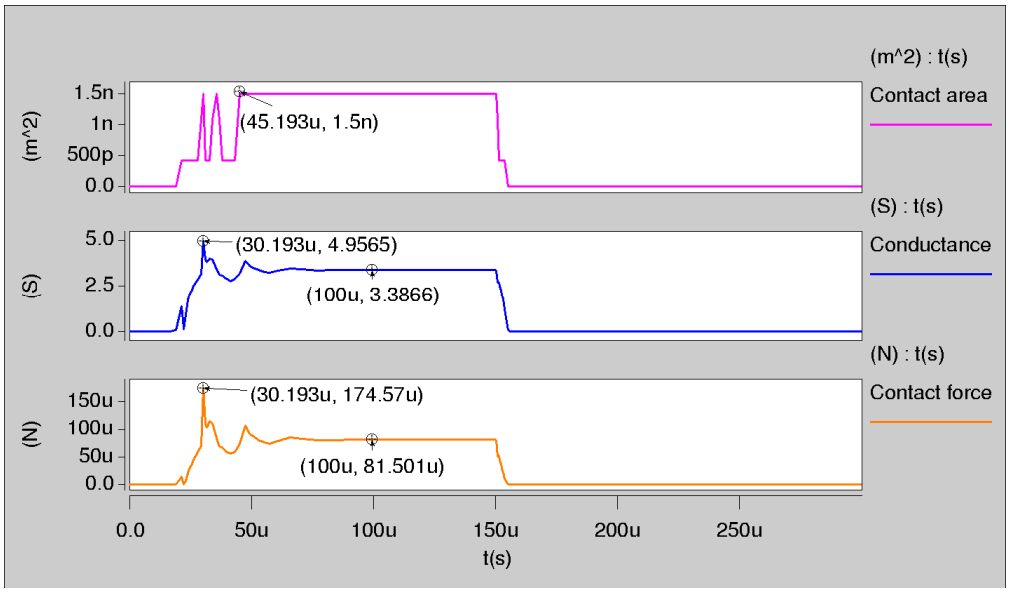

Fig. 23. Switch's characteristics under tailored actuation pulse

The conductance for each contact is 3.388S and the resulted resistance 0.295Ω. Since the two contact resistances are in parallel the total resistance will be R_c = 0.147Ω which is given by:

$$R_{sw} = R_c + R_s = 0.147 + 0.011\Omega = 0.158\Omega$$

A detailed study on using a tailored pulse for the enhancement of the pulse behavior is provided in Chapter 4.

3.3.6.Small signal frequensy analysis

Finally, the investigation on mechanical resonance frequency of the cantilever has been carried out via small-signal frequency analysis (Coventorware-Architect module) is F_0 = 12328Hz as shown in Fig. 24.

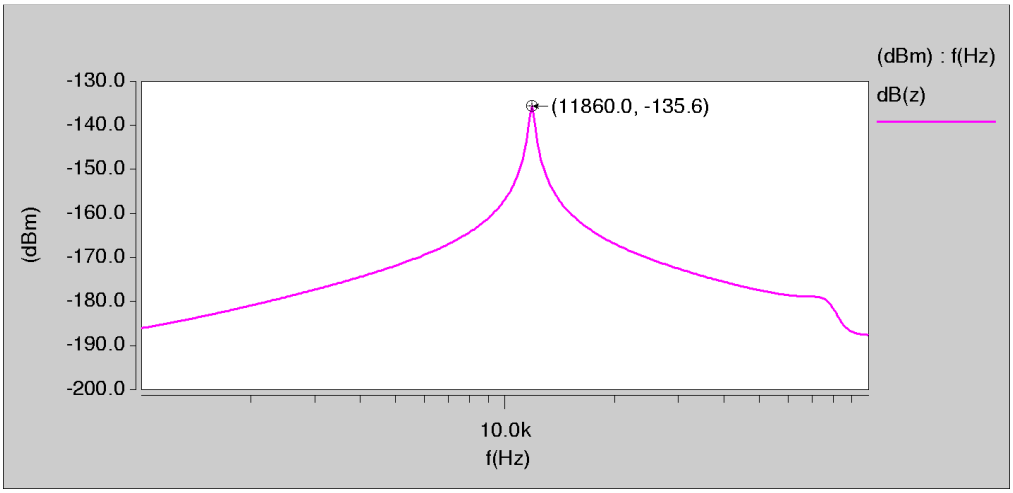

Fig. 24. The resonance frequency of the cantilever

The mechanical resonance frequency can also be calculated as [46] :

$$F_0 = \frac{1}{2\pi}\sqrt{\frac{k}{m}} = 12015Hz$$

where: k = 27.2N/m, the calculated spring constant

m=volume x dencity(Au) = 247.8x10^{-15} m^3 x 19280Kg/m^3 = 4.777x10^{-9}, the mass of the cantilever. The volume of the holes 70.8 x $10^{-15}m^3$ has been substracted from the total volume of the cantilever (318.6 x $10^{-15}m^3$)

3.3.7.Hot cycling mode of operation

The analysis on hot cycling mode of operation is presented in this section. Initially, the self actuating phenomenon is examined and the results of the switch's displacement when 1V, 10V and 20V RF signals are applied are illustrated in Fig.25. The effective voltage $V_{AC-eff} = \sqrt{2} \cdot V_p$ is 1.41V, 14.1 and 28.2V and the displacement of the cantilever is 518.87pm, 53.25nm and 191nm respectively.

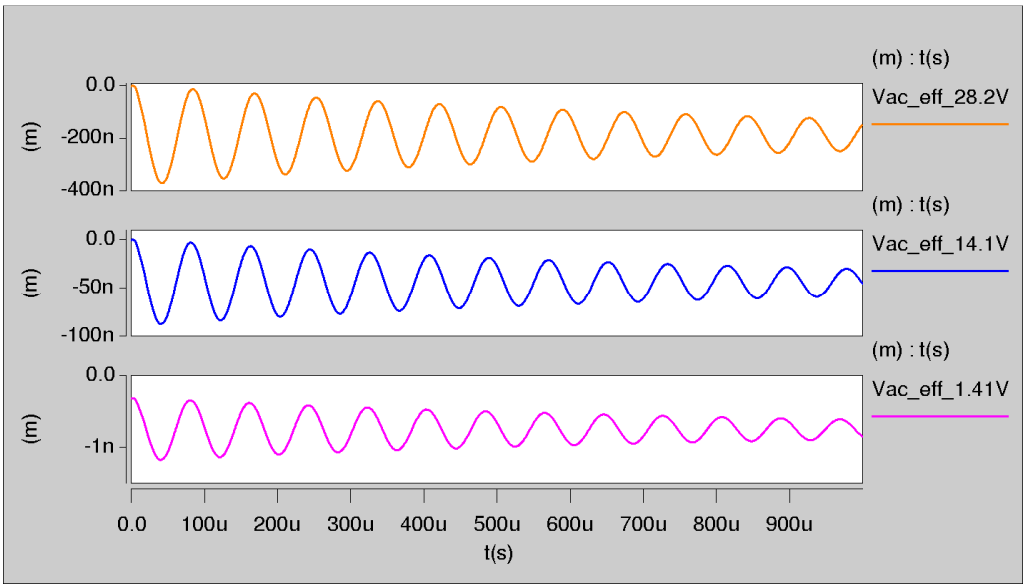

Fig. 25. Cantilever's displacement under the influence of RF signal only

Fig. 26 shows the behavior of the cantilever under hot cycling mode which means that RF signal exists during the ON-OFF operation of the switch. RF signals with amplitude of 1V, 7V 14V and 20V are applied respectively. It is obvious that the bouncing of the cantilever increases depending on the RF signal amplitude. For RF signal higher than 20V the cantilever collapses, as expected, because the corresponding V_{DC} = 28.2V, is close to the V_{arc} = 27V voltage of the switch.

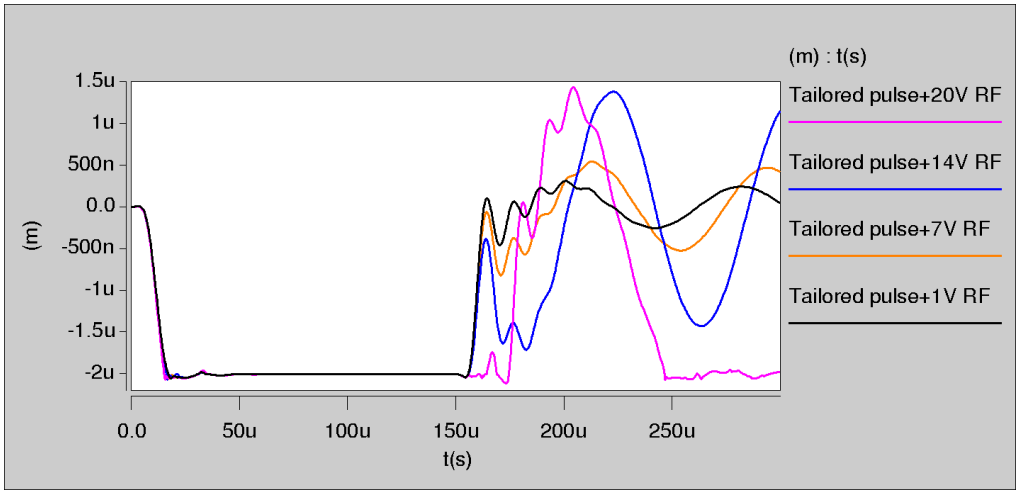

Fig. 26. Displacement under the influence of various RF signals

In Fig. 27 the effect of the various RF signals to the switching speed of the switch during the pull-down phase is shown.

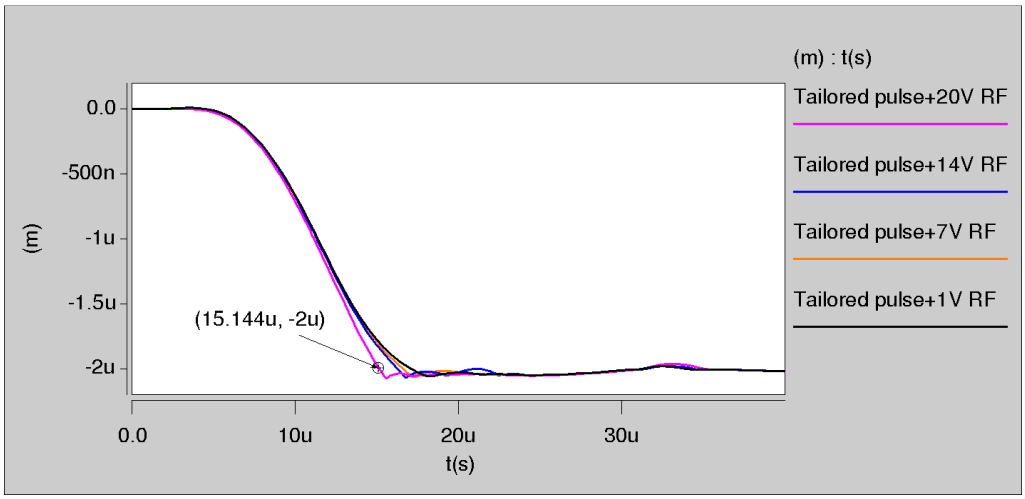

Fig. 27. Details of the pull-down phase under different RF signals

Fig. 28 shows the applied tailored actuation pulse, the displacement of the cantilever and the RF output of the switch when an RF signal with amplitude of 1V and a frequency of 2GHz is applied, in time correlation. It has to be mentioned that there is inertia to the switching operation due to the static equilibrium between the electrostatic force and the mechanical force that has to be reached before the cantilever starts to move. The switch is now switched ON 3μm before the start of the main actuation pulse (21μm instead of 24μm) and is switched OFF 6μm after the end of the main actuation pulse (56μm instead of 50μm).

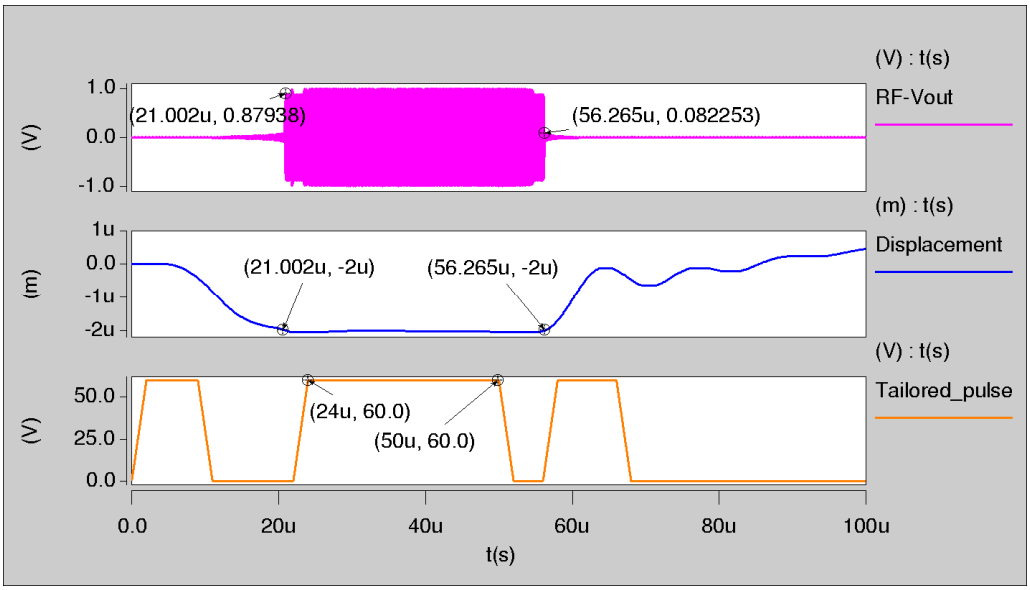

Fig. 28. Behavior of the switch under hot mode of operation

A more detailed view of the output RF signal is shown in Fig. 29. When the switch is in the OFF state, the capacitance (12.3Ff) created in the contact areas is responsible for the existence of an RF signal of about 0.78% of the initial value. When the switch is in the ON state, the contact resistance 0.257Ω and the resistance of the cantilever 0.011Ω, result to a loss of about 0.57% of the output RF signal.

The influence of the capacitor created between the cantilever and the contact area during OFF-ON and ON-OFF transitions is negligible (max. value 10% of the total amplitude). Another small disturbance is observed at the edges of the output RF signal before the final settling, which last for about 2.4μs with value the 88% of the total amplitude.

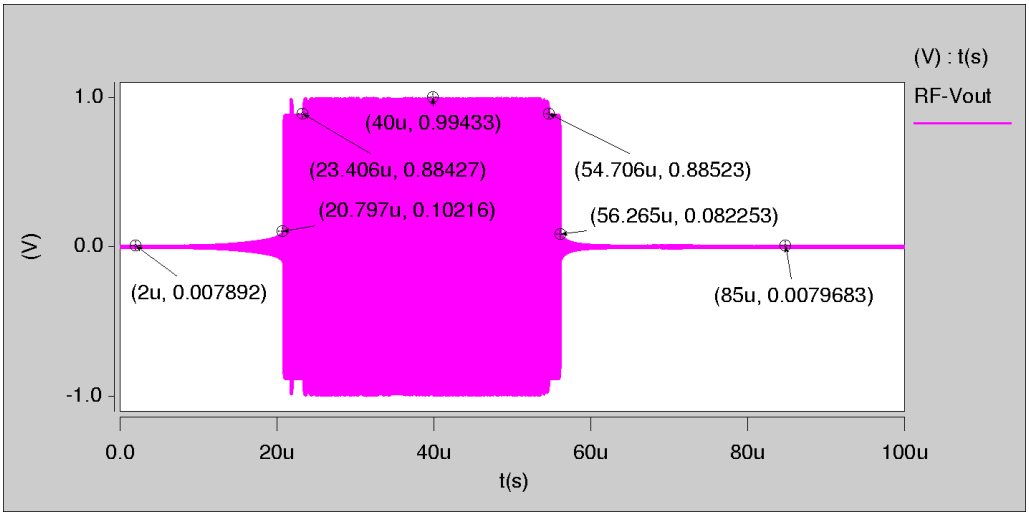

Fig. 29. Details of the RF output signal

Fig. 30 presents the results of the FFT analysis at three discrete periods of time of the output when an input signal with amplitude of 1V and frequency of 2GHz is applied. The sampling rate is defined by the expression:

$$S_R = \frac{N_{points}}{t_{start} - t_{stop}} = \frac{1024}{1\mu s - 1.2\mu s} = 5.12GHz \qquad (44)$$

where:

Npoints = specifies the number of data points to be written to the output waveform,

t_{start} = the beginning of the time segment to be analyzed

t_{stop} = the ending of the time segment to be analyzed

For the time period 2 to 2.2μsec the switch is in the OFF state and the S/N ratio is 91.6dB. For the time period 20.7 to 20.9μsec, during the transition time of the switch, the S/N ratio deteriorates to 59.4dB. For the time period 40 to 40.2μsec the switch is in the stable ON state and the S/N ratio alters again to 84.5dB.

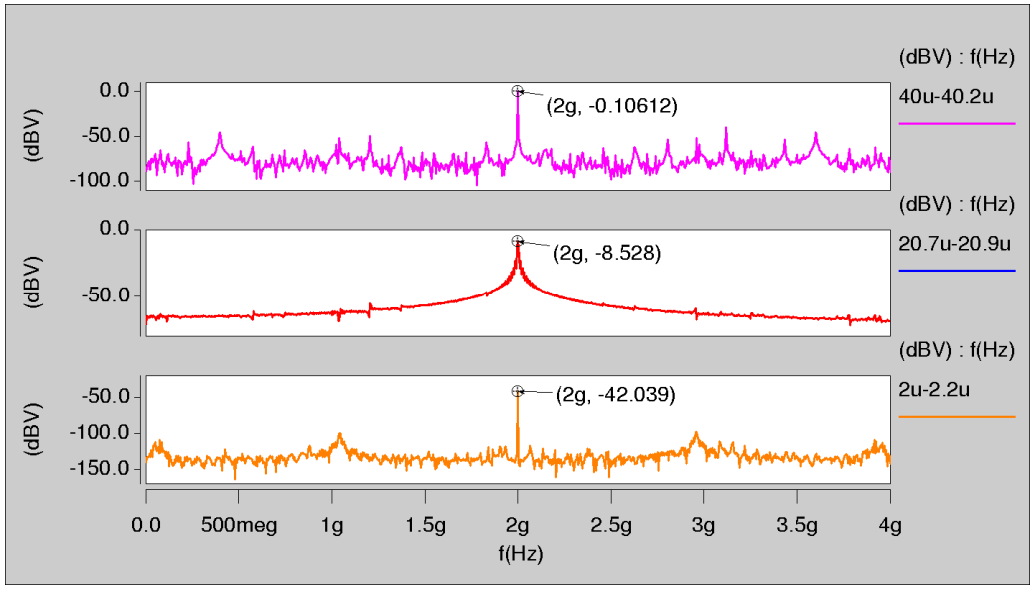

Fig. 30. FFT analysis under hot mode of operation

3.3.7.1. Cold cycling mode of operation

This section presents the simulation results of the "Hammerhead" switch under cold cycling mode of operation. In this case, the controllability of the switch is not getting affected by the RF signal that is passing through the switch as well as the power handling limitations are set exclusively by the geometry of the contact area and the cantilever.

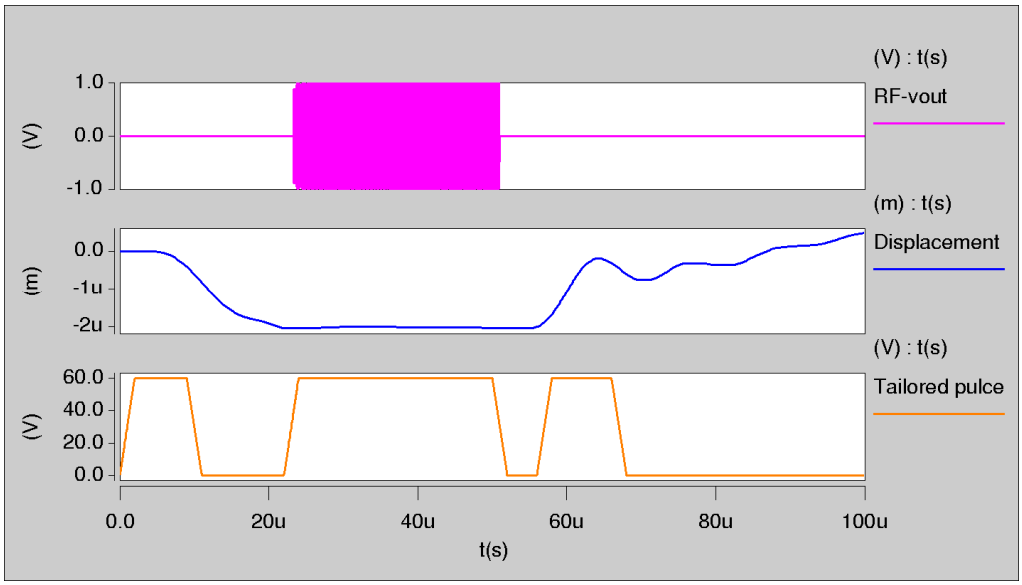

Fig. 31. Behavior of the switch under cold mode of operation

Fig. 31 shows the tailored pulse, the displacement of the cantilever and the RF output signal, when an RF signal with amplitude 1V and frequency 2GHz is applied after the switch closes while it is removed before the switch opens. Comparing the switching operation to that of Fig.31, it is clear that cold mode of operation has more discrete ON and OFF states and this difference will become more obvious as the frequency of the RF input signal increases. Nevertheless, applications such as the reconfigurable antennas will not work properly under cold cycling mode.

3.3.8.Electromagnetic analysis

A full electromagnetic wave analysis has been carried out to further investigate the S-parameters of the switch using two-port analysis from the small signal analysis menu of the Architect module. The impedance z_0 for input and output was set 50Ω.

Fig. 32 presents the Return loss and the Isolation graphs in the frequency range DC to 20 GHz, when the switch is in the OFF state. The results of the simulation are very promising as the Isolation and Return loss figures are -28dB and -0.0065dB, respectively, at 5 GHz.

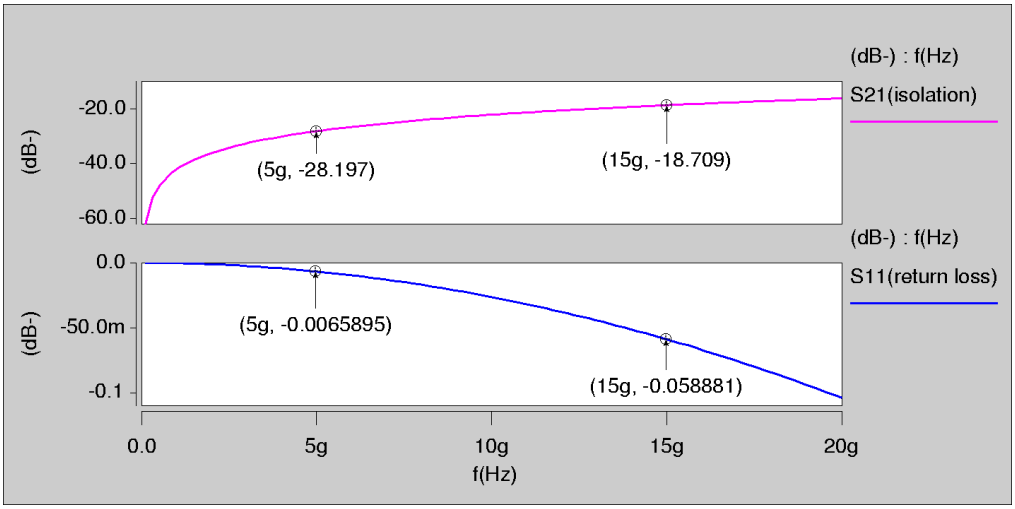

Fig. 32. Isolation and Return loss of the "Hammerhead" switch in the OFF state

In the Smith chart of Fig.33 the variation of the complex values of Isolation (S21) and Return loss (S11) can be observed for the frequency range 0-100GHz when the switch is in the OFF state. These variations are due to the relatively high value of the total capacitance (around 12.3fF), created in the contact area.

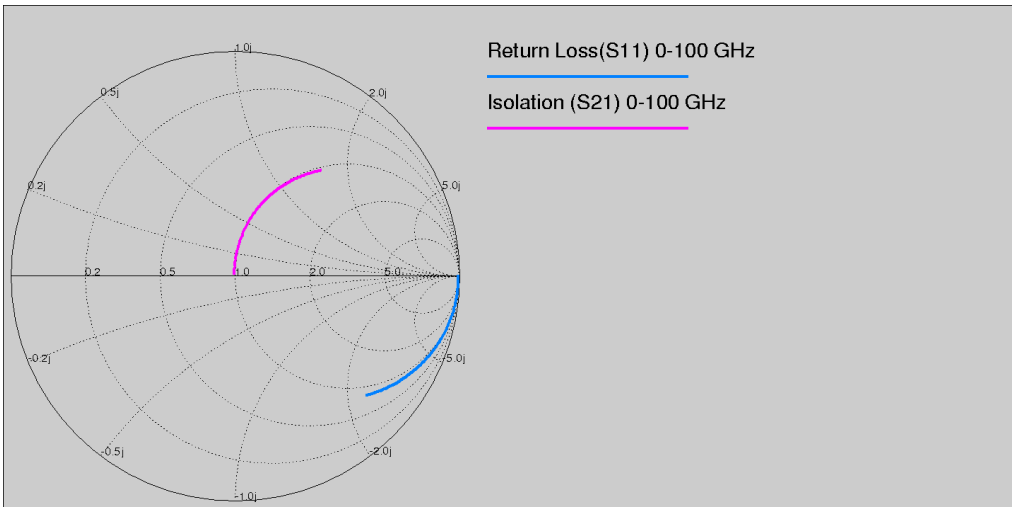

Fig. 33. Smith chart for S11 and S21 with the switch in the OFF state

The behavior of the switch is investigated also with the switch in the ON state presenting very significant results as regards to Return loss (-28.97dB) and Insertion loss (-0.019dB) at 5GHz. The results of the simulation in the frequency range DC to 20GHz are illustrated in Fig. 34.

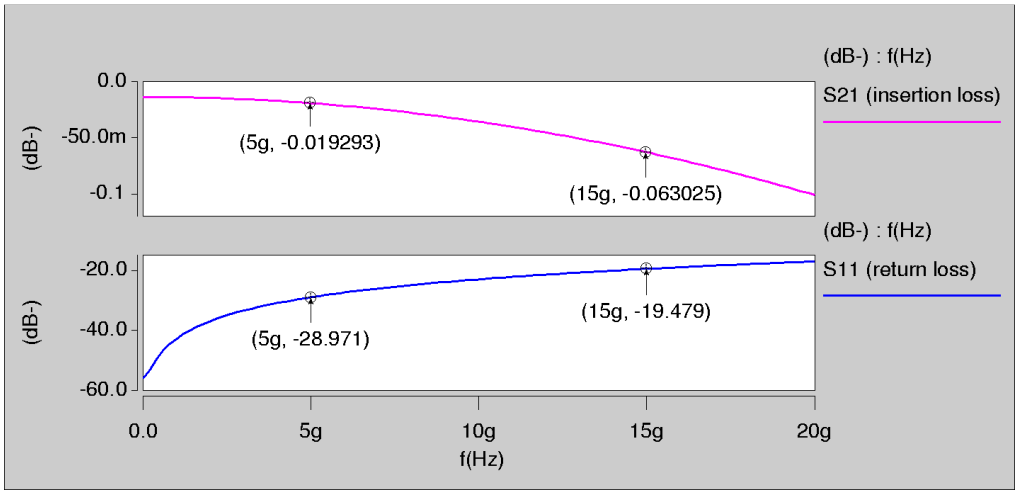

Fig. 34. Insertion and Return loss of the “Hammerhead” switch in the ON state

In Fig. 35 a Smith chart graph presents the variation of the complex values of Insertion and Return Loss for the frequency range DC to100GHZ which, in this case are due to the self-inductance of the switch.

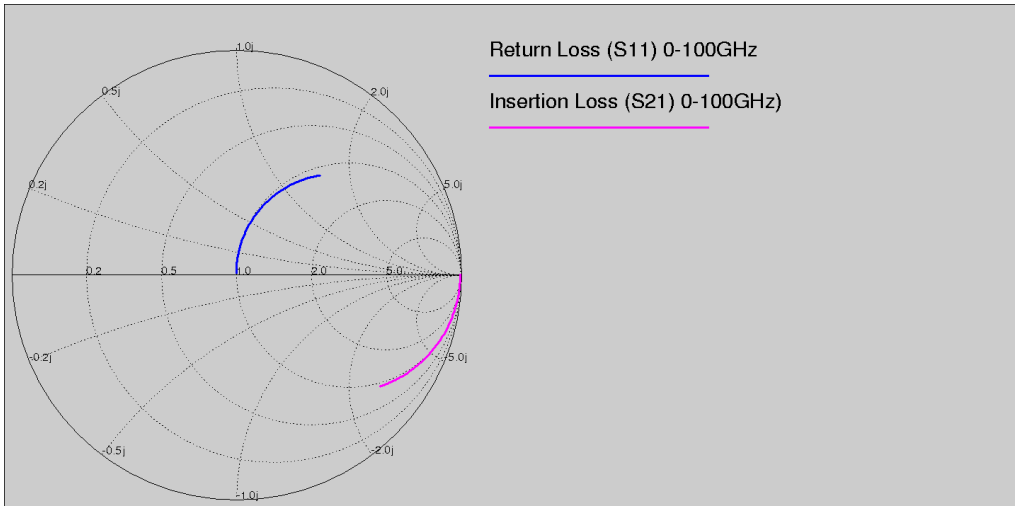

Fig. 35. Smith chart for S11 and S21 with the switch in the ON state

The resistance of the cantilever can be calculated using (35):

$$R_S = \frac{l_1 \cdot \rho}{w_1 \cdot t} + \frac{l_2 \cdot \rho}{w_2 \cdot t} = 0.01\Omega$$

The self-inductance at low frequency for a straight rectangular bar is given by (36). In the case of a non uniform cantilever, like the "Hammerhead" the inductance of two coils with different lengths and widths in series is considered.

$$L_S = 2 \cdot 10^{-7} \cdot l_1 \cdot \left[ln \frac{2l_1}{w_1 + t} + \frac{1}{2} + \frac{w_1 + t}{3l_1} \right] + 2 \cdot 10^{-7} \cdot l_2 \cdot \left[ln \frac{2l_2}{w_2 + t} + \frac{1}{2} + \frac{w_2 + t}{3l_2} \right] = 132.7pH + 17.7pH = 150.4pH$$

where: $\rho = 2.44 \cdot 10^{-8}\ \Omega \cdot m$, the resistivity of the gold,

$l_1 = 320\mu m$, the length of the first part of the cantilever plus the length of the anchor,

$l_2 = 60\mu m$, the length of the second part of the cantilever,

$w_1 = 150\mu m$, the width of the first part of the cantilever,

$w_2 = 210\mu m$, the width of the second part of the cantilever,

$t = 6\mu m$, the thickness of the cantilever.

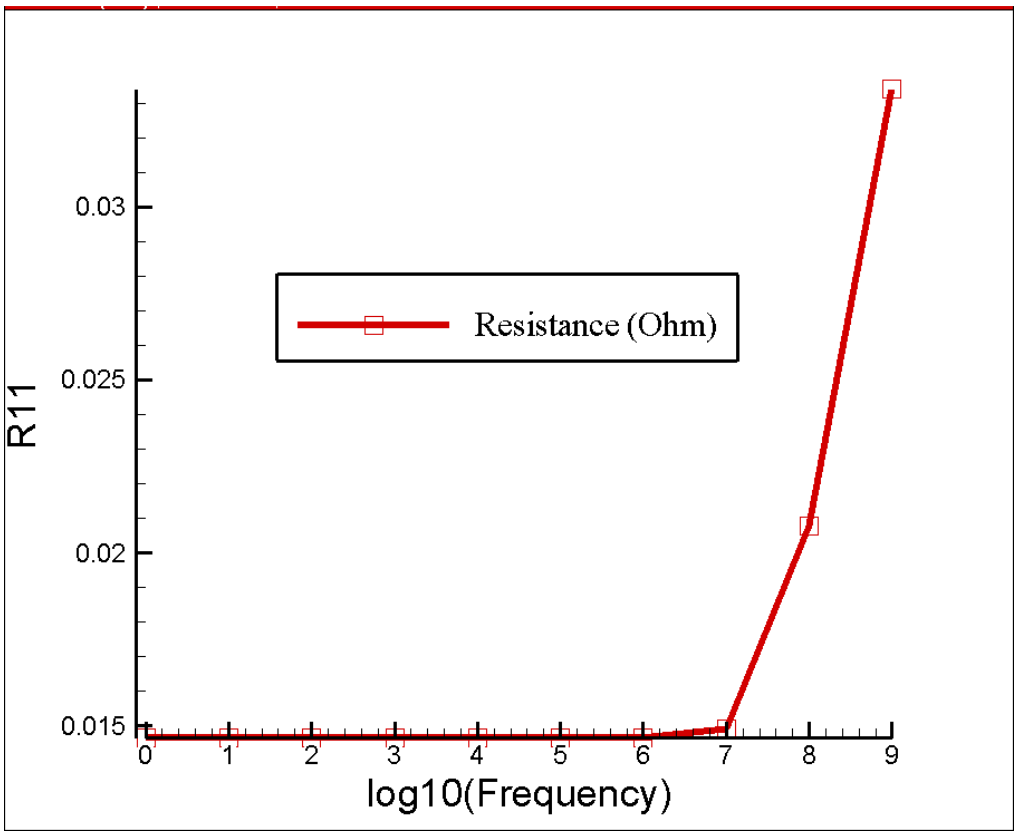

Fig. 36. The resistance of cantilever with frequency

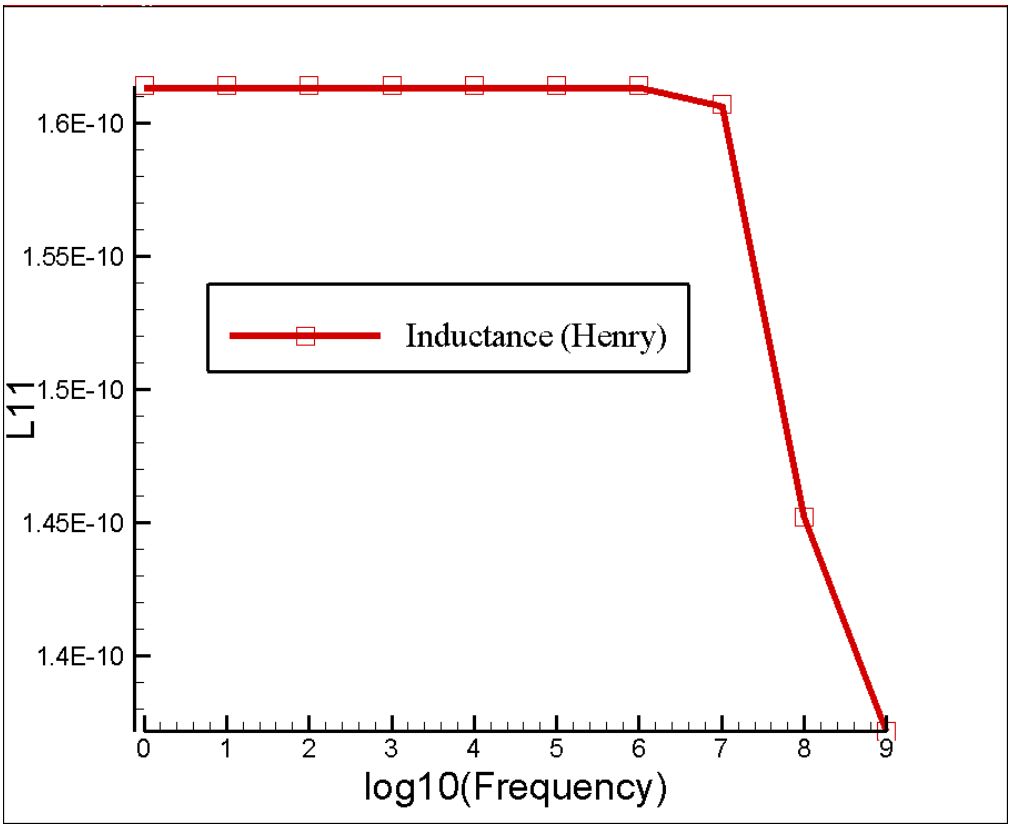

Fig. 37. The inductance of the cantilever with frequency

The resistance and the inductance of the cantilever as well as their evolution in frequency domain are extracted also using Finite Element Analysis through the Analyzer module of Coventorware as illustrated in Fig. 36 & 37. The simulated values are in good agreement with calculated values in the low frequency area.

The increase of the resistance and the decrease of the inductance with the increase of the frequency are mainly due to the skin effect. When the frequency increase, the current density is not uniform over the conductor cross section as in the case of DC currents, but rather tends to be concentrated near the surface with the depth of penetration to be depended from both the frequency and the material used (12). In the case of a flat strip structure like the cantilever the current density is greatest at the edges, considerable at the flat surfaces and least at the center as shown in Fig. 38 for the frequency of 1GHz.

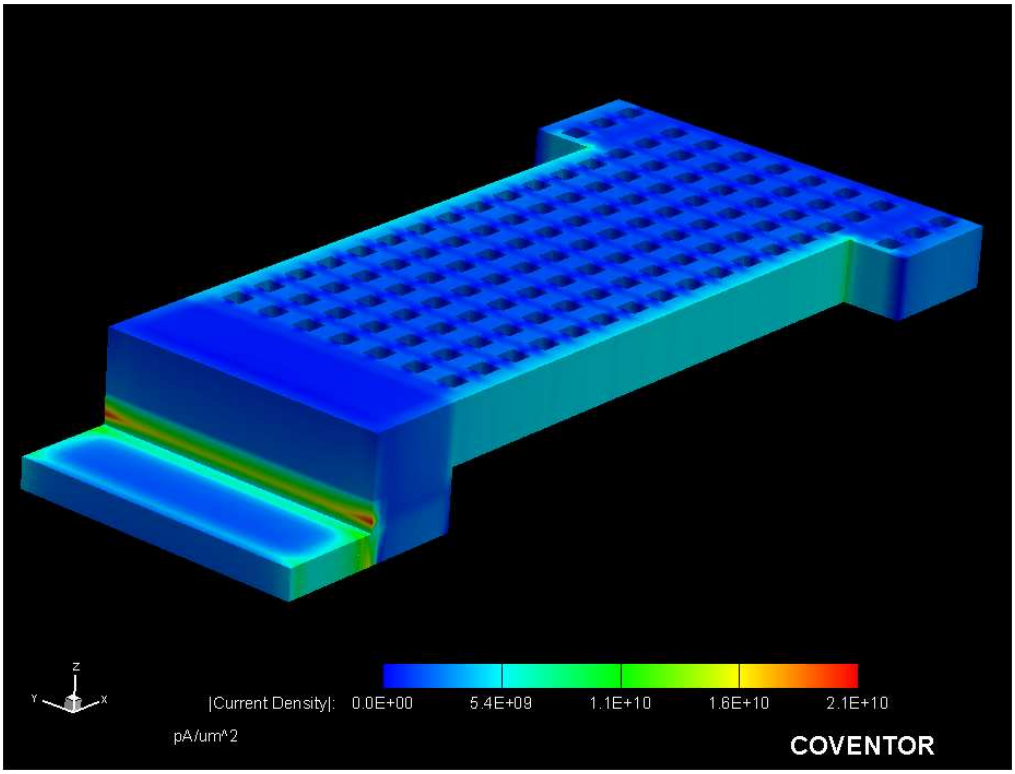

Fig. 38. The current density in the surface of the cantilever for f=1GHz

The capacitance formed in each contact area when the switch is in OFF-state is calculated as:

$$C_c = \frac{e_0 A_c}{d} = 6.645fF$$

where: A_c=1500nm^2, the area of one contact,

$\varepsilon_0 = 8.86 \text{ x } 10^{-12}$ F/m, the permittivity of free space,

d=2μm, the distance between cantilever and contacts.

And the total capacitance of the entire switch is: $C_{sw} = 2 \cdot C_c = 13.28fF$

Finally the evolution of the S-parameters (S_{11}, S_{21}) has been investigated during the transition from the OFF to the ON state, under a DC transfer analysis. The frequency of the RF input signal was 5GHz and the amplitude 1V. The results are shown in Fig. 39. It can be observed that the final transition takes place between 25-30V. Therefore, this is the voltage actuation range that has to be avoided in order to ensure reliable operation of the switch.

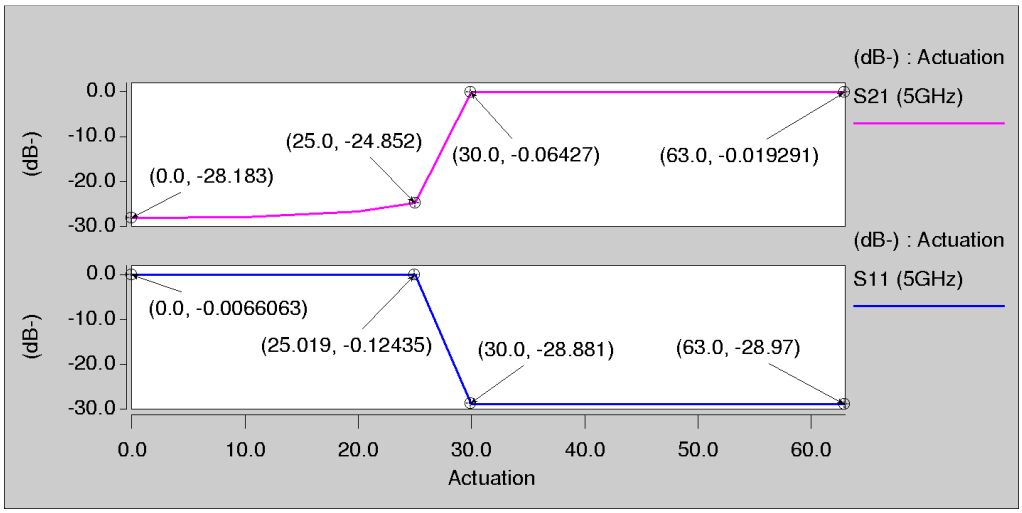

Fig. 39. Evolution of the S-parameters in 5GHz during OFF-ON transition

A summary of the simulated parameters of the “Hammerhead” in line series ohmic RF-MEMS switch is presented in Table 4.

Table 4. Performance results of the switch under tailored pulse actuation

Parameter	Value	Parameter	Value
Pulse amplitude	60V	Isolation (OFF) (S21_5GHz)	-28.2dB
RF signal (max)	20V	Return loss (OFF) (S11_5GHz)	-0.006 dB
Contact force	81.5μN	Insertion loss (ON) (S21_5GHz)	-0.019 dB
Conductance	3.38S	Return loss (ON) (S11_5GHz)	-28.9 dB
Switching time	18.5μs (OFF-ON) 15μs (ON-OFF)	SNR	91.6dB_OFF 59.4dB_Trantition 84.5dB_ON

Table 5 shows that the calculations of the main characteristics of the switch are in good agreement with the corresponding figures from the simulation of the switch.

Table 5. Comparison between simulations and calculations

	Architect module simulations	Analytical Calculations
C_c	6.15fF	6.64fF
R_s	0.014Ω (Analyzer)	0.01Ω
L_s	161pH (Analyzer)	150pH
V_p	25.234V	24.84V
$F_{c(arc)}$	2.43μN	2-3μN
$K_{(27)}$	26.5N/m (Analyzer)	27.2N/m
t_s	15.3μs	20μs
f_c	11.860KHz 12.173KHz (Analyzer)	12.015KHz

3.4. Analysis and design of an Ohmic RF-MEMS switch with “Uniform” cantilever shape

The first efforts on the design of an all metal in-line ohmic RF-MEMS switch accomplished, based on the well-known on literature structure of Fig. 4c [49]. For comparison reasons a “Uniform” switch with about the same features compared to the “Hammerhead” switch as regards length, width, thickness, perforation, height from the electrode, electrode area, protrude and distance between contacts is modelled and presented in Fig. 40. The differences between them are mainly the shape of the end of the cantilever, the dimensions of the contact area and the shape of the electrode area.

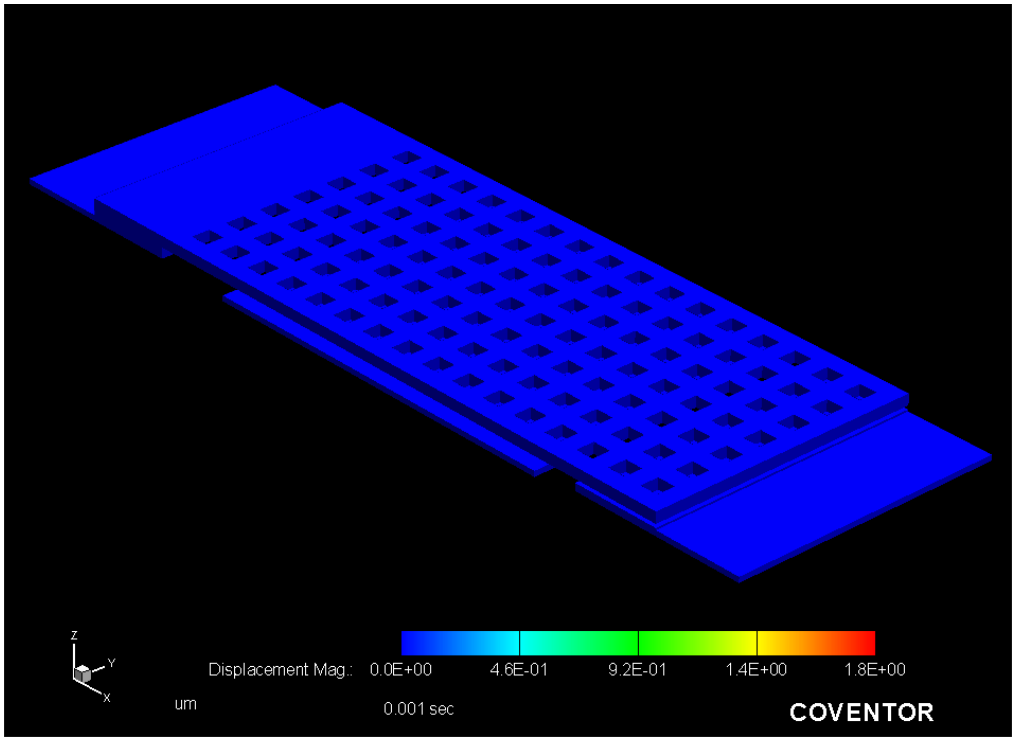

Fig. 40. The “Uniform” ohmic RF MEMS Switch

An expanded 3D view of the z axis of the uniform switch with the cantilever in arc shape deformation is shown in Fig. 41.

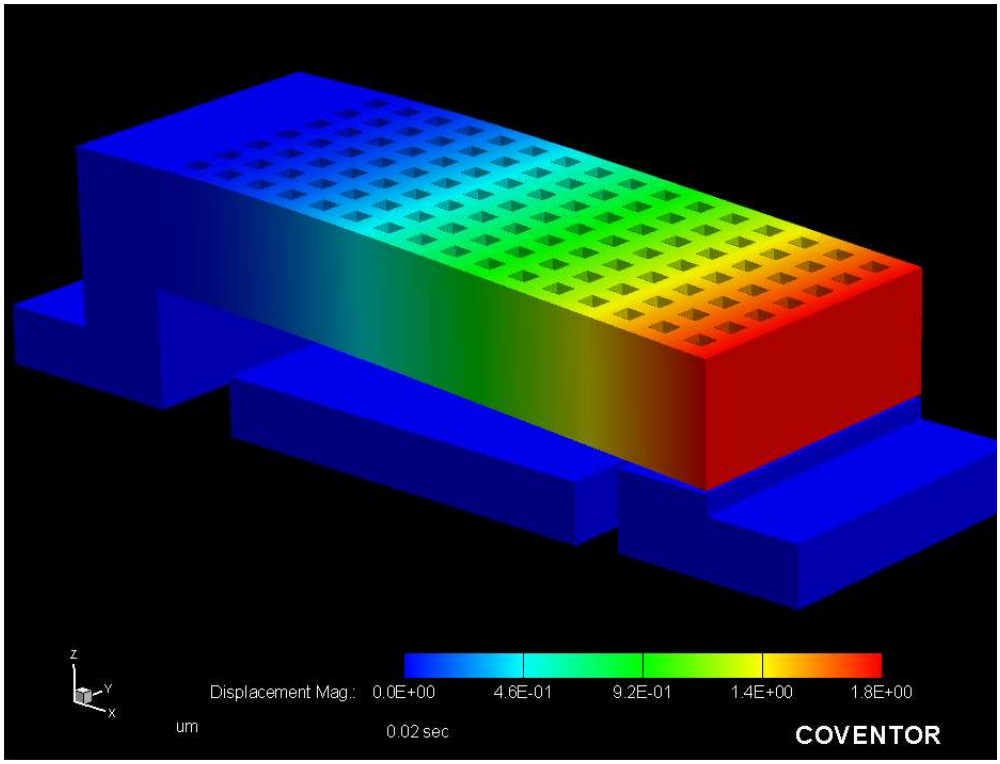

Fig. 42. An expanded view of the "Uniform" ohmic RF MEMS switch

3.4.1.DC transfer analysis

A DC transfer analysis via Architect module has been carried out by applying a ramp voltage to investigate on: actuation voltage, contact force, conductance, contact area and capacitance. A summary of the design parameters of the "Uniform" switch is presented in Table 6.

Table 6. Design parameters of the "Uniform" switch

Parameter	Value	Parameter	Value
Length (movable)	330μm	Contact force	1.61μN (V_{arc}) 75μN ($V_{s(min)}$) 120.88μN ($V_{s(max)}$)
Width	150μm	Conductance	0.47S (V_{arc}) 3.25S ($V_{s(min)}$) 4.12S ($V_{s(max)}$)
Height from electrode	3μm	Pull-down(V_p) First contact (V_{arc})	34.81V 39V

		Full contact ($V_{s(min)}$) Full contact ($V_{s(max)}$)	62V 68V
Height from contacts	2μm	Capacitance (OFF)	30.7fF
Cantilever Type	Gold	Rayleigh gas damping parameters	α=21178/s β=0.103μs
Cantilever thickness	6μm	Q_{GAS}	3.882
Holes to cantilever	Yes	Contact Area	7.5nm^2

3.4.2.Transient analysis

Initially, a transient analysis is performed under step pulse implementation with an amplitude of 60V, width p_w = 148μs, rise time t_r = 2μs and fall time t_f = 2μs.

The amplitude of 63V is chosen so as to ensure full contact (63V > 62V). This amplitude ensures immunity to switch parameters uncertainty due to the tolerances in the fabrication process, while simultaneously is lower than the maximum allowable voltage (63V < 68V) ensuring enough room for RF signal. Besides the rise and fall times have a reasonable value that can be relatively easy to be generated by fast step-up converters (slew rate = 30V/μs).

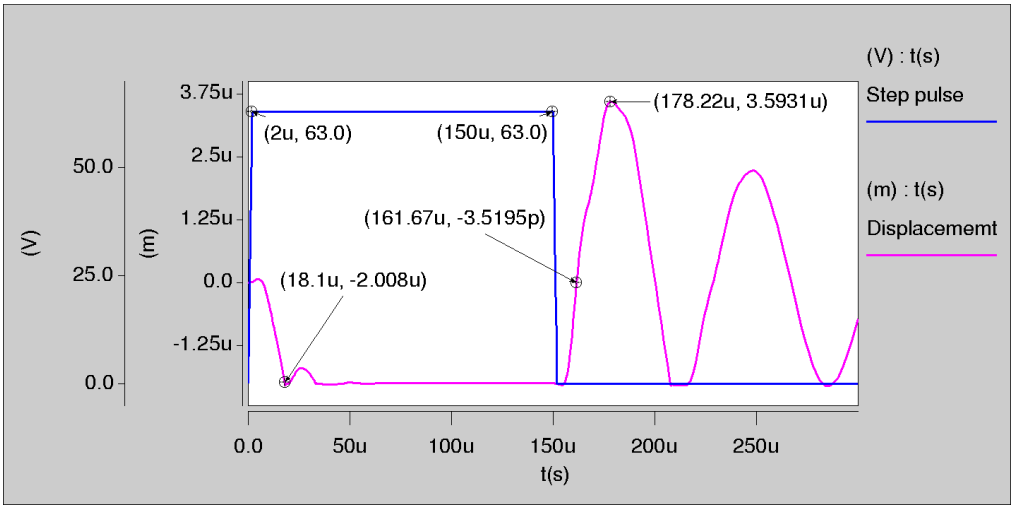

Fig. 43. Displacement under step pulse implementation

The switching time that obtained was around 18.1μs for the OFF-ON transition and around 11.67μs for the ON-OFF-transition, as shown in Fig. 43. This figure shows the fastest ON and OFF switching time that can be achieved. Moreover, the Fig. 43 also

illustrates the bouncing problems during the pull-down and release phases. Especially during the release phase, the step pulse actuation creates high bouncing phenomena with the maximum displacement to be as much as 3.59μm.

Fig. 44 illustrates other characteristics of the switch under step pulse implementation such as the contact area (7.5nm^2), the conductance (3.44S which corresponds to a resistance of 0.29Ω) and the contact force (84.4μN). Control difficulties are also observed as concerns the high initial contact force (around 850μN) due to the high impact velocity (about 22.9cm/sec) which results to high settling time during the pull-downstage of the switch (around 75μsec).

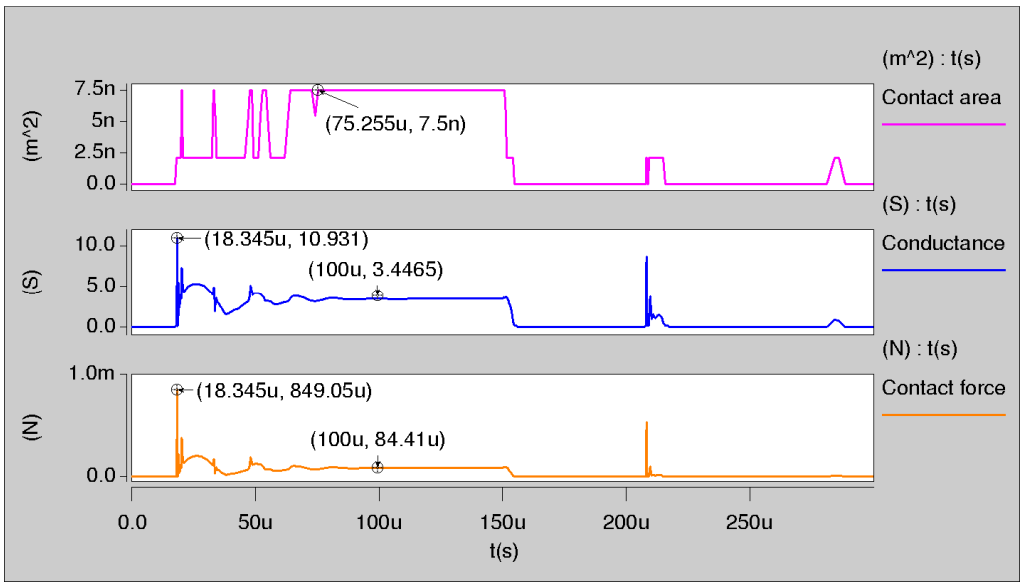

Fig. 44. Characteristics of the switch under step pulse implementation

3.4.3.Control under tailored pulse

Applying the tailored actuation pulse high impact force and bouncing phenomena have been reduced significantly, as shown in Fig. 45. Under these conditions the switching time is slightly increased to about 18.9uSec for the ON-OFF transition, 0.8μs slower compared to the step-pulse implementation. The switching time for the OFF-ON transition has been also increased about 3μs reaching 14.8μs, but the maximum variation of the cantilever over the null position during settling time is now reduced from 3.6μm to 0.6μm.

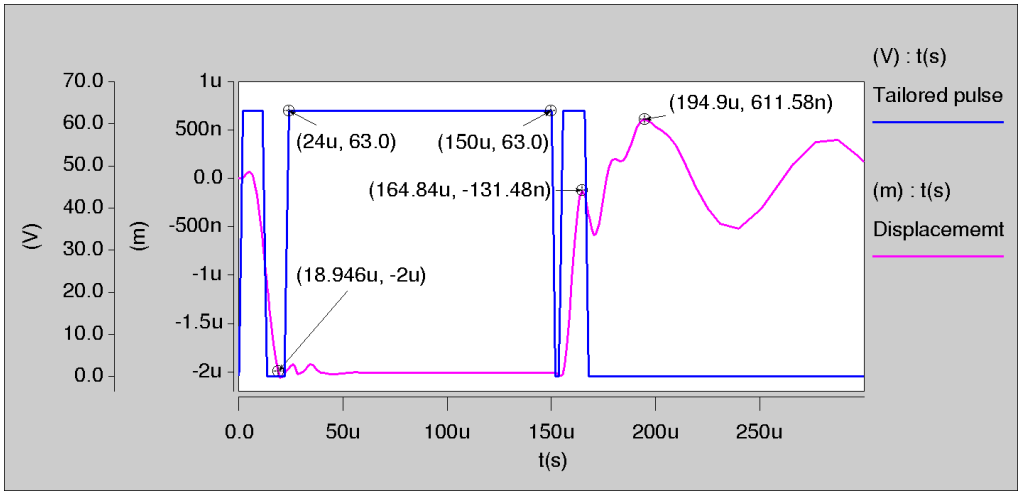

Fig. 45. Switch's behavior under tailored actuation pulse

Fig. 46 illustrates the other characteristics of the switch under tailored pulse implementation where an obvious optimization is observed. The impact velocity is reduced from 22.9 to 5.2cm/sec resulting to a degradation in the initial impact force from 849 to 211μN. The maximum conductance is reduced to 5.4S instead of 10.9S and the full contact 1.5nm^2 is obtained at about 53μs instead of 75μs, an improvement of about 30%.

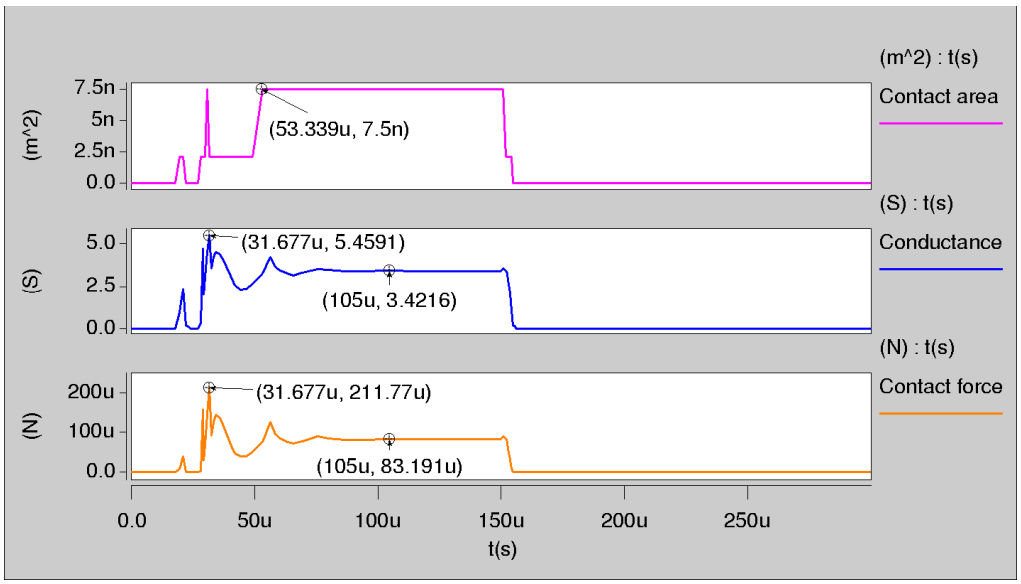

Fig. 46. Switch's characteristics under tailored actuation pulse

3.4.4.Hot cycling mode of operation

In this section, results for the “Uniform” switch under hot cycling mode operation are presented. Fig. 47 shows the behavior of the cantilever under hot cycling mode, where the RF signal is passing through during the ON-OFF transition. RF signals with amplitude of 1V, 10V 20V and 26V are applied respectively. It is obvious that the bouncing of the cantilever increases, depending on the amplitude of the RF signal. For RF signal higher than 26V the cantilever collapses, as expected, because the correspondence V_{DC}=36.6V, is close to the V_{arc}=37V voltage of the switch.

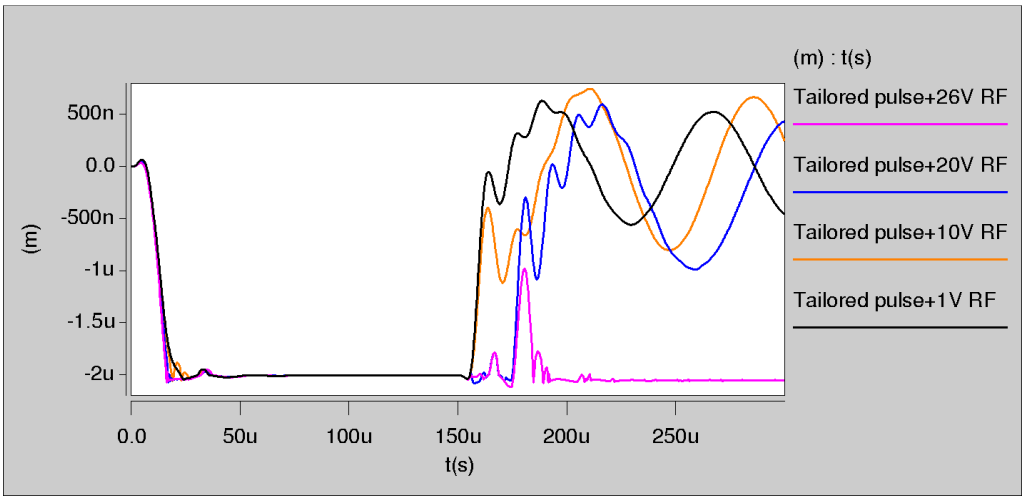

Fig. 47. Displacement under the influence of various RF signals

Fig. 48 shows the applied tailored actuation pulse, the displacement of the cantilever and the RF output of the switch when an RF signal with amplitude 1V and frequency 2GHz is applied, in time correlation. It has to be mentioned that there is a difference between the main actuation pulse and the real switching times as shown below. The switch is switched ON (90% of the signal) 0.5μm before the start of the main pulse and is switched OFF (20% of the signal) 6μm after the end of the main pulse.

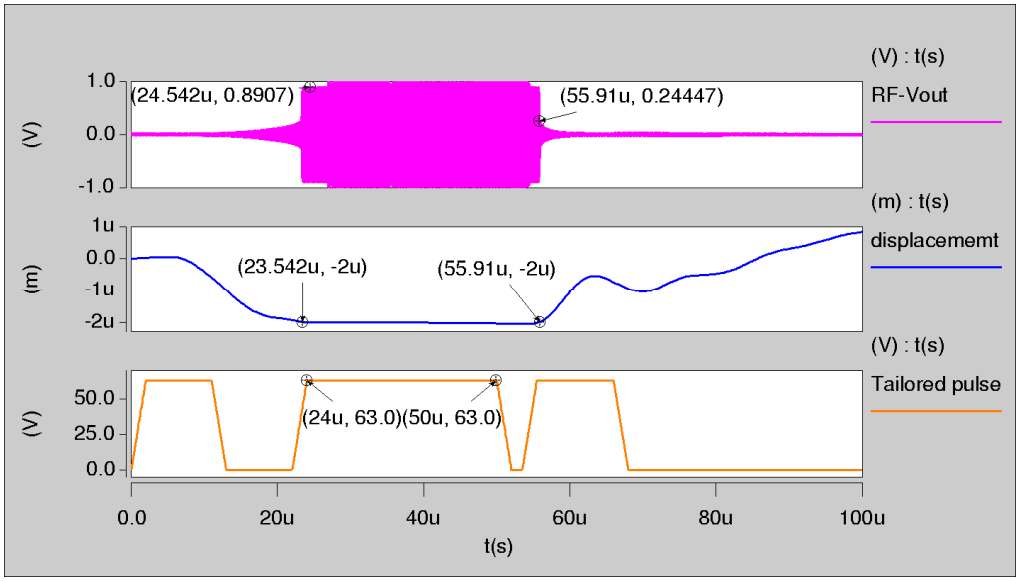

Fig. 48. Behavior of the switch under hot mode of operation

A detailed view of the output RF signal is shown in Fig. 49. The initial OFF-state capacitance of 30.7fF, which is created between cantilever and contact area, allows some undesirable signal transfer during the OFF-ON transition of the switch

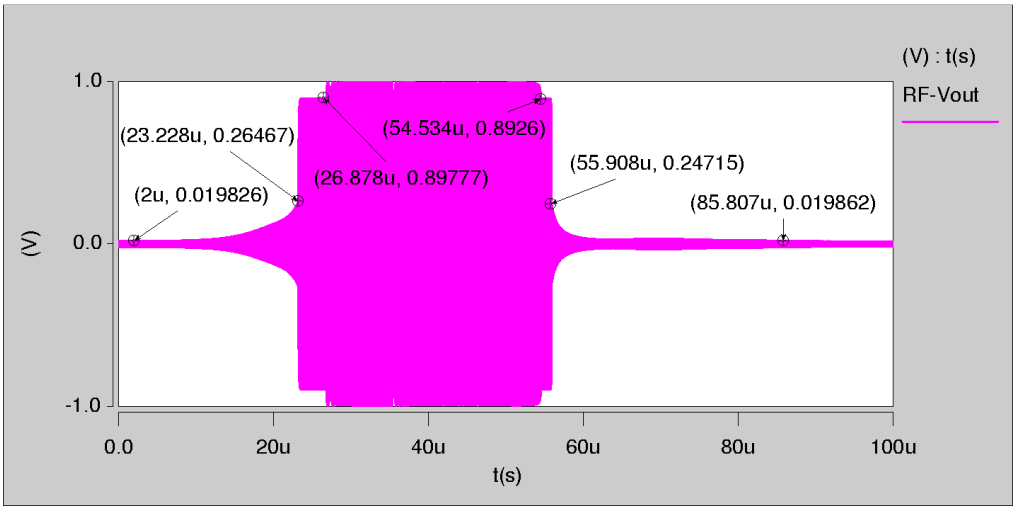

Fig. 49. Details of the RF output signal under hot mode of operation

3.4.5.Electromagnetic analysis

A full electromagnetic wave analysis has been carried out to further investigate the S-parameters of the switch using the two-port analysis from the Architect module. The characteristic impedance Z_0 for the input and output is set to 50Ω.

Fig. 50 presents the Isolation and Return loss graphs in the frequency range DC to 20 GHz, when the switch is in the OFF state. The results of the simulation are very promising considering that the Isolation and Return loss at 5GHz are -20.2dB and -0.04dB, respectively.

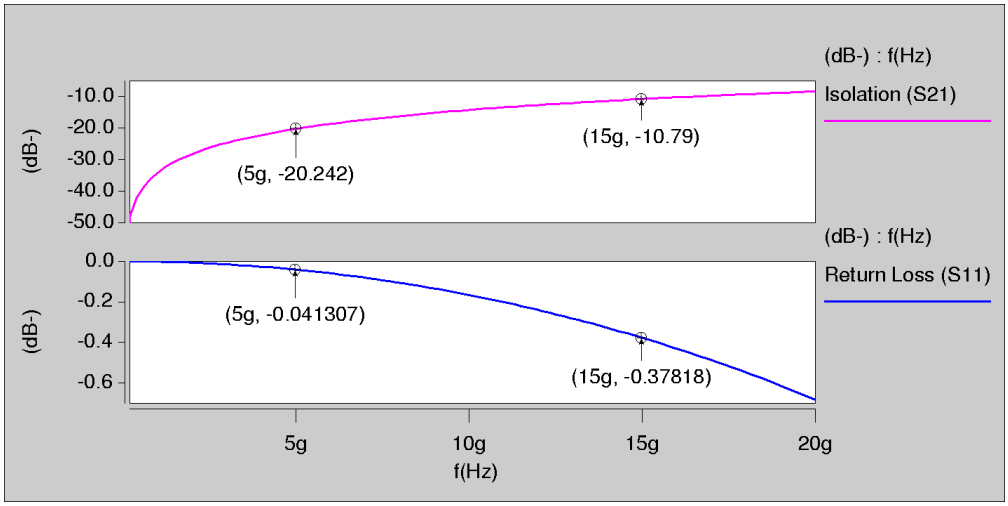

Fig. 50. Isolation and Return loss graphs of the "Uniform" switch in the OFF state

The behavior of the switch is also investigated when the switch is in the ON state presenting significant results for Return loss -48.6dB and Insertion loss -0.03dB, at 5GHz. The results of the simulation in the frequency range DC to20GHz are illustrated in Fig. 51.

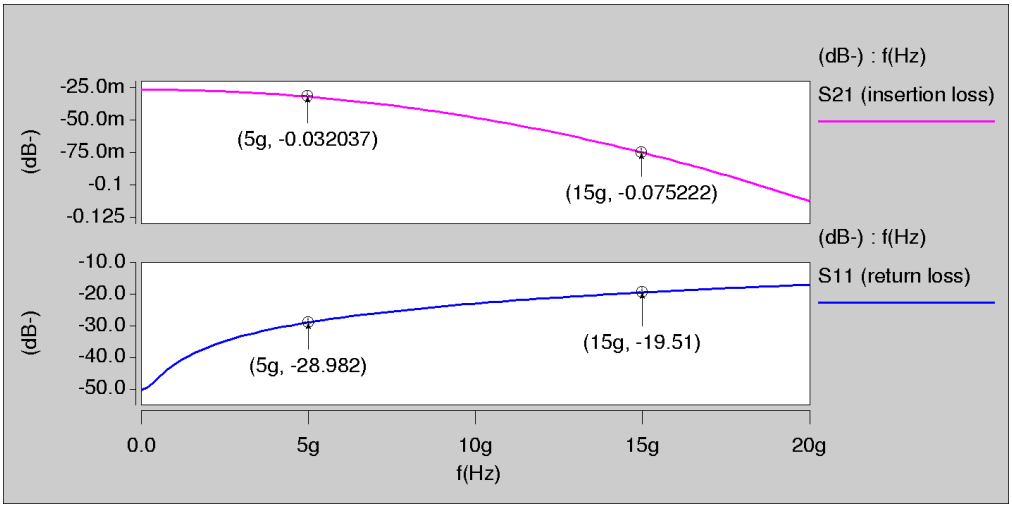

Fig. 51. Insertion and Return loss of the "Uniform" switch in the ON state

A summary of the simulated parameters of the “Uniform” in line series ohmic RF-MEMS switch is presented in Table 7.

Table 7. Performance results of the switch under tailored pulse actuation

Parameter	Value	Parameter	Value
Pulse amplitude	63V	Isolation (OFF) (S21_5GHz)	-20.2dB
RF signal (max)	26V	Return loss (OFF) (S11_5GHz)	-0.041 dB
Contact force	83.2μN	Insertion loss (ON) (S21_5GHz)	-0.032 dB
Conductance	3.42S	Return loss (ON) (S11_5GHz)	-28.98 dB
Switching Time	18.9μS (OFF-ON) 14.8μS (ON-OFF)	SNR	83.7dB_OFF 60.9dB_Transition 81.6dB_ON

3.5. Modelling of the NEU in-line series ohmic RF-MEMS switch

Currently, the only commercialized ohmic RF-MEMS design is the switch designed and developed by the Professors McGruer and Zavracky at North-Eastern University (NEU) in conjunction with Analog Devices and fabricated at Radant Technologies. Fig. 52 show a photo of the fabricated NEU switch as have been published by Guo at al [108].

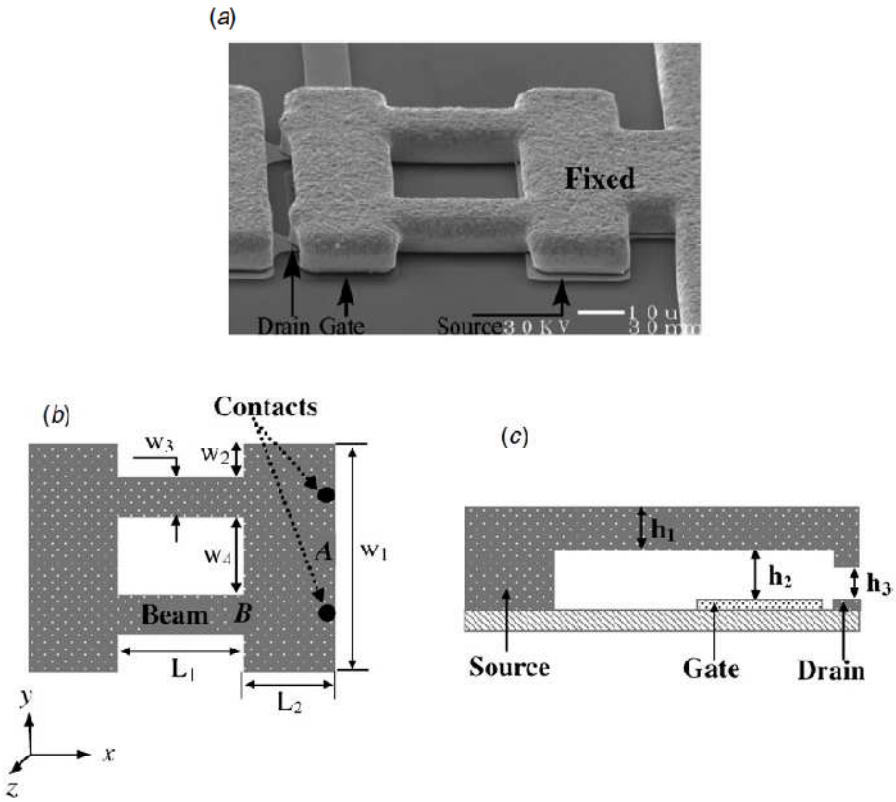

Fig. 52. (*a*) SEM micrograph of the "NEU" switch. (*b*) Top and (*c*) side views of the switch, where w_1=80μm, w_2=10μm, w_3=16μm, w_4=30μm, L_1=30μm, L_2=24μm, h_1=6μm, h_2=0.6μm and h3=0.38μm.

3.5.1.Simulations results

A design, analysis and simulation procedure is carried out through Coventorware software package under the same conditions, as they are described in the paragraph 3.3, in order to extract the operation characteristics of the "NEU" all metal in-line ohmic RF-MEMS. At first a manufacturing process and a 2D model for the switch based on the above dimensions is created under Designer modulus and then transformed in 3D under Analyzer modulus as shown in Fig. 53.

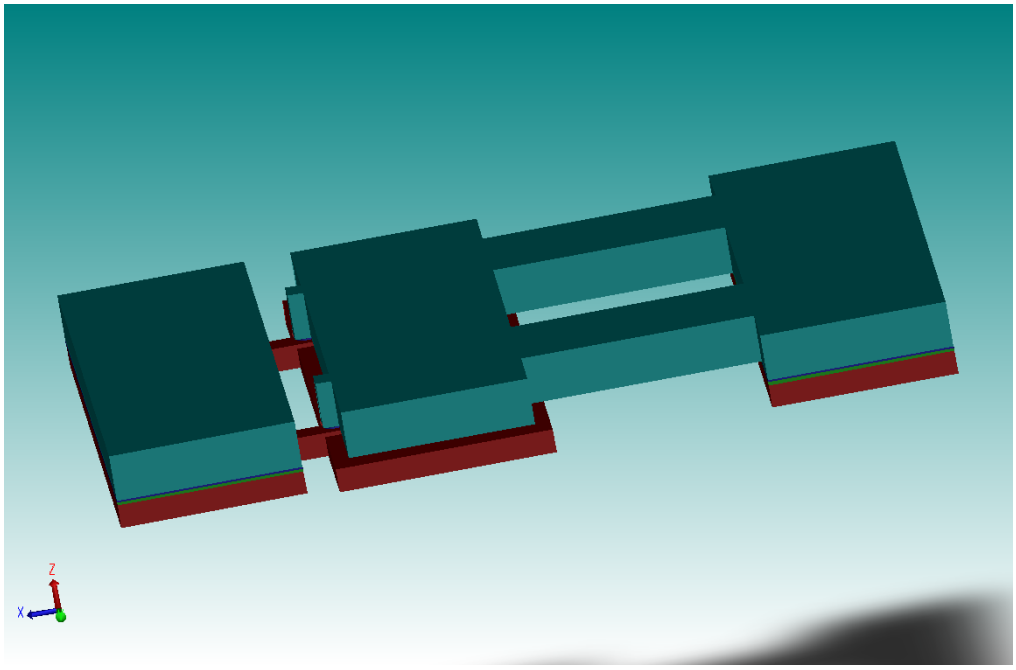

Fig. 53. The “NEU” ohmic RF MEMS switch

A view of the protruded electrode area as well as the contact areas of the “NEU” switch is presented in Fig. 54.

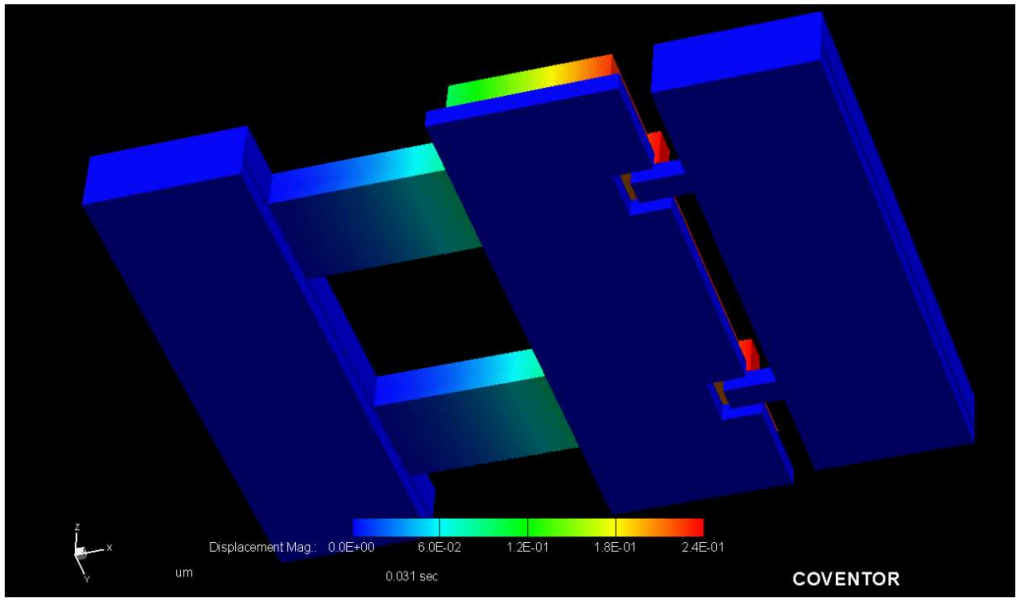

Fig. 54. Electrode and contacts view of the “NEU” ohmic RF MEMS switch

3.5.2.DC transfer analysis

A DC transfer analysis via Architect module has been carried out by applying a ramp voltage to investigate on: actuation voltage, contact force, conductance, contact area and capacitance and the results are shown in Table 8.

Table 8. Design parameters of the "NEU" switch

Parameter	Value	Parameter	Value
Length (total) 2XCantilever Actuation pad	54μm 30μm 24 μm	Contact force	11.98μN (V_{arc}) 100μN (V_s) 164.26μN ($V_{s(max)}$)
Width 2XCantilever Actuation pad	 16 μm 80μm	Conductance	0.88S (V_{arc}) 2.544S ($V_{s(min)}$) 3.26S ($V_{s(max)}$)
Height from electrode	0.6μm	Pull-in(V_p) First contact (V_{arc}) Nominal (V_s Maximum ($V_{s(max)}$)	60.194V 62.7V 83.13V 94.1V
Height from contacts	0.38μm	Capacitance (OFF)	0.822fF
Cantilever Type	Gold	Rayleigh gas damping parameters	α=406083/s β=0μs
Cantilever thickness	6μm	Q_{GAS}	5.31
Holes to cantilever	No	Contact Area	11.556pm^2

3.5.3.Transient analysis

A transient analysis is performed first under step pulse implementation with 83V amplitude, width p_w = 48μs, rise time t_r = 2 μs and fall time t_f = 2μs.

The amplitude of 83V is chosen so as to be in the middle of the useful area (63.9 < 83 < 91) capable to offer immunity to switch parameters uncertainty due to the tolerances of the fabrication process, and lower enough than the maximum allowable voltage (83 < 91) ensuring enough room for RF signals.

The switching time which is obtained under the above pulse conditions, was around 2.38μs for the OFF-ON transition and around 1.73μs for the OFF-ON transition, as shown in Fig. 55. This figure shows the fastest ON and OFF switching time that can be achieved. Besides, the same figure illustrates the bouncing problems during the pull-down (max. bounce = 174μm) and release (max. bounce = 255μm) phases. High settling times are observed also due to the stiffness of the cantilever (k ≈ 1000 N/m), which are around 11μs for the pull-down phase and around 39μs for the release-phase.

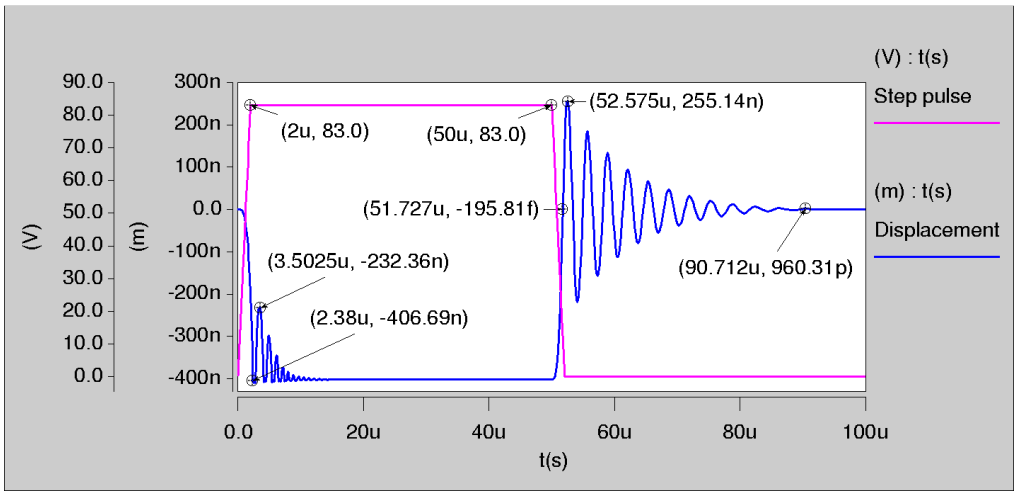

Fig. 55. Displacement under step pulse implementation

Fig. 56 illustrates the other characteristics of the switch under step pulse implementation, such as, contact area (11.566pm^2), conductance per contact area (2.53S which corresponds to a resistance of 0.394Ω) and contact force (99.3μN).

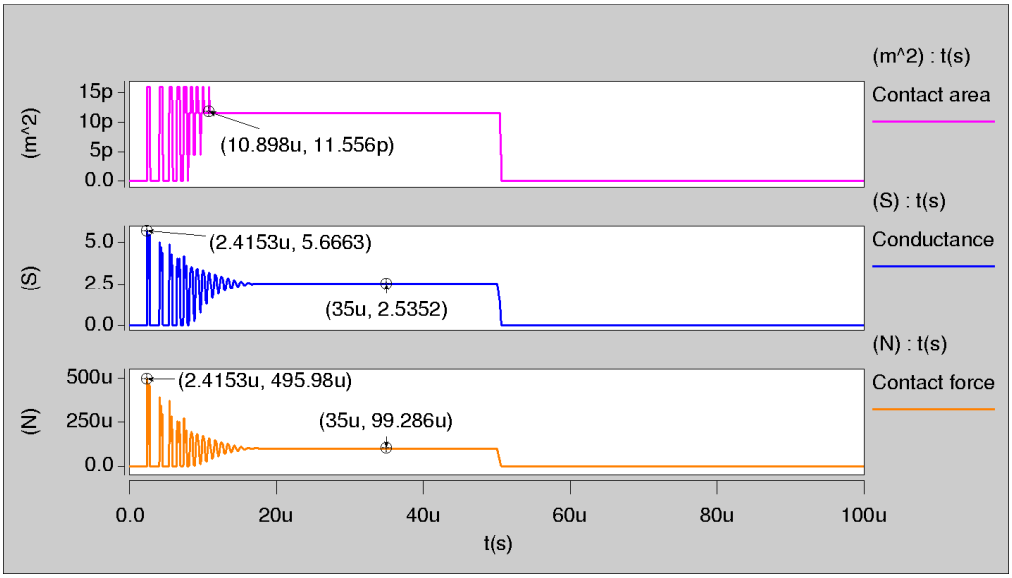

Fig. 56. Characteristics of the switch under step pulse implementation

3.5.4.Control under resistive damping

Fig. 57 & 58 illustrate the characteristics of the switch under step pulse inplementation with resistive damping. The damping resistance can be calculated as:

$$R_b C_{el} = t_r = 2\mu m => R_b \approx 66M\Omega$$

where: C_{el}=30fF, the capacitance which is created within the electrode area.

However, the switching time has been simulated to be around 2.4μs, which means that for t=2μs the cantilever has been moved and the C_{el} is much larger as the distance from the electrode has been reduced. According to the simulated results of Fig.55, the cantilever remains in the initial contition for about 1μs before starts to bend and this time interval will be used for the calculation of the correct damping resistance:

$$R_b C_{el} = t_r = 1\mu m => R_b \approx 33M\Omega$$

The results in Fig. 57 shows the difference between these two cases with respect to displacement and contact force. The simulation results with R_b = 33MΩ shows excellent response of the switch during the pull down phase as they show elimination of the bouncing and the initial impact force (the high impact velocity has been reduced to 13.2 cm/sec from 65.9cm/sec), with only a small increace in the switching time (4.34μN from 2.38μN). During the release phase a significant reduction in bouncing is also observed (169nm from 255nm).

The results with R_b = 66MΩ also shows elimination of the bouncing and the initial impact force, however with a significant increace in the switching time (7.32μN from 2.38μN) and the initial settling time. During the release phase, a better response is observed (52nm from 255nm), as the time constant RC = 2μs is very closer the period of the resonance frequency of the cantilever t_{res} = 2.9μs.

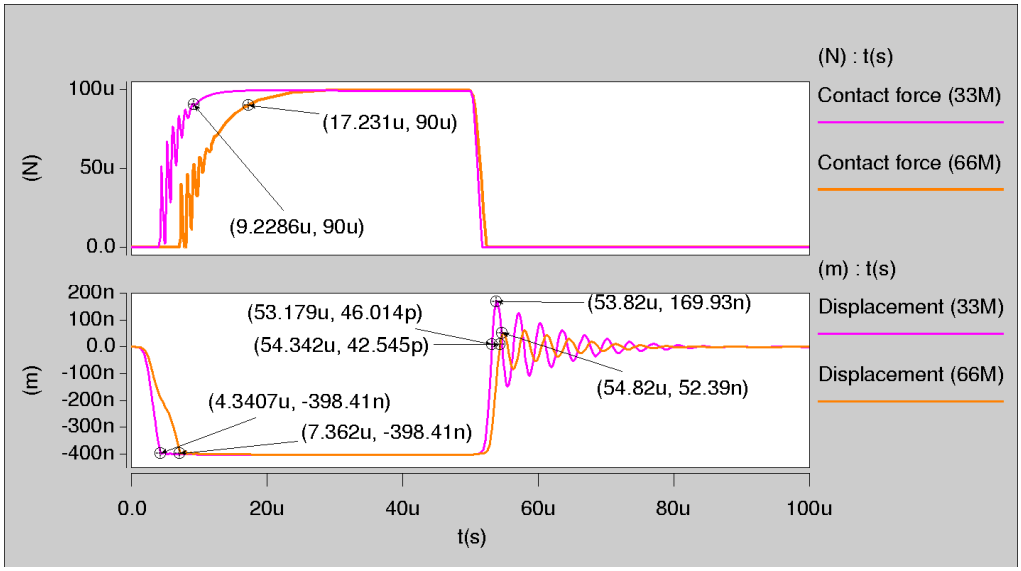

Fig. 57. Characteristics of the switch under different damping resistors

Under the above considerations the R_B = 33MΩ has been chosen for further analysis of the switch as shown in Fig. 58.

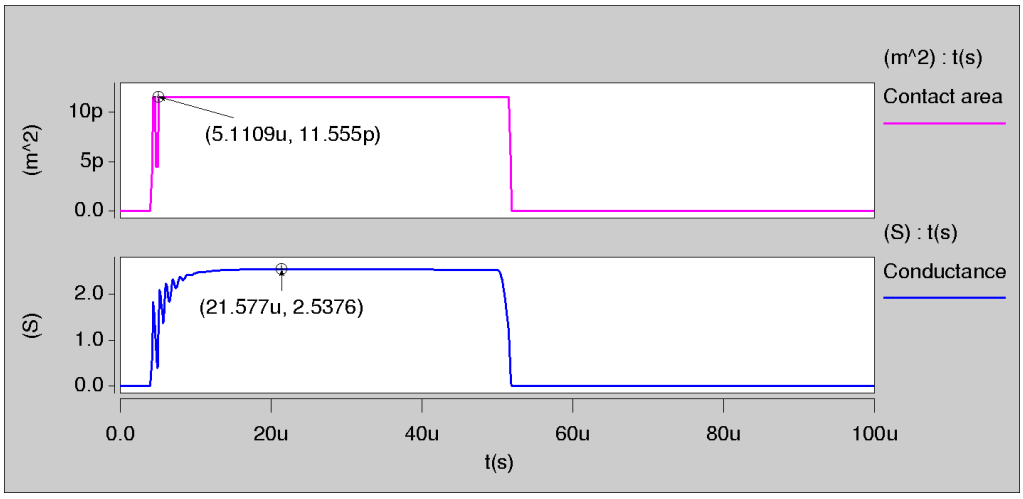

Fig. 58. Contact area and conductance of the switch with R_B = 33MΩ

3.5.5.Hot cycling mode of operation

This section presents the results from the new switch under hot cycling mode of operation, where the RF signal is passing through during the ON-OFF operation of the switch. Fig. 59 shows the displacement of the cantilever and the output of the switch when an RF signal with amplitude of 1V and frequency of 2GHz is applied at the input under step pulse actuation.

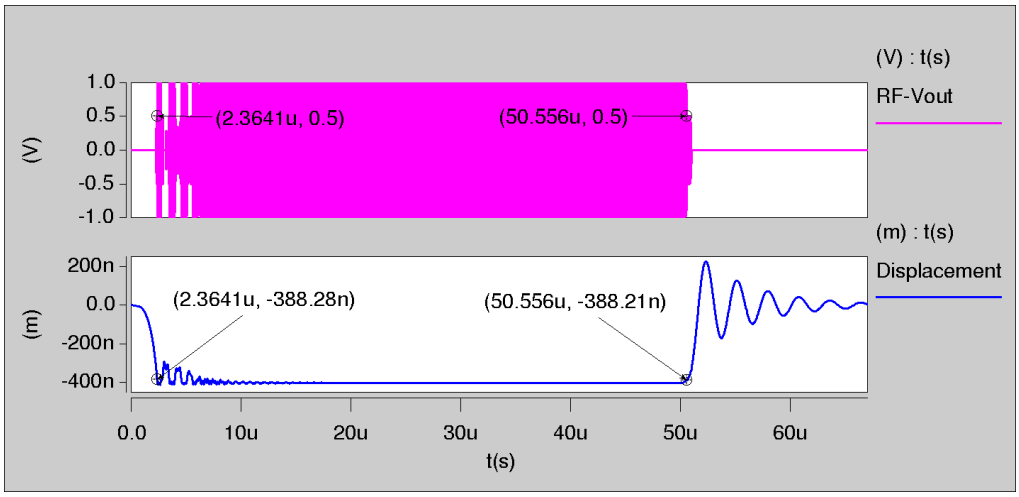

Fig. 59. Behavior of the switch under step pulse actuation

In order to handle the bouncing problems which are created under step pulse excitation, resistive damping can be used. Fig. 60 shows the displacement of the cantilever under resistively damped step pulse (damping resistance R_B = 33MΩ) and the RF output of the switch when an RF signal with amplitude 1V and frequency of 2GHz is applied, in time correlation.

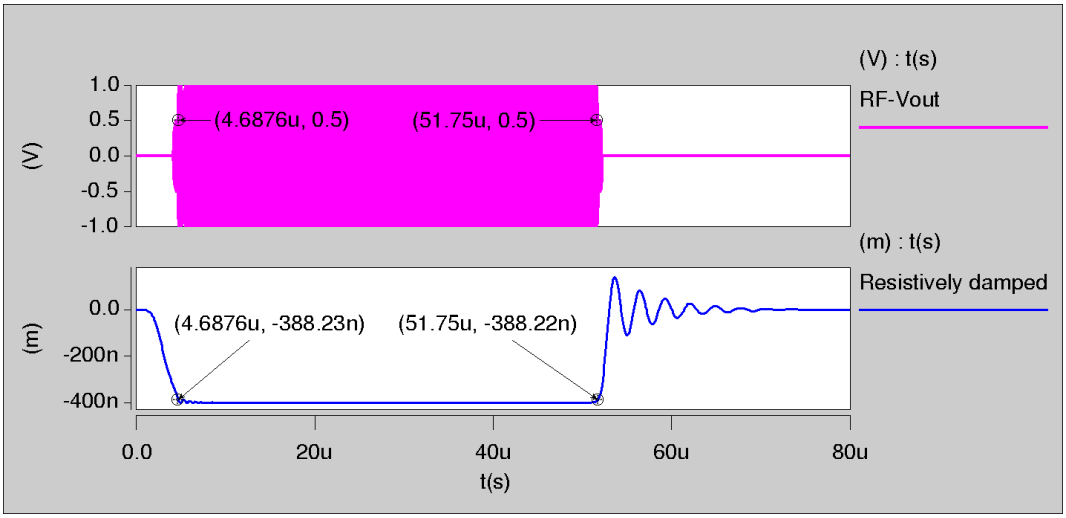

Fig. 60. Behavior of the switch under hot mode of operation

Fig. 61 shows the behavior of the cantilever when RF signals with amplitude of 10V, 45V and 100V are applied together with the resistive damped step pulse. It is obvious that the bouncing of the cantilever increases depending on the RF signal amplitude. For RF signal amplitudes higher than 45V the release time of the cantilever is

increased to 5μs as a concequence of V_{DC} = 63V, which is equal to the V_{arc} = 63V voltage of the switch.

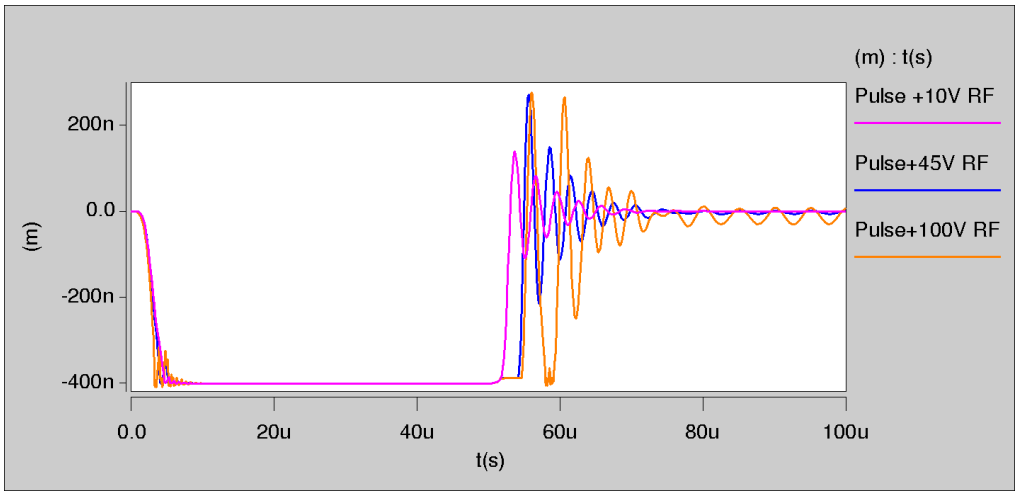

Fig. 61. Displacement under the influence of various RF signals

3.5.6.Electromagnetic analysis

A full electromagnetic wave analysis has been carried out to further investigate the S-parameters of the switch using the two-port analysis from the Architect module. The characteristic impedance Z_0 for input and output is set at 50Ω.

Fig. 62 presents the Isolation and Return loss graphs in the frequency range of DC to 20 GHz, when the switch is in the OFF state. The simulation results are excellent as the values of the Isolation and Return Loss are -51.5dB and -0.000031dB, respectively, at 5 GHz.

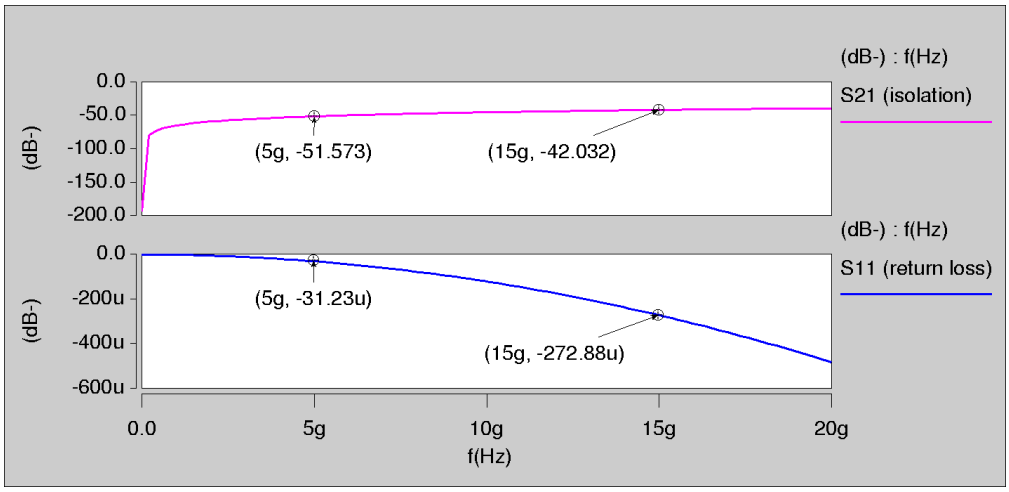

Fig. 62. Isolation and Return loss graphs of the “NEU” switch in the OFF state

The behavior of the switch is further investigated with the switch in the ON state presenting significant results with Return loss -48.77dB and Insertion loss -0.018dB at 5GHz. The results of the simulation in the frequency range DC-20GHz are illustrated in Fig. 63.

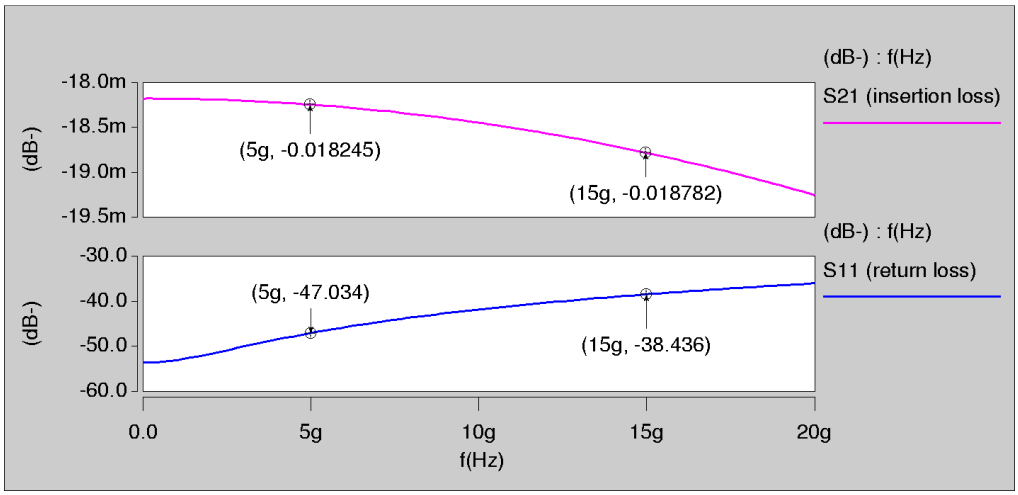

Fig. 63. Insertion and Return loss of the "NEU" switch in the ON state

A summary of the simulated parameters of the "NEU" in line series ohmic RF-MEMS switch is presented in Table 9.

Table 9. Performance results of the switch under resistive damping actuation

Parameter	Value	Parameter	Value
Pulse amplitude	83V	Isolation (OFF) (S21_5GHz)	-51.5dB
RF signal (max)	45V	Return loss (OFF) (S11_5GHz)	-0.000031 dB
Contact force	99.286μN	Insertion loss (ON) (S21_5GHz)	-0.018 dB
Conductance	2.537S	Return loss (ON) (S11_5GHz)	-47 dB
Switching Time	4.34μS (OFF-ON) 3.179μS (ON-OFF)	SNR	83.7dB_OFF 60.9dB_Trantition 81.6dB_ON

3.6. Comparison of the switches

The evaluation of the new “Hammerhead” shaped cantilever switch can be fully accomplished via a direct comparison with the classic Uniform shape cantilever switch as well as with a “NEU”-type switch, as presented by Z J Guo, N E McGruer and G G Adams [108].

The above version of “NEU” switch is chosen for comparison since it is the only one of its kind published including exact dimensions, simulations and measurements for electromechanical and electromagnetic characteristics, while significant efforts with respect to its controllability. The initial version of the above switch was presented in the paper by Prof. N E McGruer at Northwestern University [125].

In the previous paragraphs, a thorough modelling and analysis of the Hammerhead, Uniform and NEU switches has been presented based on Coventorware software package, extracting their main performance characteristics. The Hammerhead switch comprises an evolution of the Uniform switch thus a comparison in between them is attempted at the beginning. As shown in Tables 10 & 11 the “Hammerhead” switch presents a significant improvement all over the operational characteristics (Electromechanical and Electromagnetic) over the “Uniform” switch. Due to its distributed electrode area and the hammerhead shaped cantilever as well as similar dimensions to Uniform switch, it offers lower actuation voltage, produces similar contact force, better conductance and greater immunity to stiction, thanks to its greater restoring force and smaller contact area [120]. Additionally, operating under similar tailored pulse conditions, controllability is better compared to the Uniform switch since its impact velocity is reduced by around 6 times (31cm/s to 5.1cm/s) instead of 4.4 (22.9cm/s to 5.2cm/s). The smaller contact area and the higher conductance ensure better electromagnetic characteristics such as isolation and insertion loss as well.

As regards to the comparison between Hammerhead and NEU switch, a significantly lower actuation voltage (60V instead of 83V) is presented, better conductance (6.76S instead of 5.08S) combined with lower contact force, around 20%. Additionally it offers comparable restoring force due to the S-shape deformation of the cantilever [126]. The controllability of the Hammerhead is better as its switching time is slow

enough to allow time for pulse manipulation. Furthermore, the higher ratio between operating voltage and pull-in voltage 2.4 of the Hammerhead instead 1.4 of NEU, offers immunity against manufacturing or operational uncertainties. Chapter 4 provides further analyses on this subject. Nevertheless, for very fast switches, like that of the NEU, very good results can be achieved through resistive damping control.

Considering power handling, the nominal contact area of NEU switch is very small ($0.023nm^2$), thus in the active area (around the 1-2% of the nominal), the current density reaches the 10^8 A/cm^2 if a current of 10mA passes through the contact [127]. This results in the increase of temperature which in turns increase the contact resistance and the nonlinearity of the switch. For the case current excels 350mA, the contact voltage reaches the 0.45V and the contact area melts [127].

The “Hammerhead” ohmic switch can handle higher currents while it offers better linearity due to its significantly larger contact areas. Additionally, a potential temperature rise caused by high current in new switch would contribute in the contact surface asperities softening resulting to a lower contact resistance [101]. To achieve high reliability and less stiction problems under the above operating conditions clean switching environment and very low impact force has to be maintained, [102].

The electromagnetics characteristics of these switches present insertion loss of the same order as the Hammerhead has smaller contact resistance but higher inductance. The isolation figure of the NEU switch is much better due to its very small contact capacitance although the Hammerhead switch presents very good isolation in the operating frequency range.

Table 10. Comparison of Electromechanical characteristics

Parameter	HAMMERHEAD	UNIFORM	NEU
Pull-in voltage	25.2V	34.8V	60.2V
Nominal actuation voltage	60V	63V	83V
Total conductance	6.76S	3.42S	5.08S
Contact force	81.5μN	83.2μN	99μN
Impact velocity	5.1cm/s	5.2cm/s	13.2cm/s
Total contact area	$3nm^2$	$7.5nm^2$	$0.023nm^2$
Switching time OFF-ON ON-OFF	 18.5μs 15μs	 18.9μs 14.8μs	 4.34μs 3.18μs
Electrostatic force	377μN	310μN	528μN
Restoring force	214μN	123μN	358μN
RF maximum	20V	26V	45V
R_s	0.014Ω	0.0152Ω	0.006Ω
L_s	161pH	163pH	22.8pH
Total C_c	12.3fF	33.22fF	0.882fF
Resonance freq.	12.173KHz	13.554KHz	339KHz
Control	Tailored pulse	Tailored pulse	Resistive damping

Table 11. Comparison of Electromagnetic characteristics (5GHz)

Parameter	HAMMERHEAD	UNIFORM	NEU
Isolation (OFF)	-28dB	-20.2dB	-51.5dB
Return Loss (OFF)	-0.006dB	-0.041dB	-0.000031 dB
Insertion Loss (ON)	-0.019dB	-0.032dB	-0.018dB
Return Loss (ON)	-28.9dB	-28.98dB	-47 dB

3.7. Summary

In this chapter a novel “Hammerhead shaped” in-line series ohmic RF-MEMS switch design has been presented. The electromechanical (under DC transfer and transient analysis) and electromagnetic characteristics, which have been extracted through simulations under the Coventorware software package, confirmed the initial numerical calculations and have met the initial specifications, which are:

- Simplicity
- Reliability
- Controllability
- Power handling
- Remarkable electromagnetic characteristics

For comparison reasons, in order to prove the efficiency of the novel switch, other two in-line series ohmic RF-MEMS switch configurations, have been modelled and simulated under the same conditions in Coventorware. A simple Uniform shaped design with the same dimensions as Hammerhead, as well as the well known design of NEU.

4. RF-MEMS control

4.1. Introduction

A reliable ohmic RF-MEMS switch should be capable of switching very fast without settling periods to be necessary due to bouncing phenomena. Additionally, the contact force should be sufficient and constant as soon as the switch closes. During the release phase, the switch should return to its null position as fast as possible in order to be ready for the next actuation pulse. In reality, there is always a trade-off between switching speed, settling time and contact force. Fast switching under a voltage step pulse, can be achieved by increasing the amplitude of the actuation pulse. Nevertheless, one of the main problems associated with electrostatic actuation under open loop voltage control is the pull-in instability, a saddle node bifurcation phenomenon wherein the cantilever snaps-through to the underneath contact area once its displacement exceeds a certain fraction (typically 1⁄3) of the full gap. Increased cantilever pull-in velocity implies bouncing and settling time is necessary for the switch to perform its best. Moreover, the contact force during the settling period is not constant, reaching undesirable peak values when cantilever touches its corresponding contact area for the first time. That results in unstable contact resistance, power loss and arcing as far as the signal is concerned and induces local hardening, pitting or dislocations in the metal crystal structures of the materials used, reducing the reliability and the longevity of the switch [59].

Although a lot of effort has been invested in developing materials capable of maintaining high electrical contact conductance while keeping structural failures low, it still remains one of the major reasons for device failure. Different control modes (open-loop and closed-loop) have been introduced by researchers in order to control MEMS electrostatic actuation, [128], [129], [122].

In terms of the complexity for the driving and sensing electronics, an open-loop approach has advantages over closed-loop control, as it uses only driving circuits. On the other hand, open-loop driving is sensitive to parameter uncertainties.

The closed-loop control approach is significantly less sensitive to changes in system parameters, and generates oscillation-free response. Nevertheless, closed-loop produces relatively slow response and needs complicated hardware.

In terms of application requirements, when an ohmic cantilever type RF-MEMS switch is used, only two signal levels (ON and OFF) are of interest; its switching time usually varies between 2-20μs and the best way to drive it is by using open-loop control.

Generally, there are two main ways for open-loop switching control of RF MEMS switches, using Voltage drive or Charge drive control.

4.2. Voltage drive control

The analysis of the electrostatic actuated switch is based on the model of the variable capacitor with two parallel plates, as shown in Fig. 64. In this simplified one-dimensional switch model, the lower plate is anchored, while the upper plate of mass m can move attracted by an electrostatic force working against a linear restoring force, represented by an elastic constant k, in a medium represented by a linear viscous damping coefficient b.

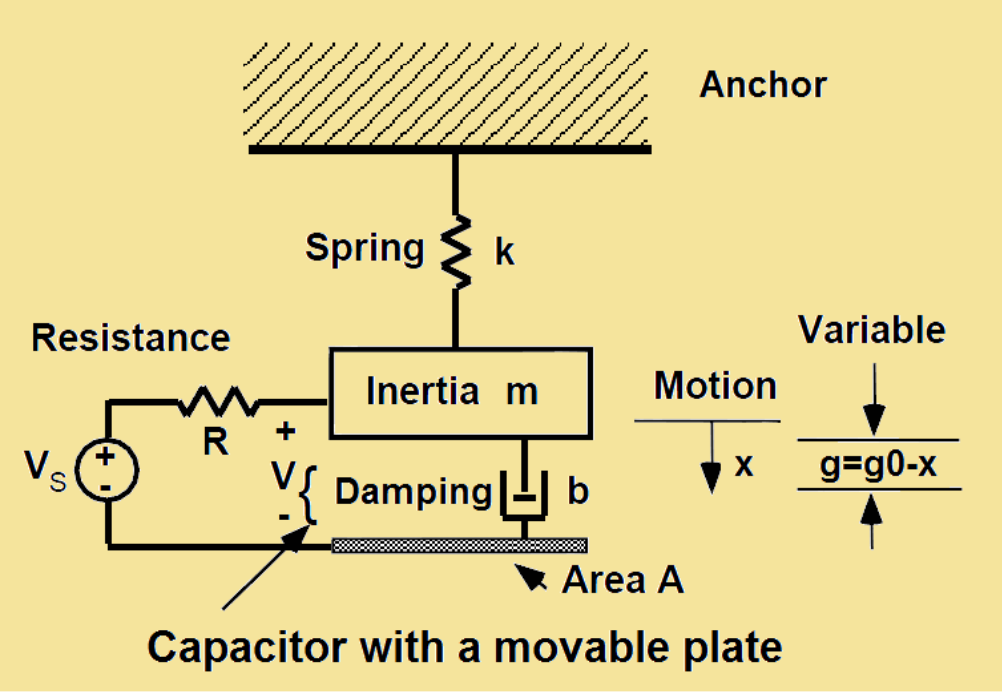

Fig. 64. Model of an electrostatically actuated variable capacitor [129]

This is essentially a mass-spring system actuated by a voltage source in series with a low value bias resistor and the electrostatic force is depended on the amplitude of V and the remaining gap between the surfaces of the capacitor g. The co–energy (U^*) for this system is given by [130]:

$$U^* = \frac{C(x)V^2}{2} \tag{45}$$

and the electrostatic force (F_{el}) at a constant voltage is:

$$F_{el} = -\frac{\partial U^*}{\partial x}\Big)_V = -\frac{\partial}{\partial x}\left(\frac{1}{2}C(x)V^2\right) = \frac{e_0 A V^2}{2(g_0 - x)^2} = \frac{e_0 A V^2}{2g^2} \tag{46}$$

The above equation states that the electrostatic force applied is always attractive and increases as the plates of the capacitor get closer. Under these circumstances the static equilibrium is reached when the electrostatic force equals the mechanical force (F_m):

$$F_m = k(g_0 - g) \tag{47}$$

and the system is stable at:

$$\frac{d}{dg}(F_e - F_m) < 0 \Rightarrow -k + \frac{e_0 A V^2}{g^3} < 0 \tag{48}$$

From the above equation the system is unstable for $g \leq \frac{2}{3}g_0$ and the pull-in voltage (V_{pi}), where the cantilever collapses to the substrate is defined as (6):

$$V_{pi} = V\left(\frac{2}{3}g_0\right) = \sqrt{\frac{8kg_0^3}{27e_0 A}}$$

4.3. Voltage drive control under tailored pulse

Observing the operation of an ohmic RF-MEMS switch under step pulse implementation at the moment the contact is made, the contact force is very high due to the high impact velocity of the cantilever. The conductance becomes very high but unstable due to the bouncing of the cantilever which follows the first contact, (due to the elastic energy stored in the deformed contact materials and in the cantilever) and it needs time to develop a stable contact force and thereof a stable conductance. This bouncing behavior increases the effective closing time of the switch. Additionally, bouncing affects the opening time (ON to OFF transition) since the cantilever needs time to settle on its null position. That behavior introduces system noise as the distance between cantilever and its corresponding contact point is not constant.

Meanwhile, the contact may get damaged by the large impact force which can be much greater than the high static contact force necessary for low contact resistance. This instantaneous high impact force may induce local hardening or pitting of materials at the contact. Besides, it may facilitate material transfer or contact welding, which is not desirable for a high-reliability switch. All the above increase the adhesive force, which is a function of the maximum contact force and they result contact stiction.

Instead of using a continuous step command to control the electrode, a tailored pulse [131] with different levels of applied voltages and time intervals can be applied, as shown in Fig. 65. The entire operation can be classified in two phases, the “pull down” phase and the “release phase”. The pull down phase mainly refers to the actuation of a contact switch from its original null position to the final contact position.

In the past few years several efforts have been made to tailor the shape of the actuation pulse using either analytical equations on a simplified single-degree-of-freedom (SDOF) model (parallel plate capacitor) on their own [132], [133], or in combination with Simplex optimization algorithms [122], [134]. All these efforts focused on the minimization of the impact force and bouncing during the pull-down phase of the switch but without taking into account damping or adhesion forces. Recently, new publications presented a more accurate solution that includes all the involved parameters [108], [135], [131], [136]. Nevertheless, the SDOF model is not considered as an accurate method to describe efficiently a non-linear system like an

RF-MEMS switch during its ON–OFF operation. Besides, it is not possible to obtain an analytical expression for damping, with the exception for a linear system with viscous damping. This implies that in all cases which are mentioned above, the tailored pulse which has been created under analytical implementation needs to be manually fine tuned in order to fulfill the requirements for soft landing and bouncing elimination.

A proper design must achieve a rapid and low impact response (ideally zero velocity) at the time of contact and fast settling once the switch is released from its contact position towards the null position. Special effort must be paid in the release phase due to the fact that considerable residual vibration at null position could be generated before settling, reducing switching rate during a repeated operation and producing undesirable noise, as the isolation of the switch is unstable, during hot switching operation [46].

For an initial estimation of the tailored pulse the analytical method presented by K.-S. Ou et al [131] is followed in order to calculate voltage amplitudes and time intervals.

The sum of potential energy, U, and kinetic energy of the switch must be equal to the applied electrostatic energy. For the system shown in Fig. 64, the energy conservation argument can be written as

$$\frac{1}{2}mv^2 + \frac{1}{2}kx^2 = F_{el} = \frac{e_0 A V^2}{2(g_0 - x)^2} \tag{49}$$

In order to achieve the condition of zero contact velocity at the moment of contact, all the electrostatic energy must be converted to potential energy at the moment the contact occurs. To achieve this goal, the applied force must be turned off once the displacement exceeds a particular middle point (x_1). By equaling the potential energy and the applied electrostatic energy the distance x_1 can be computed by:

$$\int_0^{x1} F_{el} dx = \int_0^{x_{max}} kx\, dx \tag{50}$$

$$x_1 = \frac{g_0^2 U|_{x=x_{max}}}{H_1 + g_0 U|_{x=x_{max}}} \tag{51}$$

where

$$H_1 = \frac{Ae_0 V_1^2(t)}{2} \tag{52}$$

V_1 is the selected applied voltage, which must exceed the pull-in voltage V_{PI} with a factor of about 1.4 for correct operation of the device [46]. Next the time intervals of the pulse have to be calculated. In order to achieve this, consider that:

$$v = \frac{dx}{dt} = \sqrt{\frac{2}{m}(W - U)} \tag{53}$$

where the potential energy U equals $kx^2/2$ and the work done by the external force W is defined as:

$$W = \int_0^x F_{el} dx = \frac{Hx}{g_0(g_0 - x)} \tag{54}$$

and the time interval, t1, can be found from:

$$t_1 = \int_0^{x1} \frac{1}{\sqrt{\frac{2}{m}\left(\frac{Hx}{g_0(g_0-x)} - \frac{1}{2}kx^2\right)}} dx \tag{55}$$

Following the same approach, the time t_2 when the mass reaches the target can be calculated as:

$$t_2 = t_1 + \int_{x_1}^{x_{max}} \frac{1}{\sqrt{\frac{2}{m}\left(\frac{Hx}{g_0(g_0-x)} - \frac{1}{2}kx^2\right)}} dx \tag{56}$$

For determination of V_2, the condition is not unique, since the only requirement is to ensure the contact between the switch and substrate. In general, an increase in V_2 will not increase the impact force, but instead it enhances the contact pressure and thus decreases the electrical contact resistance. For simplicity and ease of implementation, let $V_2 = V_1 = V_s$.

The same strategy discussed in the previous section can be used in the Release phase. The proposed command history is schematically shown in Fig. 65. First, at t=0, a constant voltage V_1 is applied to actuate the switch. The switch then accelerates and

moves toward the substrate. This input voltage is then ceased when $t=t_1$. The switch decelerates but still continuously moves toward the substrate. At the moment of $t = t_2$, the switch finally contacts the substrate at a negligible speed. At this moment, an input $V = V_2$ immediately kicks in to counteract the elastic restoring force and to ensure the final contact. Thus a voltage-pulse train actuation scheme, defined by the attributes listed below and schematically shown in Fig. 65, has been used to improve the dynamic response of the microswitch.

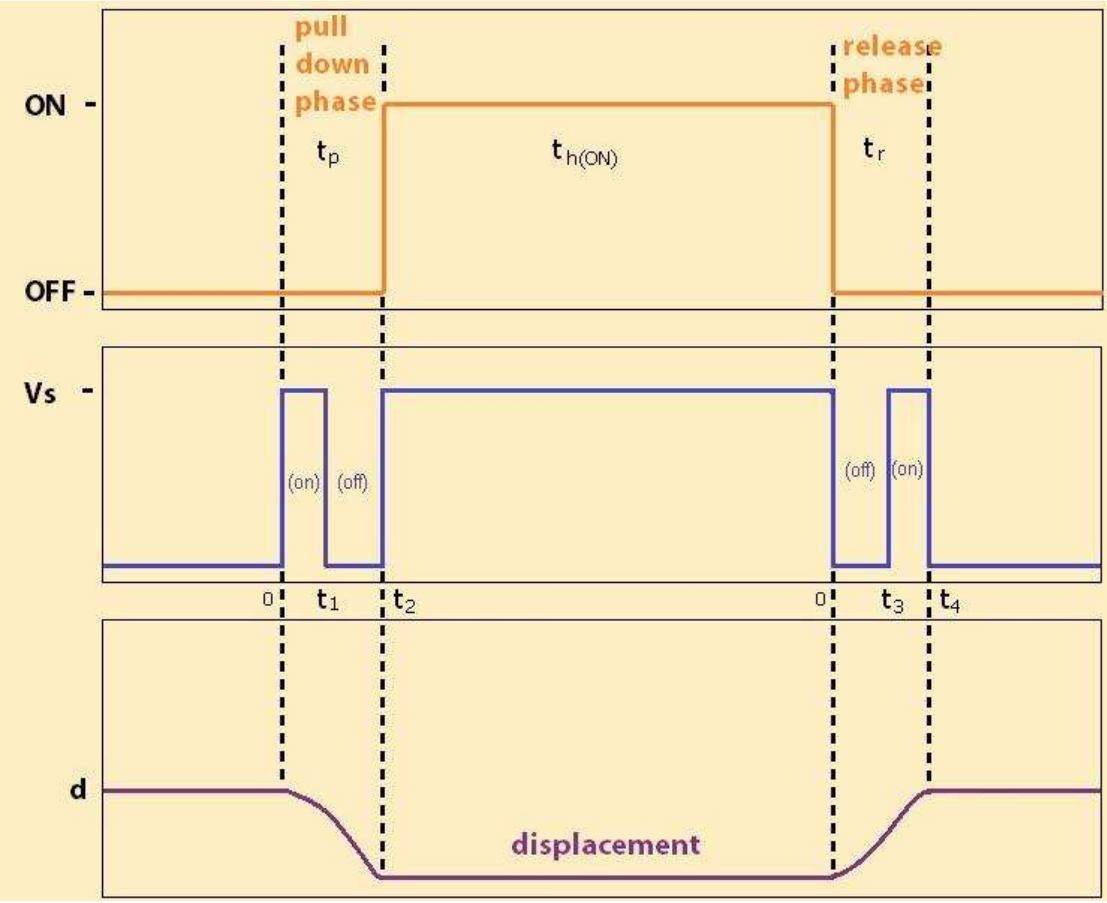

Fig. 65. The phases of the tailored actuation pulse

These attributes are:

- The amplitude of the actuation voltage *(V_s)*,
- The pull-down actuation time (t_p), which consists of the on time *($t_{p(on)}$)* and the off time *($t_{p(off)}$)*
- The hold-on time ($t_{h(on)}$)
- The release time *(t_r)* which consists of the off time *($t_{r(off)}$)* and the on time *($t_{r(on)}$)*

Making use of this open-loop control technique the bouncing of the switch after the initial contact can be eliminated and the impact force during contact can be minimized while maintaining a fast closing time.

The main drawback of the above procedure is that there are many parameters that have to be modified in order to reach a good convergence to the targets. Due to the large number of parameters and the nonlinear structure of the problem it is very difficult to work it through analytically. Thus the only solution is the implementation of an optimization method.

Recently, thanks to the rapid development of computer technology, several stochastic optimization techniques that incorporate random variation and selection such as Genetic Algorithms (GA) [137], Particle Swarm Optimization (PSO) [138] and gradient-based algorithms [139] have been implemented via computer codes to solve various problems. These optimization methods can be divided into two categories: global and local techniques. Global techniques such as GA and PSO are capable of handling multidimensional, discontinuous and nondifferentiable objective functions with many potential local maxima while they are highly independent of initial conditions. However, one of their main drawbacks is their convergence rate which is slow [140].

In contrast, for the local techniques such as the gradient-based algorithms, the main advantage is that the solution converges rapidly. However, local techniques work well only for a small number of continuous parameters and they are highly dependent on the starting point or initial guess while react poorly to the presence of discontinuities in solution spaces.

In order to bridge the weak points of these two techniques the Design of Experiments (DOE) technique can be employed, another way for achieving optimization on the target and reduction in variation around the target. DOE is a powerful statistical technique for improving product or process design and solving production problems. A standardized version of the DOE has been introduced by Dr. Genichi Taguchi, an easy to learn and apply technique for design optimization and production problem investigation [141], [142]. Taguchi's optimization technique can handle multidimensional, discontinuous and nondifferentiable objective functions with many potential local maxima while converges rapidly to the optimum result but within a well defined area.

Applying Taguchi's approach to optimize the actuation pulse of an ohmic RF MEMS switch allows soft landing (low impact force), without the expense of more switching speed as well as eliminating the bouncing phenomena. The appropriate magnitude of voltages and time intervals of the actuation pulse train can be calculated by combining a Taguchi's Optimization algorithm and Architect module of Coventorware ®).

4.4. Taguchi optimization method

Dr. Genichi Taguchi has developed a method based on Orthogonal Array (OA) experiments which offers significantly reduced variance for the experiment by setting optimum values to the control parameters. Thus the combination of Design of Experiments with optimization of control parameters is achieved in the Taguchi's Method. Orthogonal Arrays are highly fractional orthogonal designs, which provide a set of well balanced (minimum) experiments.

The optimization procedure begins with the problem consideration, which includes the initial conditions, the selection of a proper OA and an appropriate expression of the *fitness function* (*ff).* The selection of an OA depends on the number of input parameters and the number of levels for each parameter. The *ff* is a particular mathematical function and is developed according to the nature of the problem and the optimization goals.

After a simple analysis, the simulation results serve as objective functions for optimization and data analysis and an optimum combination of the parameter values can be obtained. The log functions of the outputs, named by Taguchi as Signal-to-Noise ratios (S/N), are used for prediction of the optimum result. It can be demonstrated via statistics that although the number of experiments are dramatically reduced, the optimum result obtained through the orthogonal array usage is very close to that obtained from the full factorial approach.

When the Taguchi method is implemented at the design level and the efforts are focused on the optimization of the control values, the experiments can be replaced by simulations.

In order to achieve as high convergence with the goal as possible, successive implementations of the method have to be applied. Under this procedure the optimum results of the last iteration serve as central values for the next, reducing each time with

a predefined factor the level-difference of each parameter. The procedure terminates when the level-difference becomes negligible and maximum available accuracy is reached.

The procedural steps in detail are shown below.

1. Consideration of the problem that must be solved:
2. Extraction of the *ff* and definition of the optimum goal (Minimum, Nominal or Maximum):
3. Definition of the main parameters and their estimated (center)values
4. Definition of the levels L_{init} for each parameter within ±20% of the center values. In order to describe the non-linear effect so as to gradually minimize each iteration-level's difference, an odd number of levels must be used for each input parameter.
5. Definition of the maximum resolution of the parameters.
6. Design of Experiment (DOE) using Taguchi's suggested Orthogonal Arrays $OA_n(m^k)$ in order to minimize the effect of any erroneous assumptions that have been made due to effects considered negligible, which consist of:

- n rows (number of experiments),
- k columns (number of parameters) and
- m levels (on which each parameter will vary).

7. Simulation using the module Architect of Coventorware® according to the selected OA.
8. Evaluation of the compliance of the *ff* for each combination of the levels of parameters based on the simulation results.
9. Computation of the mean value of the fitness functions of the experiment

$$\bar{Y} = \frac{1}{n}\sum_{i=1}^{i=n} Y_i \qquad (57)$$

10. Computation of the mean value for each level of each parameter

$$\bar{Y}_{m_i} = \frac{m}{n}\sum_{i=1}^{i=\frac{n}{m}} Y_{m_i} \qquad (58)$$

(Example: For the parameter A when level is 1, add the values of all corresponding *ff* and compute their mean value)

11. Consideration of the optimum level for each parameter depending on the $\bar{Y}_{m_i}$ and the nature of the goal (minimum, nominal or maximum).
12. Prediction of the optimum value of the experiment's *ff*, based on the 20Log_{10} values of $\bar{Y}$ and the $\bar{Y}_{m_i}$. (The conversion is essential in order to avoid negative values especially at the beginning, when the differences between of $\bar{Y}$ and $\bar{Y}_{m_i}$ are high)

$$Y_{O\,(Log)} = \bar{Y}_{(Log)} - \left(\bar{Y}_{(Log)} - \bar{Y}_{1m_{opt(Log)}}\right) - \cdots \left(\bar{Y}_{(Log)} - \bar{Y}_{km_{opt(Log)}}\right) \quad (59)$$

The predicted value might not be the optimum because the OA is a fractional factorial design, but never the less it shows the direction of the optimization. During the next iterations, as the gap between the mean and predicted optimum value becomes smaller, the possibility that the predicted optimum value to be the optimum value rises significantly.

13. Definition of the Reducing Percentage (RP) of the initial deference between the levels of the parameters. The RP depends on the nature of the problem and can be high for simple cases with only one optimum condition or low for more complex situations.
14. Creation of new level differences by multiplying the RP with the initial level of the parameters.

$$LD_i = L_{init} \cdot (1 - RP) \quad (60)$$

15. Creation of new levels for the next iteration by adding the estimated optimum levels of the parameters of the 1th iteration with the LD_i.
16. The procedure stops when the LD_i reaches the limits of the allowed resolution of the parameters.

4.5. Optimization of the tailored pulse

In this Thesis, for the first time, the optimization of the switch's actuation pulse with a simple and efficient way, using Taguchi's technique is presented. Optimization is achieved in collaboration with the Coventorware software package, comprising a complete solution concerning switch behavior. As a result, high switching speed with low bouncing phenomena and low impact force, is achieved.

The "Hammerhead" RF-MEMS switch is considered for the case study. The procedure followed towards the design of the switch and the optimization of the tailored pulse used for its actuation is described in a few steps, bellow.

- Initially, a step actuation pulse has been applied to the switch to observe its switching characteristics and verify that there are considerable weaknesses as far as the impact force and the bouncing phenomena are concerned.
- A tailored pulse has been applied next, instead of the single step pulse, based on previously published work [131]. The performance of the switch got better but there was still plenty of room for further improvement.
- Finally, Taguchi's optimization technique has been applied to modify the actuation pulse in order to further improve the behavior of the switch.

During the design and simulation process Coventorware® produces an output file which includes data regarding simulation conditions, design components and power sources. Importing this file to a specially customized algorithm written in C++, the simulation conditions as well as the characteristics of the switch's actuation pulse can be optimized to achieve the required performance. This is done because Coventorware® supports the AIM [143], a high-level embedded scripting language developed to control and manage user input, graphing, measurement, symbol creation and other kinds of analyses and processes in Saber applications allowing simulation control from external sources. Once the simulation is over, the custom made algorithm evaluates and processes the results written in the output file, running the optimization algorithm based on Taguchi's Method. The optimized actuation pulse parameters are then imported back to the Coventorware® file and the simulation runs again, repeating the same process up to the point the simulation results meet the goals, set at the beginning of the process.

The objective of Taguchi's algorithm is the minimization of the *ff*. According to the nature of the problem two separate optimization procedures have to be realized within two different switching operation phases. The pull-down phase ($ff_{p\text{-}d}$) and the release phase (ff_r.)

A. Pull-down phase

The $ff_{p\text{-}d}$ is suitably determined according to the next three conditions.

- Lowest contact time (highest switching speed)
- Lowest contact force (lowest conductance)
- Existence or non existence of a gap (bouncing) after the first contact up to the end of the time interval.

Thus a weighted $ff_{p\text{-}d}$ has been chosen with the form:
Search for time **gap** between the contact force measurements

If **yes** then $\rightarrow ff_{p-d} = 10^6 \cdot t_{(impact)} + 10^5 \cdot F_{(max)} + 10$

If **no** then $\rightarrow ff_{p-d} = 10^6 \cdot t_{(impact)} + 10^5 \cdot F_{(max)}$

$$ff_{p-d(Log)} = 20Log_{10}(ff_{p-d})$$

where: $t_{(impact)}$ is the time needed for the first contact to occur and $F_{(max)}$ is the maximum impact force measured during the pull-down phase.

B. Release phase

The ff_r is suitably determined according to the difference between maximum and minimum cantilever's displacement, after a predefined time, which includes the pull-down time, the switch-on time and the time that the cantilever needs to reach its zero position after the switch-off.
Thus a weighted ff_r has been chosen with the form:

$$t_{(initial)} > 163\mu sec$$

$$ff_r = 10^4 \cdot (Displacement_{max} - Displacement_{min})$$

$$ff_{r(Log)} = 20Log_{10}(ff_r)$$

where: the $t_{(initial)} > 163\mu sec$ includes the pull-down phase time, the hold-down time (ON) and the time that the switch needs to reach its null position (OFF) (These time intervals have been investigated during the step pulse implementation). The weight-factors (10^4, 10^5, 10^6) are used according to the magnitude (in micron) of the factors and factor 10 indicates the penalty that has to be paid in the case of bouncing during the pull-down phase, otherwise the *ff* could be driven to false results.

Taguchi's method is accurate within a well defined initial area. Thus, taking into account the magnitudes of the tailored actuation pulse of the previous step and considering a ± 20% deviation from these predefined values, the initial levels of the parameters for Taguchi optimization can be created, as shown in Tables 12 & 13.

Table 12. Pull-down phase (t_p) levels

V_p (Volts)	48	60	72
$t_{p(on)}$ (μsec)	5.6	7	8.4
t_f (μsec)	1.6	2	2.4
$t_{p(off)}$ (μsec)	8.8	11	13.2
t_r (μsec)	1.6	2	2.4

Table 13. Release phase (t_r) levels

V_p (Volts)	48	60	72
$t_{r(on)}$ (μsec)	3.2	4	4.8
t_r (μsec)	1.6	2	2.4
$t_{r(off)}$ (μsec)	6.4	8	9.6
t_r (μsec)	1.6	2	2.4

The number of parameters of the actuation pulse which will be calculated through the optimization process are 5 with 3 initial levels each and are considered for the two actuation phases as following:

Pull-down phase (t_p)

A. The magnitude of the pull-down pulse V_p (V)
B. The ON-state of the pulse $t_{p\text{-}on}$ (μs)
C. The fall-time of the pulse $t_{p\text{-}f}$ (μs)
D. The OFF-state of the pulse $t_{p\text{-}off}$ (μs)
E. The rise-time of the pulse $t_{p\text{-}r}$ (μs)

Release phase (t_r)

A. The magnitude of the release pulse V_r (V)
B. The OFF-state of the pulse $t_{r\text{-}off}$ (μs)
C. The rise-time of the pulse $t_{r\text{-}r}$ (μs)
D. The ON-state of the pulse $t_{r\text{-}on}$ (μs)
E. The fall-time of the pulse $t_{r\text{-}f}$ (μs)

For an OA with 5 parameters and 3 levels for each parameter a configuration with at least $n_{rows} = 1 + (k \cdot DOF_m) = 1 + (5 \cdot 2) = 11 rows$ is needed.
Where DOF_m=*m-1* means degrees of freedom and in statistical analysis it is equal to the number of the levels of a parameter minus 1.
Taguchi suggests the solution of the $OA_{18}(3^7, 2)$ that can handle up to 7 parameters with 3 levels each and one with 2 levels in an array of 18 rows. For this case 5 columns of the $OA_{18}(3^7,2)$ have been chosen to assign the five parameters in their 3 levels, thus an $OA_{18}(3^5)$ has been created, as shown in Table 14.

Table 14. $OA_{18}(3^5)$

n rows	A	B	C	D	E
1	1	1	1	1	1
2	2	2	2	2	2
3	3	3	3	3	3
4	1	1	2	2	3
5	2	2	3	3	1
6	3	3	1	1	2
7	1	2	1	3	2
8	2	3	2	1	3
9	3	1	3	2	1
10	1	3	3	2	2
11	2	1	1	3	3
12	3	2	2	1	1
13	1	2	3	1	3
14	2	3	1	2	1
15	3	1	2	3	2
16	1	3	2	3	1
17	2	1	3	1	2
18	3	2	1	2	3

Taking into account the above considerations, the Taguchi's optimization algorithm was implemented in C++ for the actuation pulse.

The optimization procedure graphs, shown in Fig. 66 & 67 present the curves of mean and optimum values for the pull-down and release phase, as they converged through Taguchi process, respectively.

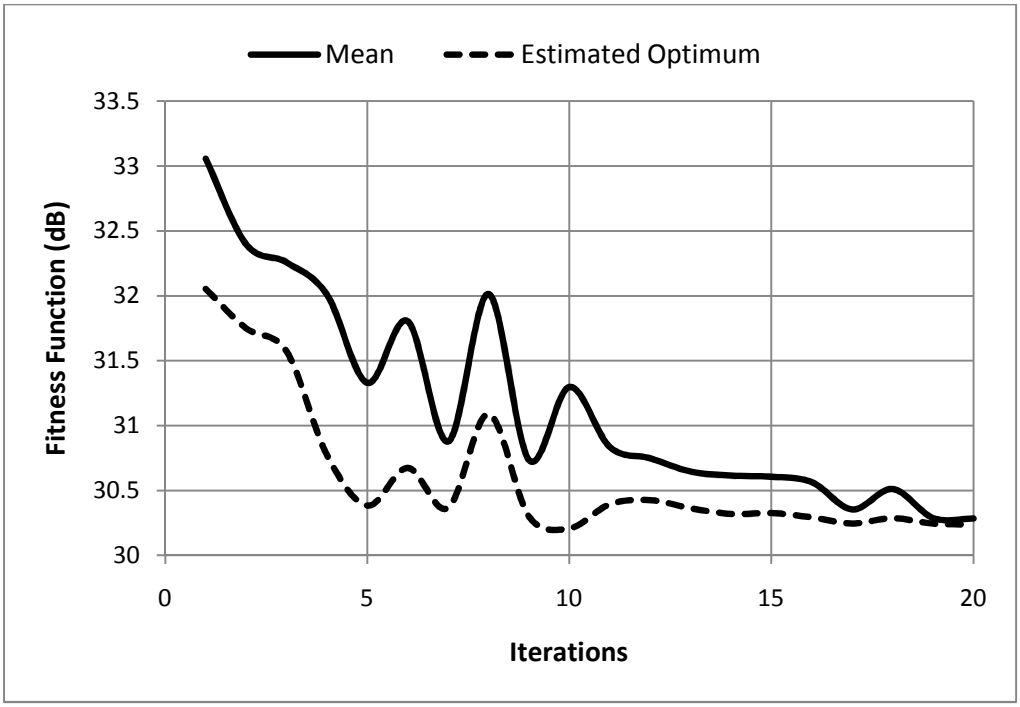

Fig. 66. Optimization procedure graph for the Pull-down phase of the switch

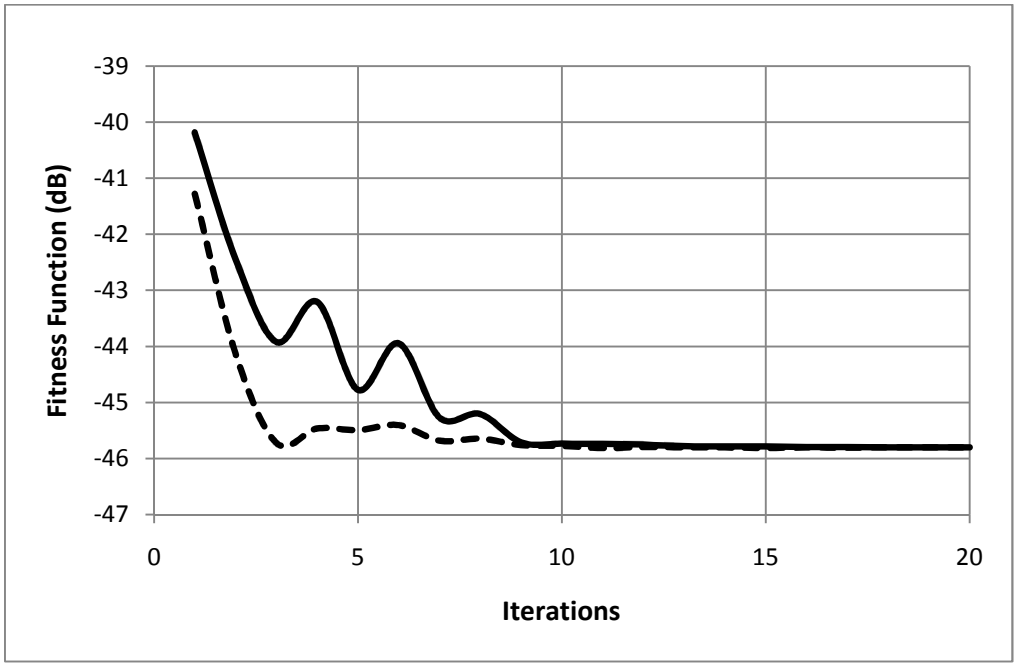

Fig. 67. Optimization procedure graph for the Release phase of the switch

The results for optimum dimensions extracted through Taguchi Optimization method after 20 iterations (less than 1 hour of processing time), for the pull-down and release switching phases of the ohmic RF-MEMS switch are illustrated in Table 15.

Table 15. Voltage and time intervals of the optimized tailored pulse

Pull-down phase (t_p)					Release phase (t_r)				
V_{p-d}	t_{p-on}	t_{p-f}	t_{p-off}	t_{p-r}	V_r	t_{r-off}	t_{r-r}	t_{r-on}	t_{r-f}
61.5V	7.3μs	1.6μs	10.2μs	2.2μs	61.5V	4.9μs	1.9μs	9.3μs	1.9μs

Continuing with the analysis, the switch is examined under transient conditions in Coventorware Architect environment. Simulations have been carried out using, initially, a step pulse as an actuation pulse, a tailored pulse and finally the optimized pulse, as described below in Tables 16, 17 and 18, respectively.

Table 16. Step pulse voltage and time values

t(μs)	0	2	150	152
V(V)	0	60	60	0

Table 17. Tailored pulse voltage and time values

t(μs)	0	2	9	11	22	24	150	152	156	158	166	168
V(V)	0	60	60	0	0	60	60	0	0	60	60	0

Table 18. Optimized tailored pulse voltage and time values

t(μs)	0	2	9.3	10.9	21.1	23.3	150	152	156.9	158.8	168.1	170.
V(V)	0	61.5	61.5	0	0	60	60	0	0	61.5	61.5	0

Simulating then, the behavior of the switch under the Optimized-Tailored pulse, the results show great improvement with respect to impact velocity (3.6cm/sec instead of 31cm/sec of the step pulse and 5.1cm/sec of the tailored pulse), which implies true '*soft landing*' of the cantilever, reducing dramatically the impact force (138μN instead of 349μN of the step pulse and 174μN of the tailored pulse), as shown in Fig. 68.

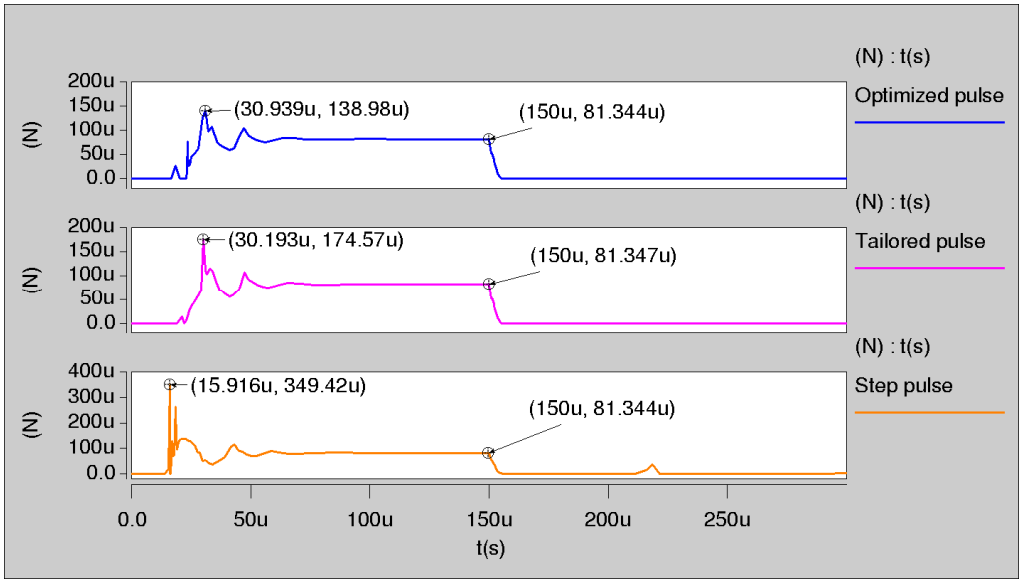

Fig. 68. Comparison of the contact forces

In the pull down phase the bouncing phenomena have been eliminated and the switching speed, is kept high (17µs), around 1.7µs slower than the step pulse (15.3µs), but around 1.5µs faster than the tailored pulse (18.5µs) as shown in Fig.69.

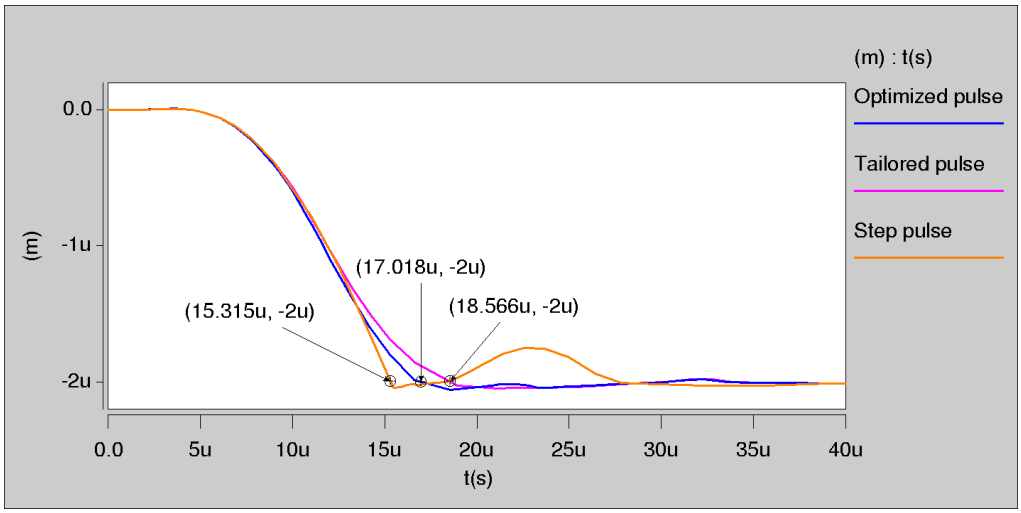

Fig. 69. Comparison of the switching behavior during the pull down phase

Similar behavior is also observed during the release phase as the ON-OFF switching speed is 13.2µs, around 0.5µs slower than step pulse (12.7µs), but around 1.7µs faster than the tailored pulse (14.9µs). Additionally, bouncing phenomena have practically eliminated (instead of max. deviation of 3.59µm for the step pulse and 0.37µm for the tailored pulse) during the release phase, as presented in Fig. 70.

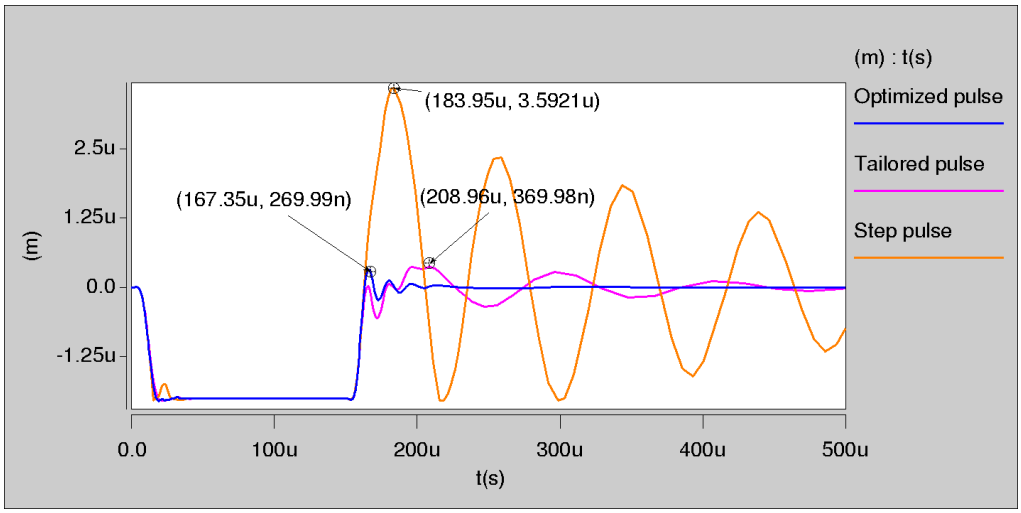

Fig. 70. Comparison of the switching behavior during the release phase

A comparison between the results implementing different actuation pulses, are shown in Table 19.

Table 19. Comparison of switching characteristics under different actuation modes

	Impact Velocity	Impact Force	Switching (pull down)	Switching (release)	Max. Bouncing Displacement
Step Pulse	31cm/s	349μN	15.3μs	13.2μs	3.59μm, -2μm
Tailored Pulse	5.1cm/s	174μN	18.5μs	14.9μs	0.37μm, -0.33μm
Optimized-Tailored Pulse	3.6cm/s	138μN	17μs	13.7μs	0.11μm, -0.09μm

4.6. Resistive damping (Charge drive control)

Another way to control the impact velocity in order to achieve soft landing and fewer bouncing phenomena is the resistive damping. This control method is also referred as charge drive and has been presented for first time by Castaner and Senturia [144] (see Apentix A.2). Under charge control the pull-in phenomenon of the Constant Voltage controlled electrostatic actuators does not exists while, if the current drive is ideal, any position across the gap is stable. The main reason for this behavior is that the applied electrostatic force is always attractive and is independent of the remaining gap of the actuator.

Charge drive control using constant current sources is mostly preferred to extend the travel range of electrostatic micro-actuators [130], [145], [146], [147], [148]. Nevertheless, there are very few references in the literature as regards charge drive control on RF MEMS. References include, a paper with numerical simulations for a capacitive RF-MEMS by Lee and Goldsmith [149] and another recently published, by Blecke et al [150], which presents a learning algorithm for reducing fabrication variability using resistive damping for the pull-down phase. None of these papers present any details on how to implement resistive damping or any results of such kind of applications. Varehest et al [151], attempted to control the bouncing of a MEMS accelerometer at its resonance frequency using a single resistor. This Thesis for the first time presents an attempt to control an ohmic RF MEMS switch using resistive damping.

In case, a constant voltage source V increase, the electrostatic force is increased due to an increase in the charge (Q).

$$F_e = \frac{QV}{2g} \tag{61}$$

Simultaneously, the increased force decreases the beam height (g), which, in turn, increases the capacitance and its charge. In other words the electrostatic energy provided by a constant voltage source V, is converted to kinetic energy, accelerating the beam [151].

$$E_k = \frac{mv^2}{2} \tag{62}$$

At $g=2/3g_0$, the increase in the electrostatic force is greater than the increase in the restoring force, resulting in an unstable condition and a collapse of the cantilever beam to the CPW line. This behavior creates a high impact force and bouncing phenomena.

When a voltage source with a large series bias resistance is used instead, the behavior of the switch is not the same. The presence of the high bias resistor changes the behavior of the source, to a rather constant capacitor current charge, which mainly depends on the resistor's value. Under these conditions the source behave like a current source and reduces the kinetic energy of the MEMS switch near the point of

contact by causing the voltage across the switch to drop in case of a rapid change in the capacitance of the electrode area.

$$V_C = V_S\left(1 - e^{-\frac{t}{RC}}\right) \quad (63)$$

For series ohmic RF-MEMS switches the capacitance created by the electrode area of switches in the up state is in the order of 0.02 to 1pF, with a final remaining gap of g>0.4μm in the down-state position. The current drown out of the source by the variable capacitor during the transition time is very small (2–20 μA) and a bias resistance R_B=10–50 MΩ is needed for an appreciable voltage drop.
The maximum initial charging current of the capacitor which is created under resistive damping between the electrode area and the cantilever during the transition time of the actuation pulse is given by:

$$i_C = C_{el}\frac{dV_C}{dt} \quad (64)$$

where:
C_{el} is the capacitance between the electrode and the cantilever in its initial position.
dV_C is the voltage drop in the capacitor
dt is the rise time of the actuation pulse

The value of the appropriate bias resistance for reducing the velocity of the cantilever through the gradual raise of the actuation voltage (29) is calculated through Ohm's law as:

$$R_B = \frac{V_C}{I_C} \quad \text{or} \quad R_B = \frac{t_r}{C_{el}} \quad (65)$$

Such a bias resistance cause soft landing with less bouncing phenomena, lower initial impact force but is also introduces additional delay to the switching time.
All the above considerations are valid only for the case that the rise time of the pulse is much smaller than the switching time tr<<ts, which means that during the rise time

of the pulse the cantilever has not started to move yet and its initial capacitance remains stable.

To eliminate bouncing phenomena, during the release phase of the switch, when the cantilever oscillates in the resonance frequency, the R_BC_{el} product must be equal to the period of the resonance frequency [151] and the R_b for this case is calculated as:

$$R_B = \frac{t_{res}}{C_{el}} \tag{66}$$

The "Hammerhead" RF-MEMS switch is considered next for the case study. For the pull-down phase the value of the damping resistance R_B depends on the values of the capacitance, created between the electrode area and the cantilever when the cantilever is in its initial position, and the rise time t_r of the applied pulse, as shown below:

$$R_b C_{el} = t_r = 2\mu m => R_b \approx 17M\Omega$$

where: C_{el}=118fF, the capacitance created in the electrode area.

Fig. 71 illustrates the characteristics of the switch under step pulse implementation with resistive damping. The results show excellent switch response during the pull-down phase. Elimination of the bouncing is observed with significant reduction in settling time (35 from 55μN) and reduction in the initial impact force (169 from 349μN) with only a small increase in the switching time (18 from 15μN). In the contrary, very poor response is observed during the release phase. Although the delay in the switching time is 3μm (15 from 12) the effect on the bouncing is very small (3.09 from 3.59μm). This phenomenon is due to the fact that the movement of the cantilever is governed by different forces.

In the release phase the free move is due to the restoring force and the mechanical resonance frequency of the cantilever and depends only on its elastic properties. Thus, a resistance that can be effective at this phase has to be proportional to the period of the resonance frequency of the cantilever. The resonance frequency of this switch is about 12.3KHz with the period around 80μs and the resulted resistance, calculated for this time, is about R_b=680MΩ, which unavoidably, is inappropriate for the pull-down phase.

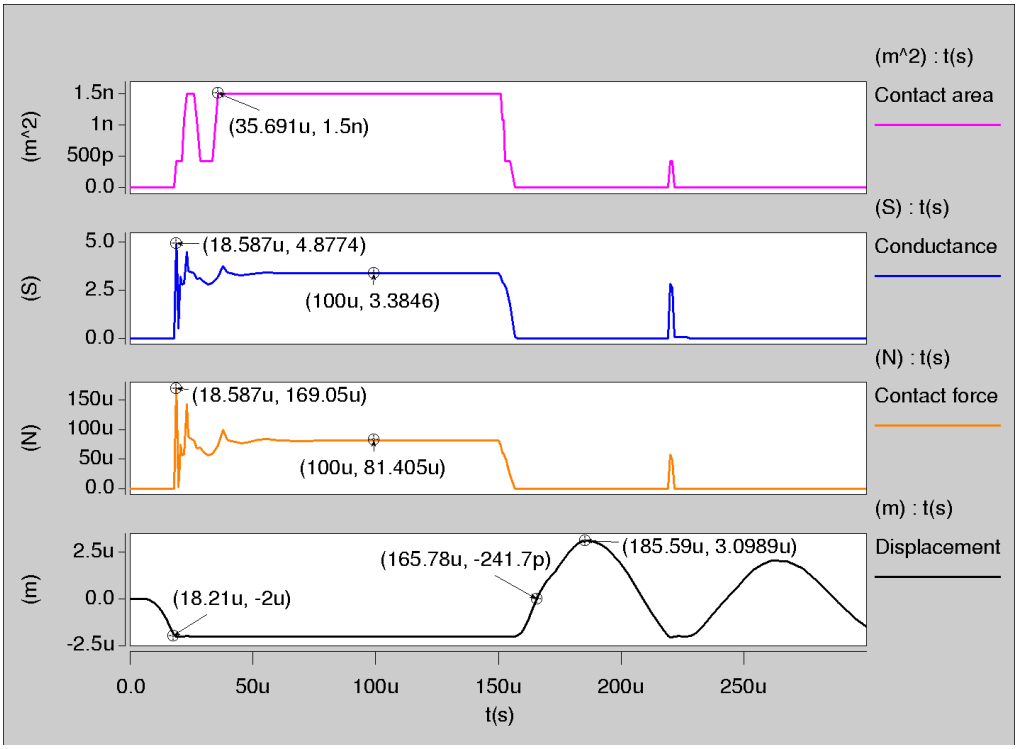

Fig. 71. Characteristics of the switch under resistive damping

The effect of damping resistance R_b=17MΩ on the step actuation pulse source (Voltage, current and power) is also shown in Fig. 72.

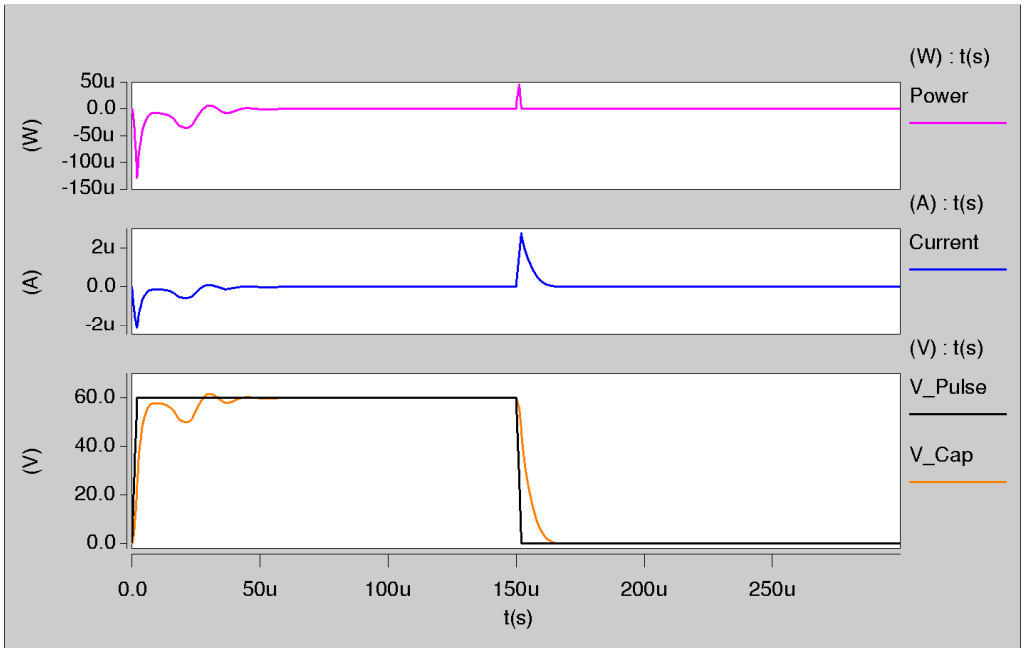

Fig. 72. Source response under Resistive damping control mode

4.7. Hybrid control mode

Another new control method for cantilever type RF-MEMS is presented in this Thesis for first time and consists of a combination of the two above techniques (Optimized tailored and resistive). The required steps for applying the Hybrid control mode for a given switch are the following.

- Consider the initial optimization procedure of paragraph 4.3
- Consider the procedure for Resistive damping of paragraph 4.4
- Consider a Taguchi optimization procedure for a switch controlled by a tailored actuation source in series with a large bias resistor.

The "Hammerhead" RF-MEMS switch is considered for the case study. As the two first steps have already implemented in the two previous paragraphs only the implementation of the third step remains. Taguchi's method is implemented taking as central values the magnitudes of the optimized tailored actuation pulse of the paragraph 1.3 and considering a ± 20% deviation from these predefined values, the initial levels of the parameters can be created, as shown in Tables 20 & 21.

Table 20. Pull-down phase (t_p) levels (Hybrid mode)

Vp (Volts)	49.2	61.5	73.8
$t_{p(on)}$ (μsec)	5.84	7.3	8.76
t_f (μsec)	1.28	1.6	1.92
$t_{p(off)}$ (μsec)	8.16	10.2	12.24
t_r (μsec)	1.76	2.2	2.64

Table 21. Release phase (t_f) levels (Hybrid mode)

Vp (Volts)	49.2	61.5	73.8
$t_{r(on)}$ (μsec)	3.92	4.9	5.88
t_r (μsec)	1.52	1.9	2.28
$t_{r(off)}$ (μsec)	7.44	9.3	11.16
t_r (μsec)	1.52	1.9	2.28

The optimization procedure graphs shown in Fig. 73 & 74 present the curves of mean and optimum values for the pull-down and release phases, as converged through Taguchi process, respectively.

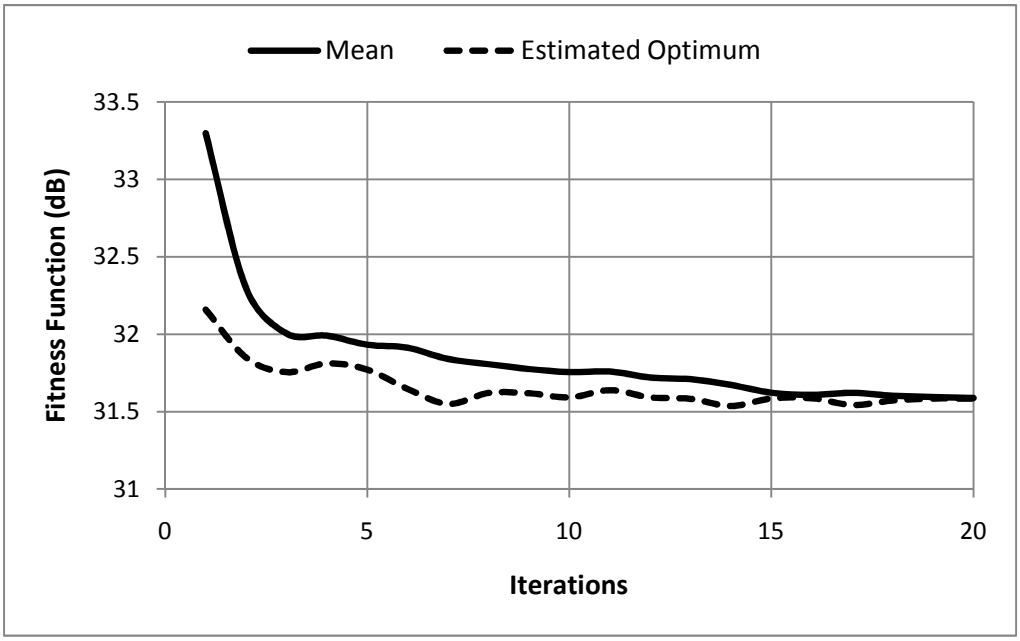

Fig. 73. Optimization procedure graph for the Pull-down phase of the switch

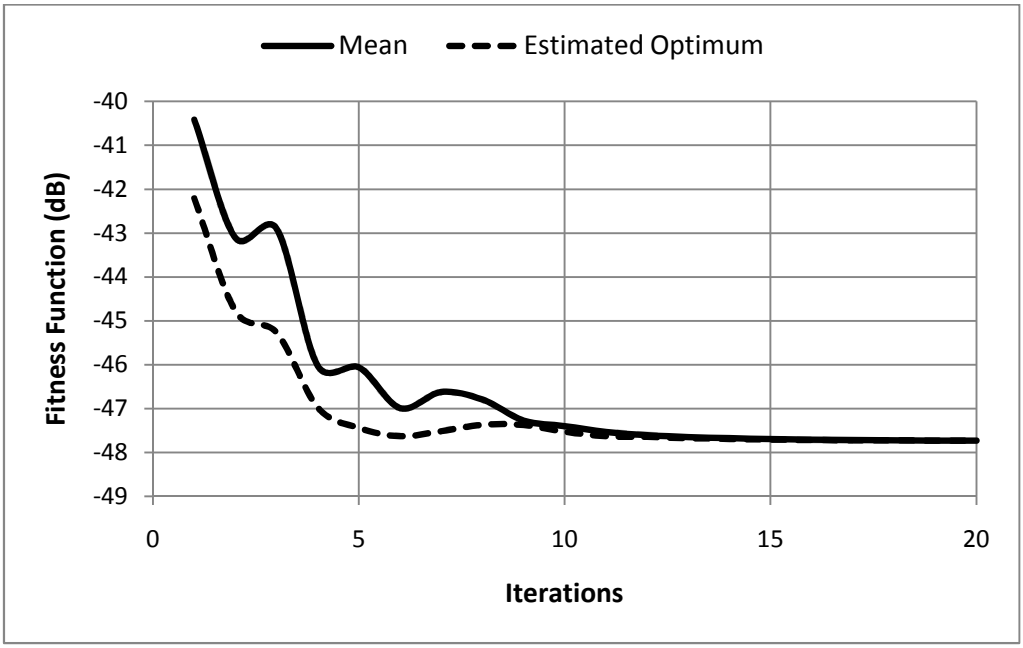

Fig. 74. Optimization procedure graph for the Release phase of the switch

The results for optimum dimensions extracted through Taguchi Optimization method after 20 iterations (less than 1 hour of processing time), for the pull-down and release switching phases of the ohmic RF-MEMS switch are illustrated in Table 22.

Table 22. Voltage and time intervals of the optimized tailored pulse (Hybrid mode)

Pull-down phase (t_p)					Release phase (t_r)				
V_{p-d}	t_{p-on}	t_{p-f}	t_{p-off}	t_{p-r}	V_r	t_{r-off}	t_{r-r}	t_{r-on}	t_{r-f}
66V	7.5μs	1.9μs	9.7μs	1.9μs	61V	6.5μs	2.2μs	8.6μs	2.2μs

Continuing the analysis, the switch is examined under transient conditions in Coventorware Architect environment. Simulations have been carried out using a voltage source with the characteristics of the optimized pulse, as described in Table 23, in series with a bias resistor of 17MΩ.

Table 23. Optimized tailored pulse voltage and time values (Hybrid mode)

t(μs)	0	2	9.5	11.4	21.1	23	150	152	158.5	160.7	169.3	171.5.
V(V)	0	66	66	0	0	60	60	0	0	61	61	0

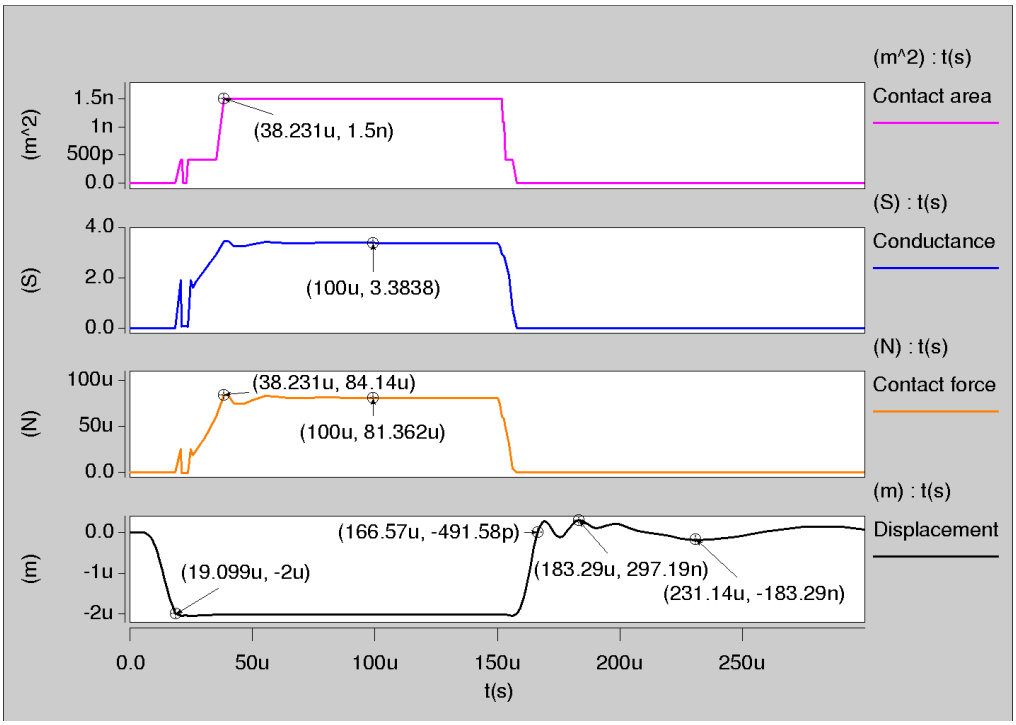

Fig. 75. Characteristics of the Hammerhead switch under Hybrid control mode

Fig. 75 illustrates the characteristics of the Hammerhead switch under Hybrid control mode. The results show excellent response during both switching phases with elimination of the bouncing and impact force in the pull-down phase and elimination of the bouncing in release phase.

The effect of damping resistance R_b=17MΩ on the tailored actuation pulse source (Voltage, current and power) is also shown in Fig. 76.

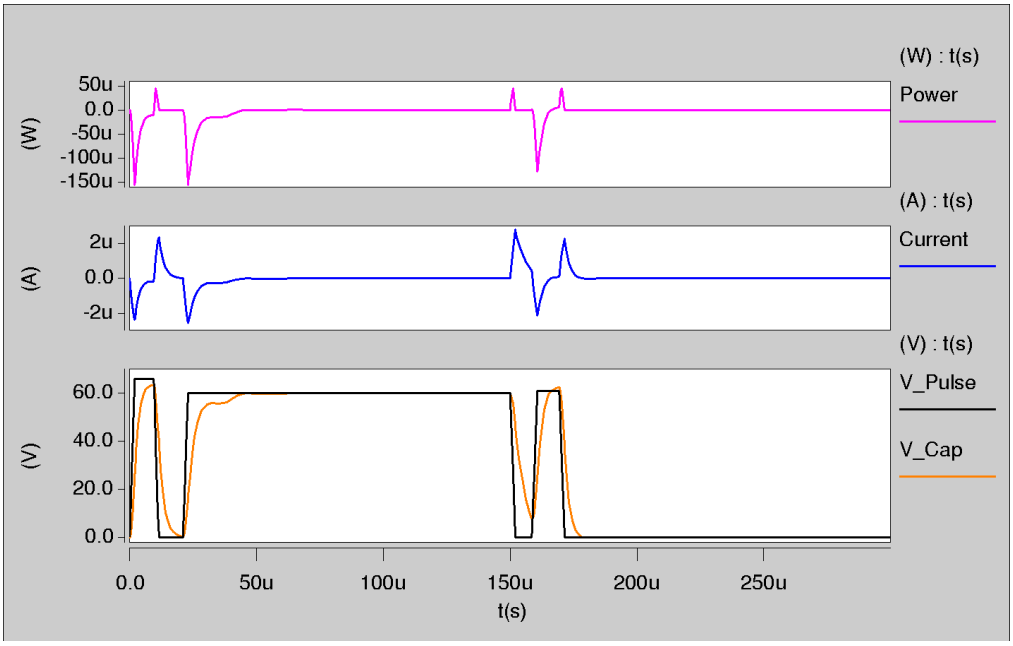

Fig. 76. Source response under Hybrid control mode

4.8. Comparison between different actuation modes

A comparison between the four actuation modes (step-pulse, step pulse with resistive damping, Taguchi optimized tailored pulse and Hybrid) that have been used, is illustrated in Fig. 77. It is obvious that the control of the switch with Optimized tailored pulse mode as well as with Hybrid mode is much better during the release phase as the swing of the cantilever is about 6-7 times smaller.

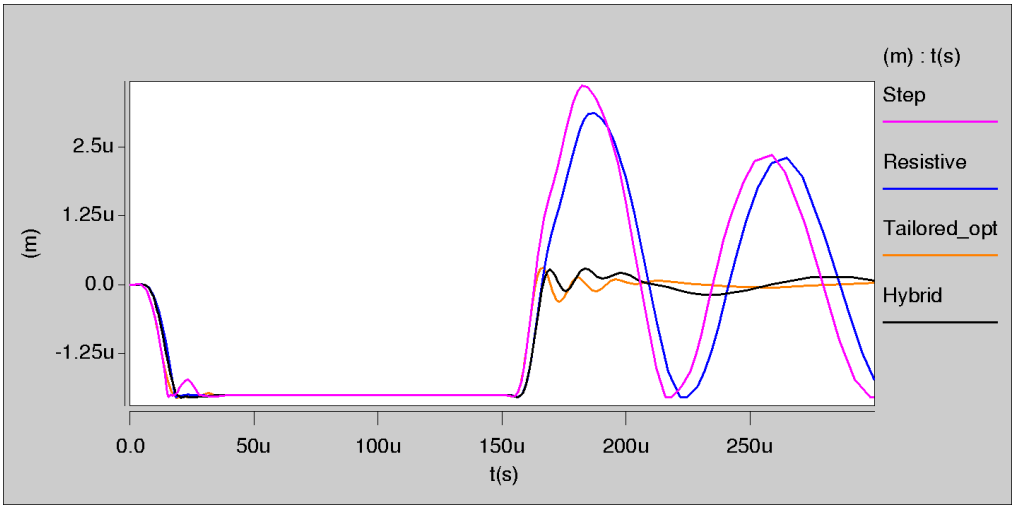

Fig. 77. Comparison between different actuation modes

In Fig. 78 a more detailed view of the pull-down phase is shown, where the actuation of the switch under Optimized tailored pulse, resistive damping or Hybrid mode presents very good behavior, around 17-19μs switching time and almost no bouncing. Under step pulse actuation the switch is faster, roughly 15μs, but with much more initial impact force and with a bounce of about 270nm high.

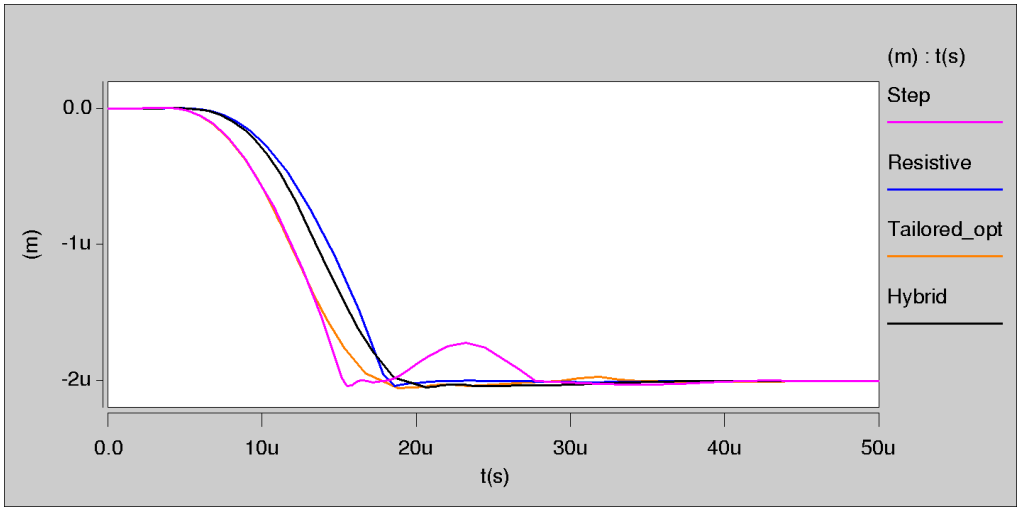

Fig. 78. Comparison between different actuation modes as concerns the pull-down phase

Comparing the impact force of the switch under the four control modes, the results show great improvement with respect to impact velocity for all three modified actuation modes 9.4cm/sec for the Resistive, 3.6cm/sec for the Optimized-Tailored and 1.4cm/sec for the Hybrid, instead of 31cm/sec of the step pulse. The Hybrid mode

excels all the others and implies true '*soft landing*' of the cantilever, reducing dramatically the impact force (84μN instead of 139 μN of the Optimized-Tailored, 317μN of the Resistive and 349μN of the Step-pulse), as shown in Fig. 79.

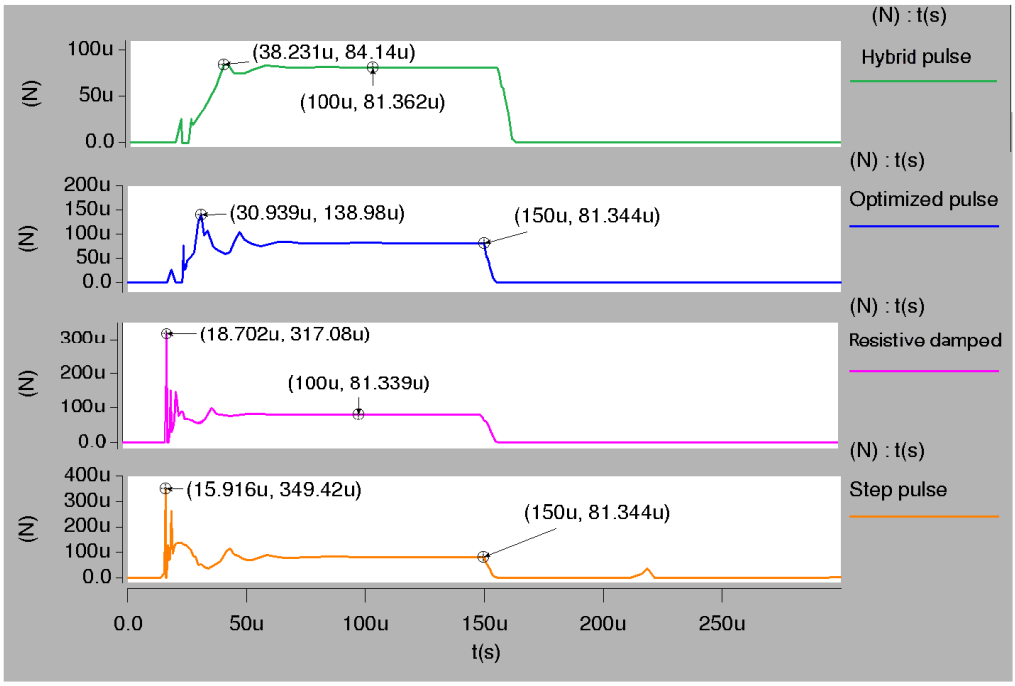

Fig. 79. Comparison of the contact forces

A comparison between the results implementing the four different actuation pulses, are shown concentrated in Table 24.

Table 24. Comparison of switching characteristics under four different contol modes

Mode	Impact Velocity	Impact Force	Switching (pull-down)	Switching (release)	Max. Bouncing Displacement
Step Pulse	31cm/s	349μN	15.3μs	13.2μs	3.59μm - 2μm
Optimized-Tailored Pulse	3.6cm/s	138μN	17μs	13.7μs	0.11μm - 0.09μm
Resistive damped	9.4cm/s	317μN	18.2μs	15.78μs	3μm - 2 μm
Hybrid	1.4cm/s	84μN	19μs	16.57μs	0.18μm - 0.18 μm

4.9. Comparison of the actuation modes under manufacturing uncertainties

Manufacturing tolerances are very difficult to avoid in real world applications. This issue becomes worse in the nano-micro world, especially in MEMS manufacturing and is one of the main reasons of malfunction [134]. Until recently all studies are referred on how to control an RF-MEMS under identical conditions and only in 2009 Blecke et al [150], presented a learning algorithm to modify the actuation control in order to face fabrication variability.

In this section, the "Hammerhead" switch is considered for fabrication and operational tolerances under the two actuation control modes which appear perfect results in nominal conditions, the Optimized-Tailored and the Hybrid are investigated. As fabrication tolerances, the thickness of the cantilever with ± 5%, the distance between cantilever and electrode with ± 5% and the elastic properties of cantilever's material (Au Young Modulus) in three levels 57MP, 78MP and 99MP are considered. As operation tolerance a deviation of ± 5% of the calculated actuation voltage amplitude is also considered.

For reliable results an out of series experiment is designed based on Taguchi's orthogonal design $OA_9 3^4$, which includes four parameters with three levels each, developed in nine series as shown in Table 25

Table 25. The four parameters in three levels assigned in a $OA_9 3^4$ ("Hammerhead")

n rows	Thickness (μm)	Height (μm)	Young modulus (MP)	Voltage (V)
1	5.7	2.75	78	57
2	5.7	3	57	60
3	5.7	3.15	99	63
4	6	2.75	57	63
5	6	3	99	57
6	6	3.15	78	60
7	6.3	2.75	99	60
8	6.3	3	78	63
9	6.3	3.15	57	57

The results considered under these conditions include the switching time (t_s), the impact force (F_{impact}), the existence of bouncing, the contact force, the magnitude of cantilever's swing during the release phase as well as the state of the switch (failure or not).

The results for the Optimized-Tailored actuation pulse are illustrated in Table 26. In cases 2 and 4 the switch has failed (the cantilever collapsed to electrode). In all other cases the switch is working but presents enough deviation of the nominal values.

Table 26. Results under optimized tailored pulse actuation mode implementation

Cases	**t_s (μs)**	**F_{impact} (μN)**	**Bounce (Y/N)**	**$F_{contact}$ (μN)**	**Release swing (μm)**	**Failure (Y/N)**
1	16.4	125.3	N	51.1	±0.38	N
2	-	-	-		-	Y
3	24.7	114.1	N	52.1	±0.88	N
4	-	-	-	-	-	Y
5	28.3	181.9	N	37.2	±0.78	N
6	26.3	165.9	N	46.8	±1.1	N
7	23.7	82.8	N	45.2	±0.78	N
8	20.2	85.1	N	55.4	±0.91	N
9	27.2	200.4	N	41.6	±1.21	N

The results for the Hybrid actuation pulse, as presented in Table 27, are shown a more stable situation without any failure under all the predefined conditions, due to the charge control that introduced through the bias resistor.

Table 27. Results under "Hybrid" actuation mode implementation

Cases	**t_s (μs)**	**F_{impact} (μN)**	**Bounce (Y/N)**	**$F_{contact}$ (μN)**	**Release swing (μm)**	**Failure (Y/N)**
1	19.6	53.4	N	46.1	±0.35	N
2	17.8	131.1	Y	90.2	±0.22	N
3	25.1	58.7	N	51.3	±0.2	N
4	15.8	264.6	Y	105.3	±0.54	N
5	31.3	100.7	N	37	±0.2	N
6	27.9	83.4	N	46.4	±0.21	N

7	22.3	52.1	N	45.1	±0.09	N
8	20.8	63.3	N	56.2	±0.25	N
9	29	81.7	N	44.6	±0.53	N

As an example of the superior performance under Hybrid mode, Fig. 80 & 81 present the contact force and displacement for the cases where the switch failed under Optimized-Tailored control.

In case 2, the only change from the nominal conditions is the thickness of the cantilever (5.7μm instead of 6μm). The results for this case under Hybrid mode are almost perfect with an exception of one small bounce during the pull down phase.

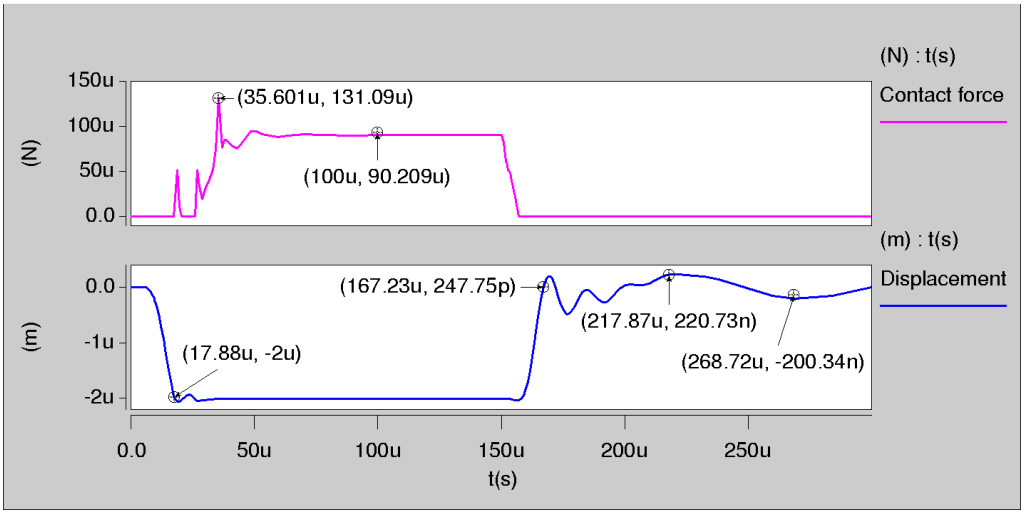

Fig. 80. Displacement and contact force figures of 2nd case under Hybrid mode

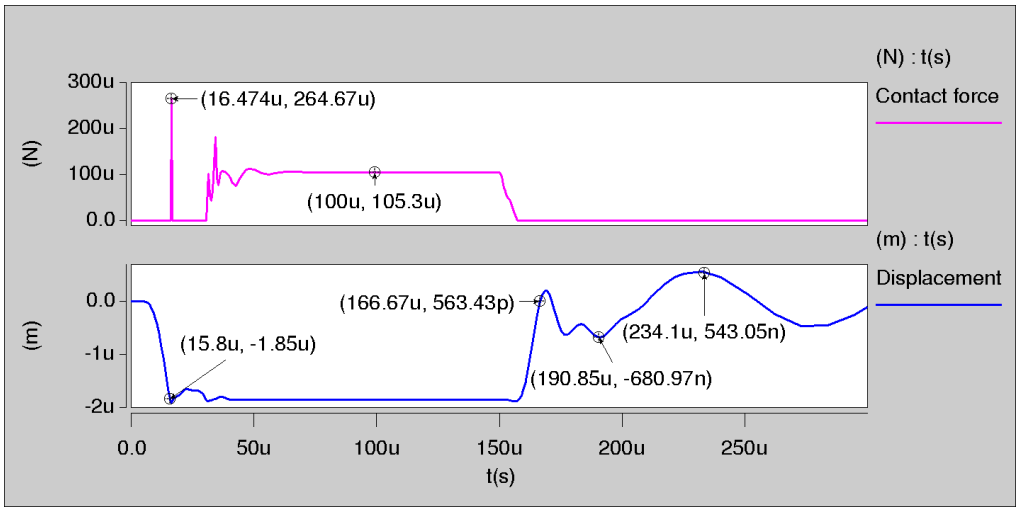

Fig. 81. Displacement and contact force figures of 4nd case under Hybrid mode

In case 4 the cantilever's height has been changed from 3 μm to 2.85μm and the actuation voltage from 60V to 63V, creating the worst case of the whole experiment. But even under these circumstances the switch under Hybrid mode has not failed as shown in Fig. 81.

Concluding, the Hybrid actuation mode, which is a combination of the tailored pulse, the resistive damping and Taguchi's optimization techniques, offers excellent switching response and remarkable robustness under manufacturing and operation tolerances and is superior over all the existing actuation modes.

4.10. NEU Control under resistive damping

In a very stiff device like the NEU switch, the actuation control under resistive damping is the only solution. Due to the small switching time as well as the high actuation voltage, it is not practical to implement a tailored control pulse. i.e. time intervals smaller than 1μs and pulses with slew-rate greater than 200V/μs are needed in order to shape a tailored pulse for this switch, as the switching time is about 1.24μs when an actuation pulse with 83V is applied. Even a fast and high voltage pulse can be generated, there are other subjects like overshooting that can render problematic for the control of the switch.

Another reason that make resistive damping control appropriate for this kind of switch is that the time constant RC calculated for the pull-down phase is near the period of the mechanical resonance frequency, achieving significant improvement in both switching operation phases of the switch.

Concluding, control under resistive damping is the only practical solution for very fast RF MEMS switches where the switching time and the period of the resonance frequency are of the same order.

Actuating the NEU switch with a voltage pulse with amplitude of 83V and tr=1μs, the correct Bias resistance is calculated as:

$$R_b C_{el} = t_r = 1\mu m => R_b \approx 33M\Omega$$

where: C_{el}=30fF, the capacitance which created within the electrode area.

Fig. 82 illustrates the characteristics of the switch under step pulse implementation with resistive damping. The simulation results with R_b=33MΩ shows excellent response of the switch during the pull-down phase as they presents elimination of the bouncing and the initial impact force (the high impact velocity has been reduced to 13.2 cm/sec from 65.9cm/sec), with only a small increase in the switching time (3.47μN from 2.38μN). During the release phase a significant reduction of the amplitude of bouncing is observed, too (174nm from 255nm).

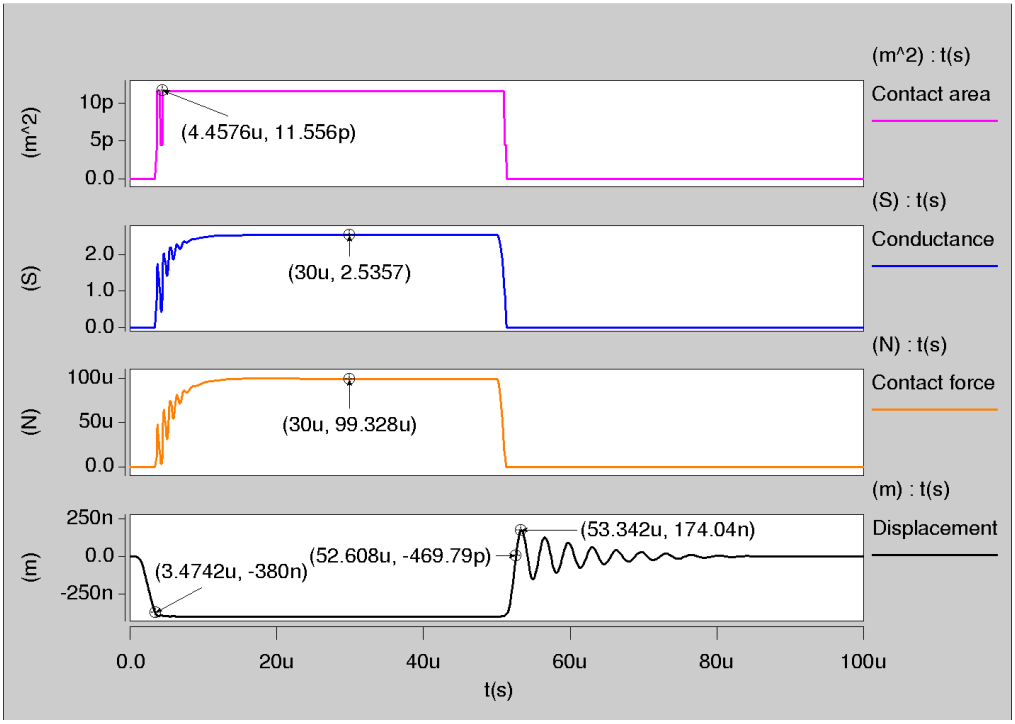

Fig. 82. Contact area and conductance of the switch with R_B = 33MΩ

The power and current requirements of the switch under step-pulse, as well as, the effect of damping resistance R_B=33MΩ on the actuation step-pulse source (Voltage, current and power) are illustrated in Fig. 83.

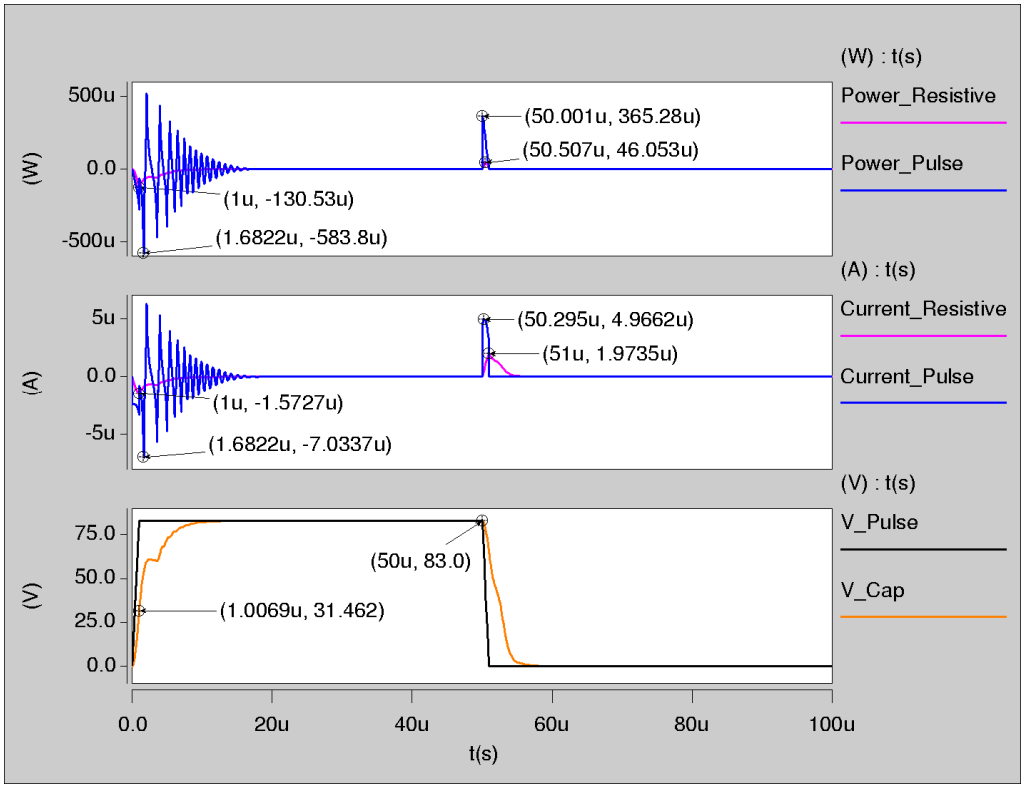

Fig. 83. Current and power consumption of the NEU switch

A comparison between step-pulse and step-pulse with resistive damping actuation modes that have been used is illustrated in Fig. 84. It is obvious that the control of the switch under resistive damping excels that of the step-pulse in both OFF-ON and ON-OFF transitions with only a slight increase of the switching times.

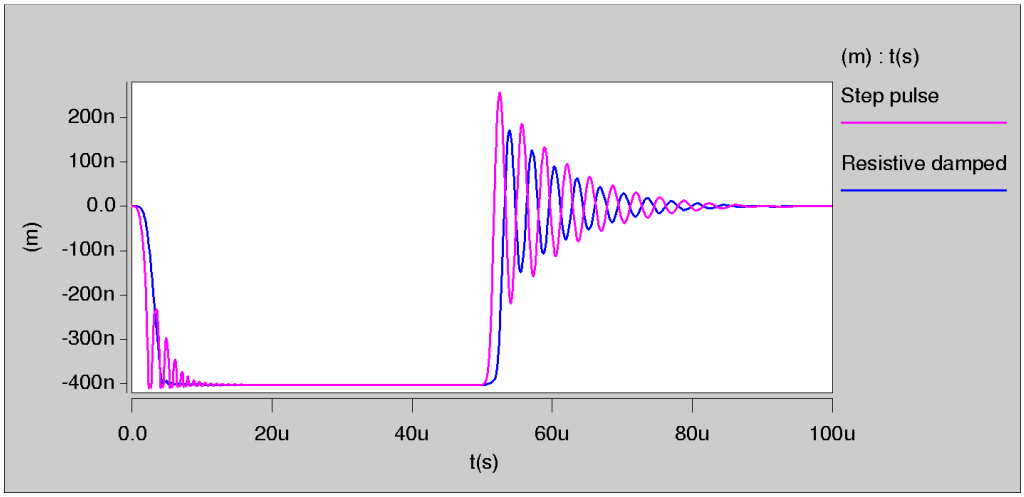

Fig. 84. Comparison between step pulse and resistive damping actuation modes

In Fig. 85 a more detailed view of the pull-down phase displacement of the cantilever between step pulse and resistive damped pulse implementation is shown.

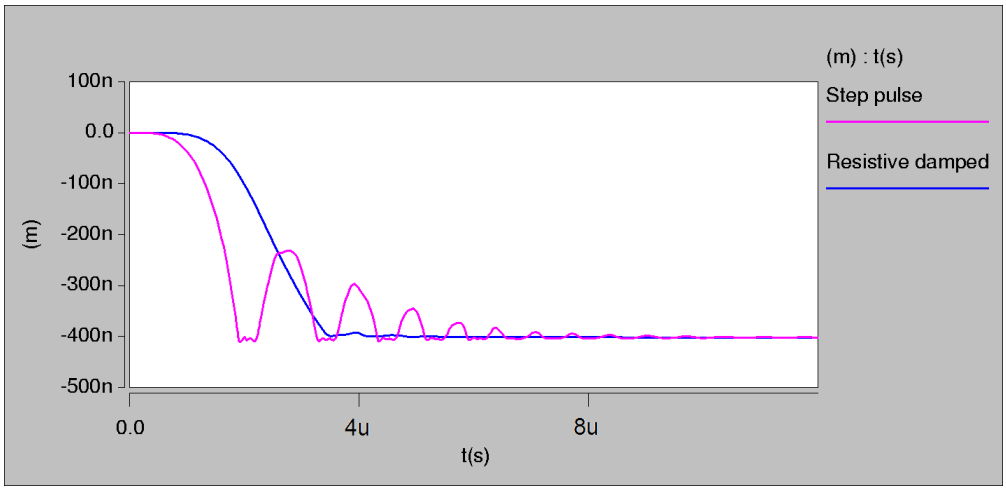

Fig. 85. Comparison between different actuation modes during the pull-down phase

The switching operation of the NEU switch is considered next under fabrication and operational tolerances. The control mode for this experiment is the resistive damping which presents perfect results under nominal conditions for this kind of switch. The experiment is held under the same conditions as in Hammerhead switch and the values of the parameters in the different levels are shown in Table 28

Table 28. The four parameters in three levels assigned in a $OA_9 3^4$ ("NEU")

n rows	Thickness (µm)	Height (µm)	Young modulus (MP)	Voltage (V)
1	5.7	360	78	79
2	5.7	380	57	83
3	5.7	400	99	87
4	6	360	57	87
5	6	380	99	79
6	6	400	78	83
7	6.3	360	99	83
8	6.3	380	78	87
9	6.3	400	57	79

The results of the experiment are illustrated in Table 29. In cases 5 and 7 the switch has failed but in most of the other cases the switch is working rather well without appearing large deviations of the nominal values.

Table 29. Results under resistive damping actuation mode implementation

Cases	**t_s (μs)**	**F_{impact} (μN)**	**Bounce (Y/N)**	**$F_{contact}$ (μN)**	**Release swing (μm)**	**Failure (Y/N)**
1	3.08	109.2	Y	105.4	±0.164	N
2	3.06	120.3	Y	114.3	±0.177	N
3	8.18	49	N	49	±0.154	N
4	3.05	137.3	Y	135.6	±0.158	N
5	-	-	-	-	-	Y
6	8.2	45.4	N	45.4	±0.163	N
7	-	-	-	-	-	Y
8	6.79	59.1	N	59.1	±0.148	N
9	6.29	51.9	N	51,9	±0.177	N

The switch has failed in cases 5 and 7 for a different reason than this of the Hammerhead switch as shown in Fig. 86 & 87. In case 5 the increase of the Young modulus (99MP instead of 57MP) and the reduction of the actuation voltage (79V instead of 83), do not allow the cantilever to bend enough (-196nm instead of -380nm). Under these conditions the switch behaves like an actuator due to the charge control.

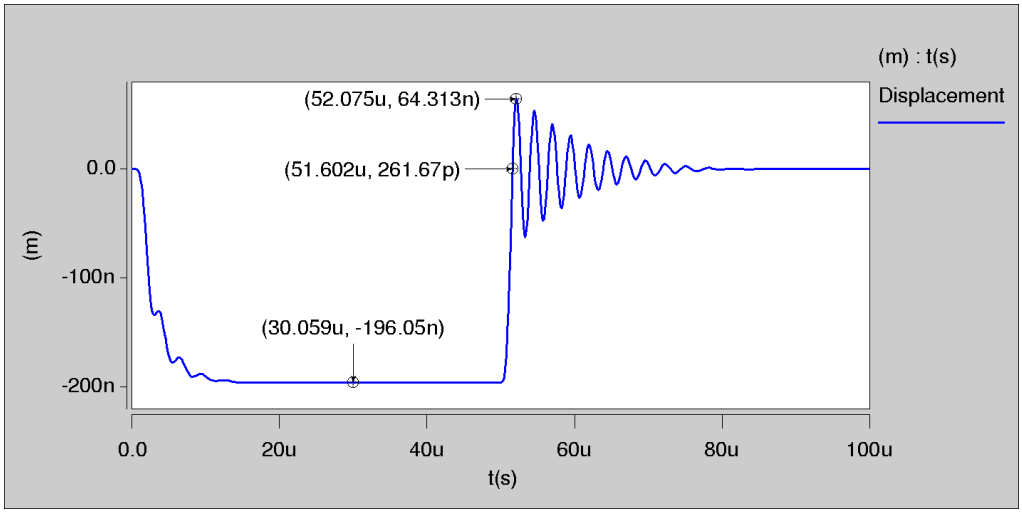

Fig. 86. The failure case 5 of the switch

In case 7 the increase of the thickness (6.3μm instead of 6μm) compensates the reduction of the height (360nm instead of 380nm) and as the other two parameters (Young modulus and voltage) remains the same as in case 5, the cantilever does not bend enough (-232nm instead of -360nm) to close the switch.

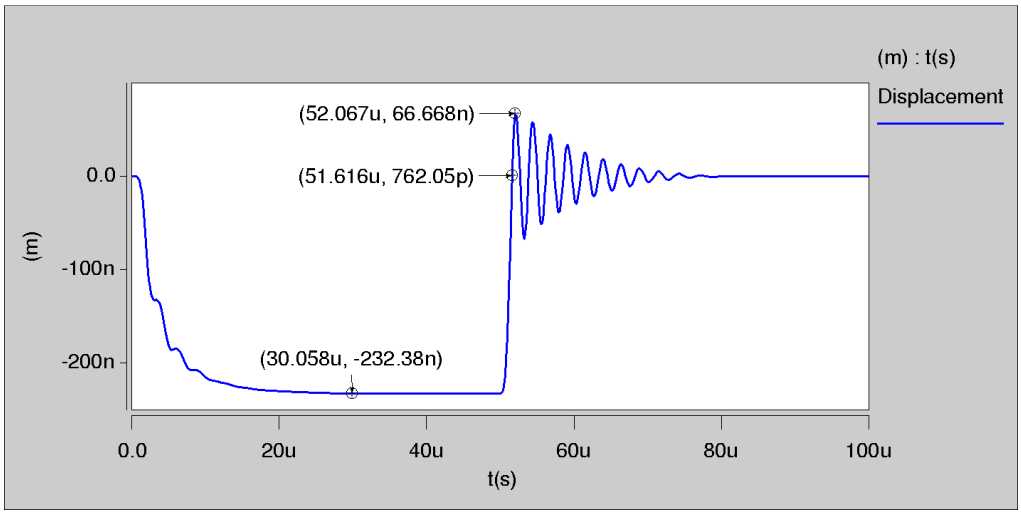

Fig. 87. The failure case 7 of the switch

4.11.Control under high pressure gas damping

Another way to control the ohmic RF MEMS switches is the damping of the cantilever movement by increasing the pressure of the gas introduced by Brown [54] and Guo et al [108].

High pressure results in increased viscosity, damping force, and spring force. With the increase in damping force the switching time is increased, but bouncing and settling times are decreased. This behavior is because at high ambient pressure, the squeeze film acts more like an incompressible layer rather than a compressible one. The increase in pressure also affects the cleanliness of the contact surfaces as at high pressures, contaminant films are formed at the switch contacts and increase the contact resistance [54]. It has to be mentioned that the method of using high pressure to increase damping force on RF MEMS switches in order to control them, presents a lot of difficulties and it is not a practical solution for real life applications [108].

4.1. Summary

In this chapter six possible ways to control the actuation of ohmic RF-MEMS switches have been presented and implemented, three of them for first time.

Apart from three well known control modes, gas damping, step pulse and tailored pulse, a novel open loop control procedure based on Taguchi's statistical optimization technique has been presented to improve the operation and, therefore the reliability and longevity of an ohmic RF-MEMS switch. The new technique allows exact calculation of the time intervals and voltage magnitudes of the actuation pulse train, achieving superior switching characteristics.

Following that, an improvement on the existing method of resistive damping (charge control) has been presented, allowing the exact calculation of the Bias resistor in order to reduce the impact force hence during the pull-down phase and the bouncing swing during the release phase.

Finally, another new technique, the Hybrid control mode, has been presented. This new open loop technique is based on the combination of the two previously mentioned methods (Taguchi's optimized tailored pulse and resistive damping). The simulation process, has been carried out in the Architect module of Coventorware® and presents true 'soft landing' with very low impact force eliminating any bouncing phenomena during the pull-down phase. Meanwhile, minimization of the bouncing during the release phase achieved, keeping the ON-OFF switching times comparable with those of the step actuation pulse. Moreover the Hybrid control mode ensures among the others immunity to manufacturing and operation uncertainties.

5. Application of RF-MEMS in reconfigurable antennas

5.1. Introduction

A reconfigurable antenna consists of antenna elements capable of individually reconfiguring their physical structure altering the polarization and frequency properties of the antenna. Nevertheless, reconfiguring one characteristic of the antenna affects the rest, i.e. frequency response reconfiguration results to pattern radiation and vice versa. This linkage is one of the largest challenges in the development of reconfigurable antennas [28].

The design diversity of reconfigurable antennas requires variable-geometry configurations, which should be precisely controlled via high quality switches. There are three types of switches that could be used for multiple element reconfigurable antenna implementations. These are GaAs FETs, Pin Diodes, and RF MEMS.

GaAs FETs switches suffers from low linearity and do not have sufficient isolation to minimize cross-interference and signal jamming from adjacent channels. Using a couple of these switches for reconfiguration of an antenna is acceptable, but when they are used in large quantities the degradation of the antenna characteristics is dramatic.

Pin diodes, on the other hand, offer good switching characteristics (inherent low insertion loss and high isolation), but they need a considerable amount of power to operate which reduces battery life time. Besides, many bias problems are generated when a large number of switches have to be used. These two disadvantages make pin-diodes inappropriate for portable complex reconfigurable antenna implementations.

Finally, RF MEMS switches are the most elegant solution for reconfigurable antennas. They offer superior RF characteristics (isolation and insertion loss) and thus they can get integrated in large quantities within the antenna structure. Additionally, they can be controlled using high resistance bias lines through a third port (actuating pad), thus the bias network of RF MEMS switches can be extensive in large antennas arrays without causing any interference and degradation to the antenna radiation

patterns. The bias network also consumes very little power, an important aspect when large numbers of switches are used, especially for mobile or satellite applications. Their small size and their ability to get integrated monolithically within the antennas elements on high efficiency microwave laminates [152], [153], make the RF-MEMS switches the ideal solution for reconfigurable antennas structures. Aiming this target a new, simple, reliable and controllable RF-MEMS switch has been designed and presented in Chapter 3.

Due to the multi scale nature of reconfigurable antennas, the numerical modelling poses serious computational challenges. Taguchi's statistical optimization technique, which has been presented in detail in Chapter 4, can handle multidimensional, discontinuous and nondifferentiable objective functions with many potential local maxima while converges rapidly to the optimum result. Nevertheless, if the searching area is defined to be larger than ±20% of the central estimated values; its performance is poor compared to the modern stochastic evolutionary methods like Particle swarm optimization (PSO). This occurs because the usual Taguchi's optimization method is not capable of efficiently checking adjacent areas, as the optimization process tends to converge constantly and the values of the parameters do not have the ability to restore their initial values. Aiming to solve this inefficiency, a variation of Taguchi's method (Grid-Taguchi) capable of searching efficiently and systematically wide areas is presented and compared with existing methods through a design of a Pattern and Frequency reconfigurable Yagi-Uda antenna.

5.2. Design and optimization of a Pattern and Frequency reconfigurable Yagi-Uda antenna

A switchable printed 3-elements Yagi-Uda antenna prototype with frequency and radiation pattern reconfiguration is considered for this study. Reconfigurable Yagi-Uda configurations have been presented in the past with Frequency [154] or Pattern [155] reconfigurability. A Pattern and Frequency reconfigurable Yagi-Uda design is presented here for the first time. The proposed reconfigurable configuration is 8 discrete antennas combined using RF-MEMS switches. As a result, this antenna can offers Gain > 6dB in two different frequencies 2.4GHz and 2.7GHz, also having the

ability to be steered in four discrete directions towards desired signals or away from interfering signals.

In the design of a printed 3-elements Yagi-Uda antenna, the most important design parameters are: the characteristics of the laminate (e_r and thickness) which determines the guided wavelength λ_g, the lengths of the elements, the width of the elements as well as the spacing between the elements. Hence, the initial center dimensions for each parameter can be defined as shown below:

The free air wavelength at 2.4GHz is λ_0 = 125mm. The substrate chosen for the antenna implementation is the microwave laminate RT/duroid® 5880 from Rogers with e_r = 2.2, tanδ = 0.0009 and thickness of 1.575mm and the guided wavelength is given by [156]:

$$e_{r(eff)} = \frac{e_r+1}{2} + \frac{e_r-1}{2\cdot\sqrt{1+12\frac{h}{w}}} = 1.76 \quad (67)$$

$$\lambda_g = \frac{\lambda_0}{\sqrt{e_{r(eff)}}} = 94mm \quad (68)$$

The initial center values are calculated as:

A. Dipole length = $\lambda_g/2$ = 47mm
B. Director length= $0.45\lambda_g$ = 42.3mm
C. Reflector length= $0.55\lambda_g$ = 51.7mm
D. Distance between the elements $h_1=h_2= \lambda_g/4$ = 23.5mm
E. Width of the elements = 1.5mm

The 3 elements Yagi-Uda antenna is shown in Fig. 88

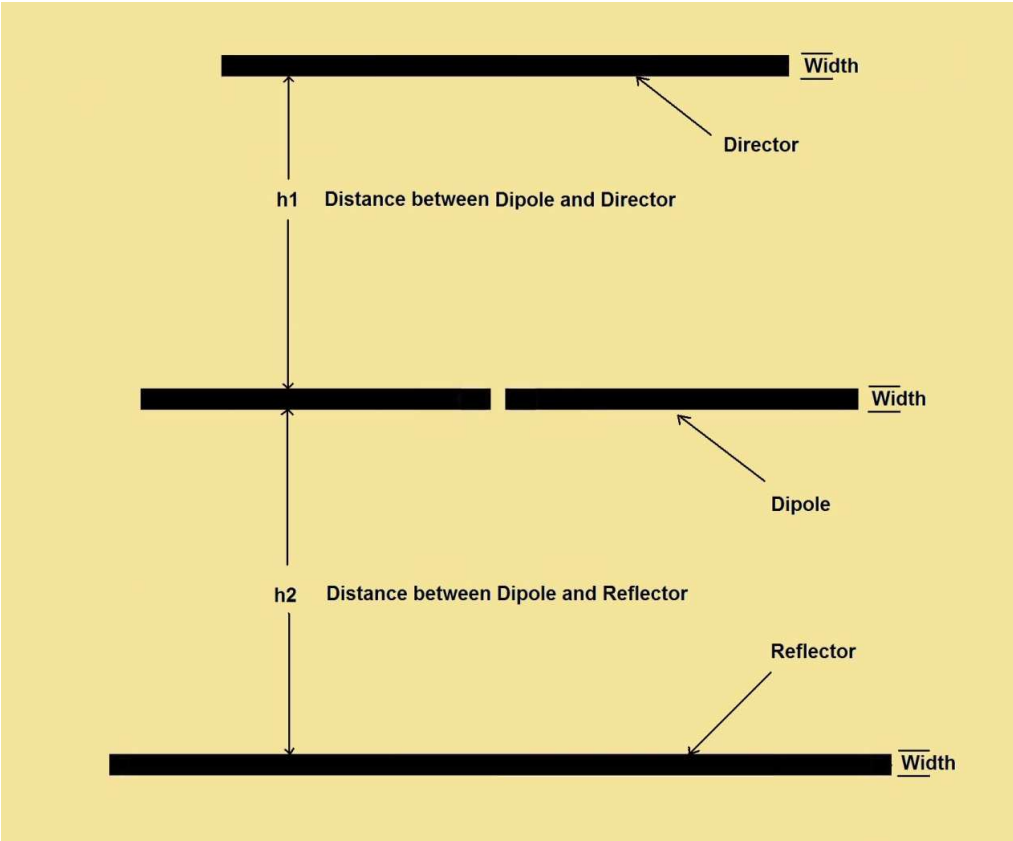

Fig. 88. The 3 element Yagi-Uda antenna

In this chapter, Taguchi's methods, as well as, PSO method for comparison and validation will be used to optimize the geometrical dimensions of the Yagi-Uda antenna, so as to simultaneously achieve good matching, gain and good front-to-back ratio of the pattern in the operating frequency range.

The objective of optimization is the minimization of a Fitness Function (FF). The FF is suitably determined according to the above conditions and the goals that have to be achieved are:

- Good input matching $S11 < -20dB$
- Gain > 6dB
- Front to back Gain Ratio $(F/B)_{dB}$ > 15dB

In order to combine the eight antennas together, another two conditions have to be taken into account.

- The distance between the elements is equalized $h_1 = h_2$.

- The length of the Reflector has to be smaller than the double of the Distance between elements plus the width of one element in order to avoid crossing between them.

Thus a weighted and scalable FF has been developed with the form:

$$FF = Term_{(S11)} + Term_{(GF)} + Term_{(F/B)} + Term_{(D)}$$

With the following conditions:

$$if\ \left|S11_{(dB)}\right| \leq 15 \quad \boldsymbol{then}\ Term_{(S11)} = 500\left(15 - \left|S11_{(dB)}\right|\right) + 4000$$

$$if\ \left|S11_{(dB)}\right| > 15\ and\ \left|S11_{(dB)}\right| \leq 30\ \ \boldsymbol{then}\ Term_{(S11)} = 250\left(30 - \left|S11_{(dB)}\right|\right)$$

$$if\ \left|S11_{(dB)}\right| > 30\ \ \boldsymbol{then}\ Term_{(S11)} = 0$$

$$Term_{(GF)} = 1000\left(8 - G_{F(dB)}\right) \qquad if\ G_{F(dB)} > 8\ \ \boldsymbol{then} \quad Term_{(GF)} = 0$$

$$Term_{(F/B)} = 300(20 - (F/B)_{dB}) \quad if (F/B)_{dB} > 20\ \ \boldsymbol{then} \quad Term_{(F/B)} = 0$$

$$Term_{(D)} = 500 \quad if[(2xDistance) + Width] \leq Reflector \quad \boldsymbol{then}\ Term_{(D)} = 0$$

And in Log10 form: $FF_{Log} = 20LogFF$

The weight-factors (1000, 500, 300, 250), the stop-factors (30, 20, 8), as well as, the scalable response of the $Term_{(S11)}$ are used to balance the different targets within the FF, in order to achieve the optimum results for all the targets, averting the possibility of domination to one over the others.

5.3. Grid-Taguchi optimization technique

A solution to the previously mentioned inefficiency is given by an evolution of Taguchi's technique, which is presented for first time in this Thesis and named as "Grid-Taguchi" technique. The main idea was to extend the searching area not randomly, but based on the exceptional properties of the Orthogonal Arrays.

The optimization procedure begins with the problem consideration, which includes among the others the searching area of each parameter. This area is defined as a percentage deviation around the initial estimated center values of each parameter and determines the initial levels L_{init}. If these levels are greater than ± 20% then two OAs in a master/slave configuration are needed to split the above levels in order to have more accurate results in a wider search area.

The initial levels of the master OA are assigned in the 2/3 of the initial deviation around the central parameter value and the master $OA_n(m^k)$ is created.

The slave $OA_{n1}(m^k)$ is defined next with the same number of parameters and levels as the master but not necessarily with the same number of rows, depending on the complexity of the problem. As central values of each parameter are defined the level values of each row of the master OA, so that as many slave OAs as the number of rows of the master OA to be created. The initial levels of each slave OA parameters are assigned in the 1/3 of the initial deviation. With this method the searching area is defined as the sum of the deviations of the two OAs. It should be noted that the master OA defines only the central values of the parameters and the optimization procedure through Taguchi's technique is executed by the slave OAs.

The procedure is completed running the slave OAs using the Taguchi's Optimization technique, as described in Chapter 4, and choosing as final result the best matching to the FF among them (for a detailed example about Grid-Taguchi technique see Apentix A.3).

With this novel technique wider areas around the estimated initial central values of the parameters are searched, sacrificing some computational time. The obvious profit by using the Grid Taguchi technique is the methodic searching of the entire, under consideration, area in the shortest possible time.

5.3.1.Grid-Taguchi optimization solution

Considering a ± 40% deviation from the center values, for an extensive search of the examined area, the initial levels can be created, as shown in Table 30.

Table 30. Initial levels (Central±40%)

		1st	2nd	3rd
A	Dipole length	28.2mm	47mm	65.8mm
B	Director length	25.38mm	42.3mm	59.22mm
C	Reflector length	31.02mm	51.7mm	72.38mm
D	Distance	14.1mm	23.5mm	32.9mm
F	Width	0.9mm	1.5mm	2.1mm

For a realistic approach in the antenna design, the resolution for all dimensions is set to 1μm. For an OA with 5 parameters of 3 levels for each parameter a configuration with at least $n_{rows} = 1 + (k \cdot DOF_m) = 1 + (5 \cdot 2) = 11 rows$ is needed. Taguchi suggests two solutions:

- the $OA_{18}(3^7, 2)$ that can handle up to 7 parameters with 3 levels each and one with 2 levels in an array of 18 rows.
- the $OA_{27}(3^{13})$ that can handle up to 13 parameters with 3 levels each in an array of 27 rows.

Since achieving four discrete targets simultaneously (good matching, gain, F/B ratio and suitable spacing) is a very complex task, it was decided to employ a larger OA to increase the possible combinations. Thus, the second solution appears more promising as it has 50% more rows for each OA and offers higher confidence level at the expense of some extra computation. For this case 5 columns of the $OA_{27}(3^{13})$ have been chosen to assign the five parameters in their 3 levels, thus an $OA_{27}(3^5)$ has been created, as shown in Table 31. According to the complexity of the design a reducing percentage of RP=0.1 has been assigned. The procedure terminates when the LD is below 1μm (minimum resolution).

Table 31. $OA_{27}(3^5)$

n rows	A	B	C	D	E
1	1	1	1	1	1
2	2	2	2	2	2
3	3	3	3	3	3
4	2	2	3	3	3
5	3	3	1	1	1
6	1	1	2	2	2
7	3	3	2	2	2
8	1	1	3	3	3
9	2	2	1	1	1
10	2	3	1	2	3
11	3	1	2	3	1
12	1	2	3	1	2
13	3	1	3	1	2
14	1	2	1	2	3
15	2	3	2	3	1
16	1	2	2	3	1
17	2	3	3	1	2
18	3	1	1	2	3
19	3	2	1	3	2
20	1	3	2	1	3
21	2	1	3	2	1
22	1	3	3	2	1
23	2	1	1	3	2

24	3	2	2	1	3
25	2	1	2	1	3
26	3	2	3	2	1
27	1	3	1	3	2

The same OA configuration is selected for slave ($OA_{27(N)}(3^5)$) with the same number of parameter levels and rows which will be repeated for N = 27 times. The initials levels of each slave OA parameters are assigned in the 1/3 of the initial deviation around the central values which are defined from each row of the master OA. Next Taguchi's technique is executed via the slave OAs in conjunction with FEKO® full wave electromagnetic solver.

FEKO® is a software suite built for the analysis of a wide range of electromagnetic problems. Applications include EMC analysis, antenna design, microstrip antennas and circuits, dielectric media, scattering analysis, etc.

Taking into account the above considerations in combination with FEKO® simulation results, the Grid-Taguchi's optimization algorithm for the Yagi-Uda antenna is implemented in C++. Using C++ code allows altering the antenna's parameters since all parameters can be entered in a text format and get processed by the program.

5.4. Single Taguchi optimization applying 3 levels and 5 levels solutions

For comparison reasons as well as in order to prove the efficiency of the Grid-Taguchi method, the same case, the 3-elements Yagi-Uda antenna is considered for optimization under the normal Taguchi's technique using 3levels and 5levels OA.

For a 3 levels Taguchi design, the same OA configuration $OA_{27}3^5$ of Table 36 is selected. The initials levels of each parameter are assigned in the ± 20% around the central values as shown in Table 32.

Table 32. Initial levels (Central±20%)

	1st	2nd	3rd
Dipole	37.6mm	47mm	56.4mm
Director	33.8mm	42.3mm	50.8mm
Reflector	41.4mm	51.7mm	62mm
Distance	18.8mm	23.5mm	28.2mm
Width	1.2mm	1.5mm	1.8mm

For a wider search area a 5 levels Taguchi design is considered. Taguchi suggests for this purpose the $OA_{25}5^6$ which consists of 6 columns (parameters) in 5 levels, each one developed in 25 rows (experiments). For the Yagi-Uda antenna case, 5 columns of the $OA_{25}(5^6)$ have been chosen to assign the five parameters in their 5 levels, thus an $OA_{25}(5^5)$ has been created, as shown in Table 33

Table 33. $OA_{25}(5^5)$

n rows	**A**	**B**	**C**	**D**	**E**
1	1	1	1	1	1
2	1	2	2	2	2
3	1	3	3	3	3
4	1	4	4	4	4
5	1	5	5	5	5
6	2	1	2	3	4
7	2	2	3	4	5
8	2	3	4	5	1
9	2	4	5	1	2
10	2	5	1	2	3
11	3	1	3	5	2
12	3	2	4	1	3
13	3	3	5	2	4
14	3	4	1	3	5
15	3	5	2	4	1
16	4	1	4	2	5
17	4	2	5	3	1

18	4	3	1	4	2
19	4	4	2	5	3
20	4	5	3	1	4
21	5	1	5	4	3
22	5	2	1	5	4
23	5	3	2	1	5
24	5	4	3	2	1
25	5	5	4	3	2

The initial levels of each parameter are assigned in the ± 40% around the central values in 5 levels with ± 20% step as shown in Table 34

Table 34. OA levels (Central±40% with ±20% step)

	1st	2st	3nd	4rd	5th
Dipole	28.2mm	37.6mm	47mm	56.4mm	65.2mm
Director	25.38mm	33.8mm	42.3mm	50.8mm	59.22mm
Reflector	31.02mm	41.4mm	51.7mm	62mm	72.38mm
Distance	14.1mm	18.8mm	23.5mm	28.2mm	32.9mm
Width	0.9mm	1.2mm	1.5mm	1.8mm	2.1mm

Next Taguchi's technique is executed under the same FF and reduced percentage of RP = 0.1 in conjunction with FEKO®

5.5. Comparison between Taguchi optimization modes

The optimized results of the 3-elements 2.4GHz Yagi-Uda antenna, obtained under the three different Taguchi optimization modes, are shown in Table 35. The results show that Grid-Taguchi technique excels towards the other two, since almost all targets have been met, due to its ability to thoroughly search over a wider area when multiple targets are required to be achieved.

Table 35. Comparison between Taguchi optimization modes

	5-levels	3-levels	Grid
Fitness Function (dB)	71.17	70.68	70.16
S11 (dB)	-30.07	-30.16	-30.28
Forward Gain (dB)	6.9	6.3	6.5
Back Gain (dB)	-4.5	-7	-8
F/B ratio	11.4	13.3	14.5

A graphical comparison between the three Taguchi optimization methods (for Grid-Taguchi the best run is considered) of the 3-elements 2.4GHz Yagi-Uda antenna, is shown in Fig. 89

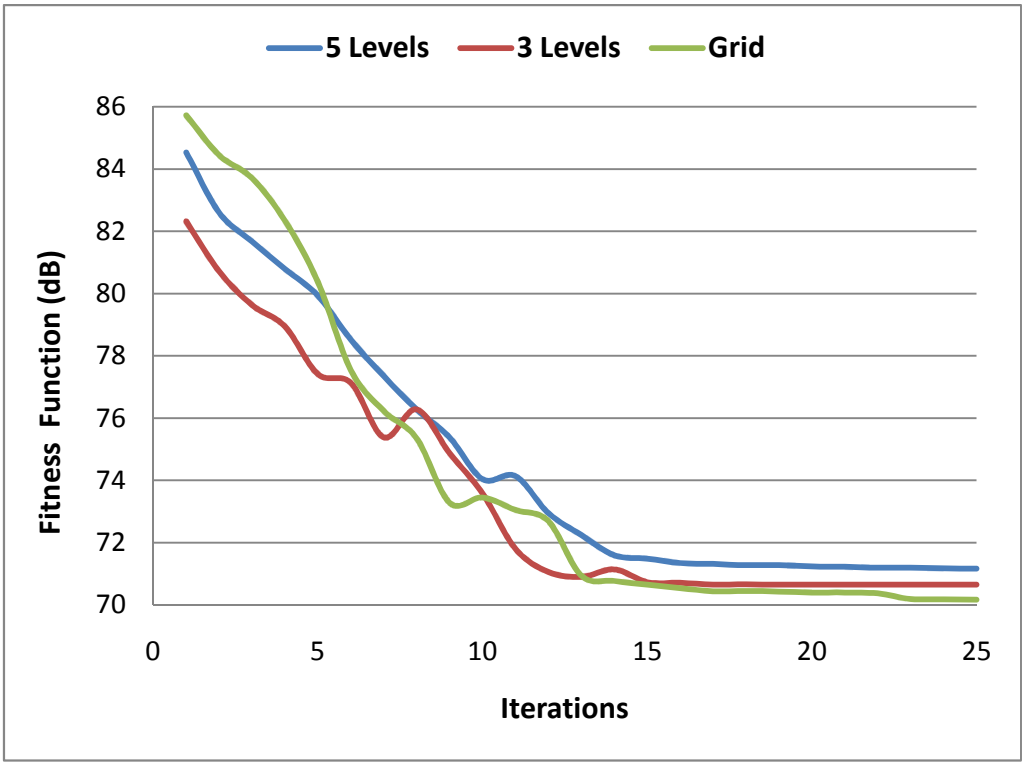

Fig. 89. Optimization graphs of Taguchi's methods

It has to be mentioned that Grid-Taguchi technique needs more computational time to get completed and hence, can only be compared under the same conditions (same number of experiments) with other optimization methods such as PSO.

5.6. PSO optimization technique

In 1995, Kennedy and Eberhart first introduced the particle swarm optimization (PSO) technique [157]. PSO is a stochastic optimization technique and belongs to the evolutionary computation techniques. The method has been proved to be robust in solving problems featuring nonlinearity and non-differentiability, multiple optima, and high dimensionality through adaptation. The PSO technique can generate a high-quality solution within shorter calculation time and stable convergence characteristic than other stochastic methods [158]. The technique is derived from the social-psychological theory and utilizes the research on swarm such as fish schooling and bird flocking. According to the research results for a flock of birds, birds find food by flocking (not individually). The observation leads to the assumption that all information is shared inside the swarm. Moreover, according to observation of behavior of human groups, the behavior of each individual (agent) is also based on behavior patterns authorized by the groups, such as customs and other behavior patterns, according to the experiences by each individual.

In the PSO algorithm, for a d-variable optimization problem, a swarm of particles are put into the d-dimensional search space with randomly chosen velocities and positions knowing their best values so far (*pbest*) and the position in the d-dimensional space. The velocity of each particle, adjusted according to its own flying experience and the other particle's flying experience.

For example, the i^{th} particle is represented as $x_i = (x_{i,1}, x_{i,2}, \dots\dots, x_{i,m})$ in the d-dimensional space. The best previous position of the i^{th} particle is recorded and represented as:

$$Pbest_i = (Pbest_{i,1}, Pbest_{i,2}, \dots\dots, Pbest_{i,m})$$

The index of best particle among all of the particles in the group is $gbest_m$. The velocity for particle *i*, is represented as:

$$v_i = (v_{i,1}, v_{i,2}, \dots\dots, v_{i,m})$$

The modified velocity and position of each particle can be calculated [159] using the current velocity and the distance from $pbest_{i,m}$ to $gbest_m$ as shown in the following formulas:

$$v_{i,m}^{(t+1)} = wv_{i,m}^{(t)} + c_1 rand()\left(pbest_{i,m} - x_{i,m}^{(t)}\right) + c_2 Rand()\left(gbest_m - x_{i,m}^{(t)}\right) \quad (69)$$

$$x_{i,m}^{(t+1)} = x_{i,m}^{(t)} + v_{i,m}^{(t+1)} \quad (70)$$

i=1,2,….,n

m=1,2,….,d

where

n	Number of particles in the group;
d	Number of members in a particle;
t	Pointer of iterations(generations);
$v_{i,m}^{(t)}$	Velocity of particle i at iteration t, $V_m^{min} \le v_{i,m}^{(t)} \le V_m^{max}$;
w	Inertia weight factor;
c_1,c_2	Acceleration constant;
rand(), Rand()	Random number between 0 and 1;
$x_{i,m}^{(t)}$	Current position of particle i at iteration t;
$pbest_i$	Best previous position of the particle I;
gbest	Best particle among all the particles in the population.

In the above procedures, the parameter V^{max} determined the regions searching resolution, or fitness, between the present position and the target position. If that is too high, particles might fly past good solutions. If V^{max} is too small, particles may not explore sufficiently beyond local solutions. In many cases, V^{max} was often set to 10–20% of the dynamic range of the variable on each dimension [160].

The constants c_1 and c_2 represent the weighting factors of the stochastic acceleration which pull each particle towards *pbest* and *gbest* positions. Low values allow particles to roam far from the target regions before being tugged back. On the other hand, high values result in abrupt movement toward, or past, target regions. Hence, the

acceleration constants c_1 and c_2 are often set to be 2.0 according to past experiences. Suitable selection of inertia weight w provides a balance between global and local explorations, thus requiring less iteration on average to find a sufficiently optimal solution. As originally developed, *w* often decreases linearly from about 0.9 to 0.4 during a run. In general, the inertia weight *w* is set according to the following equation:

$$w = w_{max} - \frac{w_{max} - w_{min}}{iter_{max}} \cdot iter \quad (71)$$

where $iter_{max}$ is the maximum number of iterations (generations), and *iter* is the current number of iterations.

5.6.1.PSO solution

For comparison reasons the same antenna with the same characteristics (Frequency, substrate), searching area and number of experiments under the same FF will be optimized via PSO technique.

Applying PSO some default values have to be considered such as:

- S=the population of particles (swarm) consisted of 15 particles. Each particle contains values of five parameters (*d*) the values of Dipole length, Director length, Reflector length, the Distance between the elements and the Width of the elements. That means that the search space has five dimensions and particles must 'fly' in a five dimensional space.
- K=the maximum number of particles that can be informed by a given one is set to 3.
- B=the solution space was bordered by absorbing walls, the borders allowed each parameter to vary 40% of the center values (as described in Table 30) from both sides.
- w=the inertia weight factor is varyied between 0.9 and 0.4, depending on the number of executed iterations as described in Eq. (71).
- c=the acceleration constants are set $c_1 = c_2 = 2$
- R=the random distribution of c is varyied between 0 and 1.

- T= randomly modified factor which modifies the position of the particles after each step if no improvement has been achieved

Finally the algorithm was executed for fair comparison for 27 runs with 675 iterations each. The optimization process involves the following steps:

1. Initialize a population of particles (swarm) with random positions and velocities in *d*-dimensions in the problem space.
2. Run FEKO and evaluate the desired optimization FF for each particle.
3. Using FEKO results, update the particles velocity. The velocity of the particles is changed according to the relative locations of *p*best and *q*best. It is accelerated in the directions of these locations of greatest fitness according to the Eq. (69). If there is not improvement compared to the previous *p*best and *q*best is modified randomly.
4. Move the particle. Once the velocity has been determined, it is simple to move the particle to its next location. The new coordinate is computed for each of the dimensions according the Eq. (70).
5. Jump to step two and repeat the procedure of steps 2, 3 and 4 until the maximum number of iterations (675) is reached.
6. Loop back to step 1 and repeat the steps 1 to 5 until the maximum number of runs is reached.

Fig. 90 shows the flow chart that describes graphically the above PSO optimization procedure.

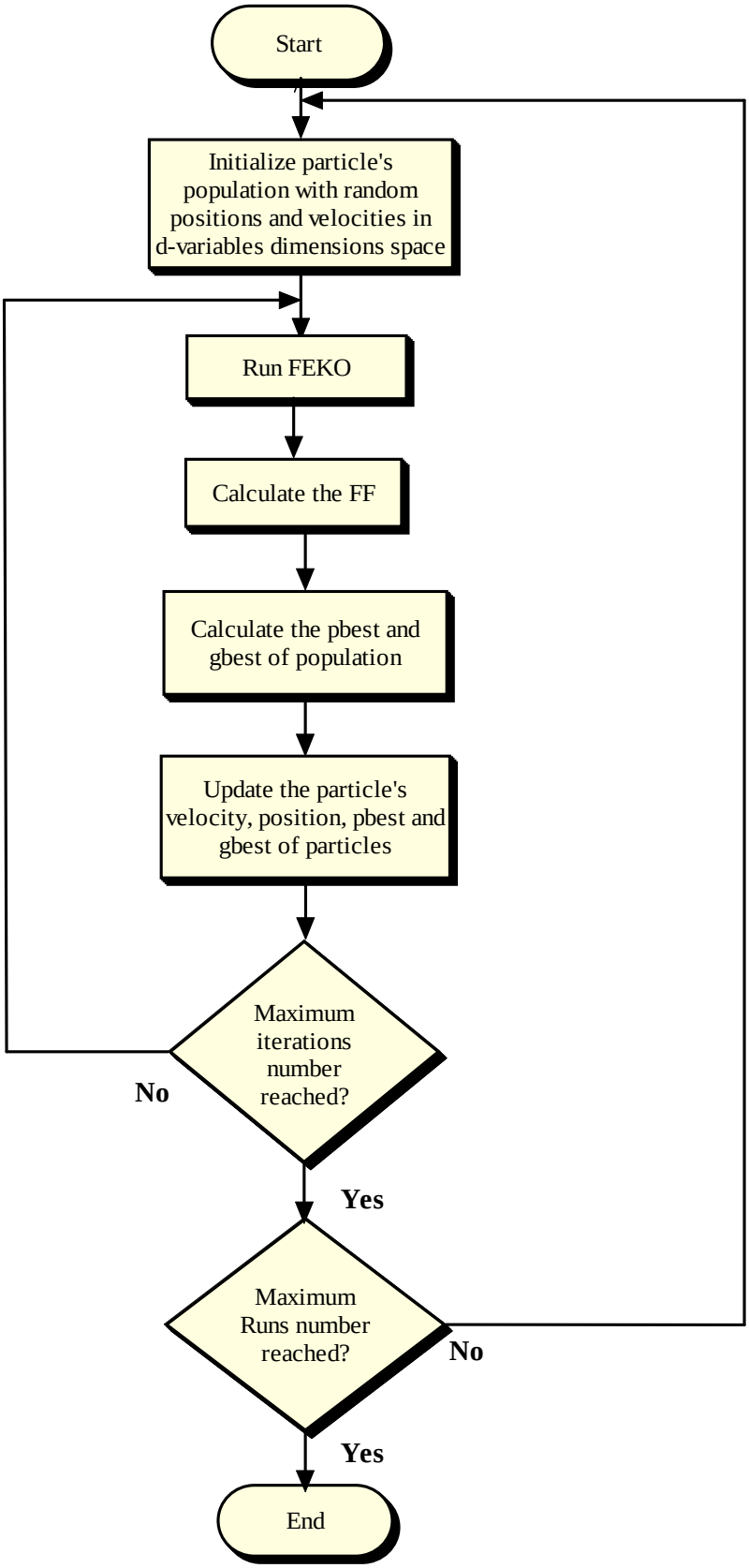

Fig. 90. The flow chart of the PSO 3 element Yagi-Uda antenna

5.7. Comparison between Grid-Taguchi and PSO

The best values of all the 27 runs (consisted of 675 iterations each) of Grid-Taguchi and PSO optimization procedures are presented in Table 36. The comparison between them shows that Grid-Taguchi's best value converge closer to the target ($FF_{(G-T)}$ = 70.168dB (3224) < $FF_{(PSO)}$=70.631dB (3600).

Table 36. Comparison between Grid taguchi and PSO results

Runs	Grid-Taguchi FF (dB)	PSO FF (dB)
1	73.994	70.681
2	70.658	71.972
3	70.747	74.508
4	70.537	71.367
5	79.492	74.488
6	71.3	71.692
7	70.537	71.648
8	71.118	72.239
9	80.527	71.539
10	71.389	72.972
11	71.117	72.271
12	74.274	71.916
13	70.168	71.834
14	70.847	73.362
15	73.568	73.406
16	72.6	73.291
17	74.09	70.883
18	72.079	73.975
19	70.426	72.206
20	70.653	71.784
21	73.805	72.019
22	73.987	73.132
23	70.22	72.189

24	70.993	74.541
25	71.669	72.433
26	72.835	71.954
27	71.383	73.35

In Fig. 91 a graphical comparison between the best values which are obtained under Grid-Taguchi and PSO for the 3-elements 2.4GHz Yagi-Uda antenna is shown. It can be concluded that a systematic search (Grid- Taguchi) can have better results than a random one (PSO) in a wide area, when multiple targets are considered simultaneously.

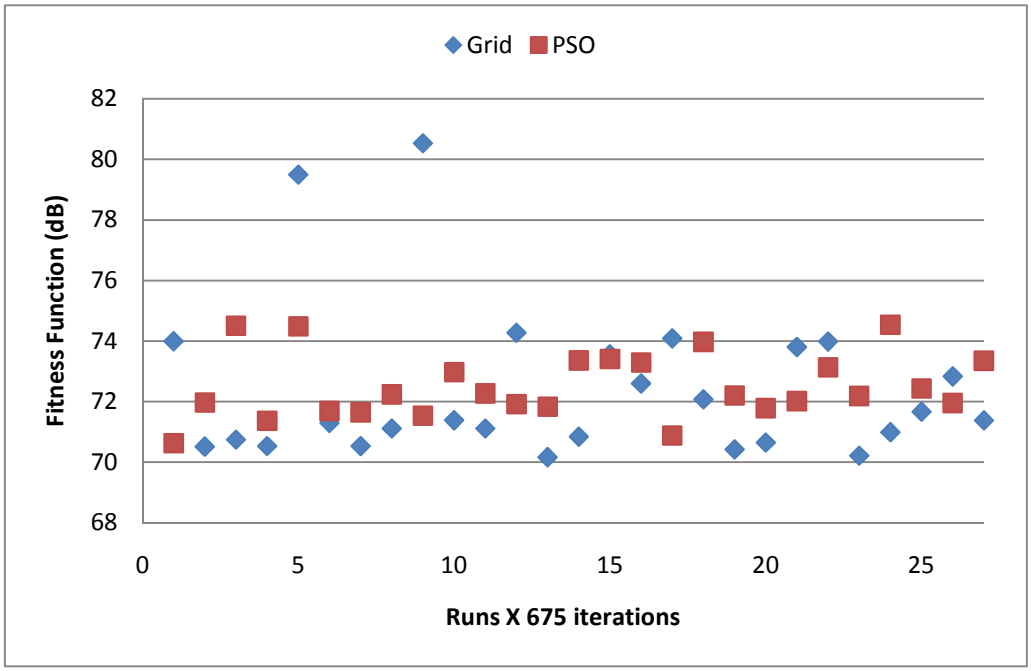

Fig. 91. Comparison between Grid-Taguchi and PSO optimization techniques

The best values of the optimized parameters under Grid-Taguchi technique for the 2.4GHz 3-element Yagi-Uda antenna as well as the simulated results are shown in Table 37.

Table 37. Results of the 2.4GHz Yagi-Uda antenna (Grid-Taguchi optimization)

Dipole	49.264mm	S11	-30.28dB
Director	40.734mm	Forward Gain	6.5dB
Reflector	53.748mm	Back Gain	-8dB
Distance between elements	28.065mm	F/B ratio	14.5dB
Width of the elements	1.818mm		

5.8. Taguchi optimization solution for 2.7GHz

After the above optimization process for the main dimensions of the Yagi-Uda antenna, the next step is to make this specific antenna frequency reconfigurable. For this reason, two of the previous optimized parameters remain stable (distance between the elements and width) and the lengths of the elements must be determined.

Based on the previously optimized values and using frequency scaling, the initial central values of the elements for the frequency of 2.7GHz are calculated. The initial levels of the master OA are assigned within ±20% deviation around the central parameter values as shown in Table 38. It has to be noticed that this process is necessary as the other two parameters of the antenna have not been scaled.

Furthermore after the end of the optimization process an evaluation of the results has to take place in order to ensure that the reconfigurable antenna is realizable. For example the gap for the switches is set to 1mm and the minimum length of every part of the reconfigurable antenna could not be smaller than 2mm.

Table 38. OA levels (Central±20%)

	1st	2nd	3rd
Dipole	35.1mm	43.8mm	52.5mm
Director	29mm	36.2mm	43.4mm
Reflector	38.1mm	47.7mm	57.2mm

For an OA with 3 parameters of 3 levels, for each parameter a configuration with at least $n_{rows} = 1 + (k \cdot DOF_m) = 1 + (3 \cdot 2) = 6rows$ is needed. Taguchi suggests the $OA_9(3^4)$ that can handle up to 4 parameters with 3 levels each in an array of 9

rows. For this case 3 columns of the $OA_9(3^4)$ have been chosen to assign the three parameters in their 3 levels, thus an $OA_9(3^3)$ has been created, as shown in Table 39.

Table 39. $OA_9(3^3)$

n rows	A	B	C
1	1	1	1
2	1	2	2
3	1	3	3
4	2	1	2
5	2	2	3
6	2	3	1
7	3	1	3
8	3	2	1
9	3	3	2

The optimization procedure graph shown in Fig. 92 presents the curves of mean and optimum values of FF for the 3-elements 2.7GHz Yagi-Uda antenna, as they converged through Taguchi process after 25X9=225 experiments.

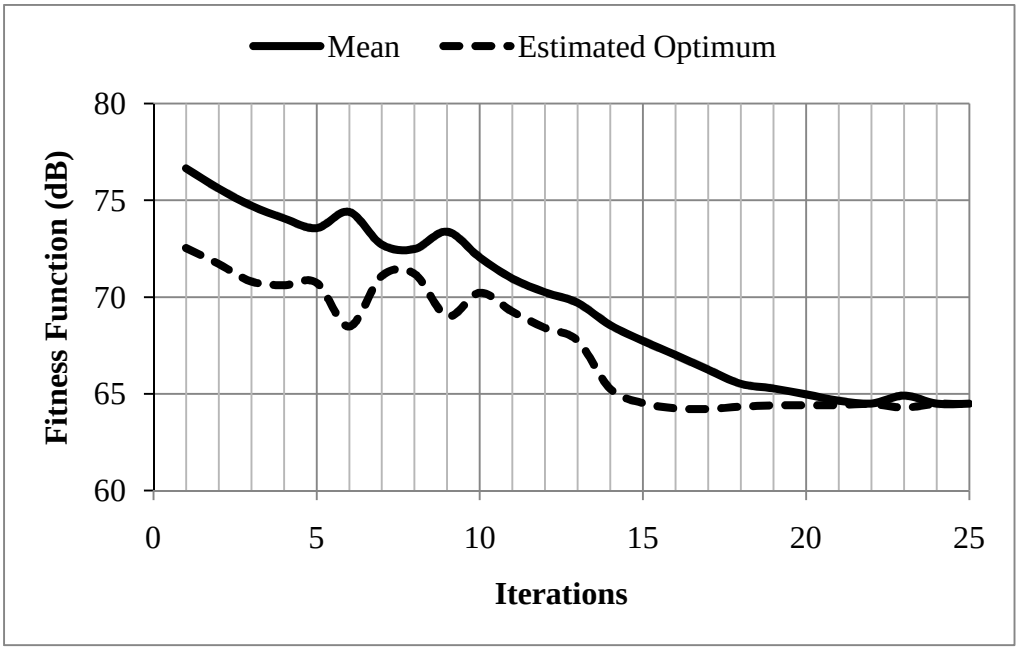

Fig. 92. The optimization process for the 2.7Ghz antenna

Table 40 presents the dimensions of the optimized parameters under Taguchi's technique for the 2.7GHz Yagi-Uda antenna as well as the simulated results.

Table 40. Results of the 2.7GHz Yagi-Uda antenna (Taguchi optimization)

Dipole	42.994mm	S11	-31dB
Director	34.916mm	Forward Gain	6.3dB
Reflector	46.724mm	Back Gain	-6.37dB
Distance between elements	28.065mm	F/B ratio	12.67dB
Width of the elements	1.818mm		

5.9. Pattern and frequency reconfigurable Yagi-Uda antenna implementation

Pattern reconfigurability of the Yagi-Uda antenna can be achieved in two directions by varying the length of the two external elements, using switches and alternating their operation between Director and Reflector as shown in Fig. 93(a). The Frequency reconfigurability from 2.4GHz to 2.7GHz of the Yagi-Uda antenna can be achieved subtracting pieces out of all elements using switches as shown in Fig.93(b).

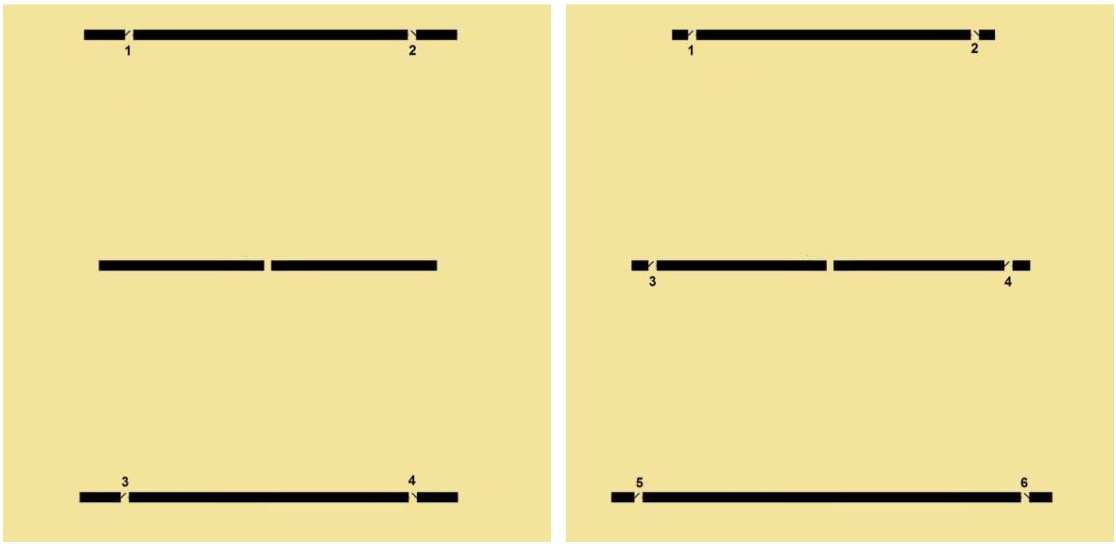

(a) (b)

Fig. 93. Pattern and Frequency 3 elements Yagi-Uda antenna configurations

Finally, a combination of the two above configurations using the optimum values of the parameters, which have been adapted and optimized through Grid-Taguchi technique to give a Frequency (2.4GHz and 2.7GHz) and Pattern (4 discrete directions) reconfigurable 3-elements Yagi-Uda antenna, as presented in Fig. 94.

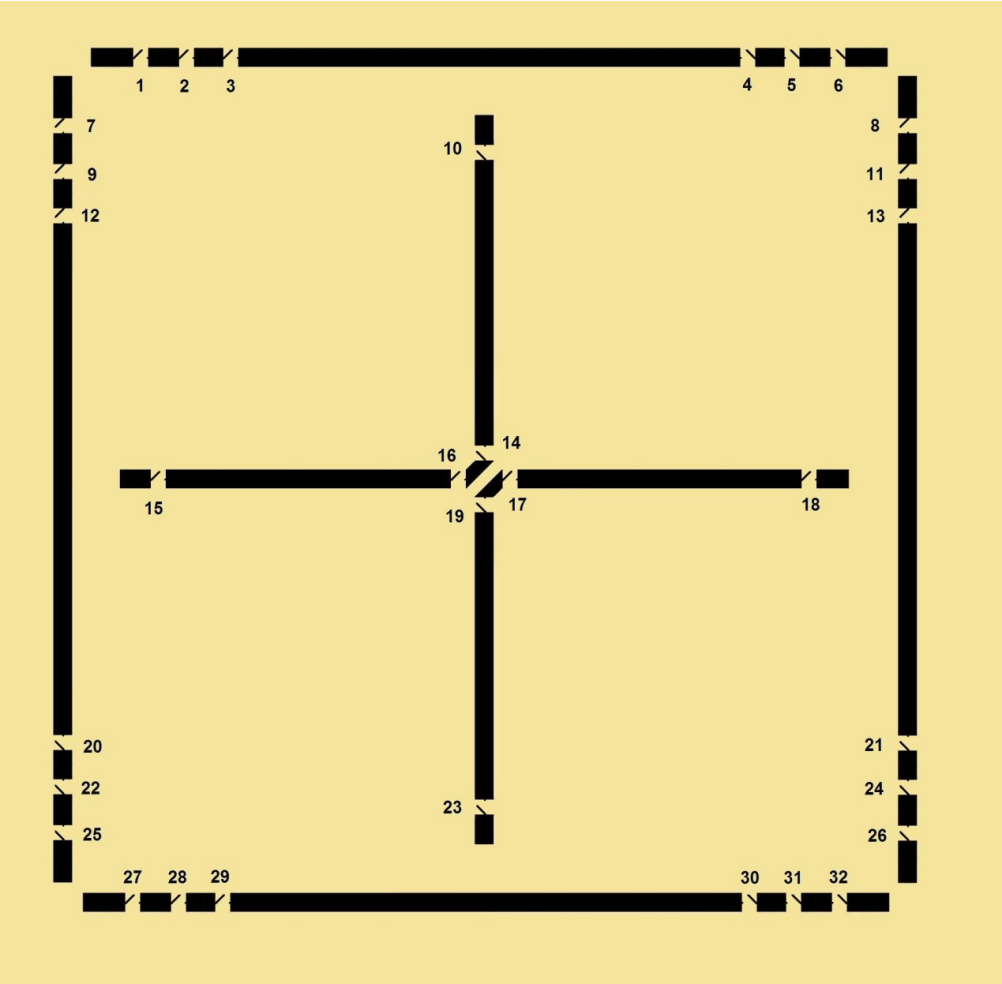

Fig. 94. The frequency and pattern reconfigurable 3 elements Yagi-Uda antenna

This configuration is comprised of 8 discrete antennas and the transition from one to the other is realized via RF-MEMS switches. Table 41 presents the state of the 32 switches for each one of the eight different modes of the antenna operations

Table 41. The state of the switches for the eight different antenna configurations

a/a	**2.4GHz North**	**2.4GHz East**	**2.4GHz South**	**2.4GHz West**	**2.7GHz North**	**2.7GHz East**	**2.7GHz South**	**2.7GHz West**
1	OFF	OFF	ON	OFF	OFF	OFF	OFF	OFF

2	OFF	OFF	ON	OFF	OFF	OFF	ON	OFF
3	ON	OFF	ON	OFF	OFF	OFF	ON	OFF
4	ON	OFF	ON	OFF	OFF	OFF	ON	OFF
5	OFF	OFF	ON	OFF	OFF	OFF	ON	OFF
6	OFF	OFF	ON	OFF	OFF	OFF	OFF	OFF
7	OFF	ON	OFF	OFF	OFF	OFF	OFF	OFF
8	OFF	OFF	OFF	ON	OFF	OFF	OFF	OFF
9	OFF	ON	OFF	OFF	OFF	ON	OFF	OFF
10	OFF	ON	OFF	ON	OFF	OFF	OFF	OFF
11	OFF	OFF	OFF	ON	OFF	OFF	OFF	ON
12	OFF	ON	OFF	ON	OFF	ON	OFF	OFF
13	OFF	ON	OFF	ON	OFF	OFF	OFF	ON
14	OFF	ON	OFF	ON	OFF	ON	OFF	ON
15	ON	OFF	ON	OFF	OFF	OFF	OFF	OFF
16	ON	OFF	ON	OFF	ON	OFF	ON	OFF
17	ON	OFF	ON	OFF	ON	OFF	ON	OFF
18	ON	OFF	ON	OFF	OFF	OFF	OFF	OFF
19	OFF	ON	OFF	ON	OFF	ON	OFF	ON
20	OFF	ON	OFF	ON	OFF	ON	OFF	OFF
21	OFF	ON	OFF	ON	OFF	OFF	OFF	ON
22	OFF	ON	OFF	OFF	OFF	ON	OFF	OFF
23	OFF	ON	OFF	ON	OFF	OFF	OFF	OFF
24	OFF	OFF	OFF	ON	OFF	OFF	OFF	ON
25	OFF	ON	OFF	OFF	OFF	OFF	OFF	OFF
26	OFF	OFF	OFF	ON	OFF	OFF	OFF	OFF
27	ON	OFF	OFF	OFF	OFF	OFF	OFF	OFF
28	ON	OFF	OFF	OFF	ON	OFF	OFF	OFF
29	ON	OFF	ON	OFF	ON	OFF	OFF	OFF
30	ON	OFF	ON	OFF	ON	OFF	OFF	OFF
31	ON	OFF	OFF	OFF	ON	OFF	OFF	OFF
32	ON	OFF	OFF	OFF	OFF	OFF	OFF	OFF

The shape, the mesh and the current distribution of a) the 2.4GHz and b) the 2.7GHz printed reconfigurable Yagi-Uda antenna, are shown in Fig. 95 a & b

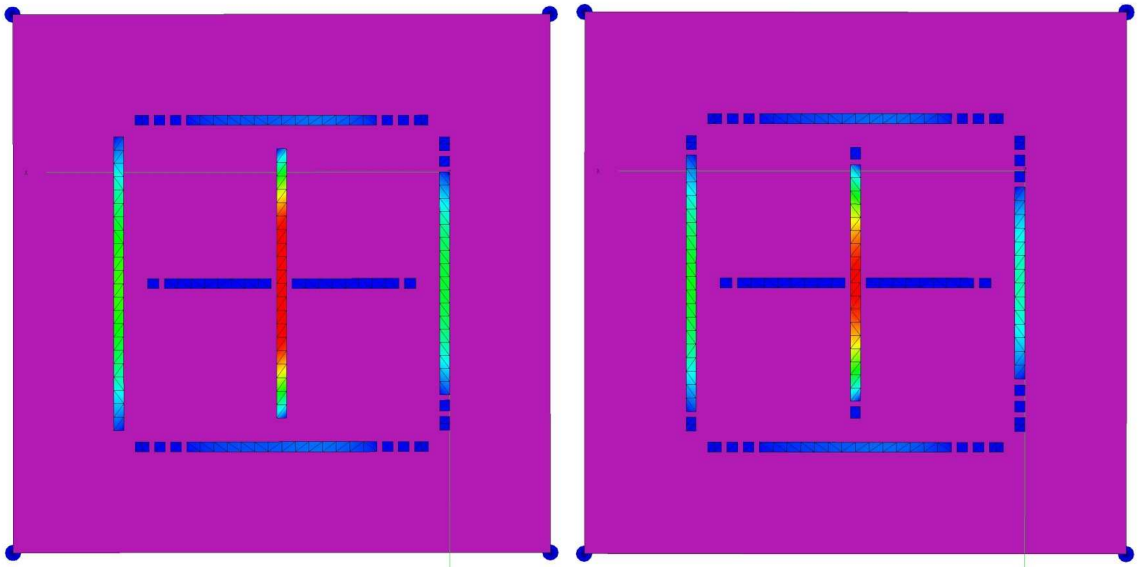

a) b)

Fig. 95. The current distribution at a) 2.4GHz and b) 2.7GHz

The co-polarization and cross-polarization E-plane and H-plane patterns of the reconfigurable multi antenna, in one direction for 2.4 and 2.7GHz, are shown in Fig. 96 (a) & (b). The simulated front-to-back ratio is as good as 12.67dB for the 2.4GHz and 10.8dB for the 2.7GHz antenna, which is in an acceptable level for a 3-element Yagi-Uda antenna with only one director. The cross-polarization of the antenna is more than 8dB below the co-polarization at the endfire direction for both frequencies. The simulated gain of the antenna is 6.4dB and 6.2dB for the 2.4 and 2.7GHz, respectively.

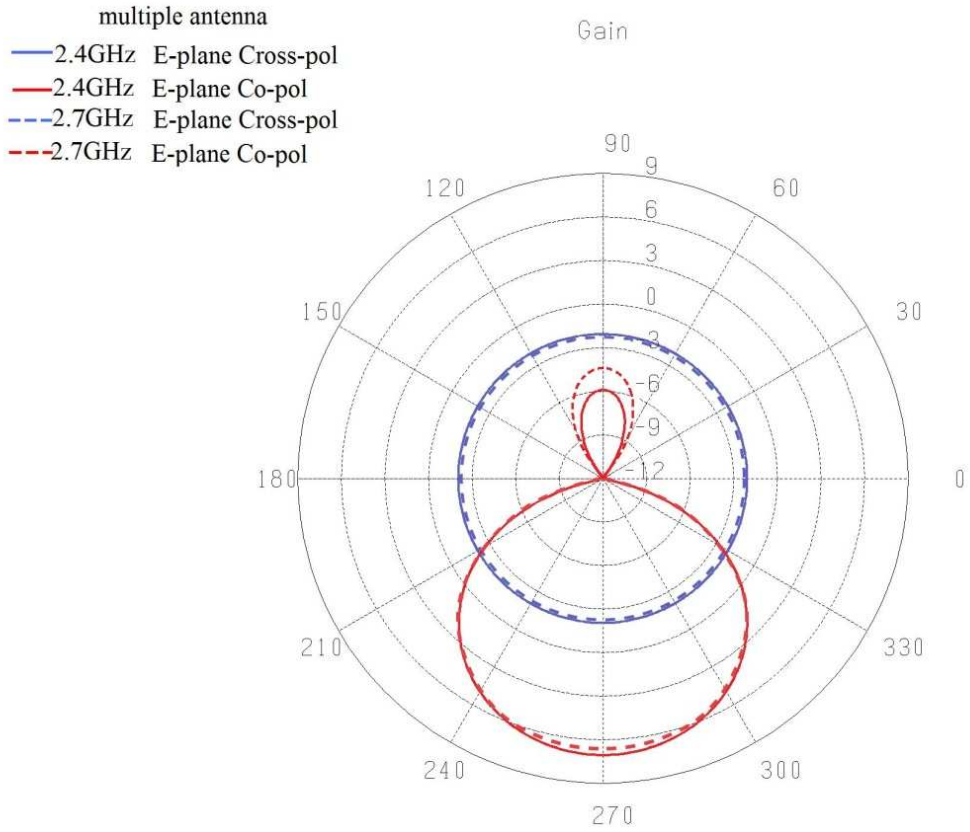

(a)

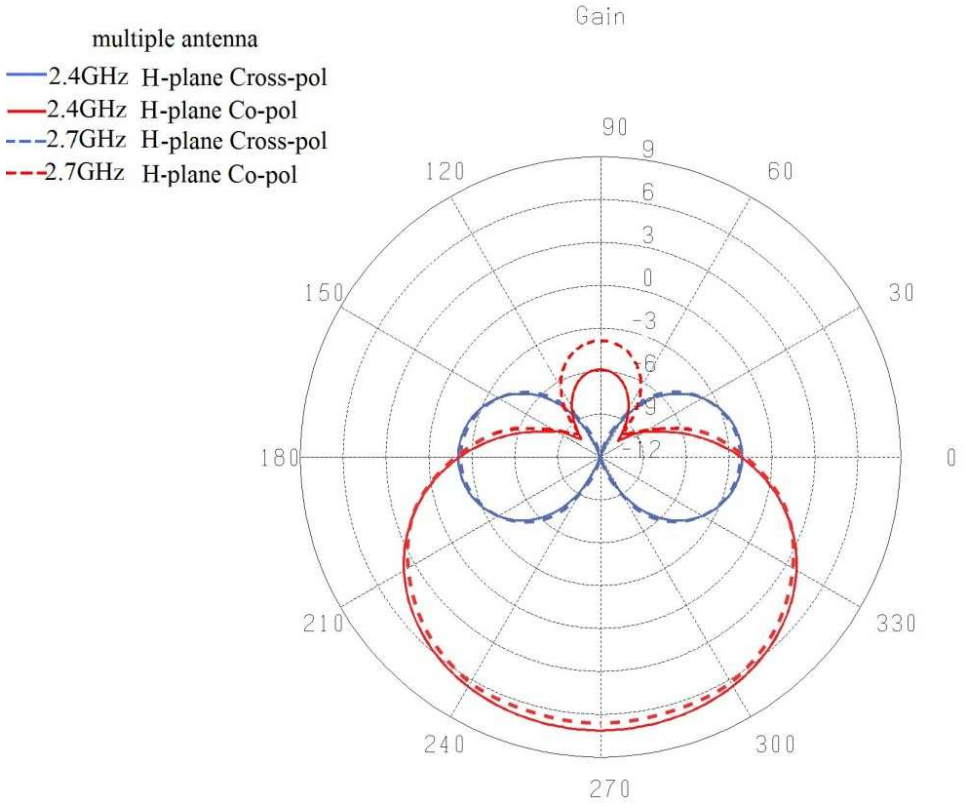

(b)

Fig. 96. Co-pol. and Cross-pol. E-plane and H-plane patterns for 2.4 and 2.7GHz

In order to investigate the effect of the rest of the elements that consist the multi-reconfigurable antenna as well as for comparison reasons, the co-polarization and cross-polarization E-plane and H-plane patterns of the single antenna at 2.4 and 2.7GHz are illustrated in Fig. 97 (a) & (b). The main difference observed, compared to the multi antenna configuration, is in the front-to-back ratio, which is around 14.5dB for 2.4GHz and 12.5dB for 2.7GHz antenna. The effect of the other elements is a degradation of about 1.5dB from the back gain and about 0.2 dB from the front gain of the antenna.

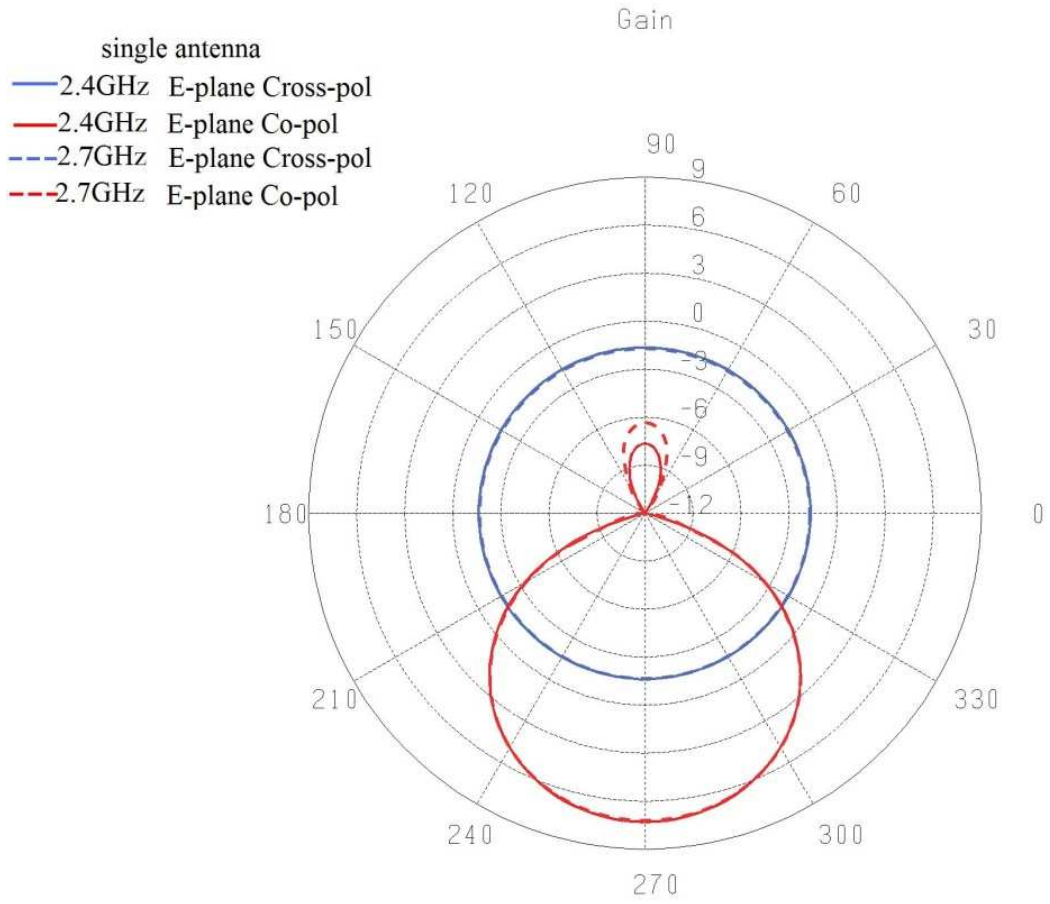

(a)

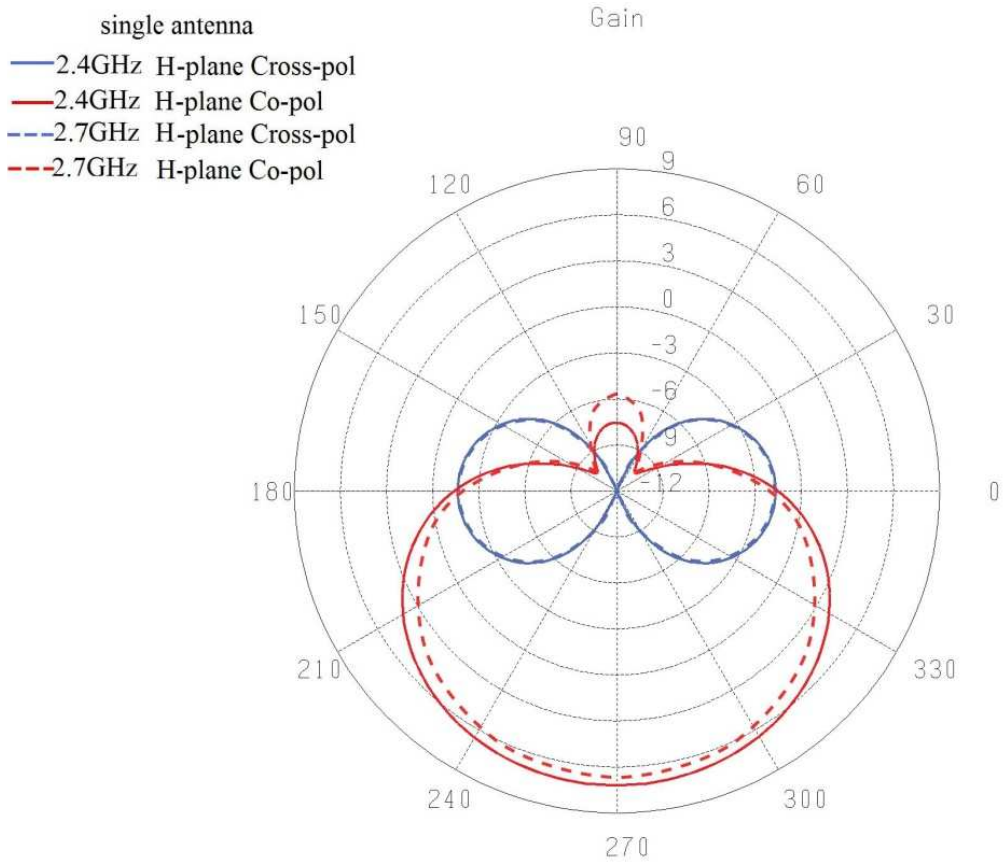

(b)

Fig. 97. Co-pol. and Cross-pol. E-plane and H-plane patterns for 2.4 and 2.7GHz for the multi antenna configuration

The reconfigurability of the multi Yagi-Uda antenna, as concerns to the E-plane Co-polarization patterns, in four discrete directions, is illustrated in Fig. 98

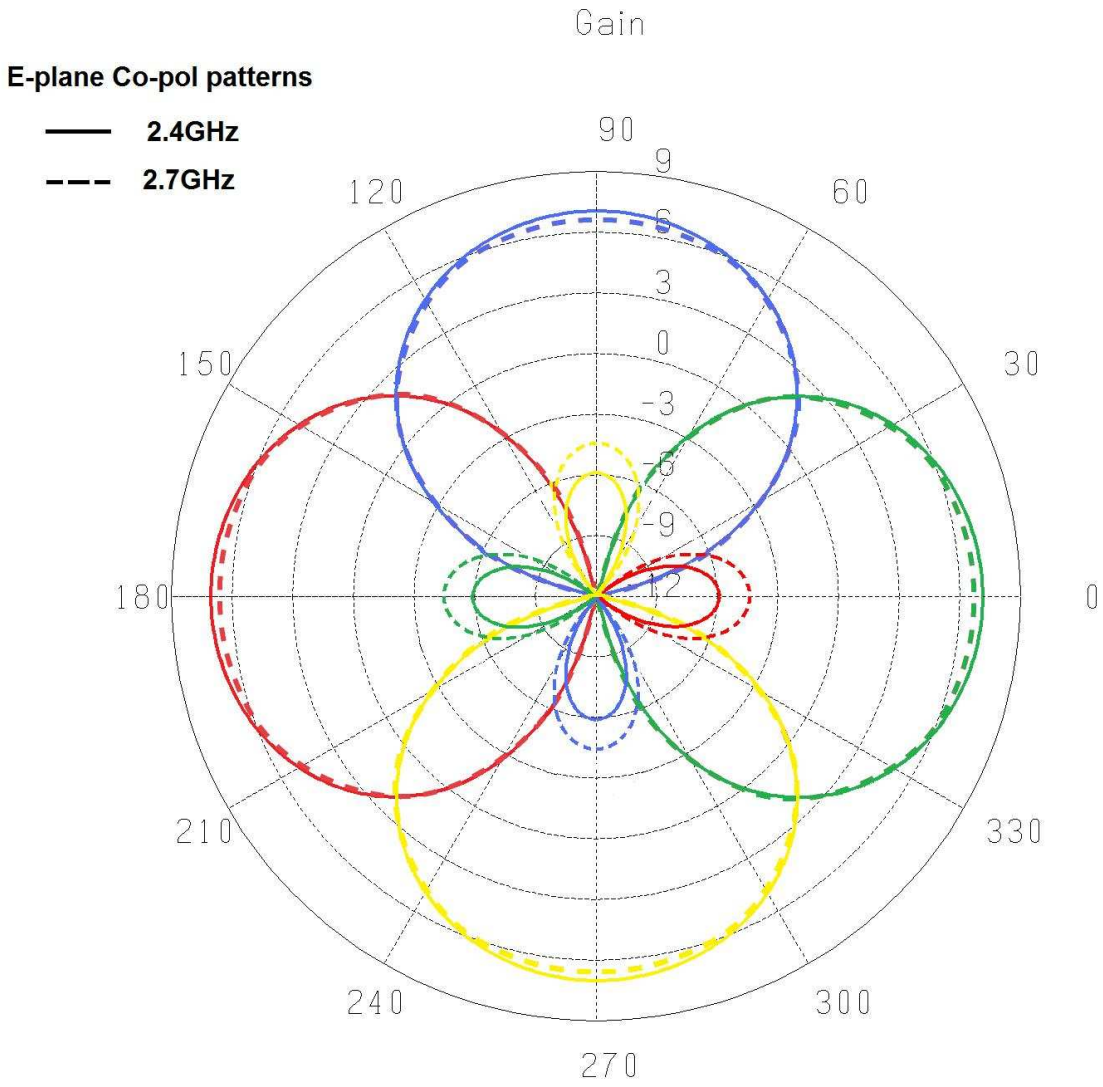

Fig. 98. Pattern reconfigurability of the multi Yagi-Uda antenna

Fig. 99 shows the simulated Return Loss results for the multi and for the single Yagi-Uda antennas. For the multi antenna the S11 value is around 27dB with a 10dB impedance BW around 230MHz at 2.4GHz and 40dB with 280 MHz BW at 2.7GHz respectively. For the single Yagi-Uda antenna configuration the S11 values are 30.3dB with 240MHz BW at 2.4GHz and 31dB with 300MHz BW at 2.7GHz.

The comparison between them indicates small differences as the values are maintained in acceptable levels for the multi antenna. A small insignificant shift of the resonance frequencies of the multi antenna is observed, too.

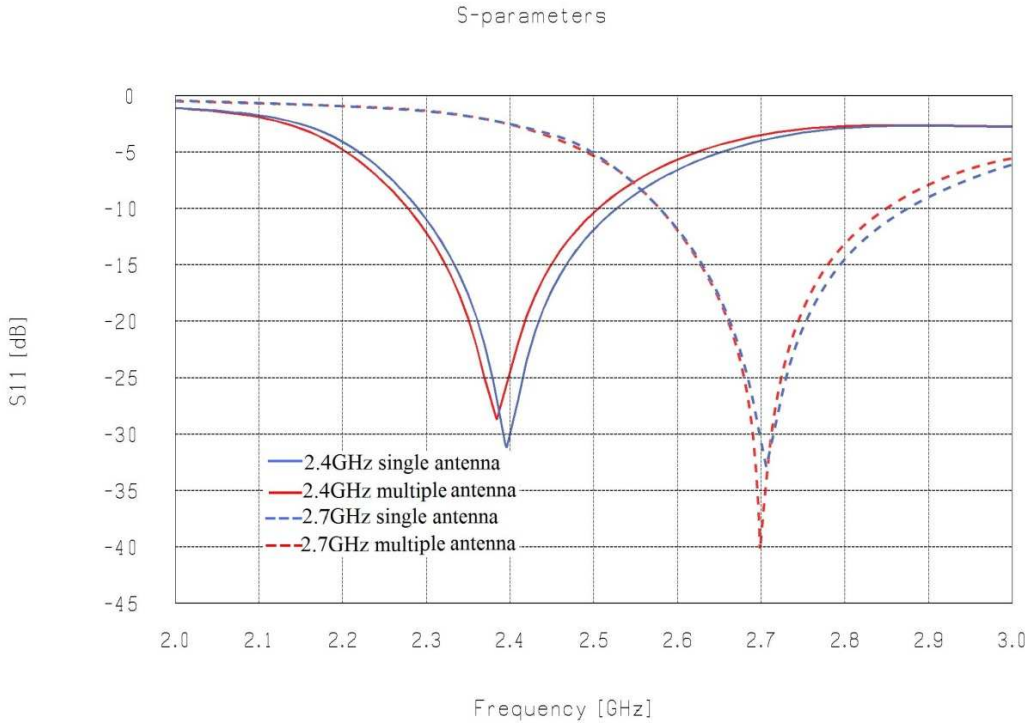

Fig. 99. S11 graphs for multi and single Yagi-Uda antenna at 2.4 and 2.7Ghz

The simulated total Gain graphs for the multi and single Yagi-Uda antennas, in the frequency range between 2 and 3GHz are illustrated in Fig 100. The results show a small degradation around 0.2dB for the multi antenna but they are still over 6dB for all the effective BW area at 2.4 and 2.7GHz.

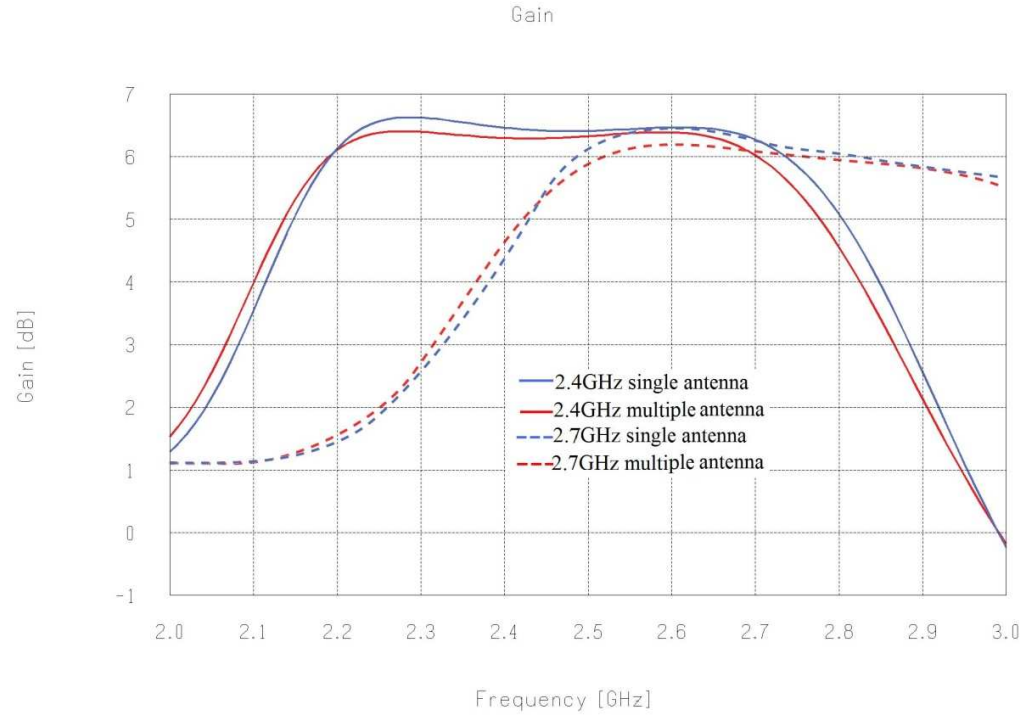

Fig. 100. Gain graphs for multi and single Yagi-Uda antenna at 2.4 and 2.7GHz

Finally the simulation results of the multi reconfigurable antenna as well as the results of the single antennas are illustrated in Table 42.

Table 42. Comparison between the single and multi reconfigurable antenna results

	Single antenna		**Multi antenna**	
	2.4GHz	**2.7GHz**	**2.4GHz**	**2.7GHz**
S11	-30.3dB	-31dB	-27.8dB	-40dB
Gain (F)	6.5dB	6.3dB	6.4dB	6.2dB
Gain (B)	-8dB	-6.4dB	-6dB	4.5dB
F/B ratio	14.5dB	12.7dB	12.4dB	10.7dB
BW(-10dB)	240MHz	300MHz	230MHz	280MHz

5.10.Summary

This chapter presented the benefits of the use of RF-MEMS switches in complex reconfigurable antennas when large quantities of such switches are required.

A novel Pattern (four discrete directions) and Frequency (2.4GHZ and 2.7GHz) reconfigurable printed 3-elements Yagi-Uda antenna implementation, which requires 32 switches, has been considered for this purpose. The specifications for this antenna involved good matching and gain, as well as, high F/B ratio in all directions and frequencies. As this antenna design was very complicated to be designed using numerical means alone, an optimizer was necessary to fulfill all the specifications.

Following that, a novel Grid-Taguchi technique which is an evolution of the Taguchi statistical optimization method has been presented. This technique presents a wider searching area for the parameters, solving the main disadvantage of the Taguchi method against the stochastic optimization methods like PSO. Additionally, the Grid-Taguchi method, searches more systematically and more efficiently in all the search area making use of the exceptional properties of the OA. On the other hand PSO uses random initialization of the parameters within the searching area for each generation.

Utilizing this method, complicated optimization goals such as matching, high Gain, and high F/B ratio have been accomplished and verified through simulations (FEKO®). Besides, in order to validate the new method, the antenna has been optimized under normal Taguchi optimization with 3 and 5 levels, as well as, under

PSO using the same conditions. The optimization procedure confirmed that Grid-Taguchi is capable of achieving better results compared to normal Taguchi and PSO under the same conditions. Finally, using the optimized parameter values, the 8-mode Pattern and Frequency reconfigurable antenna has been designed and simulated achieving exceptional results.

6. Chapter 7: Conclusions and Future work

6.1. Overview

In the demanding world of modern telecommunication systems reconfigurable antennas play a vital role. Pattern and frequency reconfigurable antennas are very complex electromagnetic structures and their radiation properties depend on the relationship between their structure i.e. length characteristics, and the radiation frequency. Thus, in order to increase flexibility and broaden the antenna application areas, RF switches are used allowing them to reconfigure their structure and dimensions.

RF MEMS switches are the most elegant solution for reconfigurable antennas. They offer superior RF characteristics (isolation and insertion loss) hence they can be integrated in large numbers within the antenna structure. Additionally, they can be controlled using high resistance bias lines, which imply that the bias network of RF MEMS switches can be extensive in large antenna arrays without interfering and degrading the antenna radiation patterns. The bias network also consumes almost no power and this is important for large antenna arrays especially for mobile or satellite implementations. Their small size and their ability to get integrated monolithically with the antennas elements on high efficiency microwave laminates, such as glass or Teflon, make the RF-MEMS switches the only solution for mm-wave reconfigurable antennas structures.

On the other hand RF-MEMS switches suffer from reliability problems. The performance and reliability of ohmic RF MEMS switches are directly related to the switch contact interface. The combination of a number of physical phenomena, such as plastic deformation, creep, joule heating, nanowire formation, arcing, and adsorbed films at the contact surface create a convoluted set of failure mechanisms, which results in contact degradation over time and permanent stiction. These phenomena are mainly caused by the existence of contaminant layers, the high impact velocity and the overheating of the contact areas

One of the most important sources of field failures for ohmic RF-MEMS switches is caused by increases in contact resistance due to contamination of the switch contacts. This is due to inappropriate packaging and it is one of the issues that has already been solved.

The high impact force during the first touch, is an outcome of the non-linear electrostatic effect which results in the collapse of the cantilever after moving 1/3 of the distance between the contacts. Lower impact force and less bouncing will reduce changes in surface topography and lessen adhesion failures in high cycle applications. This phenomenon has partially been overcome via tailored actuation pulses but there is plenty of room for amelioration since it is responsible for plastic deformation, creep and wear problems.

The last main reason for switch failure is the overheating, which is caused by excessive amount of current through very small areas. This causes micro-welding, nanowire formation and arcing phenomena and finally permanent stiction. Although significant progress has also been made in this field, a different approach can solve some problems specifically when relatively higher currents are used, as in the case of reconfigurable antennas.

In order to provide a reliable solution for the above-mentioned drawbacks of RF-MEMS switches, a novel, “Hammerhead” cantilever shape, ohmic RF-MEMS switch design has been presented in chapter 3. The main characteristics of the “Hammerhead” switch are:

- Simplicity, as it is a very simple all metal (Au) design
- Power handling, as it has relatively large contact areas capable of handling higher currents avoiding temperature rise hence minimizing linearity problems
- High restoring force, due to the S-shape deformation of the cantilever, which is capable of overcoming adhesion problems.
- Relatively low actuating operation voltage of $V_s = 60V$
- High dynamic actuating range as the pull-down voltage is $V_{pd} = 27V$
- Controllability due to the specific hammerhead shape cantilever
- Moderate switching time (15μS for the pull down phase and 18μS for the release phase) but high enough in order to apply tailored control pulse.
- Superior electromagnetic characteristics (at 5GHz the switch presents Isolation -28dB & Insertion loss -0.019dB).

Additionally, a thorough comparison between “Hammerhead” and other cantilever type ohmic RF-MEMS switches configurations such as the simple “Uniform switch” and the well known North Eastern University switch “NEU” has been undertaken.

The most significant failure mechanism of the ohmic RF-MEMS switches under high-cycle lifetime applications is the impact force and bouncing of the cantilever on the contact area. This phenomenon is related to the electrostatic control of the switch under step pulse actuation and is partially faced with tailored pulse control implementation.

A novel optimization procedure based on Taguchi’s statistical technique has been presented to improve the tailored pulse control. The new technique allows exact calculation of the time intervals and voltage magnitudes of the actuation pulse train. Testing this novel technique in “Hammerhead” switch, superior switching characteristics has been achieved. Nevertheless, all the above-mentioned improved results are valid only in the absence of any manufacturing tolerances.

Following that, an improvement of the existing method of resistive damping (charge control) has been presented, allowing the exact calculation of the Bias resistor in order to reduce the impact force during the pull-down phase, as well as, bouncing during the release phase. This technique has been tested on “Hammerhead” switch with partially good results since it is capable of improving the switching characteristics only during the pull-down phase. As concerns to the release phase, this control method has almost no effect due to the discrepancy between the order of the rise time of the actuation pulse and the period of the mechanical resonance frequency through which, the appropriate value of the Bias resistor for each switching phase is calculated. Evaluating the “NEU” switch making use of resistive damping, very good results have been extracted. This type of switch is very stiff and presents very low switching time and high mechanical resonance frequency. These features allow the implementation of a Bias resistor capable of improving switching characteristics in both phases. It has to be mentioned that for this type of stiff switches, resistive damping control is the only solution as practically there is not enough time for tailored pulse implementation.

Finally, a novel technique, the Hybrid control mode, has been presented. This new open loop technique is based on the combination of the two previously mentioned methods (Taguchi’s optimized tailored pulse and resistive damping). Testing the “Hammerhead” switch under this technique, true ‘soft landing’ with very low impact

force and elimination of any bouncing phenomena during the pull-down phase has been achieved. Meanwhile, minimization of the bouncing during the release phase has been achieved as well, keeping the ON-OFF switching time comparable to those of the step actuation pulse. Moreover the most important achievement of the Hybrid control mode is its capability to offer immunity to manufacturing and operation uncertainties of the switch, allowing it to be incorporated in large numbers within reconfigurable antenna implementations.

Innovative antenna designs, such as those using multifunction, reconfigurable antennas and antenna arrays, to perform complex and demanding system functions remain a challenge. Computational electromagnetics using advanced computing capabilities will model complex electromagnetic wave interactions, in both the frequency and time domains.

Taguchi's optimization technique can handle multidimensional, discontinuous and nondifferentiable objective functions with many potential local maxima whilst converges rapidly to the optimum result but within a well defined area. In order to solve this drawback and make it capable of searching over a wider parameter area, a novel technique has been presented in chapter 5. This new technique is based on Taguchi's optimization method named "Grid-Taguchi" and uses the exceptional properties of the Orthogonal Arrays in order to search more systematically and efficiently over large areas.

In order to validate the "Grid-Taguchi" optimization technique a complex task, involving a pattern and frequency 3 elements printed Yagi-Uda antenna, has been considered.

For comparison reasons the characteristics of the same antenna has been investigated using three methods, the normal Taguchi's method, a variation of Taguchi's method with 5 levels per parameter with double searching area and the well established stochastic optimization technique (PSO).

The results showed that "Grid-Taguchi" method excels among all the aforementioned techniques, presenting exceptional results and could become a standard for complex electromagnetic optimization issues.

6.2. Future work

The simplicity and the material choice of the “Hammerhead” RF-MEMS switch ensures high fabrication yield. Furthermore, the “Hybrid” actuation mode control is capable of providing the best switching conditions and immunity to fabrication tolerances. Additionally, Grid –Taguchi optimization technique, is capable of fulfilling all the demanding specifications of a reconfigurable antenna design.

The next step in order to continue this research would be to monolithically integrate the “Hammerhead” RF-MEMS switches within the antenna elements.

The design of a reconfigurable antenna using RF-MEMS switches could be implemented either based on the hybrid mode, that is using individual RF-MEMS switches which should be bonded into the PCB, or the integrated mode, in which each switch is fabricated on the same substrate with the antenna patches in a single manufacturing process.

With current technology it is possible to fabricate such an antenna using the hybrid method. Nevertheless, that could result in several drawbacks regarding cost and compatibility, especially when designing topologies with significant number of switches. In general, the cost of a single RF MEMS switch is very low, as it is similar to VLSI design and batch processing methodology and tools. Nevertheless, the cost gets increased dramatically due to the devise-level hermetic packaging. In addition to that, there are real estate problems due to the relatively great size of the packaging and the large number of the switches which have to be used for the complete antenna configuration.

Another important drawback of the hybrid mode is the impedance mismatching, during the packaging and assembling processes. RF MEMS switches require wire bonding in the package introducing impedance mismatch, consequently signal loss. Besides, further signal loss is introduced during the assembling, between the package and the board. Last but not least, additional signal loss is introduced due to the incompatibility between the substrates of the RF MEMS switch (usually high permittivity materials such as Si and GaAs) and the microstrip’s antenna element (usually microwave laminate PCB) due to the difference in the electrical properties of their materials. Hence, to maintain an overall good performance in hybrid mode design it is vital to use extra adapting circuitry to reduce the undesirable RF signal reflection.

In monolithic mode, the RF MEMS switches are built on the PCB substrate, under the same process with the antenna patches. Using the integrated mode reduces cost as far as the fabrication is concerned since the fabrication process needs only one packaging procedure for the entire application. Real estate problems are less as well due to the small size of the RF-MEMS switches without the packaging cells and matching as the switches are parts of the microstrip antenna structure [24], [39], [152].
Moreover, the reconfigurable antenna integration can be completed by making use of a programmable ASIC module which will further contribute towards the design of smart antenna systems as well as improving device efficiency and longevity.

- By controlling the state of the switches in order to achieve the desired antenna configuration.
- By calibrating regularly the control pulses of each switch individually, using blind tracing techniques to detect the real dimensions of each switch, which may diverge from the nominal values due to manufacturing tolerances or aging.

Finally, further research is required as regards the release time control of fast switches, like the NEU switch. Resistive damping can shrink the problem although there is plenty of room for more amelioration.

References

1. **White, f.,** *Microwave Semiconductor Engineering,* East Orleans, Massachusetts, White Publications, Inc, 1995.

2. **Wegner, J.,** *Select a Mechanical Relay or Switch*, Microwaves & RF, May, 1998.

3.**National Instruments,** *Understanding Key RF Switch Specifications,* www.ni.com.

4. **Varadan, V., Vinoy, J., and Jose, K.,** *RF-MEMS switches and micro relays,* RF-MEMS and Their Applications, John Wiley & Sons, 2003.

5. **Rebeiz, Gabriel M. and Tan, Guan-Leng,** *Introduction: RF-MEMS for Microwave Applications,* Gabriel M. Rebeiz. *RF MEMS: Theory, Design and Technology,* John Wiley & Sons, 2003.

6. **Losee, F.,** *RF Systems, Components and Circuits Handbook,* Boston, Massachusetts, Artech House, 1997.

7. **Mckillop, John,** *RF-MEMS Ready for Prime Time,* Microwave Journal, February 2007, Vol. 50, No 2.

8. **Microsemi-Watertown,** *The PIN Diode Circuit Designers' Handbook,* Microsemi Corporation, 1998.

9. **Doherty Bill,** *PIN Diode Fundamentals,* Microsemi Watertown, Micronote, Application note, Series 701.

10. **Gopinath, A. and Rankin, J.** *GaAs FET RF Switches*, IEEE Transactions on Electronic Devices, July 1985, Vol. 32, pp. 1272-1278.

11. **Skyworks,** *GaAs FETs as control Devices,* Application Note Series, [APN2015]

12. **Yao, J Jason,** *RF-MEMS from a device perspective,* IOP, Micromechanics Microengineering, April 2000.

13. **KEITHLEY,** *Configuring an Optimal RF/Microwave Switch System,* Application Note Series.

14. **Jin, Yalin and Nguyen, Cam,** *Ultra-Compact High-Linearity High-Power Fully Integrated DC–20-GHz 0.18-μm CMOS T/R Switch*, IEEE, Transactions on microwave theory and techniques, January 2007, Vol. 55, pp. 30-36

15. **Talwalkar, Niranjan,** *Thesis: Integrated CMOS Transmit-Receive Switch Using On-Chip Spiral Inductors,* December 2003.

16. **Tan, C. Y.,** *Programmable RF Attenuators,* Microbridge.

17. **Koul, S. and Bhat, B.,** *Microwave and Millimeter Wave Phase Shifters, Vol. II,* Norwood, MA, Artech House, 1991.

18. **RF, RFIC & Microwave Theory and Design,** *Phase Shifter Design Tutorial,* www.rfic.co.uk.

19. **De Los Santos, Hector,** *RF-MEMS Circuit Design for Wireless Communications,* Boston, Artech House, 2002.

20. **Malczewski, A., et al,** *X-Band RF-MEMS Phase Shifters for Phased Array Applications,* IEEE, Microwave and guided wave letters, 1999, Vol. 9, pp 517-519.

21. **Brown Elliott,** *RF-MEMS Switches for Reconfigurable Integrated Circuits,* IEEE, Transactions on microwave theory and techniques, NOVEMBER 1998, Vol. 46 pp. 1868-1880.

22. **SPECTRUM MICROWAVE,** *MEMS-based Amplified Switch Filter Bank,* www.SpectrumMicrowave.com.

23. **Entesari, K., et al,** *A 25–75-MHz RF-MEMS Tunable Filter,* IEEE, Transactions on microwave theory and techniques, 2007, Vol. 55, pp. 2399-2405.

24. **Cetiner, B. A., et al,** *Monolithic Integration of RF-MEMS Switches with a Diversity Antenna on PCB Substrate,* IEEE, Transactions on microwave theory and techniques, 2003, Vol. 51. Pp. 332-335.

25. **Atmel,** *AVR2021: AT86RF231 Antenna Diversity,* Application Note, Atmel.

26. **Vaha -Heikkila, Tauno and Rebeiz, Gabriel M,** *A 4–18-GHz Reconfigurable RF-MEMS Matching Network for Power Amplifier Applications,* International Journal of RF and Microwave Computer-Aided Engineering, 2004, Vol.14, pp. 356–372.

27. **Azarnaminy, Siamak Fouladi,** *Thesis: Reconfigurable Impedance Matching Networks Based on RF-Mems and CMOS-MEMS Technologies,* 2010.

28. **Bernhard, J. T.,** *Reconfigurable Antennas,* Morgan and Claypool Publishers, 2006.

29. **Anagnostou, D. E., et al,** *An X-band reconfigurable planar dipole antenna,* IEEE, MTT International Microwave and Optoelectronics Conference, 2005, pp.654-656.

30. **Peroulis, D., Sarabandi, K. and Katehi, L.,** *Design of Reconfigurable Slot Antennas,* IEEE, Transactions on antennas and propagation, 2005, Vol. 53, pp. 645-654

31. **Onat, S., Alatan, L. and Demir, S,** *Design of a Re-Configurable Dual Frequency Microstrip Antenna with Integrated RF-MEMS Switches,* IEEE antennas and propagation society symposium, EEE, 2004, Vol. 51, pp.1947-1954.

32. **Pringle, L., et al,** *A Reconfigurable Aperture Antenna Based on Switched Links Between Electrically Small Metallic Patches,* IEEE, Transactions on antennas and propagation, 2004, Vol. 52, pp. 1434-1445.

33. **Herd, J., Davidovitz, M. and Steyskal, H.,** *Reconfigurable Microstrip Antenna Array Geometry Which Utilizes Micro-Electro-Mechanical-Systems (MEMS) Switches,* U.S. Patent#6,198,438 B1.

34. **Krachodnok, P. and Wongsan, R.** *Design and Performance Improvement of Broad-Beam Microstrip Reflectarray,* Proceedings of the World Congress on Engineering 2007, London, UK, 2007, Vol. 1.

35. **Venneri, F., et al,** *Analysis and Design of Passive and Active Microstrip Reflectarrays,* International Journal of RF and Microwave Computer-Aided Engineering, 2003, Vol.13, pp.370-377.

36. **Hazen, J., et al,** *Stacked reconfigurable antennas for space-based radar applications,* In Proceedings, Antennas Applications Symposium, 2001, Vol.1, pp. 158-161.

37. **Spasos, M., et al,** *A novel design for an RF-MEMS resistive switch on PCB substrate,* In Proceedings, 2nd Stimesi Workshop on MEMS research and education: II, Berlin, Germany, November 2008.

38. **Spasos, M., et al,** *An ohmic RF-MEMS Switch for reconfigurable microstrip array antennas built on PCB,* WSEAS, CSECS'08, Tenerife December 2008, pp. 98-103.

39. **Spasos, M., et al,** *On the design of an Ohmic RF-MEMS Switch for reconfigurable microstrip antenna applications,* WSEAS, TRANSACTIONS on COMMUNICATIONS, 2009, Vol. 8, pp. 153-161.

40. **Spasos, M., et al,** *Design considerations of an all metal in line series RF-MEMS switch,* In Proceedings, 3rd STIMESI Workshop on MEMS and Microsystems Research and Training, Prague, Chech Republic, November 2009.

41. **Spasos, M., et al,** *Analysis and design of an all metal in line series ohmic RF-MEMS switch for microwave applications,* In Proceedings DTIP, Seville, Spain, May 2010, pp. 27-32.

42. **Spasos, M., et al,** *An easy to control all-metal in-line-series ohmic RF-MEMS switch*, Springer, *Journal of* Analog integrated circuits and signal processing, 2010, Vol.65, pp. 87-97.

43. www.memtronics.com.

44. **Larson, E., Hackett, H., Melendes, A., Lohr, F.,** *Micromachined microwave actuator (MIMAC) technology-a new tuning approach for microwave integrated circuits*, Microwave and Millimeter-Wave Monolithic Circuits Symposium Digest, IEEE, Boston, MA, 1991, Vol. pp 27-30.

45. **Oberhammer, J.,** *Thesis: Novel RF-MEMS switch and packaging concepts*, 2004.

46. **Rebeiz, Gabriel,** RF MEMS: Theory, Design, and Technology, John Wiley & Sons, 2003, ISBN: 0-471-20169-3.

*47***. Liu *B.***, *High-performance and Low-cost Capacitive Switches for RF Applications*, DARPA, 2007.

48. **Schönlinner B.,** *RF-MEMS at EADS: Concept, Designs, and Applications*, EADS, 2008.

49. **Rebeiz, G. and Muldavin, J.,** *RF-MEMS Switches and Switch Circuits*, IEEE Microwave Magazine, IEEE, December 2001, pp. 59-71.

50. **Tsuchiya, Osamu Tabata and Toshiyuki,** *Reliability of MEMS*, Weinheim, WILEY-VCH Verlag GmbH & Co., 2008.

51. **De Los Santos, H., Rassoulian, S. and Maciel, J.,** *MEMS for future microwave systems*, Microwave Symposium Digest, IEEE MTT-S International, 2005.

52. **Schimkat, J.**, *Contact materials for microrelays*, 11th Proceedings MEMS' 98, 1998, pp.190-194.

53. **Jensen, B. D., et al,** *Effect of nanoscale heating on electrical transport in RF-MEMS switch contacts*, Journal of Microelectromechanical System, 2005, Vol. 14, pp.435-446.

54. **Christopher, Brown,** *Thesis: Impact of Environmental Conditions on the Contact Physics of Gold Contact RF Microelectromechanical Systems (MEMS) Switches*, 2008.

55. **Phinney, S. Mubassar Ali and Leslie M.,** *Investigation of Adhesion During Operation of MEMS Cantilevers*, Reliability, Testing, and Characterization of MEMS/MOEMS II, Proceedings of SPIE, 2004, Vol. 53, pp. 215-226

.

56. **Yapu, ZHAO,** *Stiction and antistiction in MEMS and NEMS,* ACTA Mechanica Sinica (English Series) , February 2003, Vol. 19, pp. 1-10.

57. **Margomenos, A. and Katehi, B.,** *Fabrication and accelerated hermeticity testing of an on-wafer package for RF MEMS,* IEEE, Transactions on Microwave Theory and Techniques, 2004, Vol. 52, pp. 1626-1636.

58. **Touati, S., et al,** *Low actuation voltage totally free flexible RF-MEMS switch with antistiction system,* Proceedings on DTIP of MEMS and MOEMS, EDA Publishing, 9-11 April 2008.

59. **Newman, H., et al,** *Lifetime Measurements on a High-Reliability RF-MEMS Contact Switch,* Microwave and wireless component letters, IEEE, 2008, Vol. 18, pp. 100-102.

60. **Yang, Zhenyin,** *Thesis: Contact Material Optimization and Contact Physics in Metal-contact Microelectromechanical Systems (MEMS) Switches*, 2008.

61. **Machate, Malgorzata,** *Thesis: Joule heat effects on reliability of RF-MEMS switches*, 2003.

62. **Tan, S.G., et al,** *Electromechanical modeling of high power RF-MEMS switches with ohmic contact*, European Microwave Conference, 4-6 Oct., 2005, Vol. 3, pp. 1-4.

63. **Hyman, Dan,** *RF MEMS: A brief history and future trends,* MEMS investor journal, 10 Oct., 2005.

64. **Lin, H.H., et al,** *Mechanical Behavior of RF MEMS,* Proceedings of International Workshop on SiP/SoC Integration of MEMS, Tokyo, Japan, 2004.

65. **Young, W. and Budynas, R. G.** *Roark's Formulas for Stress and Strain,* McGraw Hill, 2002.

66. **Suhas K. and Sripadaraja, K,** *Mechanical Modeling Issues in Optimization of Dynamic Behavior of RF-MEMS Switches,* International Journal of Computer and Information Engineering, 2008, Vol. 2, pp.222-226.

67. **Patton, T. and Zabinski, S.,** *Fundamental studies of Au contacts in MEMS RF switches*, Tribology letters, Springer, 2005, Vol. 18, pp.215-230.

68. **Coutu R.,** *Thesis: Electrostatic radio frequency (RF) microelectromechanical systems (MEMS) switches with metal alloy electric contacts*, 2004.

69. **Coutu, R. and Kladitis, P.,** *Contact Force Models, including Electric Contact Deformation, for Electrostatically Actuated, Cantilever-Style, RF-MEMS Switches,* Proceedings of the NSTI Nanotechnology Conference, 2004, Vol. 2, pp. 219-222.

70. **Lai, Y-L and Tu, C.-H.,** *Design of cantilever-type microwave micromachined switches.* In Proceedings of Applied Electromagnetics, APACE 2003, August 2003, pp. 63-66.

71. **Hosseini, M., Zhu, G. and Peter, Y.-A.,** *A new formulation of fringing capacitance and its application to the control of parallel-plate electrostatic micro actuators*, Analog Integrated Circuits and Signal Processing. Springer, 2006, Vol. 53, pp. 119-128.

72. **Rabivov, L., Gupta, J. and Senturia, D.,** *The effect of release etch-holes on the electromechanical behavior of MEMS structures*, Proceedings of International Conference on Solid-State Sensors Actuators, June, 1997, pp. 1125-1128.

73. **Gupta, K.C., Garg, R., Bahl, I., Bhartia, P.,** *Microstrip Lines and Slot Lines*, Boston, USA, Artech House, 1996.

74. **Chow, L., et al,** *Skin-Effect Self-Heating in Air-Suspended RF-MEMS Transmission-Line Structures*, Journal of micromechanical systems, 2006, Vol. 15, pp. 1622-1631.

75. **Steeneken, P., et al,** *Dynamics and squeeze film gas damping of a capacitive RF-MEMS switch*, Journal of micromechanics and microengineering, IOP Publishing, 2004, Vol. 15, pp. 176-183.

76. **Semblat, J. F.,** *Rheological interpretation of Rayleigh damping*, Journal of Sound and Vibration, 1997, Vol. 206, pp. 741-744.

77. **Chowdhury, I. and Dasgupta, S.,** *Computation of Rayleigh Damping Coefficients for large systems*, The electronic Journal of Geotechnical Engineering, 2003, Vol. 8, pp.123-132.

78. **Coventor,** *Gas damping Coefficient to Rayleigh damping parameter conversion*, 2009.

79. **De Pasquale, G., Veijola, T., Somà, A,** *Gas Damping Effect on Thin Vibrating Gold Plates: Experiments and Modeling***,** Proceedings of DTIP 2009, pp 23-28.

80. **Coventorware,** www.coventor.com.

81. **Sumali H,** *Squeeze-film damping in the free molecular regime: model validation and measurement on a MEMS*, Journal of micromechanics and microengineering, IOP Publishing, 2007, Vol. 21, pp. 2231–2240.

82. **Stojanovic, G., Živanov, L. and Damj, M.,** *Compact Form of Expressions for Inductance Calculation of Meander Inductors*, Serbian journal of electrical engineering, November 2004, Vol. 1, pp. 57-68.

83. **Terman, F. E.**, *Radio Engineers' Handbook,* London, McGraw-Hill, 1950.

84. **Rhoads, J., Shaw, S.W. and Turner, K.L.,** *Nonlinear Dynamics and Its Applications in Micro- and Nano-Resonators.* Proceedings of DSCC 2008: ASME Dynamic Systems and Control Conference, Ann Arbor, Michigan, USA, October 2008. pp. 20-22.

85. **Fargas, M.A., Costa, C.R. και Shkel, A.M.,** *Modeling the electrostatic actuation of MEMS: State of the art 2005*: In Proceedings of IOC-DT-P-2005-18, Barcelona, Spain, 2005.

86. **Batra, R.C., Porfiri, M. και Spinello, D.,** *Review of modeling electrostatically actuated microelectromechanical systems,* Journal of Smart Material Structures, 2007, Vol. 16, pp.16-31.

87. **Chuang, W., et al,** *Review on the Modeling of Electrostatic MEMS,* Journal of Sensors, 2010, Vol. 10, pp. 6139-6151.

88. **Zhao, F., et al,** *Finite element analysis of the RF-MEMS switch.* In Proceedings of SPIE, 2008.

89. **Stewart, J. T.,** *Finite element modeling of resonant microelectromechanical structures for sensing applications, In* Proceedings of Micromachined Devices and Components, Austin, USA, October 1995, Vol. 1, pp.643-646.

90. **Swart, N. R., et al,** *AutoMM: Automatic generation of dynamic macromodels for MEMS devices,* Proceedings of IEEE MEMS Workshop, Heidelberg, Germany, January, 1998.

91. **Pamidighantam, S., et al,** *Pull-in voltage analysis of electrostatically actuated beam structures with fixed-fixed and fixed-free end conditions,* Journal of Micromechanics and Microengineering, 2002, pp. 458-464.

92. **O'Mahony, C., et al,** *Analysis of electromechanical boundary effects on the pull-in of micromachined fixed-fixed beams,* Journal of Micromechanics and Microengineering, 2003, Vol. 13, pp. 1317-1324.

93. **Lishchynska, M., et al,** *Modelling electrostatic behaviour of microcantilevers incorporating residual stress gradient and non-ideal anchors,* Journal of Micromechanics and Microengineering, 2005, Vol. 15, pp. 107-112.

94. **Hung, E.S., Yang, Y.J.and Senturia, S.D.** *Low-order models for fast dynamical simulation of MEMS microstructures. In* Proceedings of the IEEE International Conference on Solid State Sensors and Actuators, Chicago, IL, USA,16-19 June 1997. pp. 1101-1104.

95. **Clark, J.V., Zhou, N. and Pister, K.S.J.***Modified Nodal Analysis for MEMS with Multi-Energy Domains,* Computational Publications, Cambridge, MA, USA, 2000. pp. 723-726

96. **Younis, M.I., Abdel-Rahman, E.M. και Nayfeh, A.,** *A reduced-order model for electrically actuated microbeam-based MEMS,* Journal of Microelectromechanical Systems, 2003, Vol. 12. pp. 672-680

97. **Wen, F., Li, W. και Rong, H.,** *Creation of the macromodel of equivalent circuit and IP library for clamped-clamped beam microsensor,* Journal of Research & Progress of Solid State Electronics, 2004, Vol. 24, pp. 68-72

98. **Zhang, J. και Li, W.H.,** *Method of system-level dynamic simulation for a MEMS cantilever based on the mechanical description.*, Chinese Journal of Sensors and Actuators, 2006, Vol. 19, pp. 1376-1380

99. **Hu, Y.C., Chang, C.M. και Huang, S.C.,** *Some design considerations on the electrostatically actuated microstructures,* Journal of Sensors & Actuators, 2004, Vol. 112, pp. 155-161

100. **Wang Z, et al,** *Analysis of RF-MEMS switches using finite element-boundary integration with moment method,* Proceedings of IEEE Society International Conference on Antennas and propagation, 2003, Vol. 2, pp. 173-176.

101. **Hanqing W., and Xiaoping L.,** *RF Characteristics and Modeling of the RF-MEMS Switch Packaging***,** In proccedings IEEE, 7th International Conference on Electronics Packaging Technology, 2006.

102. **Katehi A., et al,.** *Fabrication and Accelerated Hermeticity Testing of an On-Wafer Package for RF MEMS,* IEEE Transactions on Microwave Theory and Techniques, 2004, Vol. 52, pp. 1626-1636.

103. Comsol, www.comsol.com.

104. Ansys, www.ansys.com.

105. Intellisense, www.intellisense.com.

106. Ansoft, www.ansoft.com.

107. Feko, www.feko.com.

108. **Guo, Z., McGruer, N. and Adams,** *Modeling, simulation and measurement of the dynamic performance of an ohmic contact, electrostatically actuated RF-MEMS switch,* Journal of micromechanics and microengineering, IOP Publishing, 2007, pp. 1899-1909.

109. **Saha, S.C., et al,.** *Modeling of Spring Constant and Pull-down Voltage of Non uniform RF-MEMS Cantilever, In* Proceedings IEEE International, Behavioral Modeling and Simulation Workshop, San Jose, CA, USA, Sept. 2006, pp.55-60.

110. **McClure, S.S., et al,** *Radiation effects in micro-electromechanical systems (MEMS): RF relays*, Transactions on Nuclear Science, IEEE, December 2002, Vol. 49, pp. 3197-3202.

111. **Chow, L.L.W. and Kurabayashi, K.** *Understanding and control of unstable contact resistance in RF-MEMS gold-gold direct contact switches*, In Proceedings of IEEE 23rd International Conference on Micro Electro Mechanical Systems (MEMS), Wanchai, Hong Kong, 2010, pp.771-774.

112. **Carton, A., et al,** *Investigating the Impact of Carbon Contamination on RF-MEMS Reliability*, Proceedings on antennas and propagation society International Symposium, IEEE, 2006, pp.193-196.

113. **Dyck, C., et al,** *Fabrication and Characterization of Ohmic Contacting RF-MEMS Switches,* Proceedings of MEMS/MOEMS components and their applications, SPIE, Bellingham, WA, 2004, Vol. 5344, pp. 79-88.

114. **Maligno, A., Whalley, D. and Silberschmidt, V.** *Interfacial failure under thermal fatigue loading in multilayered MEMS structures*, Proceedings on WCCM/APCOM 2010, IOP, 2010.

115. **Coutu, R., et al,** *Selecting metal alloy electric contact materials for MEMS switches*, Journal of micromechanics and microengineering, IOP Publishing, Vol. 14, pp. 1157–1164.

116. **Kwon, H., et al,** *Investigation of the electrical contact behaviors in Au-to-Au thin-film contacts for RF-MEMS switches*, Journal of micromechanics and microengineering, IOP Publishing 2008, Vol.18, pp. 105-110.

117. **Rezvanian, O., et al,** *Surface roughness, asperity contact and gold RFMEMS switch behavior*, Journal of micromechanics and microengineering, IOP Publishing, 2007, Vol.17, pp. 2006-2015.

118. **Timsit, R. S.,** *Electrical Contact Resistance: Properties of Stationary Interfaces*, Transactions on components and packaging technology, IEEE, 1999, Vol. 22, pp.1-19.

119. **McGruer, N., et al,** *Mechanical, thermal and material influences on ohmic contact type RF-MEMS switches,* Proceedings of International conference on MEMS. IEEE, Istanbul 2006, pp. 230-233.

120. **Mercado, L., et al,** *Mechanics-Based Solutions to RF-MEMS Switch Stiction Problem*, Transactions on Component and Packaging Technologies, IEEE, September 2003, Vol. 27, pp. 560-567.

121. **Ali, S. and Phinney, L.,** *Investigation of adhesion during operation of MEMS cantilevers*, Proceedings on Reliability, Testing, and Characterization of MEMS/MOEMS I, SPIE, December 2003, pp.215-226.

122. **Sumali, H., et al,** *Waveform design for pulse-and-hold electrostatic actuation in MEMS*, Elsevier, Journal of Actuators and sensors, 2006. pp. 213-220

123. **Hyman, D. and Mehregany, M.** *Contact Physics of Gold Microcontacts for MEMS Switches*, Transactions on Components and Packaging Technologies, IEEE, September 1999, Vol. 22, pp. 133-140.

124. **Liu, Lianjun,** *High Performance RF-MEMS Series Contact Switch - Design and Simulations*, Reno, NV, Electronic Components and Technology Conference, IEEE, 2007, pp. 158-164.

125. **Zavracky, P., et al,** *Microswitches and Microrelays with a View Toward Microwave Applications*, International Journal of RF and Microwave Computer-Aided Engineering, 1999, Vol. 9, pp. 338–347

126. **Zhao, Y., Wang, L. and Yu, T.**, *Mechanics of adhesion in MEMS — a review*, Adhesion Science Technology, 2003, Vol. 17, pp. 519-554.

127. **Yan, X., et al,** *Finite Element Analysis of a MEMS switch using ANSYS*, Ansys.com.

128. **Borovic, B., et al,** *Open-loop versus closed-loop control of MEMS devices: choices and issues*, IOP, JOURNAL OF MICROMECHANICS AND MICROENGINEERING, 2005, Vol.6, pp. 1917–1924.

129. **Castaner, L.,** *Drive methods for electrostatic MEMS switches*, UIC seminar, Barcelona, Spain, 2005.

130. **Senturia, S.** *MICROSYSTEM DESIGN*, Kluwer Academic Publishers, N.Y., USA, 2002.

131. **Ou, K., et al,** *A command shaping approach to enhance the dynamic performance and longevity of contact switches*, Elsevier, Journal of Mechatronics, 2008, pp. 375-389.

132. **Czaplewski, D., et al,** *A Soft-Landing Waveform for Actuation of a Single-Pole Single-Throw Ohmic RF-MEMS Switch*, IEEE, Journal of microelectromechanical systems, 2006, Vol. 15, pp. 1586-1594.

133. **Massad, J., et al,** *Modeling, Simulation, and Testing of the Mechanical Dynamics of an RF-MEMS Switch,* International Conference on MEMS, NANO and Smart Systems (ICMENS'05), 2005.

134. **Allen, M., Field, R. and Massad, J.,** *Modeling and Input Optimization under Uncertainty for a Collection of RF-MEMS Devices,* Chicago, ASME International Mechanical Engineering Congress and Exposition, November 2006.

135. **Daqaq, M. F., et al,** *Input-shaping control of nonlinear MEMS.,* Springer, Journal of Nonlinear Dynamics, 2008, Vol. 54, pp. 167-179.

136. **Do, C., et al,** *Dual-Pulse Control to Eliminate Bouncing of Ohmic RF-MEMS Switch.* Cork, Ireland, In Proceedings of ISSC 2010, June 23–24, 2010.

137. **Donelli, M., et al,** *Linear antenna synthesis with a hybrid Genetic Algorithm,* Progress In Electromagnetics Research, PIER, France 2004.

138. **Deligkaris, K., et al,** *Thinned Planar Array Design Using Boolean PSO With Velocity Mutation,* IEEE Transactions on Magnetics, 2009, Vol. 45, pp. 1490-1493.

139. **Karatzidis, D., et al,** *Gradient-based adjoint-variable optimization of broadband microstrip antennas with mixed-order prism macroelements,* AEUE International Journal of Electronics and Communications, 2008, Vol. 62, pp. 401–412.

140. **Haupt, R.,** *Comparison between Genetic and gradient-based optimization algorithms for solving electromagnetic problems,* IEEE, Transactions on Magnetics, 1995, Vol. 31, pp. 1932-1935.

141. **Taguchi, G. and Yokoyama, Y.** *Taguchi Methods: Design of Experiments, Quality Engineering, Vol. 4,* Amer Supplier Institute, 1993.

142. **Taguchi, G., Chowdhury, S. and Wu, Y.,** *Taguchi's Quality Engineering Handbook,* Wiley-Interscience, 2004.

143. **Ousterhout, J.,** *AIM superset of Tcl/Tk scripting language.* UC Berkeley.

144. **Castaner L., Senturia S.,** *Speed-Energy Optimization of Electrostatic Actuators Based on Pull-In.* IEEE, Journal of Microelectromechanical Systems, September 1999, Vol. 8, pp. 290-298.

145. **Castaner, L., et al,** *Analysis of the extended operation range of electrostatic actuators by current-pulse drive.,* Elsevier, Journal of Sensors and actuators, 2001, Vol. 90, pp. 181-190.

146. **Nadal-Guardia, R., et al,** *Current Drive Methods to Extend the Range of Travel of Electrostatic Microactuators Beyond the Voltage Pull-In Point,* Journal of Microelectromechanical Systems, 2002, Vol. 11, pp. 255-263.

147. **Jimenez V., et al,** *Transient dynamics of a MEMS variable capacitor driven with a Dickson charge pump,* Elsevier, Journal of Sensors and Actuators, 2006. pp. 89-97

148. **Pons-Nin, J., et al,** *Voltage and Pull-In Time in Current Drive of Electrostatic Actuators,* IEEE, Journal of Microelectromechanical Systems 2002, Vol. 11, pp.196-205.

149. **Lee, J. και Goldsmith, C.,** *Numerical simulations of novel constant-charge biasing method for capacitive RF-MEMS switch.* San Francisco, CA, In Proceedings of NanoTech Conference, 2003. pp.396-399.

150. **Blecke, J., et al,** *A Simple Learning Control to Eliminate RF-MEMS Switch Bounce.* IEEE, Journal of Microelectromechanical Systems, 2009, Vol. 18, pp.458-465.

151. **Varehest, M., et al,** *Resistive Damping of Pulse-Sensed Capacitive Position Sensors,* TRANSDUCERS '97, international Conference on Solid-state Sensors and Actuators, IEEE, Chicago, June 16-19, 1997.

152. **Chang, H., et al,** *Design and Process Considerations for Fabricating RF-MEMS switches on Printed Circuit Boards,* Journal of Microelectromechanical Systems, 2005, Vol. 14, pp. 1311-1322.

153. **Ghodsian, B., et al,** *Development of RF-MEMS Switch on PCB Substrates with Polyimide Planarization,* IEEE sensors journal, 2005, Vol. 5, pp. 950-955.

154. **Wahid, P., Ali, M. and DeLoach, B.,** *A reconfigurable Yagi antenna for wireless communications,* Microwave and optical technology letters, 2003, Vol. 38.

155. **Baik, J., et al,** *Switchable Printed Yagi-Uda Antenna with pattern reconfiguration,* ETRI Journal, June 2009, Vol. 31.

156. **Balanis, C. A.,** *Antenna theory (analysis and design),* WILLEY INTERSCIENCE, 2005, ISBN: 0-471-66782-X.

156. **Kennedy, J. and Eberhart, R.,** *Particle swarm optimization,* Perth, Australia, IEEE, International Conference on Neural Networks, 1995.

157. **Eberhart, R. and Shi, Y.,** *Comparison between genetic algorithms and particle swarm optimization,* Anchorage, IEEE International Conference of Evolutionary Computing, May, 1998.

158. **Eberhart, R. και Shi, Y.,** *Comparison between genetic algorithms and particle swarm optimization,* In Proccedings IEEE International Conference of Evolutionary Computing, Anchorage, USA, May, 1998.

159. **Shi, Y. και Eberhart, R. C.**, *A modified particle swarm optimizer,* In Proceedings of the IEEE international conference on evolutionary computation, 1998, pp. 69-73.

160. **Gaing, Z.-L.,** *A Particle Swarm Optimization Approach for Optimum Design of PID Controller in AVR System,* IEEE, transactions on energy conversion, 2004, pp. 384 - 391.

161. **Spasos M., Charalampidis N., Tsiakmakis K., Nilavalan R.,** *RF-MEMS Switch actuation pulse optimization using Taguchi's method,* Springer, Microsystems Technologies, 2011, (in press)

162. **Spasos M., Charalampidis N., Tsiakmakis K., Nilavalan R.,** *Optimization of a 12GHz microstrip antenna array using Taguchi's method,* International Journal of Antennas and Propagation, 2011, (Under review)

163. **Spasos M., Charalampidis N., Tsiakmakis K., Nilavalan R.,** *Improving controllability in RF-MEMS switches using resistive damping,* EUMA, MEMSWAVE, 2011, (Under review).

164. **Spasos M. and Nilavalan R.,** *On the investigation of a reliable actuation control method for ohmic RF MEMS switches,* Sensors Journal, 2011, (Under review)

165. **Spasos M. and Nilavalan R.,** *On the comparison between two all-metal in-line-series ohmic RF-MEMS switches,* Microelectronics journal, Elsevier, 2011, (Under review)

Appendix

A.1 Modelling the "Hammerhead" ohmic RF-MEMS switch in CoventorWare

The design and evaluation of the "Hammerhead" ohmic RF-MEMS switch has been carried out mainly using the Architect module, the parametric MEMS design environment of Coventoreware software package. Architect module is using lumped elements from parametric libraries for fast and accurate results in cooperation with Saber sketch of Synopsis. **Saber** is a multi-domain modeling and simulation environment that enables full-system virtual prototyping for applications in analog/power electronics and mechatronics. An example of the design and simulation process steps is described below:

- Specify the fabrication process and the material information
- Open a new schematic from the process and material database
- Create a 3D model of MEMS device using components from the appropriate multi-physics libraries or by using the comprehensive Architect component libraries
- Specify dimensions in the property window for each symbol and create a fully parametric model using only a handful of global variables
- Create a 3D image of the schematic model in Architect Scene 3D
- Create variations of the model by varying a single global parameter
- Select and manipulate the view of the individual components using the hierarchical schematic representation of the tree view
- Run simulations such as (DC analysis, Transient analysis, Frequency analysis)
- Run analysis based on simulations results (Statistic, Fourier, Stress)
- Load and animate results in 3D or monitor the progress of the simulation while it's running
- Export the model as GDSII or SAT file Layout

For a more detailed evaluation the same design can be imported from Architect as GDSII or can be rebuilt in Designer module, which performs the following actions:

- creates, imports and exports 2-D layouts of MEMS design
- manages MEMS fabrication technology data
- performs MEMS-specific design rule checks (MEMS-DRC) on layouts
- automatically generates 3-D solid models from 2-D layouts
- automatically generates efficient meshes, views and mesh quality checks
- imports and exports solid models in widely used CAD formats
- accesses Foundry Process Design Kits for standard MEMS fabrication processes

The 3D meshed solid model is examined next as a Field Element Model (FEM) in Analyzer module. In Analyzer, exact multi-physics simulations that are critical to investigate the MEMS switch behavior are performed. Such kinds of simulations include the following solvers.

- MemElectro, for electrostatic and electroquastatic analysis
- MemMech, for mechanical, thermomechanical and piezoelectric analysis
- CoSolveEM, for coupled electromechanical-static analysis
- HarmonicEM, for coupled electromechanical-frequency domain analysis
- MemPZR, for piezo-resistance analysis
- MemHenry, for electrical inductance and resistance analysis
- SpringMM, for electrostatic, mechanical or electromechanical analysis
- DampingMM, for squeezed, slide-film or free space fluid damping analysis
- InertiaMM, for proof mass or plate inertia analysis

Some of the multi-physics characteristics in Analyzer can be extracted as behavioral models in the form of macro-model in Integrator module, such as:

- Squeeze and slidefilm damping due to gas trapped in small gaps based on Reynolds equations solving
- Free-space gas flow around parts based on Stokes equations solving
- Mechanical stiffness of structural components can be modeled as linear or non-linear mechanical springs

- Electrostatic forces between electrodes can be modeled as electrostatic springs
- Inertia of inflexible components can be modeled as rigid bodies

These behavioral models then can be extracted back to Architect as components for use with the rest of the system.

A.2 Charge drive control

Under charge control Castaner L. et al [145] proved that the Pull-in phenomenon of the Voltage powered electrostatic actuators does not exists and if the current drive is ideal, any position across the gap is stable. The main reason for this behavior is that the electrostatic force that applied is always attractive and independent of the remaining gap of the actuator.

Some more publication on this field (parallel plate actuators) presents how it can be impemented [129], [130].

The energy for this system is given by:

$$W = \frac{Q^2}{2C(x)} \tag{74}$$

And the electrostatic force under constant charge conditions is computed as:

where $g = g_0 - x$

$$m\frac{d^2X}{dT^2} + b\frac{dX}{dT} + kX = \frac{Q^2}{2C_0 g_0} \tag{75}$$

$$I_s = \frac{dQ}{dT} \tag{76}$$

Making a first normalization the following non-dimensional quantities are obtained:

$$x = \frac{X}{g_0} \qquad t = \omega_0 T, \qquad q = \frac{Q}{Q_p} \qquad Q_p = \frac{3}{2} C_0 V_{PI} \qquad \omega_0 = \sqrt{\frac{k}{m}}$$

And the equation of motion can be rewritten as.

$$m\frac{d^2x}{dt^2} + \frac{b}{2m\omega_0}\frac{dx}{dt} + x = \frac{q^2}{3} \tag{77}$$

$$\frac{dq}{dt} = \frac{2}{3}i_s \tag{78}$$

Where

$$i_s = \frac{I_s}{V_{PI}\omega_0 C_0} \tag{79}$$

$$F_{el} = \frac{\partial U^*}{\partial x}\Big)_Q = \frac{Q^2}{2C_0 g_0} = \frac{q^2 k g_0}{3} \tag{80}$$

$$F_m = kX = kg_0 x \tag{81}$$

By normalizing these two forces we obtain the normalized electrostatic f_e and mechanical f_m forces as follows

$$f_e = \frac{F_e}{kg_o} = \frac{q^2}{3}, \tag{82}$$

$$f_m = \frac{F_m}{kg_0} = x \tag{83}$$

And the stability condition becomes

$$\left(\frac{d}{dx}\left(\frac{q^2}{3} - x\right)\right) < 0 \tag{84}$$

The value of the left hand side is always -1 and hence the condition in the above equation is satisfied for any value of x provided q is constant. From the above equation is concluded that the electrostatic force that applied is always attractive and independent of the distance.

A.3 Grid Taguchi optimization technique

As an example, an optimization problem consisting of three parameters with central estimating values A=10, B=20, C=30 and a search area of about ±45% around them is considered. For this case an $OA_9(3^3)$ consist of 3columns, 3 levels for each parameter and 9 rows is defined as the master OA (Table A1). The initial deviation is calculated as:

$$L_A = A \pm \left(0.45A\frac{2}{3}\right) = 10 \pm 3 \quad (85)$$

And the three levels of the parameter A are defined as:

1A=7, 2A=10 and 3A=13

In the same way substituting the values of B and C to the above equation their levels are calculated as:

1B=14, 2B=20 and 3B=26

1C=21, 2C=30 and 3C=39

The master $OA_9(3^3)$ with the calculated levels is shown in Table A2.

Table A1. $OA_9(3^3)$

	A	**B**	**C**
1	1	1	1
2	1	2	2
3	1	3	3
4	2	1	2
5	2	2	3
6	2	3	1
7	3	1	3
8	3	2	1
9	3	3	2

Table A2. Master OA levels

	A	**B**	**C**
1	7	14	21
2	7	20	30
3	7	26	39
4	10	14	30
5	10	20	39
6	10	26	21
7	13	14	39
8	13	20	21
9	13	26	30

The *1st* slave OA is created with central values A_1=7, B_1=14, C_1=21 from the values of the first row of Table A2 and the initial deviation of each parameter as:

$$L_{A(S)} = A_1 \pm \left(0.45A\frac{1}{3}\right) = 7 \pm 1.5$$

And the levels of the parameter $\mathbf{A_1}$ are defined as:

1$\mathbf{A_1}$=5.5 2$\mathbf{A_1}$=7 3$\mathbf{A_1}$=8.5

In the same way, substituting the values of B_1 and C_1 to the above equation their levels are calculated as:

1B_1=11 2B_1=14 3B_1=17

1C_1=16.5 2C_1=21 3C_1=25.5

The 2nd slave OA is created having central values A_2=7, B_2=20, C_2=30 from the values of the second row of Table A2 and the levels of the parameters as:

1A_2=5.5 2A_2=7 3A_2=8.5

1B_2=17 2B_2=20 3B_2=23

1C_2=25.5 2C_2=30 3C_2=34.5

Substituting the calculated levels in Table A1 the slave OA for the second row is created as shown in Table A4.

Substituting the calculated levels in Table A1 the slave OA for the first row is created as shown in Table A3.

Table A3. *1st* slave OA levels

	A_1	**B_1**	**C_1**
1	5.5	11	16.5
2	5.5	14	21
3	5.5	17	25.5
4	7	11	21
5	7	14	25.5
6	7	17	16.5
7	8.5	11	25.5
8	8.5	14	16.5
9	8.5	17	21

Table A4. *2nd* slave OA levels

	A_2	**B_2**	**C_2**
1	5.5	17	25.5
2	5.5	20	30
3	5.5	23	34.5
4	7	17	30
5	7	20	34.5
6	7	23	25.5
7	8.5	17	34.5
8	8.5	20	25.5
9	8.5	23	30

The 3rd slave OA is created having central values A_3=7, B_3=26, C_3=39 from the values of the third row of Table A2 and the levels of the parameters as:

$1A_3$=5.5	$2A_3$=7	$3A_3$=8.5
$1B_3$=23	$2B_3$=26	$3B_3$=29
$1C_3$=34.5	$2C_3$=39	$3C_3$=43.5

Substituting the calculated levels in Table A1 the slave OA for the third row is created as shown in table A5.

Table A5. *3rd* slave OA levels

	A_3	**B_3**	**C_3**
1	5.5	23	34.5
2	5.5	26	39
3	5.5	29	43.5
4	7	23	39
5	7	26	43.5
6	7	29	34.5
7	8.5	23	43.5
8	8.5	26	34.5
9	8.5	29	39

The 4th slave OA is created having central values A_4=10, B_4=14, C_4=30 from the values of the fourth row of Table A2 and the levels of the parameters as:

$1A_4$=8.5,	$2A_4$=10	$3A_4$=11.5
$1B_4$=11,	$2B_4$=14	$3B_4$=17
$1C_4$=25.5,	$2C_4$=30	$3C_4$=34.5

Substituting the calculated levels in Table A1 the slave OA for the fourth row is created as shown in table A6.

Table A6. *4th* slave OA levels

	A_4	**B_4**	**C_4**
1	8.5	11	25.5
2	8.5	14	30
3	8.5	17	34.5
4	10	11	30
5	10	14	34.5
6	10	17	25.5
7	11.5	11	34.5
8	11.5	14	25.5
9	11.5	17	30

The 5^{th} slave OA is created having central values A_4=10, B_4=20, C_4=39 from the values of the fifth row of Table A2 and the levels of the parameters as:

$1A_5$=8.5, $2A_5$=10 $3A_5$=11.5
$1B_5$=17, $2B_5$=20 $3B_5$=23
$1C_5$=34.5, $2C_5$=39 $3C_5$=43.5

Substituting the calculated levels in Table A1 the slave OA for the fifth row is created as shown in table A7.

Table A7. 5^{th} slave OA levels

	A_5	**B_5**	**C_5**
1	8.5	17	34.5
2	8.5	20	39
3	8.5	23	43.5
4	10	17	39
5	10	20	43.5
6	10	23	34.5
7	11.5	17	43.5
8	11.5	20	34.5
9	11.5	23	39

The 6^{th} slave OA is created having central values A_6=10, B_6=14, C_6=30 from the values of the sixth row of Table A2 and the levels of the parameters as:

$1A_6$=8.5, $2A_6$=10 $3A_6$=11.5
$1B_6$=23, $2B_6$=26 $3B_6$=29
$1C_6$=16.5, $2C_6$=21 $3C_6$=25.5

Substituting the calculated levels in Table A1 the slave OA for the sixth row is created as shown in table A8.

Table A8. 6^{th} slave OA levels

	A_6	**B_6**	**C_6**
1	8.5	23	16.5
2	8.5	26	21
3	8.5	29	25.5
4	10	23	21
5	10	26	25.5
6	10	29	16.5
7	11.5	23	25.5
8	11.5	26	16.5
9	11.5	29	21

The 7^{th} slave OA is created having central values A_7=13, B_7=14, C_7=39 from the values of the seventh row of Table A2 and the levels of the parameters as:

$1A_7$=11.5	$2A_7$=13	$3A_7$=14.5
$1B_7$=11	$2B_7$=14	$3B_7$=17
$1C_7$=34.5	$2C_7$=39	$3C_7$=43.5

Substituting the calculated levels in Table A1, the slave OA for the seventh row is created as shown in table A9.

Table A9. 7^{th} slave OA levels

	A_7	**B_7**	**C_7**
1	11.5	11	34.5
2	11.5	14	39
3	11.5	17	43.5
4	13	11	39
5	13	14	43.5
6	13	17	34.5
7	14.5	11	43.5
8	14.5	14	34.5
9	14.5	17	39

The 8^{th} slave OA is created having central values A_8=13, B_8=20, C_8=21 from the values of the eighth row of Table A2 and the levels of the parameters as:

$1A_8$=11.5	$2A_8$=13	$3A_8$=14.5
$1B_8$=17	$2B_8$=20	$3B_8$=23
$1C_8$=16.5	$2C_8$=21	$3C_8$=25.5

Substituting the calculated levels in Table A1 the slave OA for the eighth row is created as shown in table A10.

Table A10. 8^{th} slave OA levels

	A_8	**B_8**	**C_8**
1	11.5	17	16.5
2	11.5	20	21
3	11.5	23	25.5
4	13	17	21
5	13	20	25.5
6	13	23	16.5
7	14.5	17	25.5
8	14.5	20	16.5
9	14.5	23	21

The 9^{th} slave OA is created having central values A_9=13, B_9=26, C_9=30 from the values of the ninth row of Table A2 and the levels of the parameters as:

$1A_9$=11.5	$2A_9$=13	$3A_9$=14.5
$1B_9$=23	$2B_9$=26	$3B_9$=29
$1C_9$=25.5	$2C_9$=30	$3C_9$=34.5

Substituting the calculated levels in Table A1 the slave OA for the ninth row is created as shown in table A11.

Table A11. 9^{th} slave OA levels

	A_9	**B_9**	**C_9**
1	11.5	23	25.5
2	11.5	26	30
3	11.5	29	34.5
4	13	23	30
5	13	26	34.5
6	13	29	25.5
7	14.5	23	34.5
8	14.5	26	25.5
9	14.5	29	30